
Probing many-body physics with multiorbital quantum gases

Nelson Darkwah Oppong



München 2021

Probing many-body physics with multiorbital quantum gases



Dissertation an der Fakultät für Physik
Ludwig-Maximilians-Universität München

vorgelegt von

Nelson Darkwah Oppong

aus Tönisvorst

München, den 4. März 2021

Tag der mündlichen Prüfung: 15. April 2021

Erstgutachter: Prof. Immanuel Bloch

Zweitgutachterin: Prof. Meera Parish

Weitere Prüfungskommissionsmitglieder: Prof. Jan von Delft, Prof. Jan Lipfert

Zusammenfassung

Diese Arbeit präsentiert zwei Experimente, welche für die Realisierung von Vielteilchenphysik mit einem orbitalen Freiheitsgrad ultrakalte Atome verwenden. Insbesondere werden im Rahmen dieser Arbeit experimentelle Techniken entwickelt, um das Fermi-Polaron-Problem in der Nähe einer orbitalen Feshbach-Resonanz zu untersuchen und die Relaxationsdynamik im eindimensionalen Fermi-Hubbard-Modell mit ungleichen Massen zu analysieren.

Quasiteilchen wie das Fermi-Polaron sind ein elementarer Bestandteil von Landaus Fermi-Flüssigkeits-Theorie und finden umfangreiche Anwendung bei der Beschreibung wechselwirkender Elektronensysteme. Im ersten Teil dieser Arbeit benutzen wir die kürzlich entdeckte orbitale Feshbach-Resonanz in Ytterbium, um multiorbitale Fermi-Polaronen in Mischungen aus Atomen im Grundzustand und metastabilen Uhrenzustand zu erzeugen. Zu diesem Zweck setzen wir spektroskopische Messungen auf dem Uhrenübergang ein und identifizieren das attraktive als auch das repulsive Polaron im Vielteilchenspektrum des zweidimensionalen Teilchen-Bad-Systems. Außerdem bestimmen wir weitere wichtige Eigenschaften dieses Quasiteilchens—nämlich das Residuum und die Lebensdauer. Die Resultate unserer Messungen stimmen gut mit einer spezifischen Vielteilchentheorie überein und bestätigen damit die Bedeutung orbitaler Wechselwirkungen für das Fermi-Polaron-Problem.

Im zweiten Experiment untersuchen wir das Fermi-Hubbard-Modell für ungleiche Massen mit Ytterbium-Atomen, die in einem zustandsabhängigen optischen Gitter für den Grundzustand und metastabilen Uhrenzustand gefangen sind. In diesen beiden Zuständen werden Atome präpariert und entsprechen dabei schweren und leichten Teilchen, die sehr unterschiedliche dynamische Zeitskalen aufweisen. Zuletzt wurden solche Modelle ausführlich im Zusammenhang von Lokalisierungs- und Thermalisierungsprozessen in isolierten Quanten-Vielteilchen-Systemen erforscht. Um die Nicht-Gleichgewichtsdynamik in unserem System zu untersuchen, zeichnen wir die Dichte der leichten Spezies auf, nachdem das externe Fallenpotential geändert wurde. Auf diese Weise identifizieren wir eine starke Unterdrückung des Transports zu frühen Zeiten und eine langsame Relaxation zu späten Zeiten mit signifikanter Abhängigkeit von der dynamischen Zeitskala und der Wechselwirkungsstärke beider Spezies. Unsere Ergebnisse zeigen, dass Metastabilität und extrem langsame Thermalisierung aufgrund dynamischer Einschränkungen auftreten können.

Die in dieser Arbeit entwickelten Experimente zu multiorbitaler Vielkörperphysik ebnen den Weg für Quantensimulatoren, die offene Fragen zu Theorien kondensierter Materie beantworten könnten.

Abstract

This thesis reports on two experiments employing ultracold atoms to realize many-body physics in the presence of an orbital degree of freedom. In particular, we develop the experimental techniques to probe the Fermi polaron problem across an orbital Feshbach resonance and examine the relaxation dynamics in the one-dimensional mass-imbalanced Fermi-Hubbard model.

Quasiparticles like the Fermi polaron constitute an elementary part of Landau's Fermi liquid theory and find extensive application in the description of interacting electron systems. In the first part of this thesis, we exploit the recently observed orbital Feshbach resonance in ytterbium to produce multiorbital Fermi polarons in mixtures of ground state and clock state atoms. To this end, we employ clock-line spectroscopy and identify the repulsive as well as attractive polaron in the many-body spectrum of the two-dimensional impurity-bath system. We also determine other important quasiparticle properties, namely, the residue and lifetime. Our measurement results agree well with a tailored many-body theory, thereby confirming the relevance of orbital interactions for the Fermi polaron problem.

In the second experiment, we study the mass-imbalanced Fermi-Hubbard model with ytterbium atoms trapped in a state-dependent optical lattice for the ground and metastable clock state. Atomic populations are prepared in both of these states and correspond to heavy and light particles exhibiting vastly different dynamical time scales. Recently, such models have been extensively explored in the context of localization and thermalization in isolated quantum many-body systems. To probe non-equilibrium dynamics in our system, we record the density of the light species after adjusting the external trapping potential. In this way, we identify a strong suppression of transport at early times and slow relaxation at late times, with a significant dependence on the dynamical time scale and interaction strength of both species. Our results demonstrate the emergence of metastability and extremely slow thermalization due to dynamical constraints.

The implementations of multiorbital many-body physics established within this thesis pave the way for quantum simulators that could shed light on open questions in condensed-matter theory.

Contents

Introduction	1
1 Multiorbital physics with ultracold ytterbium	7
1.1 Electronic structure of neutral ytterbium	7
1.2 Interactions in orbital mixtures	9
1.2.1 Elastic scattering in ultracold gases	9
1.2.2 Nuclear spin states	11
1.2.3 Orbital interaction channels	12
1.2.4 Orbital Feshbach resonances	14
1.3 State-dependent optical lattices	16
1.3.1 The multiorbital Fermi-Hubbard model	19
1.3.2 The Kondo model	19
1.3.3 The mass-imbalanced Fermi-Hubbard model	22
1.4 Production and probing of multiorbital Fermi gases	22
1.4.1 Producing degenerate Fermi gases	22
1.4.2 Preparing multiorbital mixtures	23
1.4.3 High-resolution absorption imaging	25
2 Fermi polarons	27
2.1 The single quasiparticle problem	27
2.1.1 Chevy’s variational wave-function ansatz	28
2.1.2 The Green’s function approach	29
2.2 Phenomenology in two dimensions	31
2.2.1 The self-energy	32
2.2.2 Quasiparticles and their energy landscape	33
2.2.3 Finite momentum and temperature	35
2.3 The quasi-two-dimensional regime	38
2.3.1 Open-channel orbital interactions	40
2.3.2 The effective two-channel model	41
2.3.3 The multiorbital Fermi polaron	44

3	Multiorbital polarons in two-dimensional Fermi gases	46
3.1	Population-imbalanced multiorbital Fermi gases	46
3.1.1	Producing spin-imbalanced mixtures	47
3.1.2	Preparing quasi-two-dimensional ensembles	48
3.1.3	Populating the second orbital	49
3.2	Characterization of the initial state	50
3.2.1	Effective parameters	51
3.2.2	In-situ thermometry	53
3.3	Inverse clock-line spectroscopy	56
3.3.1	Initial-state interactions	56
3.3.2	Transfer rates	57
3.3.3	The many-body spectrum	58
3.4	Coherent Rabi oscillations	61
3.4.1	The quasiparticle residue	63
3.4.2	Damping of the repulsive polaron	65
3.5	Decay of the repulsive branch	67
3.5.1	Three-body recombination	69
3.6	Frustrated interactions	70
3.6.1	Fermi-liquid description of the medium	71
3.6.2	Quasiparticle energies with two Fermi seas	73
3.7	Discussion	74
4	Absence of thermalization in quantum many-body systems	75
4.1	Thermalization in isolated quantum systems	75
4.1.1	Eigenstate thermalization	76
4.2	Evading thermalization	78
4.2.1	Anderson localization	79
4.2.2	Many-body localization	80
4.2.3	Self-localization of mixtures	83
4.3	The mass-imbalanced Fermi-Hubbard chain	84
4.3.1	Single-particle localization	86
4.3.2	Quasi-many-body localization	86
4.3.3	Few-body bound states	91
5	Slow relaxation in mass-imbalanced Fermi-Hubbard chains	95
5.1	Tunable heavy-light mixtures in optical lattices	95
5.1.1	One-dimensional systems	96
5.1.2	Tuning the hopping ratio	97
5.1.3	Tuning the interaction strength	99
5.2	Probing transport	101
5.2.1	Numerical simulations	102
5.2.2	Translation of the trap minimum	105
5.2.3	Stark localization	106

5.3	Mobility in the mixture	108
5.3.1	Initial state preparation	109
5.3.2	Inhibited transport	110
5.3.3	The mass-balanced regime	112
5.4	Late-time dynamics	115
5.4.1	Probing relaxation time scales	116
5.4.2	Dissipative dynamics	119
5.5	Discussion	122
Conclusions and outlook		123
Appendices		126
A	Derivation of the Fermi polaron self-energy	126
B	Derivation of the low-energy scattering amplitude	130
C	Fermi gases in two dimensions	133
D	Approximate calculations of the dynamical correlator	135
E	Density dynamics of the heavy species	137
References		138

Introduction

The detailed study of many-body physics with ultracold quantum gases has seen remarkable progress in the last two decades [1, 2]. Various experiments can now probe complex quantum systems in regimes challenging to access with simulations on classical computers [2, 3], thereby realizing parts of Feynman’s vision for analog quantum simulations [4]. These advancements have paved the way for exploring numerous open questions ranging from condensed-matter physics and strongly correlated materials [5–7] to more fundamental aspects such as ergodicity and thermalization in isolated quantum systems [8–10].

Discoveries at the forefront of research on cold atomic systems have been primarily driven by the development of groundbreaking experimental techniques. This particularly applies to optical lattices, which offer a defect-free potential landscape for fermionic atoms simulating interacting electrons in a crystal [2]. In contrast to real materials, the kinetic and interaction energy of these atoms can be adjusted freely by varying the power of a laser beam or the strength of an external magnetic field [1]. Such an unprecedented level of control and flexibility opens the door for quantum simulation experiments of models highly relevant in solid-state theory, most notably the Fermi-Hubbard model [11]. In this context, pioneering work has employed alkali atoms in optical lattices to engineer tailored quantum matter that resembles the Fermi-Hubbard model, as clearly demonstrated by probing its Mott-insulating phase [12, 13]. Remarkably, subsequent experiments have also observed and characterized antiferromagnetic order emerging at low temperatures [14–18], where the doped Fermi-Hubbard model is believed to describe unconventional superconductivity [6].

While the conceptual appeal of the Fermi-Hubbard model lies in its simplified single-orbital description of more complex materials, it does not capture fascinating multiorbital phenomena such as heavy fermions, orbital ordering, or colossal magnetoresistance [5, 7]. In this context, orbitals describe the spatial wave function of electrons and thereby determine their (directional) mobility and interactions in strongly correlated materials [5, 7]. Improving our limited understanding of the physics governing these materials calls for the simulation of the associated multiorbital models in the well-controlled setting of ultracold atoms [19–25]. Nevertheless, previous work in this setting has mainly focused on single-orbital physics since orbital-dependent mobility schemes for alkali atoms have been plagued by short lifetimes, increased complexity, and limited flexibility [26–29].

A promising avenue for realizing an orbital degree of freedom in cold atomic systems has emerged with the use of different atomic species whose electronic structure offers more flexibility [30]. In contrast to alkali metals, alkaline-earth(-like) atoms, such as strontium and ytterbium, feature a metastable electronic state known as clock state due to its application

in atomic clocks [31]. The ultranarrow clock transition connecting these two states has enabled optical lattice clocks to reach record precision and accuracy at the level of a few parts in 10^{-18} [32–34]. For example, this astonishing level of sensitivity has also allowed strontium and ytterbium clocks to join the search for dark matter [35, 36]. Besides atomic clocks, alkaline-earth(-like) atoms have been considered for a broad range of quantum simulations and potential applications, for example, exotic quantum magnetism [19, 37, 38], artificial gauge fields [39], (lattice) gauge theories [40, 41], and quantum computation schemes [42].

In tailored optical potentials, known as state-dependent lattices [43–45], the clock state together with the ground state can be utilized as an orbital degree of freedom such that atomic mobility robustly depends on the orbital state. Fermionic strontium and ytterbium isotopes also possess a nuclear spin, which naturally leads to spin-exchange interactions between atoms occupying distinct spin and orbital states [45–47]. In this way, numerous multiorbital Hamiltonians from solid-state theory, for example, the double-exchange [25] or Kondo lattice model [19], can be implemented with this type of atoms and state-dependent optical potentials. First efforts probing orbital mixtures of alkaline-earth(-like) atoms have been devoted to the characterization of few-body physics, including the two-body interactions between atoms in the same or distinct orbital states [46, 48–53]. Specifically, ytterbium has emerged as a promising species in this context due to an orbital Feshbach resonance at accessible magnetic fields [54–56], offering a powerful tuning “knob” for controlling interactions of orbital mixtures. This feature is complemented by a high level of experimental flexibility with two naturally abundant fermionic isotopes and favorable interaction parameters [46, 53].

Recent advances have significantly improved the theoretical understanding and control of orbital ytterbium mixtures [30, 57], paving the way for experimental studies of impurity-bath physics at variable interaction strength [58, 59]. Problems of this form lie at the heart of various interesting phenomena [60–62]. For example, the Kondo effect, which describes the dramatically altered transport properties in dilute magnetic alloys, has eventually been explained with the coupling of localized impurity spins to a band of conduction electrons [61]. In Landau’s Fermi liquid picture [63], coupling a mobile impurity to a fermionic medium leads to the formation of a quasiparticle, known as Fermi polaron. This quasiparticle possesses strongly modified single-particle properties like an effective mass or finite lifetime [64, 65], arising due to entanglement with its surrounding medium. Experimental probes of these properties in ytterbium quantum gases can benchmark existing theories of the Fermi polaron [64–66] due to the increased complexity of interactions across the orbital Feshbach resonance [57, 67–70].

The phenomenology of the Fermi polaron has been widely studied with ultracold quantum gases featuring interaction-tunability across Feshbach resonances [71–76]. Precise measurements of the quasiparticle properties have opened the door to a particularly fruitful exchange between experiment and theory [66, 77, 78], exemplified by the prediction and observation of metastable repulsive polarons [73, 74, 79–81]. Lately, novel experimental techniques have further improved our understanding of Fermi polarons by probing their dynamical formation with many-body interferometry [82], analyzing their dependence on the medium temperature [83], and observing the crossover to a molecular state [84]. In the context of this thesis, we probe the Fermi polaron across the orbital Feshbach resonance in two dimensions, complementing previous realizations with alkali atoms [74, 75]. In particular, Fermi polarons in two-dimensional

systems are relevant for semiconductor devices, as demonstrated by the recent observations of Fermi polaron-polaritons [85]. Our experimental results also allow benchmarking theoretical descriptions for systems exhibiting more complex forms of interaction [67–70].

The non-equilibrium time evolution of controllable quantum states under tailored many-body Hamiltonians can be directly examined by holding atomic ensembles in optical traps for variable duration. Experiments of this form offer a direct way to investigate how isolated quantum systems thermalize [86–89], a topic that has seen greatly renewed interest over the last decades [8–10]. While efficient numerical approaches like matrix product state algorithms exist, the fast growth of entanglement usually limits classical simulations to one spatial dimension and either small particle numbers or short duration [90]. Experiments with ultracold atoms provide an alternative way to explore non-equilibrium dynamics by directly employing a quantum resource for simulating the time evolution of many-body Hamiltonians. Recently, this technique has enabled the first experimental observation of many-body localization with ultracold fermions in a disordered optical lattice [91, 92]. This intriguing phase of quantum matter describes non-integrable systems, which fail to thermalize such that a finite memory of an initial state can persist for arbitrarily long times—even in the presence of interactions [93]. Such non-ergodic behavior could find potential applications in quantum devices by preserving delicate states [94, 95].

In light of the remarkable experimental findings, also featuring other platforms [96, 97], a plethora of theoretical work has targeted this newly established field at the intersection of statistical, quantum, and condensed-matter physics [98–100]. In numerous theoretical studies, a central question has emerged concerning the existence of many-body localization in translationally invariant systems without any form of static disorder [100]. Diverse model systems have been proposed and analyzed in this context [101–106]. In particular, the mass-imbalanced Fermi-Hubbard model can already be accessed experimentally in a fully tunable manner with orbital ytterbium mixtures. Here, the orbital degree of freedom discussed above corresponds to heavy and light particles which move with vastly different time scales in a one-dimensional lattice [104, 105]. Finite interactions between the two species introduce dynamical constraints, which are believed to cause an extremely slow thermalization with features reminiscent of many-body localization [105]. Emergent metastability makes numerical calculations in this regime extremely challenging [104, 105] and calls for an experimental realization, which we present within this thesis.

This thesis

The work presented in this thesis builds on and extends the techniques developed for ultracold ytterbium over recent years. In particular, we report on two experimental studies probing many-body physics in the presence of an orbital degree of freedom. By engineering a state preparation technique for population-imbalanced Fermi gases, we create multiorbital Fermi polarons in the two-dimensional layers of a single-axis optical lattice. These quasiparticles and their properties are precisely characterized by utilizing spectroscopic techniques and the clock transition. Specifically, we probe the coherent nature of the Fermi polaron in two dimensions

with Rabi oscillations between weakly and strongly interacting impurity states. For these measurements, the orbital Feshbach resonance [54–56] allows us to analyze a broad range of interaction strengths, all the way from weak to strong repulsive or attractive interactions. By comparing theoretical predictions and experimental results, we identify a manifestation of the multiorbital Fermi polaron in the many-body spectrum.

In a second experiment, we employ the recently developed state-dependent lattice techniques [43] to probe non-equilibrium dynamics in an interacting mixture of heavy and light particles. The study of localization in such systems dates back to work from Kagan and Maksimov in the context of helium physics [107] and has lately been investigated intensively for the realization of many-body localization in translationally invariant systems [101–103, 105]. In our experiment, the mass-imbalanced Fermi-Hubbard model is implemented by populating the ground and clock state, which exhibit vastly different dynamical scales in the state-dependent lattice. By gradually translating the external confinement, we precisely study the relaxation dynamics of the system at variable interaction strength and mass imbalance. In this way, we identify the emergence of extremely slow relaxation and behavior reminiscent of ergodicity and thermalization at late times.

Outline

This thesis is divided into six chapters, which are structured as follows.

Chapter 1 reviews the electronic structure of fermionic ytterbium and explains how the ground and clock state give direct access to orbital degrees of freedom in quantum simulation experiments. To this end, we also discuss the scattering properties of atoms within the same or distinct orbitals, which are also relevant for the orbital Feshbach resonance. We illustrate the operating principle of state-dependent and state-independent optical traps, starting with calculating the polarizabilities in the ground and clock-state orbitals. Lastly, we briefly explain the essential experimental techniques that allow us to routinely prepare and probe deeply degenerate Fermi gases and orbital mixtures.

We review the theoretical description for Fermi polarons in **Chapter 2**. By deriving the quasiparticle self-energy within the ladder approximation, we gain access to properties such as the quasiparticle energy and residue. Then, these concepts are generalized to the situation of our experiment, which features strong harmonic confinement and orbital interactions. Having laid the theoretical ground, we present the experimental results for the multiorbital Fermi polaron in **Chapter 3**. First, we explain the techniques and measurements to prepare and characterize ensembles of population-imbalanced gases in the two-dimensional layers of a single-axis optical lattice. We then compare our measurement results for the quasiparticle energy, the residue, and the repulsive polaron lifetime with theoretical predictions. Complementary to our experimental observations, we also discuss recent developments concerning the theoretical description of the repulsive Fermi polaron.

Chapter 4 examines thermalization and its absence in isolated quantum systems. Specifically, we review the phenomenology of many-body localization and the emergent metastability in heavy-light mixtures. Here, our attention lies on non-equilibrium density dynamics in the mass-imbalanced Fermi-Hubbard model, which we analyze with numerical exact diagonaliza-

tion techniques. **Chapter 5** covers our measurements of the non-equilibrium density dynamics in one-dimensional Fermi-Hubbard chains with a finite mass imbalance. This system is realized using the ytterbium orbitals as light and heavy species in a state-dependent lattice, and we first discuss the experimental techniques to tune the mass imbalance and interaction strength. We then introduce a transport measurement technique, which allows us to observe the emergence of extremely slow relaxation at strong interactions and significant mass imbalance.

The **final chapter** briefly summarizes the central findings of this thesis and presents an outlook on potential future work in the light of the most recent advances with ultracold alkaline-earth(-like) atoms.

Publications

The central results presented in this thesis have been published or appeared as preprints in the following references:

- **N. Darkwah Oppong**, G. Pasqualetti, O. Bettermann, P. Zechmann, M. Knap, I. Bloch, and S. Fölling, *Probing transport and slow relaxation in the mass-imbalanced Fermi-Hubbard model*, [arXiv:2011.12411](#)
- **N. Darkwah Oppong**, L. Riegger, O. Bettermann, M. Höfer, J. Levinsen, M. M. Parish, I. Bloch, and S. Fölling, *Observation of Coherent Multiorbital Polarons in a Two-Dimensional Fermi Gas*, *Phys. Rev. Lett.* **122**, 193604 (2019)

During the course of this thesis, the following additional research articles have been published or appeared as preprints:

- H. S. Adlong, W. E. Liu, F. Scazza, M. Zaccanti, **N. Darkwah Oppong**, S. Fölling, M. M. Parish, and J. Levinsen, *Quasiparticle Lifetime of the Repulsive Fermi Polaron*, *Phys. Rev. Lett.* **125**, 133401 (2020)
- O. Bettermann, **N. Darkwah Oppong**^{*}, G. Pasqualetti^{*}, L. Riegger, I. Bloch, and S. Fölling, *Clock-line photoassociation of strongly bound dimers in a magic-wavelength lattice*, [arXiv:2003.10599](#) (* equal contribution)
- A. Sotnikov, **N. Darkwah Oppong**, Y. Zambrano, and A. Cichy, *Orbital ordering of ultracold alkaline-earth atoms in optical lattices*, *Phys. Rev. Research* **2**, 023188 (2020)
- L. Riegger, **N. Darkwah Oppong**, M. Höfer, D. R. Fernandes, I. Bloch, and S. Fölling, *Localized Magnetic Moments with Tunable Spin Exchange in a Gas of Ultracold Fermions*, *Phys. Rev. Lett.* **120**, 143601 (2018)
- S. L. Campbell, R. B. Hutson, G. E. Marti, A. Goban, **N. Darkwah Oppong**, R. L. McNally, L. Sonderhouse, J. M. Robinson, W. Zhang, B. J. Bloom, and J. Ye, *A Fermi-degenerate three-dimensional optical lattice clock*, *Science* **358**, 90 (2017)

CHAPTER 1

Multiorbital physics with ultracold ytterbium

We present here an overview of realizing multiorbital physics with ultracold quantum gases of ytterbium atoms. To begin, we introduce the electronic structure of neutral ytterbium and show how the long-lived clock state provides access to an orbital degree of freedom. For the fermionic isotopes ^{171}Yb and ^{173}Yb , we discuss the relevant interorbital and intraorbital interaction channels. We also explain the concept of optical lattices and how they can be engineered to introduce mobility strongly dependent on the orbital state. In this way, Hamiltonians of multiple interesting solid-state systems can be realized, which we illustrate for relevant examples. Lastly, we describe the key experimental techniques to prepare and probe multiorbital Fermi gases of ytterbium, providing the starting point for the experiments presented in Chapters 3 and 5.

1.1 Electronic structure of neutral ytterbium

Ytterbium, a rare-earth element from the lanthanide series, occurs naturally as one of seven stable isotopes with proton numbers $Z = 168, 170, 171, 172, 173, 174,$ and 176 [113]. The most abundant isotope ^{174}Yb (natural abundance $\approx 32\%$) is bosonic. For the experiments presented in this thesis, we employ the two fermionic isotopes ^{173}Yb (natural abundance $\approx 16\%$) and ^{171}Yb ($\approx 14\%$). Only these two isotopes possess a non-vanishing nuclear spin $I = 1/2$ for ^{171}Yb and $I = 5/2$ for ^{173}Yb . Neutral ytterbium finds applications in a variety of cold atom experiments, ranging from atomic clocks [31] to search for new physics [114] and experiments probing quantum many-body physics [30].

The electronic configuration of neutral ytterbium takes the form $[\text{Xe}]4f^{14}6s^2$ [115] with two valence electrons on the outer shell, similar to alkaline-earth metals like strontium, making ytterbium an *alkaline-earth-like* element. The two valence electrons and their spin give rise to helium-like energy levels with a singlet ($S = 0$) and triplet ($S = 1$) manifold. Figure 1.1 shows some of the lowest-lying energy levels together with their spin-orbit $L-S$ coupling term symbols and optical transitions relevant for our experiments. Generally, selection rules forbid dipole transitions between the singlet and triplet manifolds as they involve a spin-flip ($S \rightarrow S \pm 1$). However, the $L-S$ coupling scheme becomes less accurate with growing nuclear charge Z and the relevance of $j-j$ coupling increases for heavy atoms like ytterbium [116]. For instance, the 3P_1 state in the triplet manifold acquires a finite admixture of the 1P_1 state

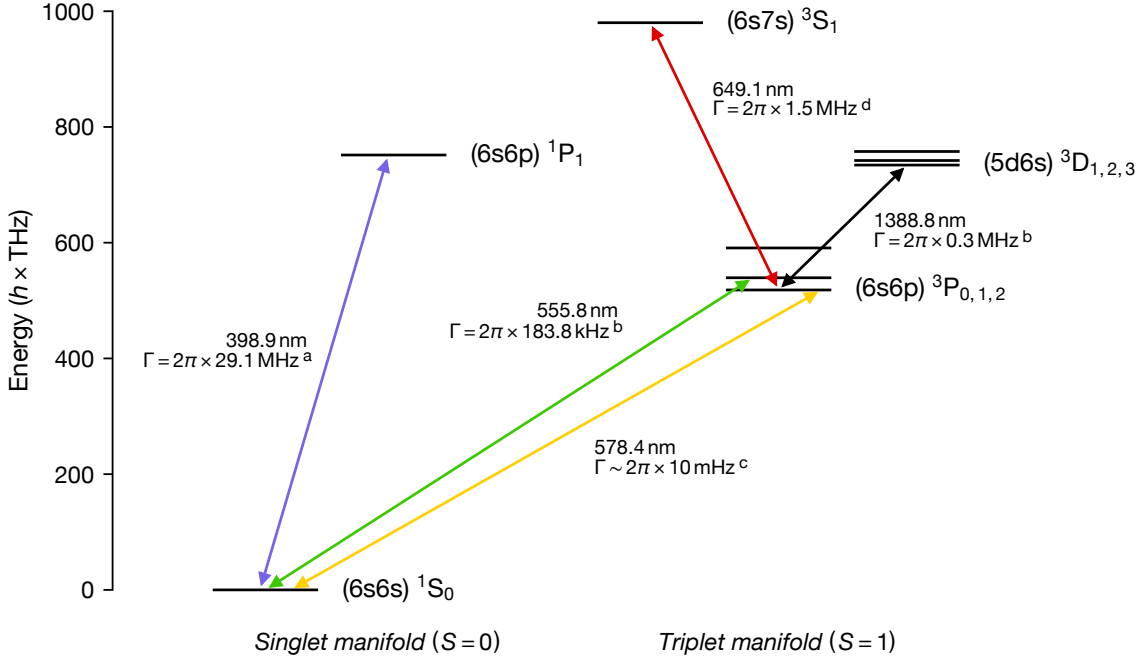


Figure 1.1 | Electronic states and optical transitions. Energy level diagram of low-lying electronic states in neutral ytterbium with their corresponding term symbols $(^{2S+1})L_J$. Relevant optical transitions are indicated by arrows labeled with the vacuum transition wavelengths as well as natural linewidths Γ inferred from radiative lifetimes and approximate branching ratios calculated within the $L-S$ coupling scheme. The energy values shown in this figure are adapted from Ref. [115].

^a Takasu et al. [48].

^b Beloy et al. [118].

^c Porsev et al. [119].

^d Cho et al. [120].

from the singlet manifold, which makes the *intercombination line* connecting the 1S_0 ground state and the 3P_1 excited state weakly allowed [117].

Cooling and imaging transitions.—In our experiment, we employ the nearly closed $^1S_0 \rightarrow ^1P_1$ cycling transition for Zeeman-slowing the atomic beam from a thermal source [121]. Moreover, the large photon scattering rate of this broad transition enables our in-situ absorption imaging with relatively short laser pulses (see Section 1.4.3). With a natural linewidth of only ≈ 180 kHz, we employ the intercombination line for narrow-line laser cooling in our magneto-optical trap and state preparation across the different nuclear spin states in the ground state using an optical pumping technique [121]. For example, this preparation technique enables our measurements of the Fermi polaron discussed in Chapter 3 (see Section 3.1.1).

Clock transition.—The finite nuclear spin $I \neq 0$ of the fermionic isotopes gives rise to the hyperfine structure. Moreover, the associated hyperfine interaction leads to a small admixture of the 1P_1 , 3P_1 , and 3P_2 states to the bare 3P_0 state [117]. In this way, the doubly forbidden $^1S_0 \rightarrow ^3P_0$ transition acquires a small finite coupling for the fermionic species ^{171}Yb and ^{173}Yb [119].¹ The natural linewidth of this transition of order 10 mHz [119] is tiny, a

¹For the bosonic isotopes, a similar mixing and coupling can be induced with an external magnetic field [122].

remarkable feature shared with other alkaline-earth(-like) atoms. Notably, the insensitivity of the 1S_0 and 3P_0 states to magnetic fields ($J = 0$) makes this *clock transition* well suited for applications in atomic clocks. The small linewidth combined with the optical transition frequency yield an enormously large quality factor $Q \sim 10^{17}$ [31], a fundamental advantage compared to the microwave transition of ^{133}Cs , defining the current standard of the second [123]. Remarkable progress in the construction of ultrastable optical cavities and laser systems have enabled optical frequency measurements with unprecedented precision and accuracy [31]. For example, this has also given experimental access to gravitational time dilation across small and large distances [124, 125]. On the other hand, the ultranarrow linewidth is associated with a particularly long lifetime $\gg 10$ s of the 3P_0 clock state against decay to the lower-lying ground state. In this way, the metastable clock state can also be utilized as an *orbital degree of freedom* [19], as explored in the next section.

1.2 Interactions in orbital mixtures

In addition to precision spectroscopy, the metastable 3P_0 clock state (denoted $|e\rangle$) together with the 1S_0 ground state (denoted $|g\rangle$) also enables quantum simulation of multiorbital many-body physics. Here, we focus on the fermionic isotopes since they are particularly suitable for mimicking electrons in solid-state materials. Before discussing the details of interacting atoms in the same or different orbitals, we give a brief introduction to collisions in ultracold quantum gases and the relevant quantities such as the s -wave scattering length. The collisions in ultracold quantum gases are directly connected to the short-range interactions, which provide a central building block for implementing and probing many-body physics. Hence, the following discussion of elastic scattering enables us to calculate relevant experimental parameters and engineer interactions tailored to multiorbital models of interest.

1.2.1 Elastic scattering in ultracold gases

For the dilute limit of ultracold quantum gases [1], we focus on elastic two-body collisions, where the asymptotic wave function after the collision in the center-of-mass frame can be described by the ansatz [126]

$$\psi(\mathbf{r}) \sim e^{i\mathbf{k}\cdot\mathbf{r}} + f(\mathbf{k}, \theta) \frac{e^{ikr}}{r} \quad (1.1)$$

with the relative coordinate \mathbf{r} . The first term of this wave function describes an incident plane wave, and the last part describes an outgoing spherical wave as a result of the scattering process. The above form defines the scattering amplitude $f(\mathbf{k}, \theta)$, related to the physical observable of the scattering cross section $\sigma(\mathbf{k}, \theta) = |f(\mathbf{k}, \theta)|^2$. The incident wave vector \mathbf{k} provides an axis of rotational symmetry for the problem, and the wave function as well as scattering amplitude can be expressed in terms of spherical harmonics, known as partial-wave expansion. For the

small collisional energies and short-range interactions in cold atomic gases, only the lowest partial wave (s -wave) contributes to the scattering amplitude [1]. It then becomes independent of the angle θ and can be expanded around $k = 0$ taking the form [126]

$$f(k) \stackrel{k \rightarrow 0}{=} \frac{-1}{a_s^{-1} - r_{\text{eff}}k^2/2 + ik}, \quad (1.2)$$

which defines the s -wave scattering length a_s , and the effective range r_{eff} . This parameter determines the first-order energy-dependent correction of the scattering amplitude. The properties of a_s are largely determined by the energy of the least-bound state in the molecular potential of the atomic pair. This strong dependence can be exploited with Feshbach resonances to greatly enhance or suppress the scattering length (see Section 1.2.4).

Let us emphasize a critical point regarding the scattering of indistinguishable fermions: Since the wave function for s -wave collisions is isotropic and spatially symmetric, $f(k)$ vanishes for this case and only scattering at higher odd partial waves $l = 1, 3, \dots$ becomes relevant, e. g., p -wave collisions. However, their contribution becomes negligible at low enough temperatures due to a centrifugal barrier $\sim l^3$, and a fermionic ultracold gas of indistinguishable particles can be well described by a non-interacting Fermi gas [1]. This has an important consequence: evaporative cooling of fermionic atoms usually either requires another species or additional internal states to enable collisions once the gas reaches the quantum-degenerate regime. While collisions in the s -wave scattering channel are strongly suppressed for the same internal state, atoms occupying distinct internal states do interact in the s -wave channel since the additional degree of freedom enables the antisymmetrization of the wave function.

The molecular potential giving rise to the interatomic interactions and collisional properties generally takes a complicated form. Instead of the real interaction potential, a pseudo-potential with a much simpler form can be employed. This potential still yields the scattering amplitude in Eq. (1.2) for $r_{\text{eff}} \rightarrow 0$ and relates the relevant physical quantities, i. e., the interaction strength to the s -wave scattering length, which can be determined experimentally. In the following, we consider the Fermi pseudo-potential [1]

$$V(\mathbf{r}) = \frac{4\pi\hbar^2}{m} a_s \delta^3(\mathbf{r}), \quad (1.3)$$

which describes zero-range ‘‘contact’’ interactions in an atomic pair (atomic mass m) captured by the Dirac delta distribution.² For the description of atoms in a specific internal pair state $|\alpha\rangle$, we consider a projection operator $\hat{P}_\alpha = |\alpha\rangle\langle\alpha|$, such that $V(\mathbf{r}) \rightarrow V(\mathbf{r})\hat{P}_\alpha$. The above pseudo-potential also establishes a notion for the relation between the nature of interactions and the sign of the s -wave scattering length: repulsive interactions ($V > 0$) correspond to $a_s > 0$ and attractive interactions ($V < 0$) are found for $a_s < 0$. In contrast, a vanishing a_s signals a non-interacting regime. From the above pseudo-potential, we calculate the interaction

²This form of the pseudo-potential only holds for wave functions regular at the origin $\mathbf{r} = 0$. Otherwise, the Dirac delta distribution has to be regularized with $\delta^3(\mathbf{r}) \rightarrow \delta^3(\mathbf{r})\partial_{r,r}$ [127], which can introduce additional complexity.

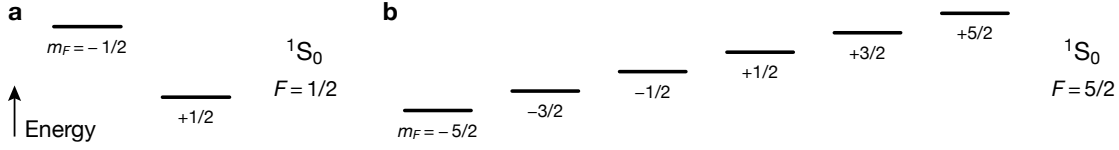


Figure 1.2 | Nuclear spin degree of freedom in the ground state. Illustration of the Zeeman splitting in the 1S_0 ground state for different nuclear spin states (black lines) at finite magnetic field for the two fermionic isotopes (a) ^{171}Yb with nuclear spin $I = 1/2$ and (b) ^{173}Yb with $I = 5/2$.

strength between two particles according to their second quantization creation (annihilation) operators $\Psi_{1,2}^\dagger$ ($\Psi_{1,2}$) at the spatial coordinates $\mathbf{r}_{1,2}$ [128],

$$U = \frac{4\pi\hbar^2}{m} a_s \int d\mathbf{r}_1 \int d\mathbf{r}_2 \Psi_1^\dagger(\mathbf{r}_1) \Psi_2^\dagger(\mathbf{r}_1) \delta^3(\mathbf{r}_1 - \mathbf{r}_2) \Psi_2(\mathbf{r}_2) \Psi_1(\mathbf{r}_2). \quad (1.4)$$

This formalism allows us to determine the interaction strength of atomic pairs in an optical lattice, as discussed in Section 1.12.

1.2.2 Nuclear spin states

In the ground and clock state of fermionic ytterbium, the total electronic angular momentum J vanishes and the nuclear spin alone gives rise to multiple m_F states, each corresponding to a projection of the atomic total angular momentum $F = I + J = I$ onto the quantization axis with $m_F \in \{-F, -F + 1, \dots, +F\}$. Six distinct nuclear spin states exist for ^{173}Yb ($I = 5/2$) and two for ^{171}Yb ($I = 1/2$), as shown for the ground state in Fig. 1.2. Since ^{171}Yb possesses a positive nuclear magnetic moment $\mu_I = 0.4919\mu_N$ (nuclear magneton μ_N), nuclear spin states with values $m_F > 0$ experience a negative Zeeman shift at positive magnetic fields, while the sign is reversed for ^{173}Yb with $\mu_I = -0.6776\mu_N$ (see Fig. 1.2) [113].

In contrast to the spin-changing collisions typically found in alkali atoms, scattering processes of $|g\rangle$ or $|e\rangle$ atoms preserve the population across different m_F states.³ This conservation of the nuclear spin state arises due to the vanishing electronic angular momentum $J = 0$ in the $|g\rangle$ and $|e\rangle$ states [19]. Intuitively, this can be understood by considering that the nuclear spins of two atoms only couple once their nuclei are brought together close enough, which generally does not occur for the rather low density in cold atomic gases. Crucially, the conservation of the nuclear spin gives rise to a special unitary symmetry described by the $SU(N)$ group of degree N , a generalization of $SU(2)$ describing the two-valued spin of the electron. While this symmetry remains $SU(2)$ for ^{171}Yb , the heavier species ^{173}Yb provides access up to $SU(N = 6)$, where $N \leq 6$ can be readily probed by preparing atoms across a subset of the m_F states [121]. This property of fermionic ytterbium and other alkaline-earth elements, particularly strontium, gives access to exotic physics of $SU(N)$ symmetric interactions in the controlled setting of ultracold atomic systems [38]. From a practical perspective, the symmetry manifests itself in a single scattering length describing the collisional properties for an arbitrary combination of nuclear spin states. Since the experiments presented in this thesis mostly employ only two nuclear

³This symmetry is expected to be violated on a level $< 10^{-3}$, which generally has no relevance for our experiments [19, 46, 55].

Table 1.1 | Scattering lengths and two-body loss coefficients of fermionic ytterbium isotopes

Isotope	s-Wave scattering lengths (Bohr radius a_0)				Two-body loss coefficients (cm^3s^{-1})	
	a_{gg}	a_{ee}	a_{eg}^+	a_{eg}^-	β_{eg}^-	β_{ee}
^{171}Yb	$-2.8(3.6)^a$	$104(7)^b$	$240(4)^b$	$389(4)^b$	$\leq 2.6(3) \times 10^{-16}{}^b$	$4.8(2.1) \times 10^{-12}{}^b$
^{173}Yb	$199.4(2.1)^a$	$306(10)^c$	$1878[37]^d$	$219.7(2.2)^d$	$< 3 \times 10^{-15}{}^c$	$2.2(6) \times 10^{-11}{}^c$

^a Kitagawa et al. [130].

^b Bettermann et al. [111]; $\beta_{eg}^+ \approx \beta_{eg}^-$ reported (within measurement uncertainty).

^c Scazza et al. [46]; a_{ee} inferred from reported value of $(a_{ee} - a_{gg})$; reported results suggest $\beta_{eg}^+ \gg \beta_{eg}^-$.

^d Höfer et al. [55]; value in brackets denotes a numerical fit error (experimental uncertainty most likely larger).

spin states, the large spin symmetry only plays a minor role. For a comprehensive discussion of the $\text{SU}(N)$ symmetry of ultracold ytterbium gases within the context of our experiment, the interested reader should consult Ref. [129].

1.2.3 Orbital interaction channels

We now turn to the interactions of ultracold ytterbium gases, in particular, between atomic pairs, which either occupy the same or distinct orbitals. For this purpose, we consider that each of the atoms occupies a distinct nuclear spin state with $m_F < m_{F'}$, labeled $|\downarrow\rangle$ and $|\uparrow\rangle$, respectively. While these states are fixed for ^{171}Yb ($m_F = \pm 1/2$), we choose the $m_F = \pm 5/2$ states for ^{173}Yb in most of our experiments (without loss of generality).

First, we consider interactions between atoms in the same orbital state $\alpha \in \{g, e\}$ described by the antisymmetrized pair states $|\alpha\alpha\rangle \equiv |\alpha\alpha\rangle \otimes (|\uparrow\downarrow\rangle - |\downarrow\uparrow\rangle) / \sqrt{2}$, which feature the s -wave scattering lengths a_{gg} and a_{ee} (see Table 1.1). Notably, these scattering lengths are distinct as the electronic properties of atoms in either of the two orbitals differ strongly. While ^{173}Yb possesses a sizable ground state scattering length $a_{gg} \approx 200a_0$ (Bohr radius a_0), it almost vanishes for the isotope ^{171}Yb . In contrast, the scattering length in the $|e\rangle$ orbital has an appreciable value for both species with $\approx 300a_0$ and $\approx 100a_0$, respectively (see Table 1.1).

Interorbital interaction.—For the e - g pair, there are two distinct interaction states as dictated by the total antisymmetry of the fermionic wave function under particle exchange. These are the orbital “triplet” $|eg^+\rangle$ state and the “singlet” $|eg^-\rangle$ state [19],

$$|eg^+\rangle = \frac{1}{2}(|ge\rangle + |eg\rangle) \otimes (|\uparrow\downarrow\rangle - |\downarrow\uparrow\rangle) \quad \text{and} \quad |eg^-\rangle = \frac{1}{2}(|ge\rangle - |eg\rangle) \otimes (|\uparrow\downarrow\rangle + |\downarrow\uparrow\rangle). \quad (1.5)$$

Each of these states is associated with an interatomic interaction potential and the corresponding interorbital scattering lengths a_{eg}^\pm , which have been determined precisely via spectroscopy on the clock transition—both for ^{173}Yb [46, 47] and ^{171}Yb [53, 111, 131] (see Table 1.1).

A finite magnetic field $B > 0$ does not only introduce a spin-dependent potential, i. e., the Zeeman shift, but also an orbital-dependent energy shift. This differential Zeeman shift originates from a small admixture of other states to the $^3\text{P}_0$ clock state (see Section 1.1), which causes a larger magnetic-field sensitivity compared to the $J = 0$ ground state [117]. The differ-

⁴The orbital “singlet” state $|eg^-\rangle$ also describes the interorbital pair states for the same spin state ($|\downarrow\downarrow\rangle$ or $|\uparrow\uparrow\rangle$).

ential Zeeman shift is given as $\delta = B\delta\mu = \delta g\Delta m_F\mu_B$ with the differential Landé g-factor δg and $\Delta m_F = m_F - m_{F'}$, the difference of the m_F value in the ground and clock state. The value of the differential magnetic moment $\Delta\mu/\Delta m_F$ can be obtained from clock-line spectroscopy and takes the value $-h \times 399.0(1)$ Hz/G and $h \times 110.7(5)$ Hz/G for ^{171}Yb and ^{173}Yb , respectively [108, 111]. Besides the linear Zeeman shift, a finite second-order (quadratic) Zeeman shift originates from magnetic-field induced cross coupling of electronic energy levels within the singlet or triplet manifold [117]. This effect also manifests as an increased coupling strength of the clock transition at large magnetic fields. However, the second-order Zeeman shift $\approx -h \times 60$ mHz/G² [111, 132] has little relevance for the work presented in this thesis, and we only consider it when addressing the clock transition at large magnetic fields.

Importantly, magnetic-field induced mixing of the interorbital interaction channels leads to significantly modified scattering properties, as explored in the following. For the atomic pair, we first introduce a different basis, a simple superposition of the singlet and triplet states,

$$\begin{aligned} |o\rangle &= \frac{1}{\sqrt{2}}(|g \uparrow\rangle \otimes |e \downarrow\rangle - |e \downarrow\rangle \otimes |g \uparrow\rangle) = \frac{1}{\sqrt{2}}(|eg^+\rangle + |eg^-\rangle) \\ |c\rangle &= \frac{1}{\sqrt{2}}(|e \uparrow\rangle \otimes |g \downarrow\rangle - |g \downarrow\rangle \otimes |e \uparrow\rangle) = \frac{1}{\sqrt{2}}(|eg^+\rangle - |eg^-\rangle). \end{aligned} \quad (1.6)$$

The above eigenstates of the Zeeman-Hamiltonian correspond to the situation in ^{173}Yb , whereas the spin states have to be altered ($\downarrow \rightarrow \uparrow$ and $\uparrow \rightarrow \downarrow$) for ^{171}Yb since the sign of the nuclear magnetic moment μ_I differs for the two isotopes. For the above basis and at finite magnetic field, the Hamiltonian describing the Zeeman, kinetic, and interaction energy of an atomic e - g pair takes the form [57]

$$\hat{\mathcal{H}} = \delta |c\rangle\langle c| + \sum_{\alpha \in \{o,c\}} \left(-\frac{\hbar^2}{m} \nabla^2 \right) |\alpha\rangle\langle \alpha| + V_{\text{dir}}(\mathbf{r}) \sum_{\alpha \in \{o,c\}} |\alpha\rangle\langle \alpha| + V_{\text{ex}}(\mathbf{r}) \sum_{\alpha, \beta \in \{o,c\}, \alpha \neq \beta} |\alpha\rangle\langle \beta| \quad (1.7)$$

with the direct interaction energy $V_{\text{dir}}(\mathbf{r}) = [V_+(\mathbf{r}) + V_-(\mathbf{r})]/2$ and the spin-exchange interaction energy $V_{\text{ex}}(\mathbf{r}) = [V_+(\mathbf{r}) - V_-(\mathbf{r})]/2$. Here, $V_{\pm}(\mathbf{r})$ denotes the interaction potential of the singlet and triplet channels defined in Eq. (1.5). As we will see later in this chapter, the presence of spin-exchange interaction coupling the two orbitals $|g\rangle$ and $|e\rangle$ gives direct experimental access to interesting many-body physics with ultracold ytterbium atoms. In contrast to strontium, ytterbium provides two fermionic isotopes with a distinct ordering of the interorbital scattering lengths a_{eg}^{\pm} , allowing to probe the regimes $V_{\text{ex}} > 0$ with ^{173}Yb as well as $V_{\text{ex}} < 0$ with ^{171}Yb [46, 53].

Since the interactions are short-ranged, we expect the Hamiltonian to be dominated by the interaction potentials for small distances, whereas the Zeeman term dominates at large separation and sizable magnetic fields. As a consequence, the eigenstates at short distance are the singlet and triplet states from Eq. (1.5), whereas the superposition states $|o\rangle$ and $|c\rangle$ from Eq. (1.6) are eigenstates at large separation. In a deep optical lattice, the kinetic term in Eq. (1.7) becomes strongly suppressed and the interaction takes discrete values. For this setting, the altered nature of the pair eigenstates can be probed spectroscopically by adjusting the magnetic field strength continuously. Then, the interaction eigenenergies of the effective

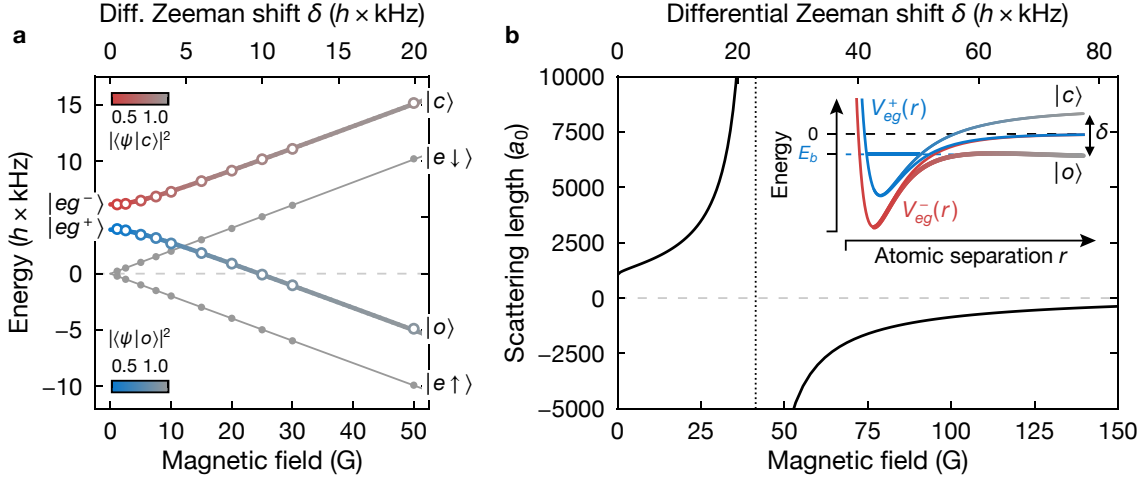


Figure 1.3 | Interoorbital interaction channels at finite magnetic field. (a) Interaction energies of ^{171}Yb measured with clock-line spectroscopy in a deep three-dimensional optical lattice (adapted from Ref. [111]). Filled circles show the magnetic-field dependence of the single-particle states $|e \uparrow\rangle$ and $|e \downarrow\rangle$, whereas empty circles correspond to the interorbital pair states that continuously evolve from $|eg^{\pm}\rangle$ to $|o, c\rangle$. Solid lines show numerical fits, and the color gradient indicates the overlap of the magnetic-field dependent state $|\psi\rangle$ with $|o, c\rangle$. Energies are shown relative to the mean of $|e \uparrow\rangle$ and $|e \downarrow\rangle$. (b) s -Wave scattering length in the open channel $|o\rangle$ across the orbital Feshbach resonance (dotted line) in ^{173}Yb , calculated with the theoretical model from Ref. [55]. The inset schematically shows the relevant molecular potentials and how a finite magnetic field induces a detuning of the open and closed channel. This allows bringing the open channel $|o\rangle$ into resonance with the least-bound state at energy E_b . Note that the roles of the orbital singlet and triplet states are reversed between ^{171}Yb and ^{173}Yb .

two-level system take the magnetic-field dependent values $E_{\pm}(\delta) = V_{\text{dir}} \pm \sqrt{V_{\text{ex}}^2 + \delta^2}$ [46, 111]. Figure 1.3(a) displays a measurement of these interaction energies determined from clock-line spectroscopy of ^{171}Yb in an optical lattice.

Inelastic collisions.—So far, we have only discussed the elastic interaction channels for intra- and interorbital pairs. However, inelastic scattering processes are also present and can be accounted for with a finite imaginary part of the otherwise purely real s -wave scattering length. In particular, e – e and e – g pairs are prone to inelastic collisions as collisional partners in these pair states can change their internal state due to a finite coupling to various molecular potentials [19]. Crucially, a significant energy release accompanies the decay from $|e\rangle$ to $|g\rangle$, typically leading to escape from the trap. The differential equation for the time-dependent atomic density, $dn(t)/dt = -\beta n^2(t)$, captures this loss process. The most significant loss coefficient β_{ee} exceeds the interorbital parameter β_{eg}^- by more than four orders of magnitude (see Table 1.1). For typical experiments, this results in a quick loss of e – e pairs from the trap. However, this dissipative process can be strongly suppressed by employing spin-polarized samples or isolating individual $|e\rangle$ atoms in an optical lattice.

1.2.4 Orbital Feshbach resonances

Feshbach resonances are one of the most potent and widely used tools in the field of ultracold atoms. They allow the s -wave scattering length of a collisional pair to be tuned with an external

magnetic field [see Fig. 1.3(b)]. Across a Feshbach resonance, the nature of interactions in an ultracold atomic gas can be adjusted freely from repulsive to attractive.

The key ingredients for a Feshbach resonance are two interaction channels or potentials whose energy splitting at large particle distance can be tuned by an external magnetic field. These two interaction potentials are labeled closed and open channel, with the latter having the smaller energy at sizable separations. If the two interaction channels are coupled at small atomic separation, a collisional pair entering the open channel couples to the bound states in the closed interaction channel. Crucially, the closed channel and its least bound state can be shifted relative to the entrance channel by adjusting its energy with an external field [see inset of Fig. 1.3(b)]. Once the bound state is brought into resonance with the open channel, the collisional pair in the entrance channel interacts resonantly, with the scattering length approaching infinity. Moreover, as the bound-state energy is tuned over the energy of the entrance channel, the scattering length also flips its sign from $+\infty$ to $-\infty$. An arbitrary value of the scattering length can then be selected by setting the detuning of the entrance channel relative to the bound state by choosing an appropriate magnetic field [133].

By closely inspecting the Hamiltonian in Eq. (1.7), we find that an $e-g$ pair of ytterbium atoms features the relevant ingredients for a Feshbach resonance. Specifically, the spin-exchange interaction V_{ex} provides a finite coupling between the open and closed channel, $|o\rangle$ and $|c\rangle$, respectively.⁵ For ^{173}Yb , there fortunately exists a shallow bound state with $E_b \approx h \times 30$ kHz in the triplet interaction potential [55]. Therefore, only a small tuning of the entrance energy is required, with the orbital Feshbach resonance occurring at ≈ 40 G [54–56]. The location of this Feshbach resonance has another important consequence: The detuning of open and closed channel at 40 G is still comparable to typical scales in many-body systems such as the Fermi energy, which can lead to frustrated interactions (see Chapter 3). In contrast, the corresponding molecular state of ^{171}Yb in the singlet channel has a much larger binding energy $E_b \approx h \times 300$ kHz. Hence, reaching a resonantly interacting regime requires a relatively large magnetic field of ≈ 1300 G [111]. In this thesis, we utilize the orbital Feshbach resonances of both isotopes to probe many-body physics as a function of interaction strength, either in the case of multiorbital Fermi polarons with ^{173}Yb (see Chapter 3) or for a mixture of heavy and light particles with ^{171}Yb (see Chapter 5).

Feshbach resonances can be categorized into the two limiting cases of *broad* and *narrow* resonances. These terms are motivated by the magnetic-field dependence of Feshbach resonances in alkali atoms. A more quantitative characterization can be determined from the dimensionless resonance strength $s_{\text{res}} > 0$ accounting for the magnetic-field dependence of the open and closed channel detuning [133], which differs strongly for alkali and alkaline-earth(-like) atoms. Here, $s_{\text{res}} \gg 1$ describes a broad Feshbach resonance, and $s_{\text{res}} \ll 1$ corresponds to a narrow resonance. For this case, the admixture of the closed channel becomes relevant over a larger range of magnetic fields such that the interactions commonly have to be described by a coupled two-channel approach [133]. The two-body problem then has two key parameters as a function of the magnetic field: the bound-state energy and the coupling or admixture

⁵Feshbach resonances in alkali atoms commonly occur between hyperfine states in the ground-state manifold. However, the absence of electronic spin ($S = 0$) inhibits this form of Feshbach resonance for $e-g$ pairs of alkaline-earth(-like) atoms.

of the closed channel. For both isotopes ^{171}Yb and ^{173}Yb , the resonance strength takes the values $s_{\text{res}} \approx 0.15$ [111, 134], indicating a narrow Feshbach resonance. In combination with the relatively long on-resonance lifetime of ^{173}Yb [55, 56], this allows probing many-body physics outside the “universal” regime of broad Feshbach resonances, which can be parameterized by the s -wave scattering length alone. This unique property has inspired many proposals for unusual pairing as well as impurity physics (see Ref. [57] and references therein). The details of the orbital Feshbach resonance in ^{173}Yb are explained in Ref. [134], whereas for the isotope ^{171}Yb , a more detailed study will appear elsewhere [135].

1.3 State-dependent optical lattices

Fermionic atoms trapped in optical lattices can mimic electrons moving in a crystal, enabling quantum simulation experiments of solid-state phenomena in a defect-free system, where kinetic and interaction energy are freely tunable [2, 11]. In this section, we explore how the orbital degree of freedom enables the study of more complex Hamiltonians describing orbital phenomena in solid-state systems. For ytterbium atoms in state-dependent optical lattices, the ground and clock state can take on the roles of electrons occupying different orbitals in a crystal.

In our experiment, optical lattices are produced by retro-reflecting a monochromatic laser beam with wavelength λ , which results in a standing wave intensity pattern and a corresponding potential for the atoms arising from the dipole force. Neglecting the envelope of the laser beam intensity, the single-particle Hamiltonian for a one-dimensional optical lattice takes the form

$$\hat{\mathcal{H}}_{\text{OL}} = -\frac{\hbar^2}{2m}\nabla^2 - V \sin^2(kx). \quad (1.8)$$

Here, the intensity I_0 of the laser controls the lattice depth $V = I_0/(2\epsilon_0 c) \text{Re}[\alpha(\lambda)]$ considered in units of the photon recoil energy $E_{\text{rec}} = \hbar k^2/(2m)$ with wave vector $k = 2\pi/\lambda$. The atomic ac polarizability $\alpha(\lambda)$ quantifies the magnitude of the atomic dipole induced by the electric field of the laser light and thereby also the strength of ac Stark shift and the dipole potential [136]. For the above spatially periodic Hamiltonian, Bloch’s theorem yields the eigenstates and eigenenergies, which take the form of Bloch (wave) functions and multiple energy bands [1].

Once the lattice depth becomes sizable compared to the energy scale E_{rec} , the lowest band takes the form of a cosine dispersion $E(q) = -2t \cos(qd)$ with quasimomentum q , band width $4t$, and lattice spacing $d = \lambda/2$ [1]. Apart from the transverse motion of the atoms, a system restricted to the lowest energy band can be approximated by the tight-binding model as hopping between neighboring lattice sites dominates,

$$\hat{\mathcal{H}}_{\text{TB}} = -t \sum_i \left(\hat{c}_i^\dagger \hat{c}_{i+1} + \text{h.c.} \right). \quad (1.9)$$

Here, \hat{c}_i^\dagger and \hat{c}_i are operators, which create or destroy a single fermionic atom on lattice site i . In general, the hopping amplitude t becomes exponentially suppressed with increasing lattice depth V and can be obtained from a numerical band structure calculation [1]. The Hamiltonian $\hat{\mathcal{H}}_{\text{TB}}$ and its generalization to multiple dimensions provide the starting point for simulating solid-state phenomena in the well-controlled setting of ultracold atoms with crystal-

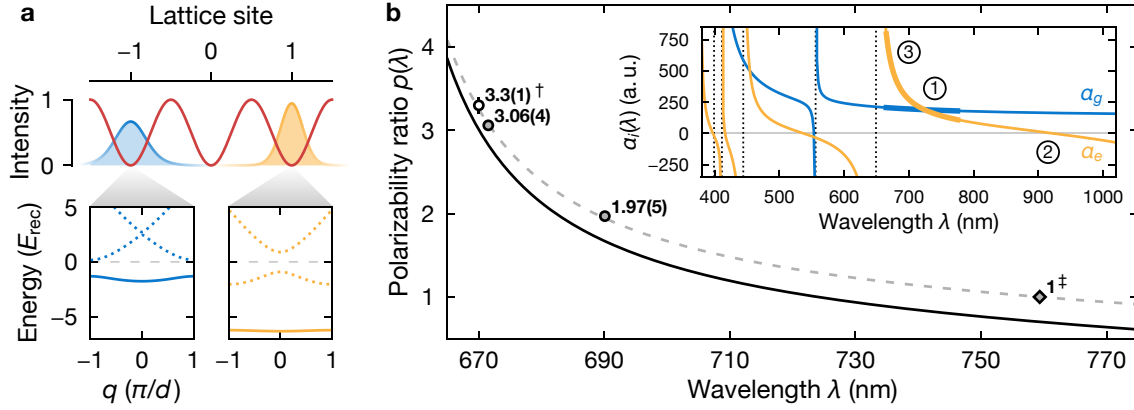


Figure 1.4 | Polarizability ratio of e - g mixtures in state-dependent lattices. (a) Schematic illustration of state-dependent optical lattices for orbital mixtures. The red line indicates the lattice potential with blue (yellow) areas showing the probability density (squared Wannier functions) of $|g\rangle$ ($|e\rangle$) atoms for lattice depth $V = 3E_{\text{rec}}$ ($9E_{\text{rec}}$) and polarizability ratio $p = 3$. (Bottom) Band structure of $|g\rangle$ (blue) and $|e\rangle$ atoms (yellow) with lowest band (solid line) and higher bands (dotted lines). (b) Comparison of experimentally determined polarizability ratios (markers) and theoretical predictions (solid line) from the simplified calculation in Ref. [132]. Filled markers show measurements with ^{171}Yb , whereas the empty point corresponds to ^{173}Yb . For the values determined within this work (filled circles), methods are explained in Chapter 5 (see Section 5.1.2). The dashed line shows the empirical relation $\rho(\lambda) = 1 + \sum_n \Delta_n / [(c/\lambda_n) - (c/\lambda)]$ with numerically fitted (fixed) parameters $\Delta_1 = 38.9(4)$ THz ($\lambda_1 = 649.1$ nm), $\Delta_2 = 103.9(10)$ THz ($\lambda_2 = 1388.8$ nm), and the vacuum speed of light c . The inset displays the scalar polarizability in atomic units (1 a. u. = $4\pi\epsilon_0\alpha_0^3$) with dotted lines indicating atomic transitions. The thick lines indicate the range of the main panel, and regimes ①-③ are explained in the main text.

[†] Riegger et al. [43].

[‡] Lemke et al. [137]; $\rho(\lambda_m) = 1$ inferred from the magic wavelength $\lambda_m = 759.35594(2)$ nm of ^{171}Yb .

like potentials produced by laser light. In the following, we employ Wannier functions $w(x)$ in the lowest band to describe the atomic density in optical lattices [1]. These wave functions are related to the Bloch functions by a Fourier transform and are therefore maximally localized on a single lattice. For example, this feature can be convenient for calculating the interaction strength of an atomic on-site pair following Eq. (1.4) [1].

The atomic polarizability of the $|g\rangle$ and $|e\rangle$ states differs since the accessible transitions within the singlet and triplet manifold occur at distinct transition wavelengths. This provides the unique opportunity to realize optical lattices with different lattice depths for atoms in either orbital [Fig. 1.4(a)] while operating the trap still far detuned from all relevant atomic transitions, which minimizes off-resonant photon scattering and heating [136]. Generally, the polarizability can be divided into a scalar, vector, and tensor part [138], where the scalar polarizability dominates for our typical experimental parameters (laser polarization). The scalar polarizability $\alpha_i(\omega)$ of state $|i\rangle$ in a many-level atom can be determined by summing over all relevant transitions to final states $|f\rangle$ with their reduced electric dipole matrix element $\langle i||\mathbf{d}||f\rangle$ [138],

$$\alpha_i(\omega) = \frac{2}{3} \sum_{f \neq i} \frac{\omega_{if}}{\hbar(\omega_{if}^2 - \omega^2)} |\langle i||\mathbf{d}||f\rangle|^2. \quad (1.10)$$

Here, $\omega = 2\pi c/\lambda$ denotes the angular frequency of the external laser field and $\hbar\omega_{if}$ the energy separating the states $|i\rangle$ and $|f\rangle$. Since isotope shifts of the relevant optical transition are of order GHz, the polarizability only differs negligibly for ^{171}Yb and ^{173}Yb over an extensive range of relevant wavelengths. While the above formula appears straight-forward to calculate, determining the precise value of the matrix elements for a many-electron atom becomes non-trivial. Nevertheless, a combination of experimentally measured lifetimes and advanced theoretical calculations of the electronic structure allows for reasonably good estimates [139, 140].

For the qualitative discussion in this section, however, we consider approximate results obtained by summing over a limited number transition and inferring matrix elements from measured radiative lifetimes as well as estimated branching ratios (L - S coupling scheme). This calculation of the scalar polarizability in the ground and clock state is identical to the results discussed in Ref. [132]. We refer the interested reader to this reference for the detailed calculation and a comparison to more accurate calculations. The inset in Fig. 1.4(b) displays the dependence of the scalar atomic polarizability $\alpha_{g,e}(\lambda)$ on the trapping-light wavelength λ for ytterbium atoms either in the $|g\rangle$ or $|e\rangle$ state. We also compare the calculation results to experimentally determined values of the polarizability ratio $p(\lambda) = \alpha_e(\lambda)/\alpha_g(\lambda)$ [see the main panel in Fig. 1.4(b)], which describes the ratio of the lattice depths for $|e\rangle$ and $|g\rangle$ atoms. The behavior of the polarizability ratio at variable wavelengths can be classified into three distinct regimes:

Magic wavelengths ①.—At this wavelength, the polarizability ratio precisely takes the value one, and hence the depth of an optical lattice becomes identical for $|g\rangle$ and $|e\rangle$ atoms. This type of trap enables the precise and accurate operation of optical lattice clocks as the transition frequency becomes independent of the local trap depth, which typically varies across an atomic ensemble [31]. Hence, large ensembles of atoms can be interrogated with minimal systematic shifts or broadening [31]. In our experiment, we employ optical lattices operated at the magic wavelength ≈ 759.4 nm [137] for precision spectroscopy, calibration measurements, and state-independent trapping, e. g., to realize two- or one-dimensional systems (see Chapters 3 and 5). In such a lattice, the hopping amplitudes as well as Wannier functions of $|g\rangle$ and $|e\rangle$ atoms are identical and do not exhibit a dependence on the orbital degree of freedom.

Tune-out wavelengths ②.—This kind of wavelength marks unique points of the polarizability ratio where either the excited or ground-state polarizability vanishes, as recently demonstrated for the alkaline-earth atom strontium [44]. This provides the experimental capability to manipulate atoms in a single orbital selectively while simultaneously leaving the other unaffected. The polarizability shown in the inset of Fig. 1.4(b) strongly suggests that tune-out wavelengths also exist for ytterbium, which currently still lacks an experimental demonstration.

State-dependent wavelengths ③.—This range of wavelengths corresponds to the generic case with unequal polarizabilities of both orbital states, the focus of this section. For our experimental realization of a state-dependent optical lattice with wavelength 671.5 nm, the polarizability ratio takes the value $p \approx 3$ [see Fig. 1.4(b)]. Hence, the lattice depth for $|e\rangle$ atoms is much deeper compared to $|g\rangle$ atoms, a vital feature to minimize lossy e - e collisions. In an optical lattice operated at a state-dependent wavelength, $|g\rangle$ and $|e\rangle$ atoms are also described by a tight-binding Hamiltonian but with distinct hopping amplitude $t_{g,e}$ for each orbital. Since the hopping amplitude depends exponentially on the lattice depth V , adjusting the lattice depth also tunes the relative ratio of the hopping amplitudes t_e/t_g .

1.3.1 The multiorbital Fermi-Hubbard model

For a state-dependent lattice giving rise to the hopping amplitudes $t_g \neq t_e$, the Hamiltonian of an interacting e - g mixture in the lowest band and at zero magnetic field can be described by a multiorbital single-band Fermi-Hubbard model [19], as illustrated in Fig. 1.5(a),

$$\begin{aligned} \hat{H}_{\text{m-orb}} = & - \sum_{\langle ij \rangle, \alpha, \sigma} t_\alpha \left(\hat{c}_{i\alpha\sigma}^\dagger \hat{c}_{j\alpha\sigma} + \text{h.c.} \right) + \sum_{i, \alpha, \sigma \neq \sigma'} U_{\alpha\alpha} \hat{n}_{i\alpha\sigma} \hat{n}_{i\alpha\sigma'} + V_{\text{dir}} \sum_{i, \sigma, \sigma'} \hat{n}_{ie\sigma} \hat{n}_{ig\sigma'} \\ & + V_{\text{ex}} \sum_{i, \sigma, \sigma'} \hat{c}_{ig\sigma}^\dagger \hat{c}_{ie\sigma'}^\dagger \hat{c}_{ig\sigma'} \hat{c}_{ie\sigma}. \end{aligned} \quad (1.11)$$

Here, $\langle ij \rangle$ denotes the set of neighboring lattice sites depending on the chosen dimensionality and $\hat{c}_{i\alpha\sigma}^\dagger$ ($\hat{c}_{i\alpha\sigma}$) are the fermionic creation (annihilation) operators for an atom on lattice site i in the orbital state $\alpha \in \{g, e\}$ and nuclear spin state σ . While the large spin symmetry of ^{173}Yb gives access to up to six spin states, we only consider two distinct states with $\sigma \in \{\downarrow, \uparrow\}$ in the following. Furthermore, $\hat{n}_{i\alpha\sigma} \equiv \hat{c}_{i\alpha\sigma}^\dagger \hat{c}_{i\alpha\sigma}$ are number operators, and the interaction energies $U_{\alpha\alpha}, V_{\text{dir}} = (U_{eg}^+ + U_{eg}^-)/2, V_{\text{ex}} = (U_{eg}^+ - U_{eg}^-)/2$ are obtained from the associated s -wave scattering lengths and the Wannier functions $w_\alpha(\mathbf{r})$ following the prescription in Eq. (1.4),⁶

$$U_{\alpha\beta}^\gamma = \frac{4\pi\hbar^2}{m} a_{\alpha\beta}^\gamma \int d\mathbf{r} |w_\alpha(\mathbf{r})|^2 |w_\beta(\mathbf{r})|^2 \quad (1.12)$$

with $\gamma \in \{-, +\}$ for interorbital interactions and γ dropped for intraorbital interactions.

The Hamiltonian in Eq. (1.11) provides the starting point for studying orbital phenomena in solid-state systems in the clean and well-controlled setting of ultracold atoms. While this generic Hamiltonian can also be realized with other alkaline-earth(-like) atoms, the availability of two fermionic isotopes with distinct interaction properties and accessible Feshbach resonances make ytterbium a particularly versatile atomic species for studies in this direction.

1.3.2 The Kondo model

While the central topics of this thesis are not concerned with Kondo physics, we still comment on its potential realization with ytterbium motivated by the profound impact such an experimental observation could have. Only recently, the relevant scattering lengths of ^{171}Yb have been found to be particularly favorable for such an experimental implementation [53, 111, 131]. The Kondo model (or s - d model) describes the coupling of a localized spin \mathbf{S} ($S = 1/2$) to the spins of itinerant electrons in the conduction band with dispersion $\epsilon_{\mathbf{k}}$ as described by the Hamiltonian [5],

$$\hat{H}_K = \sum_{\mathbf{k}, \sigma \in \{\downarrow, \uparrow\}} \epsilon_{\mathbf{k}} \hat{c}_{\mathbf{k}\sigma}^\dagger \hat{c}_{\mathbf{k}\sigma} - J \sum_{\mathbf{k}, \mathbf{k}'; \sigma, \sigma' \in \{\downarrow, \uparrow\}} \mathbf{S} \cdot \left(\hat{c}_{\mathbf{k}'\sigma'}^\dagger \boldsymbol{\tau}_{\sigma'\sigma} \hat{c}_{\mathbf{k}\sigma} \right) \quad (1.13)$$

with $\boldsymbol{\tau}$ the vector of the Pauli matrices and the spin-exchange term $J < 0$. This seemingly simple model reproduces the anomalous resistance minimum in dilute alloys of transition metals at low temperatures, a phenomenon that puzzled theoretical physicists for decades [142].

⁶This approximate approach breaks down for large scattering lengths once the interaction energy becomes comparable to the band gap. This can be an issue for the large triplet scattering length a_{eg}^+ of ^{173}Yb , but approaches to renormalize the interaction strengths do exist [127, 141].

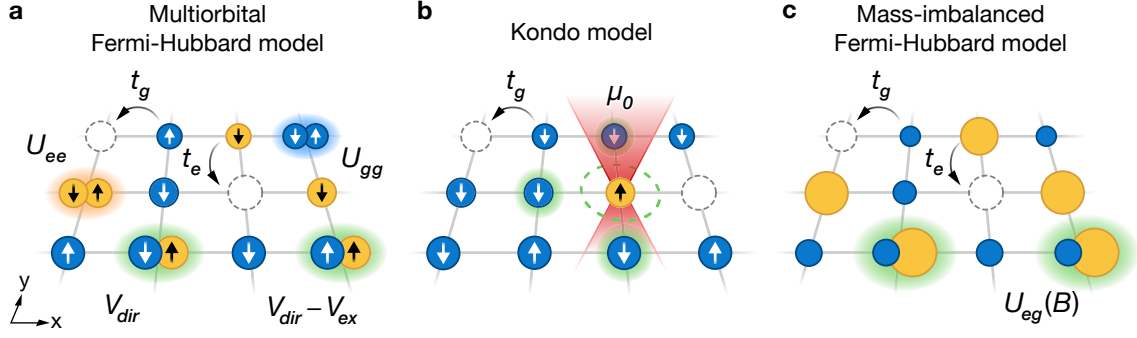


Figure 1.5 | Many-body physics with multiorbital mixtures in state-dependent lattices. Schematics of various multiorbital many-body models accessible with ultracold ytterbium atoms in state-dependent lattices. Blue (yellow) circles show $|g\rangle$ ($|e\rangle$) atoms with arrows indicating the nuclear spin state. Note that the models are not restricted to the illustrated case of a square two-dimensional lattice. (a) Generic multi-orbital Fermi-Hubbard model with relevant Hubbard parameters, including the hopping amplitudes $t_{g,e}$ and the various interaction energies $U_{gg,ee}$ and $V_{dir,ex}$. (b) Kondo model with a single $|e\rangle$ impurity localized by an optical tweezer (red) that also cancels the direct on-site interaction $V'_{dir} = -\mu_0$. Here, we also indicate the formation of the Kondo singlet with a green dashed line. (c) Mass-imbalanced Fermi-Hubbard model with a light ($|g\rangle$) and heavy ($|e\rangle$) species as well as a magnetic-field tunable interspecies interaction strength $U_{eg}(B)$. Panel (a) of this figure is adapted from Ref. [25].

Kondo’s seminal work on the above model employed a perturbative expansion of the scattering rate and predicted a logarithmic divergence at the characteristic temperature T_K consistent with the anomalous behavior of the resistivity [61]. Intuitively, the Kondo effect can be understood along the lines of asymptotic freedom, a concept from quantum chromodynamics and particle physics [143]: At high temperature, the impurity spin decouples from the conduction electrons and becomes essentially free. Once we lower the temperature, however, the coupling grows continuously, and itinerant electrons increasingly screen the localized spin by forming a “many-body” singlet state, which allows the impurity spin to lower its energy [see Eq. (1.13)]. This results in a spinless scattering center dramatically altering the conduction properties. The logarithmic divergence identified by Kondo signals the breakdown of perturbation theory and motivated a plethora of new theoretical approaches, most notably Wilson’s renormalization group approach [144]. While the experimental work on the subject could have been considered complete after the seventies [142], the observation of the Kondo effect in quantum dots led to renewed interest at the turn of the centuries [145–148].

Opportunities for ultracold atoms lie primarily in the study of non-equilibrium dynamics with local spin and charge resolution [149], such as the formation of the Kondo screening cloud, which has recently been observed in a quantum dot device [150, 151]. Moreover, the Kondo model has been extended to the case of many impurities in a lattice (Kondo lattice model) for the description of various materials featuring heavy-fermion behavior sometimes accompanied by unconventional superconductivity [5]. Here, coherence effects between localized spins on distant lattice sites significantly modify the phenomenology compared to the Kondo effect of an isolated impurity [152]. The Kondo lattice model features intriguing phases arising from a competition of Kondo-screening and long-range magnetic ordering due to the Ruderman-Kittel-Kasuya-Yosida (“RKKY”) mechanism [143]. Quantum simulation

experiments with ultracold ytterbium atoms could shed light on open questions regarding the associated phase diagram [19–21, 143].

For an experimental realization of the Kondo model, we consider the isotope ^{171}Yb , which naturally features antiferromagnetic spin-exchange interaction ($V_{\text{ex}} < 0$) consistent with real materials exhibiting the Kondo effect.⁷ The $|g\rangle$ atoms take on the role of the conduction electrons and a single $|e\rangle$ atom on the lattice site $i = 0$ mimics the localized electron. While the hopping of the $|e\rangle$ atoms remains finite in a state-dependent lattice, a suitable choice of the lattice wavelength and depth makes $t_e \ll t_g$ negligibly small such that for typical measurement time scales, we disregard $t_e \approx 0$. Since we only consider a single $|e\rangle$ atom, the e – e interactions are also not relevant. Moreover, the interaction term $U_{gg} \approx 0$ essentially vanishes due to the extremely small ground state scattering length of ^{171}Yb (see Table 1.1). With these preconditions, Eq. (1.11) can be simplified to resemble the form of the Kondo Hamiltonian [155],⁸

$$\hat{\mathcal{H}}_K^{(\text{exp})} = -t_g \sum_{\langle ij \rangle, \sigma \in \{\downarrow, \uparrow\}} (\hat{c}_{ig\sigma}^\dagger \hat{c}_{jg\sigma} + \text{h.c.}) - V_{\text{ex}} \sum_{\sigma, \sigma' \in \{\downarrow, \uparrow\}} \mathbf{S}_{0e} \cdot (\hat{c}_{0g\sigma}^\dagger \boldsymbol{\tau}_{\sigma, \sigma'} \hat{c}_{0g\sigma'}) + V'_{\text{dir}} \sum_{\sigma \in \{\downarrow, \uparrow\}} \hat{n}_{0g\sigma}. \quad (1.14)$$

Here, the $|e\rangle$ spin operator $\mathbf{S}_{0e} = (1/2) \sum_{\sigma, \sigma'} \hat{c}_{0e, \sigma}^\dagger \boldsymbol{\tau}_{\sigma, \sigma'} \hat{c}_{0e, \sigma'}$ corresponds to Abrikosov's pseudo-fermion representation [156]. Besides the Kondo coupling $J = V_{\text{ex}}$, the Hamiltonian features a repulsive (scalar) interaction term $V'_{\text{dir}} = (V_{\text{dir}} - V_{\text{ex}}/2) > 0$, a consequence of the positive interorbital scattering lengths $a_{eg}^\pm > 0$. This presents a central drawback for experimental implementations since this term strongly suppresses the coupling to the impurity spin giving rise to the Kondo effect in the first place [157]. Intuitively, this can be understood by considering that the $|g\rangle$ occupancy on the central site with the impurity ($|e\rangle$ atom) becomes strongly suppressed due to the direct interaction $V'_{\text{dir}} > 0$. With a quantum gas microscope [158–160], this repulsive direct interaction could be canceled using a local attractive optical potential $-\mu(\hat{n}_{0g\downarrow} + \hat{n}_{0g\uparrow})$ (optical tweezer), which would restore the ground state occupancy of the $|e\rangle$ site once $\mu = (V_{\text{dir}} - V_{\text{ex}}/2)$ [155, 157]. An entirely different approach could be the preparation of a single $|e\rangle$ atom on every lattice site, giving direct experimental access to the Kondo lattice model [19], where the scalar interaction term merely becomes a global energy offset.

Although currently not in direct reach of our experiment, we consider a scenario where the last term in Eq. (1.14) can be canceled, and we recover Eq. (1.13). In this limit, we calculate the Kondo temperature T_K , which describes the regime where the scattering of the spin impurity starts to become dominant, and a many-body singlet state forms between the impurity and the conduction electrons. This temperature exhibits an exponential scaling [5],

$$k_B T_K = D \sqrt{2|J|\rho_0} \exp \left[-\frac{1}{2|J|\rho_0} + \mathcal{O}(J\rho_0) \right] \quad (1.15)$$

with ρ_0 the density of states at the Fermi surface and $\rho_0 \approx 1/(D\pi)$ for a half-filled conduction band in a one-dimensional state-dependent lattice with (half) band width $D = 2t_g$ [161]. In the weak coupling limit $|J\rho_0| \ll 1$ of the above relation, we estimate a Kondo temperature on

⁷The isotope ^{173}Yb exhibits ferromagnetic spin-exchange interaction ($V_{\text{ex}} > 0$), but we have recently demonstrated a confinement-induced tuning mechanism of this parameter [43, 153]. Besides, Floquet engineering has been proposed to realize anisotropic Kondo Hamiltonians with singlet formation despite $V_{\text{ex}} > 0$ [154].

⁸This can be explicitly shown using the relation $\boldsymbol{\tau}_{ij} \cdot \boldsymbol{\tau}_{kl} = 2\delta_{il}\delta_{kj} - \delta_{ij}\delta_{kl}$ with the Kronecker delta δ_{ij} .

the order $k_B T_K \sim t_g$ for typical parameters. This appears to be a promising temperature regime within reach of future experiments that can also eliminate the unfavorable effects of V'_{dir} . While theoretical proposals exist for measuring the anomalous conduction directly [155], signatures of the Kondo effect could alternatively be observed in spin relaxation dynamics at variable temperature or magnetic field [45–47]. Here, a substantial deviation from the linear temperature scaling of the spin relaxation rate $\hbar\Gamma \sim k_B T$, known as Korringa law [154, 162], occurs in the vicinity of the Kondo temperature [163].

1.3.3 The mass-imbalanced Fermi-Hubbard model

Lastly, we consider a regime in the presence of a sizable magnetic field B , such that the Zeeman shift far exceeds the interaction terms $U_{\alpha\alpha}$ and $V_{\text{ex,dir}}$. This strongly suppresses the spin-exchange and allows us to tune the interaction strength utilizing the orbital Feshbach resonance and a variable magnetic field. If atoms are prepared in the two single-particle states $|e \downarrow\rangle$ and $|g \uparrow\rangle$ of the open channel [see Eq. (1.6)], their population remains constant and we drop the explicit spin state with the replacement $|e \downarrow\rangle \rightarrow |e\rangle$ and $|g \uparrow\rangle \rightarrow |g\rangle$. In this regime, the Hamiltonian with the Feshbach-tunable interaction parameter $U_{eg}(B)$ is given as

$$\mathcal{H}_{\text{FH}} = - \sum_{\langle ij \rangle, \alpha \in \{g, e\}} t_\alpha \left(\hat{c}_{i\alpha}^\dagger \hat{c}_{j\alpha} + \text{h.c.} \right) + U_{eg}(B) \sum_i \hat{n}_{ig} \hat{n}_{ie}, \quad (1.16)$$

which resembles a form of the Fermi-Hubbard model when the states $|g\rangle$ and $|e\rangle$ are identified with spin- \downarrow and spin- \uparrow . This experimental realization provides versatility since both the interaction strength and the ratio between the hopping amplitudes t_g and t_e , i. e., the mass imbalance, become tunable. In Chapter 5, we utilize this tunability to study thermalization and relaxation in the one-dimensional mass-imbalanced Fermi-Hubbard model systematically, which features particularly interesting regimes of emerging metastability (see Chapter 4).

1.4 Production and probing of multiorbital Fermi gases

Our experimental apparatus has entered a mature stage such that the technical details have largely remained unaltered compared to previous thesis work, and interested readers are encouraged to consult Refs. [121, 129, 132, 134]. This section focuses on the essential steps and parameters to produce and probe deeply degenerate Fermi gases of ^{171}Yb or ^{173}Yb with an orbital degree of freedom.

1.4.1 Producing degenerate Fermi gases

The first step towards producing multiorbital quantum gases entails producing multi-component degenerate Fermi gases in the ground state of either ^{171}Yb or ^{173}Yb with the desired population across the nuclear spin states. Here, we give a brief overview of typical experimental sequences that allow us to prepare these degenerate gases routinely. After capturing atoms from a Zeeman-slowed beam (broad $^1S_0 \rightarrow ^1P_1$ transition) and subsequent cooling in a magneto-optical trap (MOT) on the narrow $^1S_0 \rightarrow ^3P_1$ transition for 8-12 s, the non-degenerate atomic gas is loaded

into a red-detuned crossed optical dipole trap (ODT) operated at the wavelength 1064 nm. Subsequently, we cool the gas to quantum degeneracy over ≈ 20 s by successively lowering the ODT potential depth against gravity. The forced evaporation procedures for the isotopes ^{171}Yb and ^{173}Yb differ significantly, and therefore, we explain the details separately.

The scattering length $a_{\text{gg}} \approx 0$ (see Table 1.1) in the ground state of ^{171}Yb almost vanishes, which makes thermalization through collisions extremely slow, hindering efficient evaporative cooling. To circumvent this practical issue, we instead employ sympathetic cooling with the bosonic species ^{174}Yb . The sizable interspecies scattering length $a_{\text{gg}}^{171-174} = 429(13)a_0$ [130] allows for fast thermalization and efficient cooling. To this end, the crossed ODT is loaded with both species simultaneously from a dual-frequency MOT, which we realize by frequency modulation of the laser light using an electro-optical modulator (QUBIG PM9-VIS) [164]. This produces a carrier tuned to the $^1\text{S}_0 \rightarrow ^3\text{P}_1$ transition in ^{171}Yb and a ≈ 3.8 GHz detuned sideband for the same transition in ^{174}Yb . We load $\approx 10^6$ ^{171}Yb and $\approx 1.5 \times 10^6$ ^{174}Yb atoms into the crossed ODT for our experimental parameters. At the end of the evaporative cooling sequence, typically $2\text{--}60 \times 10^3$ ^{171}Yb atoms remain distributed equally across the two nuclear spin states $m_F \in \{-1/2, +1/2\}$ in the ground state. This deeply degenerate gas typically has a temperature of $T \approx 0.15T_F$ (Fermi temperature T_F), which we determine by numerically fitting the in-situ column density with the theoretical prediction for a non-interacting Fermi gas. Although most of the ^{174}Yb atoms are lost from the trap during forced evaporation, we employ a short isotope-selective pulse on the $^1\text{S}_0 \rightarrow ^1\text{P}_1$ transition to ensure no residual ^{174}Yb atoms are left.

The preparation of degenerate ^{173}Yb gases follows a much simpler procedure due to a larger scattering length $a_{\text{gg}} \approx 200a_0$ in the ground state (see Table 1.1). Here, we load $2\text{--}3 \times 10^6$ ^{173}Yb atoms into the crossed ODT and perform forced evaporation to reach quantum degeneracy. At the end of this procedure, typically $5\text{--}30 \times 10^3$ atoms per spin state remain at the temperature $T \approx 0.2T_F$. This temperature strongly depends on the number of involved spin states as evaporative cooling becomes increasingly inefficient with a reduced number of collisional partners in the s -wave collisional channel, which becomes dominant at low temperatures.

Since collisions preserve the nuclear spin state, we prepare the desired population across the six different m_F states of ^{173}Yb at the beginning of the evaporative cooling. To this end, we employ a sequence of optical pumping pulses on the $^1\text{S}_0 \rightarrow ^3\text{P}_1$ transition between the $F = 5/2$ and $F' = 7/2$ manifolds at a magnetic bias field ≈ 50 G [121]. In Chapter 3, we discuss this procedure for the production of strongly spin-imbalanced mixtures for studies of the Fermi polaron. For the experiments presented in this thesis, both nuclear spin states of ^{171}Yb are utilized. Optical pumping for this species (between the $F = 1/2$ and $F' = 3/2$ manifolds) is only required for certain calibration measurements that rely on spin-polarized samples.

1.4.2 Preparing multiorbital mixtures

Generally, a requirement for utilizing the clock state as orbital degree of freedom is a narrow laser, which allows preparing g – e mixtures of ^{171}Yb or ^{173}Yb with high fidelity and probing the system with high-resolution spectroscopy. Fortunately, the precision measurement community has pioneered the development of ultranarrow lasers, and nowadays, ultrastable optical cavities have become commercially available products. Phase-locking a diode laser to such a cavity

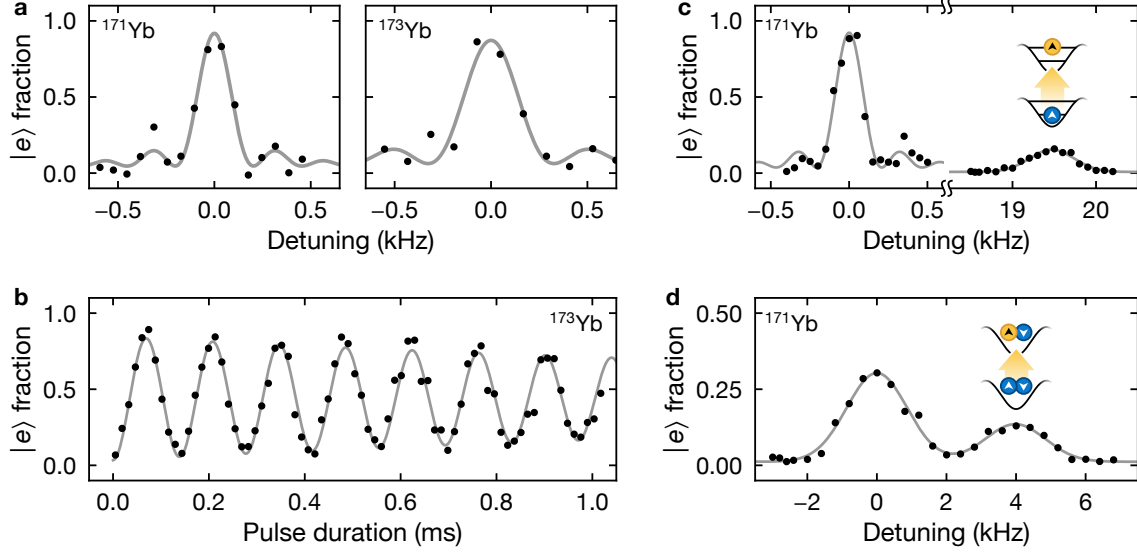


Figure 1.6 | Clock-line spectroscopy as powerful experimental probe. Circles show the fraction of atoms detected in the $|e\rangle$ state, solid lines correspond to numerical fits. Detunings of the clock laser are given relative to the single-particle transition and scanned with an acousto-optical modulator. The top-right and top-left labels indicate the isotope employed for the corresponding measurement. (a) Clock-line spectroscopy in a (left) three-dimensional or (right) single-axis magic-wavelength lattice. The observed full width at half maximum (left) 234(13) Hz and (right) 377(22) Hz are comparable to the Fourier limit of the rectangular-shaped clock laser pulse. (b) Fast on-resonance Rabi oscillation in a deep single-axis magic-wavelength lattice with fitted Rabi frequency $\Omega = 2\pi \times 7.21(1)$ kHz. (c) Spectroscopy of pair states in a three-dimensional lattice generated from a combination of magic-wavelength and state-dependent wavelengths. Here, we show the single-particle transition and two-particle transition (inset schematic) with an interaction shift of ≈ 4 kHz. (d) Spectroscopy of motional states in a three-dimensional magic-wavelength lattice with the carrier transition at zero detuning and the red sideband transition at ≈ 19.5 kHz (inset schematic).

using the Pound-Drever-Hall technique [165, 166] allows reducing the linewidth of the laser dramatically. To achieve the short-term stability required to address the ultranarrow clock transition coherently, we lock our clock laser to a cavity formed by an ultra-low-expansion (ULE) spacer and two optically contacted mirrors (STABLE LASER SYSTEMS) [121]. This allows us to probe the clock transition with Fourier-limited pulses down to a full width at half maximum of ~ 200 Hz [see Fig. 1.6(a)]. We operate the ULE cavity at a temperature close to the zero crossing of its coefficient of thermal expansion [121]. In this configuration, we find a remaining linear frequency drift of ≈ 1.7 kHz per day,⁹ which can be easily canceled by feed-forward on the cavity offset lock. With this procedure, a residual non-linear frequency drift ~ 100 Hz per day remains, which we cancel with daily calibration measurements.

We have recently upgraded our clock laser system with a fully commercial product (TOPTICA TA pro), combining an external cavity diode laser as seed and a tapered power amplifier.¹⁰ In

⁹This value describes the drift of the cavity relative to the frequency of the 1156 nm light. The second harmonic generation of 578 nm light also doubles the drift relative to the atomic clock transition.

¹⁰The measurements in Chapter 3 have been realized with an intermediate upgrade of the clock laser system, that combined the preexisting home-built seed laser [121] with a commercial tapered power amplifier (TOPTICA BoostA pro). However, the parameters discussed in this section also approximately apply to this system.

contrast to our previous home-built seed laser, frequency modulation of the current now works reliably over a wide bandwidth ~ 1 MHz, which allows us to lock the seed laser onto the ULE cavity with fast current feedback alone [167]. This system produces up to 650 mW of fiber-coupled 1156 nm light, which we subsequently frequency-doubled with a home-built resonant second-harmonic-generation cavity [121]. At the location of the atoms, we estimate a maximum total 578 nm clock laser power of ≈ 100 mW and intensity ≈ 150 W/cm² [132] by measuring the optical power in front of the vacuum chamber. This abundance of available laser power allows us to drive single-particle Rabi oscillations with frequencies up to $\Omega \sim 2\pi \times 10$ kHz [see Fig. 1.4(b)], a significant increase compared to the capabilities of our previous laser system [121].

The clock laser has become the key tool in our experiment, and the apparatus features three independent beam paths, which allow the clock transition to be addressed along arbitrary lattice axes. In general, we employ at least a single lattice axis along the direction of the driving clock laser beam to operate deep in the Lamb-Dicke regime, where recoil-free spectroscopy can be performed. We employ the clock laser for a variety of measurements, which include: calibration of the single-particle clock frequency, measuring the trap depth by addressing sideband transitions [see Fig. 1.6(c)], probing few-body and many-body interaction shifts in orbital mixtures [see Fig. 1.6(d), also see Chapter 3], and populating the second orbital with high fidelity for utilizing the orbital Feshbach resonance (see Chapter 5). Figure 1.6 shows typical application examples illustrating the versatility of this experimental tool.

To detect ¹⁷¹Yb (¹⁷³Yb) atoms in the $|e\rangle$ state, we employ a repumping scheme on the $^3P_0 \rightarrow ^3D_1$ transition between the $F = 1/2$ and $F' = 3/2$ ($F = 5/2$ and $F' = 7/2$) hyperfine manifolds [32]. Fortunate branching ratios allow transferring nearly all $|e\rangle$ atoms back to the $|g\rangle$ ground state via the intermediate and short-lived 3P_1 states by only scattering few photons. With this procedure, we estimate that $< 5\%$ of the $|e\rangle$ atoms are transferred to the long-lived 3P_2 state, which are most likely subsequently lost from the trap. The $^3P_0 \rightarrow ^3D_1$ transition (wavelength ≈ 1389 nm) is driven with a free-running distributed feedback laser (NTT ELECTRONICS NLK1E5GAAA) [168]. The relatively large short-term frequency fluctuations of the free-running laser (and finite power) make laser pulses of duration ~ 1 ms necessary to deplete the $|e\rangle$ state fully, which leads to motional blurring and other undesired effects. In the future, stabilizing the laser to an optical cavity should allow us to significantly reduce the minimum pulse duration to $\ll 100$ μ s [169] and avoid issues associated with much longer pulses.

1.4.3 High-resolution absorption imaging

We primarily probe the atomic system with absorption imaging, which yields the in-situ atomic density integrated along the line of sight. To this end, we drive the $^1S_0 \rightarrow ^3P_1$ transition with $\lambda = 399$ nm resonant light between the hyperfine manifolds $F = 1/2$ and $F' = 3/2$ for ¹⁷¹Yb, or $F = 5/2$ and $F' = 7/2$ for ¹⁷³Yb. We employ a small bias field of ≈ 1 G such that the Zeeman shift only negligibly splits transitions between individual m_F states. The alignment of the magnetic field and polarization of the imaging light ensure that predominantly σ^\pm transitions are driven. For ¹⁷³Yb, the atomic population across different nuclear spin states is pumped to the stretched states $m_F = \pm 5/2$ after scattering a few photons. The

imaging light is collected with a quadruplet objective lens (LENS-OPTICS) characterized by the numerical aperture $NA = 0.27$ and diffraction-limited resolution $\approx 1 \mu\text{m}$ [129]. In the current setting, imperfections and limited possibilities for corrections deteriorate the imaging resolution to $\approx 3 \mu\text{m}$, as inferred from a measurement of the modulation transfer function [170].

The complex structure of the multiple transitions between distinct m_F states and imperfect laser polarization generally reduces the absorption cross section σ_{eff} by a factor of ≈ 1.5 -3 compared to the resonant cross section $\sigma = 3\lambda^2/(2\pi)$ of a two-level atom [138]. Since the scattering of imaging photons heats the atomic sample, we employ short imaging pulses 5-15 μs to make these effects negligible. At the same time, this requires sizable imaging intensities for the light to fully penetrate dense atomic clouds. These high intensities typically far exceed the saturation intensity with $I_{\text{img}} \approx 2\text{-}12I_{\text{sat}}$ causing a non-linear response of the atoms, which we account for with a modified Lambert-Beer law relating the absorbed light collected on our camera and the atomic column density $n(x, y)$ [171],

$$n(x, y) = \frac{1}{\sigma_{\text{eff}}} \left\{ \ln \left[\frac{I_{\text{in}}(x, y)}{I_{\text{out}}(x, y)} \right] + \frac{I_{\text{in}}(x, y) - I_{\text{out}}(x, y)}{I_{\text{sat}}^{\text{eff}}} \right\}. \quad (1.17)$$

Here, $I_{\text{out}}(x, y)$ denotes the intensity detected after the light has penetrated the atomic cloud, and we determine the incident intensity $I_{\text{in}}(x, y)$ from a reference image without atoms. The second term in the above relation accounts for the saturation of the optical transition with the effective saturation intensity $I_{\text{sat}}^{\text{eff}} > I_{\text{sat}}$. For quantitative measurements, we determine the value of $I_{\text{sat}}^{\text{eff}}$ by measuring the absorbed intensity of nearly identical atomic samples for variable incident light intensity. Requiring that Eq. (1.17) results in the same density independent of the incident intensity yields $I_{\text{sat}}^{\text{eff}}$ [171]. Generally, we perform this procedure for each nuclear spin mixture relevant in the experiment although the typical parameters vary only by $\approx 10\%$ across different spin-state populations.

For the many-body measurements discussed in this thesis, comparing experimental and theoretical results quantitatively requires the knowledge of the absolute atom number. To this end, we analyze the atomic shot noise of thermal atomic samples with correlation lengths below our imaging resolution. In this regime, the noise of the detected local density n_i follows a Poisson distribution with variance $\Delta n = (n_i - \langle n_i \rangle)^2 = \langle n_i \rangle$. This relation allows determining the absolute atom number directly from many realizations (absorption images) of a nearly identical sample. Such a procedure fixes the effective cross section σ_{eff} in Eq. (1.17). Note that we account for the finite noise correlations from the imaging system itself with the methods from Ref. [170].

CHAPTER 2

Fermi polarons

This chapter introduces the Fermi polaron, a quasiparticle which forms when immersing a single impurity in a Fermi sea. First, we briefly review a theoretical framework for Fermi polarons and solve the quasiparticle problem in two dimensions for the short-ranged interactions of ultracold atomic gases. Then, we focus on applying our findings to practical realizations and discuss the quasi-two-dimensional geometry relevant for experiments utilizing the strong confinement of optical lattices. Moreover, we show the differences that arise in the quasiparticle problem for orbital mixtures of ^{173}Yb atoms. The analysis in this chapter paves the way for presenting the observation of multiorbital Fermi polarons covered in Chapter 3. The theoretical results explained in this chapter have been partly published in Ref. [109].

2.1 The single quasiparticle problem

A central question in condensed matter physics is how the description of electrons changes when interactions are introduced. Generally, there is no guarantee that the picture of single particles with a well-defined dispersion relation still applies. For instance, this picture breaks down in one dimension, where excitations are described by collective modes [172, 173]. For many systems of interacting fermions in two or more dimensions, Landau's *Fermi liquid* theory provides a powerful picture in terms of quasiparticles [63]. The essence of this theory is that as interactions are introduced, the free particle becomes adiabatically connected to a quasiparticle. While the single-particle properties of this quasiparticle are significantly modified, the ground state remains a filled Fermi sea with a sharp Fermi surface. This allows for describing complex systems in terms of their quasiparticles to determine relevant characteristics of a material.

The *Fermi polaron* corresponds to the quasiparticle that forms when immersing an interacting impurity into a Fermi sea, which results in particle-hole excitations. Intuitively, this quasiparticle can be understood as a local density enhancement or depletion of the medium, depending on the nature of interactions. The Fermi polaron presents a minimal example of Landau's Fermi liquid [63], thereby enabling direct comparison of theoretical predictions with experimental observations [71–76, 84, 109]. In particular, ultracold quantum gases provide an ideal testbed to study the Fermi polaron as they provide a clean setting—free of undesired disorder and with precise interaction tunability. Notably, the Fermi polaron has also found

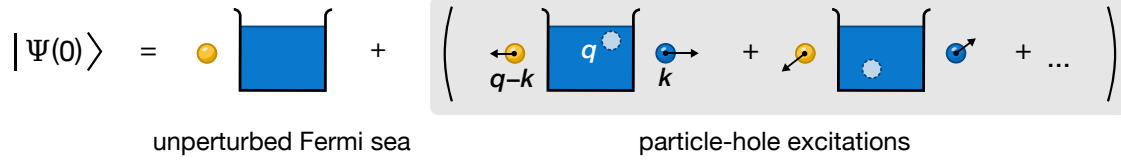


Figure 2.1 | Illustration of Chevy's variational wave-function ansatz. Different components of the wave-function ansatz, i. e., the unperturbed Fermi sea and particle-hole excitations (gray box), illustrated for an impurity at rest ($p = 0$). The yellow circle corresponds to the impurity, whereas the Fermi sea (with holes) and the excited particle are shown in blue.

applications in the description of the extremely dense matter inside neutron stars [174, 175]. This section discusses a variational wave-function ansatz and the Green's function approach for the quasiparticle problem of the Fermi polaron.

2.1.1 Chevy's variational wave-function ansatz

For the theoretical description of the Fermi polaron, we consider a single impurity interacting with the majority particles in a Fermi sea. An instructive approach for this problem is the Chevy ansatz [64], which we briefly discuss in the following. In the non-interacting limit, we obtain the wave function of an impurity with momentum \mathbf{p} and an unperturbed Fermi sea,

$$|\Psi_0(\mathbf{p})\rangle = \left(\hat{c}_{\mathbf{p}\downarrow}^\dagger |0\rangle_\downarrow\right) \otimes |\text{FS}\rangle_\uparrow. \quad (2.1)$$

Here, the wave function is written in its second-quantized form, $|\text{FS}\rangle_\uparrow$ describes the state of the Fermi sea, and $\hat{c}_{\mathbf{p}\downarrow}^\dagger$ denotes the fermionic creation operator for an impurity with momentum \mathbf{p} . We assign the two spin states $\sigma \in \{\downarrow, \uparrow\}$ to the impurity and particles from the Fermi sea, respectively. This notation is inspired by the typical experimental realization that involves a multi-component Fermi gas with a strong population imbalance between two spin states. For simplicity and without loss of generality, we assume that the impurity resides in a different internal state but is otherwise similar to the particles in the Fermi sea, in particular, the masses are identical, $m = m_\downarrow = m_\uparrow$. Starting from Eq. (2.1), we can now construct Chevy's wave-function ansatz for an interacting impurity [64],

$$|\Psi(\mathbf{p})\rangle = \sqrt{|Z_{\mathbf{p}}|} \left(\hat{c}_{\mathbf{p}\downarrow}^\dagger |0\rangle_\downarrow\right) \otimes |\text{FS}\rangle_\uparrow + \sum_{q < k_F < k} \phi_{\mathbf{p};\mathbf{k}q} \left(\hat{c}_{(\mathbf{p}+\mathbf{q}-\mathbf{k})\downarrow}^\dagger |0\rangle_\downarrow\right) \otimes \left(\hat{c}_{\mathbf{k}\uparrow}^\dagger \hat{c}_{\mathbf{q}\uparrow} |\text{FS}\rangle_\uparrow\right) \quad (2.2)$$

with $k_F = \sqrt{2mE_F}/\hbar$ the Fermi wave vector and E_F the Fermi energy, which corresponds to the chemical potential of the majority particles at zero temperature. The above form is motivated by the underlying physics and how we expect the interacting impurity to change the state of the medium. The squared overlap with the non-interacting wave function from Eq. (2.1) reduces according to $|Z_{\mathbf{p}}| \in [0, 1]$. The remaining weight $(1 - |Z_{\mathbf{p}}|)$ is contributed by particle-hole excitations of the Fermi sea, which originate from the finite interactions between impurity and medium and are described by the sum in Eq. (2.2). These particle-hole excitations correspond to a hole at $q < k_F$ and a particle above the Fermi surface at $k > k_F$, as illustrated in Fig. 2.1.

The trial wave function in Eq. (2.2) allows us to find the energy E of the impurity by minimizing the energy functional $\lambda(E) = \langle \Psi(\mathbf{p}) | (\hat{\mathcal{H}} - E) | \Psi(\mathbf{p}) \rangle$. This can be achieved with a variational method, i. e., calculating the gradient with respect to the coefficients $Z_{\mathbf{p}}$ and $\phi_{\mathbf{p};\mathbf{k}\mathbf{q}}$. The Hamiltonian for the description of interactions between the impurity and Fermi sea generally takes the form [64]

$$\hat{\mathcal{H}} = \sum_{\mathbf{k}, \sigma \in \{\downarrow, \uparrow\}} \frac{\hbar^2 k^2}{2m} \hat{c}_{\mathbf{k}\sigma}^\dagger \hat{c}_{\mathbf{k}\sigma} + \frac{\Omega}{g} \sum_{\mathbf{k}, \mathbf{k}', \mathbf{q}} \hat{c}_{(\mathbf{k}+\mathbf{q})\uparrow}^\dagger \hat{c}_{(\mathbf{k}'-\mathbf{q})\downarrow}^\dagger \hat{c}_{\mathbf{k}'\uparrow} \hat{c}_{\mathbf{k}\downarrow} \quad (2.3)$$

with g the coupling constant determining the interaction between impurity and Fermi sea, Ω the volume of the system, and \mathbf{q} the momentum exchanged in the scattering process. In general, g takes a relatively simple form for the dominant s -wave interactions in ultracold quantum gases [64, 176], but still contains the relevant details of the dimensionality and interaction channels.

The minimization of the energy functional $\lambda(E)$ yields an implicit equation for the energy of the impurity immersed in the Fermi sea [64],

$$E - \frac{p^2}{2m} = \sum_{q < k_F} \left\{ \frac{1}{g} - \sum_{k > k_F} \frac{1}{E - (2m)^{-1} [\hbar^2 k^2 + \hbar^2 q^2 - (\mathbf{p} + \hbar \mathbf{q} - \hbar \mathbf{k})^2] + i\varepsilon} \right\}^{-1}. \quad (2.4)$$

Here, the small imaginary term $\varepsilon > 0$ allows us to find solutions corresponding to excited states of the system with $E > 0$ and finite lifetime, in contrast to the ground state. Indeed, such an excited state exists, namely, the repulsive Fermi polaron [80, 81]. This quasiparticle appears in addition to the attractive Fermi polaron, which corresponds to the ground state (see Section 2.2). Note that above imaginary contribution can also be derived rigorously by minimizing a time-dependent functional in the variational procedure [177].

2.1.2 The Green's function approach

The Chevy ansatz provides an intuitive picture for the underlying physics, but the calculation of experimentally relevant quantities can be done more rigorously with methods from quantum field theory, as commonly used in condensed matter physics [178]. In this context, Green's function G appears as a propagator, which contains the relevant physics and provides the elementary building block for Feynman diagrams [179]. Dyson's equation relates the dressed propagator G and the propagator of the free particle $G_0 = [E - p^2/(2m)]^{-1}$ via the self-energy Σ . This quantity describes the energy that a particle acquires due to its interactions with the surrounding medium. We schematically illustrate the underlying idea of the perturbative expansion and how it reduces to a geometric series in Fig. 2.2(a). For the problem of the Fermi polaron, Green's function describes the propagation of a single impurity at momentum \mathbf{p} in the medium with the form [178]

$$G(\mathbf{p}, E) = \frac{1}{E - p^2/(2m) - \Sigma(\mathbf{p}, E)}. \quad (2.5)$$

From Green's function, all relevant quasiparticle properties can be derived, and the problem reduces to finding an expression for the self-energy $\Sigma(\mathbf{p}, E)$, which can still be an exceptionally

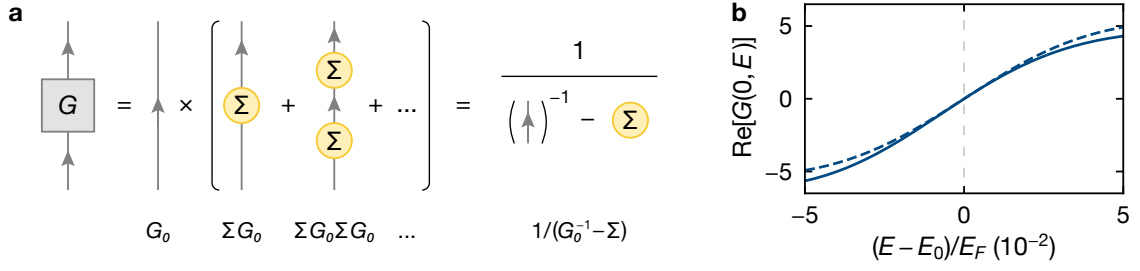


Figure 2.2 | Green's function approach for the Fermi polaron. (a) Illustration of Dyson's equation adapted from Ref. [179]. We schematically show how the full propagator G , free propagator G_0 , and the self-energy Σ are related by the summation over an infinite perturbative expansion, which can be identified as a geometric series shown on the right. (b) Example showing an expansion of the polaron Green's function $G(0, E)$ around a quasiparticle pole at energy E_0 . The solid line corresponds to Eq. (2.5) calculated for the self-energy Σ , and the dashed line corresponds to the expansion defined in Eq. (2.7) with the appropriate parameters Z and Γ .

difficult task. For the Fermi polaron, the summation over the Feynman diagrams contributing to the self-energy can be truncated by considering at most one single particle-hole excitation of the Fermi sea—in analogy to Chevy's variational wave-function ansatz [64, 65]. Formally, we make the expansion [66]

$$\Sigma(\mathbf{p}, E) = \Sigma^{1\text{PH}}(\mathbf{p}, E) + \Sigma^{2\text{PH}}(\mathbf{p}, E) + \dots \quad (2.6)$$

and neglect terms with more than one particle-hole excitation (1PH approximation) such that $\Sigma(\mathbf{p}, E) \equiv \Sigma^{1\text{PH}}(\mathbf{p}, E)$ in the following discussion. This approach is also known as ladder approximation due to the visual appearance of the corresponding Feynman diagrams [81]. Fortunately, the 1PH approximation already yields reasonably accurate results, verified by diagrammatic quantum Monte Carlo studies, that consider higher-order Feynman diagrams beyond single particle-hole excitations at the cost of finite statistical errors [77]. Nevertheless, the approximative nature of this approach underlines the importance of experimental evidence, which has been able to benchmark the results of the description in terms of the ladder approximation (see, e. g., Refs. [73, 76]). The underlying reason for the accuracy of theoretical predictions, despite neglecting excitations beyond single-particle hole pairs, is believed to originate from a fortunate canceling of higher-order Feynman diagrams [77]. Within the 1PH hole approximation, the Green's function approach is equivalent to the Chevy ansatz, and the implicit relation in Eq. (2.4) defines the self-energy of the Fermi polaron [65].

In the vicinity of a pole E_0 , determined by $E_0 = \Sigma(\mathbf{p}, E_0)$ and corresponding to a quasiparticle with energy E_0 , we can approximate Green's function in Eq. (2.5) with the general form [178]

$$G(\mathbf{p}, E \rightarrow E_0) \approx \frac{Z}{E - E_0 - p^2/(2m^*) + i\Gamma}, \quad (2.7)$$

which contains the quasiparticle residue Z , effective mass m^* , and damping Γ . The quasiparticle residue quantifies the weight of the quasiparticle peak in the spectrum, which we have introduced as the overlap with the non-interacting wave function [see Eq. (2.2)]. The

damping Γ quantifies the width of the quasiparticle peak, which can be associated with a finite lifetime of the quasiparticle in certain systems [110]. As we will see in Chapter 3 (see Sections 3.4), there is a caveat to a generalized association of Γ with the lifetime, particularly for the repulsive polaron in ultracold Fermi gases.

We can extract the properties of the quasiparticle with energy E_0 by comparing Eqs. (2.5) and (2.7). For an impurity at rest ($p = 0$), we find the residue and damping [81],

$$Z = \left\{ 1 - \partial_E \operatorname{Re} [\Sigma(0, E)]|_{E=E_0} \right\}^{-1} \quad \text{and} \quad \Gamma = -Z \operatorname{Im} [\Sigma(0, E_0)]. \quad (2.8)$$

Interactions with the medium result in a mass enhancement with respect to the bare mass m of the free impurity [81],

$$\frac{m^*}{m} = Z^{-1} \left\{ 1 + \partial_{[p^2/(2m)]} \operatorname{Re} [\Sigma(\mathbf{p}, E_0)]|_{p=0} \right\}^{-1}. \quad (2.9)$$

Another central result of the Green's function approach is the spectral function [178],

$$A(0, E) = -\frac{1}{\pi} \operatorname{Im} [G(0, E)], \quad (2.10)$$

which is related to the linear response of the in-medium impurity for an excitation at energy E in the experiment (see Section 3.3.2 in Chapter 3) [180]. Remarkably, the above quasiparticle properties have been determined quite precisely in various experiments with ultracold atoms [71–76, 84, 109].

2.2 Phenomenology in two dimensions

Having established the theoretical framework for the description of Fermi polarons in terms of their Green's function, we now proceed with a theoretical calculation in two dimensions (2D). First, we explain the parameterization of interactions in 2D and calculate the self-energy explicitly for short-range interactions, as typically found in ultracold quantum gases. Then, we discuss the structure of the many-body spectrum and the appearance of the quasiparticle branches corresponding to attractive and repulsive polaron. Finally, we explore the effects of finite momentum and temperature, which typically play a role in experiments. We note that the key elements of the phenomenology discussed in this section also apply to the three-dimensional case (see, e. g., Ref. [66]).

Due to the dominance of s -wave scattering in ultracold quantum gases, Fermi polarons can usually be described in terms of a few universal parameters. In 2D, the low-energy s -wave scattering amplitude takes the form [181]

$$f(k) = \frac{4\pi}{i\pi - \ln(k^2 a_{2D}^2)}, \quad (2.11)$$

which defines the s -wave scattering length $a_{2D} > 0$. In contrast to three dimensions (3D), the low-energy scattering amplitude depends explicitly on the momentum k and diverges

logarithmically for $k \rightarrow 0$. For the short-range interactions in ultracold quantum gases, the scattering length is related to the energy of the bound state ϵ_b with

$$a_{2D} = \frac{\hbar}{\sqrt{m\epsilon_b}}. \quad (2.12)$$

The dimensionless quantity $\ln(k_F a_{2D})$ with Fermi wave vector $k_F = \sqrt{2mE_F}/\hbar$ and scattering length a_{2D} parameterizes the interaction strength of Fermi gases in 2D [182]. In general, $\ln(k_F a_{2D}) > 0$ can be associated with attractive and $\ln(k_F a_{2D}) < 0$ with repulsive interactions. We note that this contrasts with the typical parameterization $1/(k_F a)$ in 3D, where $1/(k_F a) > 0$ indicates the repulsive regime.

2.2.1 The self-energy

To explore the phenomenology in ultracold 2D Fermi gases, we solve the Fermi polaron problem in the limit of a zero-momentum impurity and a zero-temperature medium. Note that the following calculation only holds for interactions with a negligible effective range, as in the case of broad Feshbach resonances (see Section 1.2.4 in Chapter 1). In Section 2.3, we will discuss how more complex interactions in orbital mixtures of ultracold ^{173}Yb can modify certain properties of the Fermi polaron. Nevertheless, the phenomenology remains mostly unchanged with only minor adjustments for our experimental parameters.

In two dimensions, the coupling constant g for s -wave collisions takes the form [177]

$$\frac{1}{g} = - \sum_{\mathbf{k}} \frac{1}{\epsilon_b + \hbar^2 k^2 / (2m)} \quad (2.13)$$

with $\epsilon_b > 0$ the binding energy of the molecular bound state in 2D, which can be related to the scattering length with Eq. (2.12). Here, we have set the volume of the system to $\Omega \equiv 1$. For the chosen regime, the implicit energy relation in Eq. (2.4) can be solved analytically except for the outer integral over the momentum below the Fermi surface (see Appendix A.1). In the thermodynamic limit, where the sums can be replaced with integrals, the self-energy then takes a relatively simple form,

$$\frac{\Sigma(0, E)}{E_F} = 2 \int_0^1 dy \left\{ \ln\left(\frac{\epsilon_b}{E_F}\right) - \ln \left[1 - \frac{E}{2E_F} - \frac{y}{2} \pm \sqrt{\left(1 - \frac{E}{2E_F}\right)^2 - y} \right] \right\}^{-1}, \quad (2.14)$$

which we solve numerically to obtain the spectral function and other quasiparticle properties. Here, the symbol \pm denotes the sign function with $\pm = \text{sgn Re}[1 - E/(2E_F)]$. Lastly, we note that similar calculations in the limit of 1PH have been performed much earlier for the description of thin ^3He films [183]. These perturbative results generally agree well with the quasiparticle energies extracted from Eq. (2.14) at weak coupling [176].

2.2.2 Quasiparticles and their energy landscape

The results of the numerical calculations are shown in Fig. 2.3. First, we focus on the spectral function $A(0, E)$ [see Eq. (2.10)] and the general features appearing in the many-body spectrum of the dressed impurity as a function of the interaction strength. The resulting energy landscape features two distinct quasiparticle branches, one at positive energies $E_+ > 0$, and one at negative energies $E_- < 0$ (see Fig. 2.3). The former is known as attractive and the latter as repulsive Fermi polaron in accordance with the sign of their energy. In the following, we briefly discuss their (quasiparticle) properties (see Fig. 2.4) as well as the feature between the two quasiparticle peaks known as the molecule-hole continuum (see ② in the main panel of Fig. 2.3).

Attractive polaron ①.—The quasiparticle at negative energies $E_- < 0$ corresponds to the ground state of the system within the 1PH approximation of the self-energy [64]. It has been first observed in ultracold 3D Fermi gases [71, 72] and later also in 2D Fermi gases [74]. This attractive polaron has vanishing energy for weak binding, $\epsilon_b \ll E_F$ [$\ln(k_F a_{2D}) \gg 0$]. In this limit, the quasiparticle energy can be approximated by $E_-/E_F \approx -2/\ln(2E_F/\epsilon_b)$ [184], an accurate estimate within a few percent for $\ln(k_F a_{2D}) \geq 2$. The quasiparticle residue Z_- vanishes for strong binding, $\epsilon_B \gg E_F$ [$\ln(k_F a_{2D}) < 0$], indicating that the wave function of the attractive polaron becomes increasingly dominated by an incoherent background of particle-hole excitations [see Fig. 2.4(a)]. In this regime, the absolute value of the energy grows approximately linearly with the binding energy ϵ_b , $E_-/E_F \approx -(\epsilon_b/E_F + 0.582)$ [185]. This suggests that the attractive Fermi polaron remains the ground state of the system for arbitrarily strong binding $\epsilon_b \rightarrow \infty$. However, the result can be understood as an artifact of the simplified ansatz with only a single particle-hole excitation.

Another eigenstate exists at negative energies, i. e., the dressed molecule corresponding to a particle from the background Fermi sea tightly bound to the impurity [185]. Similar to the polaron, interactions with the surrounding medium can dress this molecule. Crucially, this state cannot be described within the 1PH approximation, as the description of the non-interacting state already requires a single particle-hole pair. Extending the ansatz in Eq. (2.2) to an additional particle-hole pair provides the approximate energy of this dressed molecule [185], which has also been calculated in diagrammatic Monte Carlo studies [186, 187]. At the critical interaction parameter $\ln(k_F a_{2D}) \approx -1$ [177, 186, 187], the energies of the dressed molecule and attractive polaron cross. This indicates that the molecule indeed corresponds to the ground state in this regime, making the attractive polaron an excited state for $\ln(k_F a_{2D}) \lesssim -1$. In two dimensions, the exact nature of this transition point or crossover region remains a subject of debate [177, 185–189], although recent experimental results have shed light on the situation in 3D [84].

Molecule-hole continuum ②.—Between the two quasiparticle peaks [see $\ln(k_F a_{2D}) \gtrsim -0.5$ in Fig. 2.3], the spectrum exhibits a particularly weak and broad feature. This molecule-hole continuum arises due to the impurity forming a bound molecule with a single particle from the Fermi sea [176]. Naturally, this excitation can have a large range of energies due to the momentum spread of the medium, $0 < p < \hbar k_F$. Because of its small weight in the spectrum, the molecule-hole continuum only plays a minor role when probing spectra experimentally in

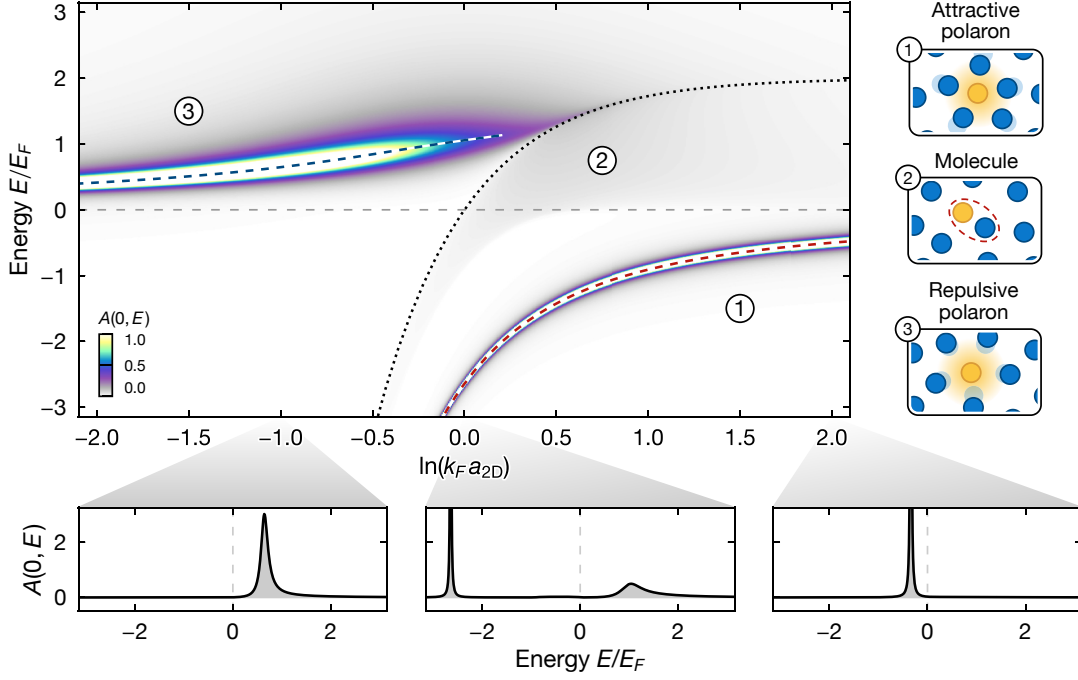


Figure 2.3 | Energy landscape in two dimensions. Spectral function $A(p = 0, E)$ of the Fermi polaron numerically calculated within the 1PH approximation. The blue (red) dashed lines correspond to the quasiparticle energies E_- (E_+) of the attractive (repulsive) polaron, calculated from Eq. (2.14). Note that a finite broadening has been applied to the spectrum with the replacement $E \rightarrow E + 0.01iE_F$, and the plot range is truncated to increase the contrast at small amplitudes. In the three right panels, illustrations of different polaron states and the bound molecular state are shown with yellow and blue circles depicting the impurity and particles from the Fermi sea, respectively. The bottom panels display spectra for $\ln(k_F a_{2D}) = -1, 0$, and 2 (from left to right).

the linear response regime. However, for strong drive, the molecule-hole continuum becomes increasingly relevant as also experimentally observed in a mass-imbalanced 3D Fermi gas [73].

Repulsive polaron ③.—The quasiparticle at positive energies $E_+ > 0$ corresponds to the repulsive Fermi polaron, which has been observed for the first time shortly after the attractive Fermi polaron [73, 74]. Importantly, this eigenstate corresponds to an excited state of the system, which can decay to lower-lying states, i. e., the attractive polaron or the (dressed) molecule. The repulsive polaron energy depends much weaker on the interaction parameter $\ln(k_F a_{2D})$ compared to the attractive polaron. Its energy reaches a maximum close to E_F before it becomes ill-defined as indicated by the vanishing quasiparticle residue Z . Here, the damping Γ quickly approaches the order of the Fermi energy [see Figs. 2.4(a,b)]. Similarly to the case of the attractive polaron, we can approximate the energy of the repulsive polaron in the limit of strong binding, $\epsilon_b \gg E_F$ [$\ln(k_F a_{2D}) \ll -2$], using $E_+/E_F \approx 2/\ln(\epsilon_b/E_F)$ [190], which agrees with the full expression on the percent level for $\ln(k_F a_{2D}) \leq -2$. In Fig. 2.4(b), we show the damping Γ of the repulsive polaron, which has often been associated with its lifetime against decay into lower-lying states. However, the experimental results in Chapter 3 (see Section 3.4.2) show that Γ can rather be understood as the width of the quasiparticle peak giving rise to many-body dephasing [110].

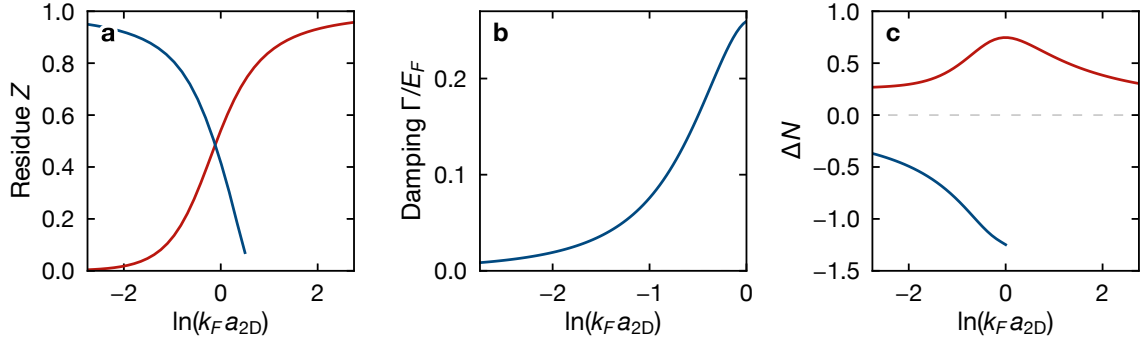


Figure 2.4 | Quasiparticle properties. Parameters of the attractive (red) and repulsive (blue) Fermi polaron calculated within the 1PH approximation. (a) Quasiparticle residue Z , (b) damping Γ of the repulsive polaron, and (c) approximate number of particles ΔN in the dressing cloud of the impurity according to Eq. (2.15).

To motivate the illustrations in Fig. 2.3, which schematically shows the local medium density in the vicinity of the Fermi polaron, we estimate the number of particles from the Fermi sea in the dressing cloud,

$$\Delta N \approx -\frac{\partial E_{\pm}}{\partial E_F} = -\left[\frac{1}{2} \partial_x \varepsilon_{\pm}(x) + \varepsilon_{\pm}(x) \right] \Big|_{x=\ln(k_F a_{2D})}. \quad (2.15)$$

This equation can be obtained from the chemical potential (quasiparticle energy) under the assumption that the density far away from the impurity remains unchanged [81]. Here, the last term applies to $\varepsilon_{\pm}(x) = E_{\pm}(x)/E_F$. In Fig. 2.4(c), we show the result for the density enhancement and depletion for variable interaction parameters. As naively expected, the number of particles in the dressing cloud of the polaron increases for attractive interactions. This regime energetically favors a density enhancement in close proximity of the impurity. In contrast, for the repulsive polaron, $\Delta N < 0$, which indicates that the density of particles from the Fermi sea is reduced in the proximity of the impurity. Notably, $|\Delta N| \lesssim 1$ for both attractive and repulsive interactions, even in the regime of strong interactions with $\ln(k_F a_{2D}) \sim 0$. This shows that the local density modulation in the vicinity of the Fermi polaron has a rather small magnitude, which generally also applies to 3D, as experimentally observed in Ref. [83].

2.2.3 Finite momentum and temperature

Finite momentum ($p > 0$) and temperature ($T > 0$) both affect the properties of the Fermi polaron and play a role in typical experiments with ultracold atoms, as illustrated in Fig. 2.5. This section considers finite-momentum and finite-temperature effects individually, which simplifies the theoretical calculations but still permits a qualitative discussion of the phenomenology.

The former arises since the preparation of a single impurity at $p = 0$ is usually impractical in experiments. Instead, a strongly imbalanced two-component Fermi gas is prepared, e. g., by populating two spin states [see Fig. 2.5(b)]. In this configuration, the impurities correspond to a minority Fermi sea and consequently occupy non-zero momentum states. Although

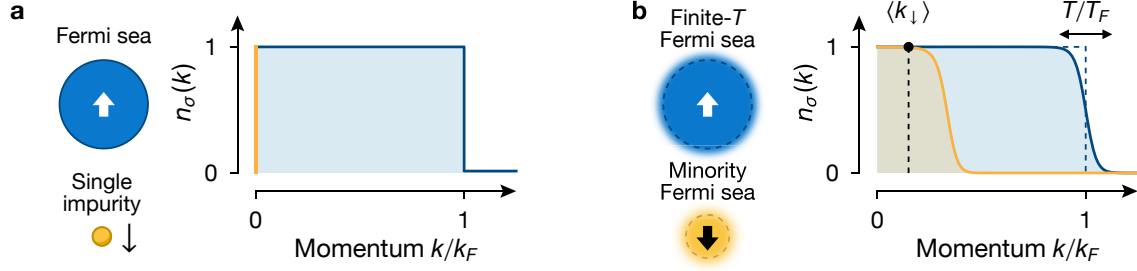


Figure 2.5 | Emergence of finite-momentum and finite-temperature effects. Each panel shows a schematic on the left and the associated momentum distribution $n_\sigma(k)$ on the right (blue: majority Fermi sea, yellow: minority Fermi sea and impurity). (a) Simplified theoretical description with single impurity at zero momentum and zero-temperature Fermi sea. (b) Typical experimental realization of an impurity system with a strongly imbalanced two-component Fermi sea (both with finite temperature), majority \uparrow -component, and minority \downarrow -component. The finite minority concentration gives rise to a finite impurity momentum spread with mean momentum $\langle k_\downarrow \rangle > 0$ (dashed black line).

their momentum is usually significantly smaller than the Fermi momentum of the majority Fermi sea, it still affects the many-body spectrum and the quasiparticle properties, which we explore in the following.

For finite momentum $\mathbf{p} \neq 0$, the integration over the relative angle of \mathbf{p} and \mathbf{q} has to be considered, and we obtain the following expression for the self-energy (see Appendix A.2),

$$\frac{\Sigma(\mathbf{p}', E)}{E_F} = \frac{2}{\pi} \int_0^1 dq' q' \int_0^{2\pi} d\theta \left[\ln\left(\frac{\epsilon_b}{E_F}\right) - \ln\left(E(q') \pm \sqrt{\left[E(q') + \frac{r^2}{2}\right]^2 - r^2}\right) \right]^{-1}, \quad (2.16)$$

where $\mathbf{p}' = \mathbf{p}/(\hbar k_F)$, $E(q') = 1 - [E/E_F + q'^2]/2$, $r = (q' + p' \cos \theta)$, and $\pm = \text{sgn Re}[E(q') + r^2/2]$. From this expression for the self-energy, we numerically calculate the finite-momentum spectral function $A(p, E) \equiv A(|\mathbf{p}'|, E)$. We show this result for three interaction parameters in Fig. 2.6, illustrating the dependence of both quasiparticle branches on the impurity momentum. For small momentum $p \ll \hbar k_F$, the change of the quasiparticle energy is determined by the dispersion $\sim p^2/(2m^*)$ with the effective mass m^* [see Eq. (2.9)]. Notably, this relation has enabled obtaining the effective mass experimentally from the quasiparticle energy shift at variable mean impurity momenta [76]. For large momentum, the many-body spectrum changes significantly: First, we observe that the dispersion of both the repulsive and attractive polaron approaches that of a free particle [see Figs. 2.6(a) and 2.6(c)]. Hence, the Fermi polaron essentially becomes a free particle at large momenta, and its quasiparticle energy approaches zero, when measured relative to a free particle at the same momentum. This agrees with a naive expectation, as the kinetic energy becomes the dominant energy scale, and the interaction with particles from the Fermi sea then only has a perturbative effect on the impurity. Our second observation concerns the molecule-hole continuum, which affects the attractive polaron at large momenta and strong interactions, $\ln(k_F a_{2D}) \sim 0$, as shown in Fig. 2.6(b). In this regime, the attractive polaron peak merges with an enlarged molecule-hole continuum, and the narrow quasiparticle peak ceases to exist.

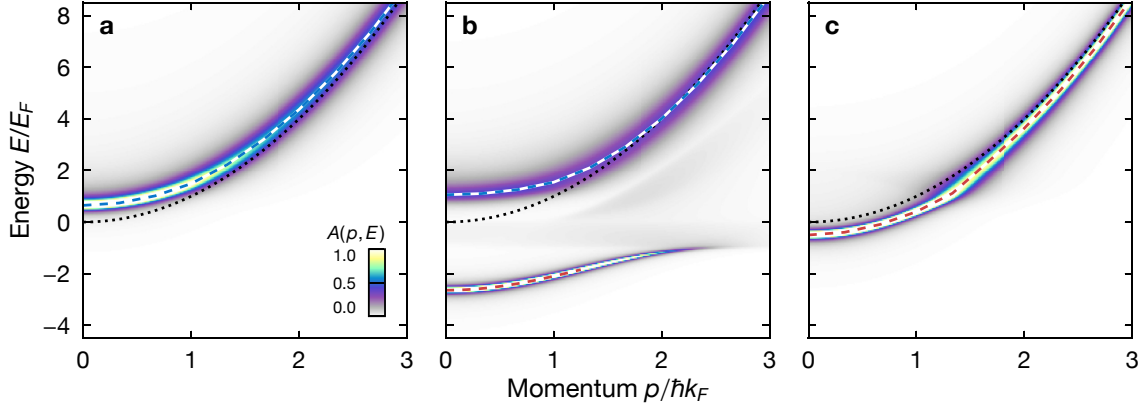


Figure 2.6 | Finite-momentum Fermi polaron. Numerical calculation of the spectral function $A(p, E)$ within the 1PH approximation for variable momentum $p \in [0, 3\hbar k_F]$ with the Fermi momentum k_F . Here, the interaction parameters are (a) $\ln(k_F a_{2D}) = -1$ (repulsive polaron), (b) 0 (both quasiparticle branches), and (c) 2 (attractive polaron). The dotted line indicates the dispersion of the free particle, $E(p) = p^2/(2m)$, and the dashed blue (red) lines show the dispersion of the attractive and repulsive polaron. Note that a finite broadening has been applied to the spectrum with the replacement $E \rightarrow E + 0.05iE_F$, and the plot range is truncated to increase the contrast at small amplitudes.

In experiments with ultracold atoms in 2D, temperatures are typically $T/T_F \sim 0.2$ (Fermi temperature T_F) [74, 109]. At this temperature, the Fermi surface of the medium acquires a non-negligible finite broadening $\sim T/T_F$, in contrast to the sharp distribution at zero temperature [see Fig. 2.5(a)]. For finite temperature $T > 0$, the integrals in Eq. (2.14) are changed considerably as the momentum distribution does not anymore feature an infinitely sharp edge. By considering the difference between the zero- and finite-temperature results, we obtain the self-energy at finite temperature T (see Appendix A.3),

$$\frac{\Sigma(0, E; T)}{E_F} = 2 \int_0^1 dy F(yE_F, T) \left\{ \ln\left(\frac{\epsilon_b}{E_F}\right) - \ln\left[E' - \frac{y}{2} \pm \sqrt{E'^2 - y}\right] + \Delta_T(y) \right\}^{-1} \quad (2.17)$$

with the Fermi-Dirac distribution $F(x, T) = [e^{(x-\mu)/(k_B T)} + 1]^{-1}$ and the chemical potential μ . Here, the expressions denote $E' = 1 - E/(2E_F)$, $\pm\sqrt{a^2 - b} = \text{sgn}(\text{Re } a)\sqrt{a^2 - b}$, and the term $\Delta_T(y)$ accounts for the finite-temperature contributions,

$$\Delta_T(y) = \int_0^\infty dx \frac{F(xE_F, T=0) - F(yE_F, T)}{\pm\sqrt{[x - E/(2E_F)]^2 - xy}}. \quad (2.18)$$

Figure 2.7 shows the results of the numerically calculated finite-temperature spectral function $A(0, E; T)$ at variable interaction strength. For all interaction parameters and increasing temperature, we can observe a significant broadening of the quasiparticle peaks, signaling a finite decay width. This also applies to the attractive polaron, which otherwise corresponds to a Dirac delta distribution at zero temperature. Moreover, the width of the quasiparticle peaks quickly approaches the scale set by the Fermi energy. This agrees with our expectation as the quasiparticle picture should break down once the Fermi surface becomes ill-defined. In

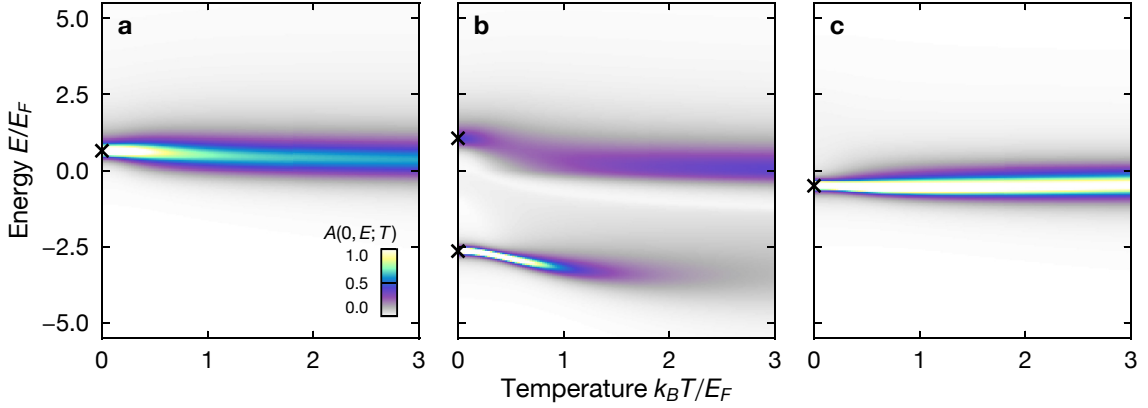


Figure 2.7 | Finite-temperature medium. Numerical calculation of the spectral function $A(0, E; T)$ within the 1PH approximation for variable temperature $k_B T \in [0, 3E_F]$ and interaction parameters (a) $\ln(k_F a_{2D}) = -1$ (repulsive polaron), (b) 0 (both quasiparticle branches), and (c) 2 (attractive polaron). The black crosses indicate the quasiparticle energies at zero temperature. Note that a finite broadening has been applied to the spectrum with the replacement $E \rightarrow E + 0.05iE_F$, and the plot range is truncated to increase the contrast at small amplitudes.

addition to the broadening, the absolute value of the quasiparticle energy increases at finite temperature, particularly for the attractive polaron [cf. black crosses in Fig. 2.7]. This could be caused by an enlarged phase space for the particle-hole excitations.

Recently, the temperature dependence of the many-body spectrum has been probed experimentally for a 3D Fermi gas [83]. In their experiment, Yan et al. prepare a thermal equilibrium state of a strongly spin-imbalanced Fermi gas and probe its spectral response as a function of temperature. For strong interactions, the authors observe a broadening of the quasiparticle peak and an increase of absolute quasiparticle energy for the attractive polaron, in agreement with theoretical calculations [191–193]. At a critical temperature of $T \approx 0.75T_F$, they also find a surprisingly sharp jump of the attractive polaron energy to approximately zero [83]. This could be intuitively understood as the merging of both quasiparticle branches once the temperature exceeds the gap between the attractive and repulsive branches.

Finally, we note that our finite-momentum and finite-temperature calculations do not fully capture the physics in typical experiments with a finite number of impurities. Here, the finite impurity density can also lead to collective effects, i. e., polaron-polaron interactions [82], which are not accounted for with a single-impurity ansatz and require a treatment within Fermi-liquid theory [194]. However, theoretical studies in 3D suggest that these effects are rather small [195], as also confirmed by the good agreement of single-impurity descriptions and experimental measurements [71–74, 76, 84, 109].

2.3 The quasi-two-dimensional regime

The quasi-two-dimensional (quasi-2D) regime describes the geometry of ultracold quantum gas experiments, where strong harmonic confinement restricts the momentum of particles to two dimensions. Most commonly, experiments employ a single-axis optical lattice for

this purpose. For typical accessible confinement strengths, the range of the microscopic interactions between the atoms still has a much shorter length scale than the one set by the external confinement [182]. As a consequence, the scattering of individual particles needs to be described in 3D, with only the momentum restricted to 2D. The additional complexity of the external confinement can be absorbed into “renormalized” quantities, allowing for the description of experiments with the formalism of a purely 2D geometry. We note that detailed derivations for the quantities discussed in this section can be found in Ref. [182].

In the experiment, the reduced dimensionality is achieved with a strong trap along a single axis, assumed to be the z -axis in the following. For an approximately harmonic confinement potential, the single-particle Hamiltonian then takes the form

$$\hat{H}_0 = \sum_{\substack{p_x, p_y \\ n=0}} \left[\frac{p_x^2 + p_y^2}{2m} + \left(n + \frac{1}{2} \right) \hbar\omega_z \right] |p_x, p_y; n\rangle \langle p_x, p_y; n|. \quad (2.19)$$

Here, (p_x, p_y) denotes the momentum in the (x, y) -plane, ω_z corresponds to the trapping frequency. Also, we assume the gas only occupies the ground state $n = 0$ of the harmonic oscillator potential. For fermionic quantum gases, this can be achieved at sufficiently low temperatures $T \ll \hbar\omega_z/k_B$ and with strong confinement such that $\hbar\omega_z \ll E_F$.

The finite harmonic confinement along the z -axis modifies the two-body scattering process as determined by the characteristic length scale $l_z = \sqrt{\hbar/(m\omega_z)}$ of the harmonic oscillator. For typical experiments, this length scale takes a much larger value than the range of the interatomic interaction potential $l_z > 10 \text{ nm} \gg r_w \sim 0.1 \text{ nm}$. The s -wave scattering length can then be determined from a low-energy expansion of the scattering amplitude [182],

$$\frac{a_{2D}}{l_z} = \sqrt{\frac{\pi}{B}} \exp\left(-\sqrt{\frac{\pi}{2}} \frac{l_z}{a_{3D}}\right) \quad (2.20)$$

with the numerical factor $B \approx 0.905$ [182] and a_{3D} the s -wave scattering length in 3D.

In general, the binding energy ϵ_b of the dimer in quasi-2D cannot simply be calculated from Eq. (2.12), which only applies to the limit $l_z/a_{3D} \ll -1$. Here, the size of the dimer becomes much larger than l_z such that it spreads out in the (x, y) -plane. In contrast, for $l_z/a_{3D} \gg 1$, we expect the confinement effects to be negligible since the dimer has a much smaller size than l_z . By determining the pole of the T-matrix for the two-body problem (binding energy of the molecular bound state), we can find a relation that smoothly interpolates between these two limits. The binding energy ϵ_b can be obtained from the implicit equation [182]

$$\frac{l_z}{a_{3D}} = \mathcal{F}\left(\frac{\epsilon_b}{\hbar\omega_z}\right) = \int_0^\infty \frac{du}{\sqrt{4\pi u^3}} \left[1 - \frac{e^{-u\epsilon_b/(\hbar\omega_z)}}{\sqrt{(1 - e^{-2u})/(2u)}} \right], \quad (2.21)$$

where the integral has to be determined numerically.¹ We note that our experiment generally operates in the regime $0 \leq l_z/a_{3D} \leq 1$, where the above description needs to be applied.

¹The integrand has a singularity at $u = 0$, which can cause slow convergence and numerical instabilities for common numerical integration techniques such as the Gauss-Legendre quadrature. Instead, we find that the double-exponential formula [196], also known as Tanh-Sinh quadrature, converges particularly well.

In conclusion, we have established a direct relationship between the experimental quantities (confinement length scale l_z and scattering length a_{3D}) and the single theoretical quantity in the purely 2D geometry (scattering length a_{2D} or binding energy ϵ_b). For the Fermi polaron problem in 2D, we are now equipped with the tools to describe typical experiments with strongly confined ultracold fermions using the experimentally accessible parameters E_F , a_{3D} , and l_z . Next, we discuss the deviation from this universal regime for ^{173}Yb atoms in the vicinity of the orbital Feshbach resonance.

2.3.1 Open-channel orbital interactions

Our experiment employs ultracold ^{173}Yb atoms in the ground and clock state to realize strongly interacting Fermi gases and probe Fermi polarons. For these two states, we can tune the interaction strength with the magnetic field utilizing an orbital Feshbach resonance [54–56], as explained in Chapter 1 (see Section 1.2.4). Following Ref. [109], we calculate the magnetic-field-dependent scattering length for the orbital Feshbach resonance in ^{173}Yb and a quasi-2D geometry. We also introduce an effective two-channel model for the orbital Feshbach resonance, that significantly simplifies the description of the interaction parameters and the Fermi polaron problem for interorbital interactions.

For the description of an interacting $e-g$ pair in two distinct nuclear spin states at finite magnetic field $B > 0$, we employ the open and closed channel states, $|o\rangle$ and $|c\rangle$, introduced in Chapter 1 (see Section 1.2.3). These states are directly related to the “triplet” $|+\rangle = (|o\rangle + |c\rangle)/\sqrt{2}$ and “singlet” $|-\rangle = (|o\rangle - |c\rangle)/\sqrt{2}$ states describing the interatomic interaction potentials.² The finite magnetic field introduces the effective detuning $\delta = \Delta\mu B$ between the open and closed channel, determined by $\Delta\mu = h \times 554(3)\text{Hz/G}$ [109] for the experimentally relevant nuclear spin states with $m_F = \pm 5/2$ (see Section 1.2.3 in Chapter 1 and Chapter 3).

The Hamiltonian describing an $e-g$ pair in a harmonic trap takes, analogously to Eq. (2.19), the following form [109]

$$\begin{aligned} \hat{\mathcal{H}}_{eg} = & \sum_{\mathbf{p},n} 2E_{\mathbf{p}n} |o; \mathbf{p}n\rangle \langle o; \mathbf{p}n| + (2E_{\mathbf{p}n} + \delta) |c; \mathbf{p}n\rangle \langle c; \mathbf{p}n| \\ & + \sum_{\mathbf{p},\mathbf{p}';n,n'} \gamma_{nn'} (U_+ |+\rangle \langle +; \mathbf{p}'n'| + U_- |-\rangle \langle -; \mathbf{p}'n'|). \end{aligned} \quad (2.22)$$

Here, the first line describes the non-interacting part with the two-dimensional momentum $\mathbf{p} = (p_x, p_y)$, the eigenstates of the harmonic oscillator labeled by $n \geq 0$, and $2E_{\mathbf{p}n} = p^2/m + \hbar\omega_z(n + 1/2)$. The second line describes the triplet and singlet interaction energies U_{\pm} , where $\gamma_{nn'}$ is a numerical factor determined by the harmonic oscillator wave functions [182]. The form of $\hat{\mathcal{H}}_{eg}$ illustrates how the scattering problem now involves two coupled channels, which can significantly alter the scattering properties. The vacuum T-matrix for the two-body scattering problem in the ground state $n = n' = 0$ and at energy E , can be obtained from the

²Compared to the discussion in Chapter 1, we have dropped the explicit state labels such that $|\pm\rangle \equiv |eg^{\pm}\rangle$.

Lippmann-Schwinger equation and the above Hamiltonian [109]. In the basis of open and closed channel, it takes the form

$$\mathbf{T}^{(\text{vac})}(E) = \frac{\sqrt{8\pi}\hbar^2}{m} \left[\mathbf{R} \begin{pmatrix} l_z/a_+ & 1 \\ 1 & l_z/a_- \end{pmatrix} \mathbf{R} - \begin{pmatrix} \mathcal{F}[-E/(\hbar\omega_z)] & 0 \\ 0 & \mathcal{F}[(-E + \delta)/(\hbar\omega_z)] \end{pmatrix} \right]^{-1}. \quad (2.23)$$

Here, $a_+ = 1878a_0$ and $a_- = 219.7a_0$ (Bohr radius a_0) [55] denote the scattering lengths in 3D, $l_z = \sqrt{\hbar/(m\omega_z)}$ the characteristic length scale of the harmonic oscillator, and $\mathcal{F}(x)$ corresponds to the transcendental function defined in Eq. (2.21). The matrix $\mathbf{R} = \begin{pmatrix} 1 & 1 \\ 1 & -1 \end{pmatrix} / \sqrt{2}$ describes the basis change when considering the non-interacting $|o, c\rangle$ and interaction eigenstates $|\pm\rangle$. In the following, we account for the effective ranges $r_+ = 216a_0$ and $r_- = 126a_0$ with the implicit replacement [55]

$$\frac{1}{a_{\pm}} \rightarrow \frac{1}{a_{\pm}} - \frac{1}{2}mr_{\pm} \left(E - \frac{\delta}{2} + \frac{1}{2}\hbar\omega_z \right). \quad (2.24)$$

Having defined the two-body T-matrix and the relevant atomic properties, we now discuss the scattering amplitude, which determines the interaction between an e - g pair in a strong harmonic trap. Formally, the scattering amplitude in quasi-2D can be obtained by projecting Eq. (2.23) onto the open channel $|o\rangle$ [109],

$$f_{\text{q2D}}(E) = \sqrt{2\pi} \left\{ \frac{l_z^2/(a_-a_+) - \frac{1}{2}\mathcal{F}[(-E + \delta)/(\hbar\omega_z)](l_z/a_- + l_z/a_+)}{l_z/a_- + l_z/a_+ - 2\mathcal{F}[(-E + \delta)/(\hbar\omega_z)]} - \frac{1}{2}\mathcal{F}\left(\frac{-E}{\hbar\omega_z}\right) \right\}^{-1}. \quad (2.25)$$

While this scattering amplitude fully captures the two-body problem of an e - g pair in a quasi-2D geometry, it is not directly related to the relevant quantities for the many-body problem of the Fermi polaron. Moreover, four seemingly independent parameters, i. e., l_z , a_- , a_+ , and δ , emerge in the description of the two-body problem [see Fig. 2.8(a)].

2.3.2 The effective two-channel model

In this section, we derive the parameters of an effective model for the orbital Feshbach resonance, which significantly simplifies the theoretical description of the many-body problem. In particular, we consider a two-channel model with the Hamiltonian [110]

$$\hat{\mathcal{H}}_{\text{2ch}} = \sum_{\mathbf{k}, \sigma \in \{\uparrow, \downarrow\}} \frac{\hbar^2 k^2}{2m} \hat{c}_{\mathbf{k}\sigma}^\dagger \hat{c}_{\mathbf{k}\sigma} + \sum_{\mathbf{k}} \left(\frac{\hbar^2 k^2}{4m} + \nu \right) \hat{a}_{\mathbf{k}}^\dagger \hat{a}_{\mathbf{k}} + g \sum_{\mathbf{k}, \mathbf{k}'} \left(\hat{a}_{\mathbf{k}}^\dagger \hat{c}_{\mathbf{k}', \uparrow} \hat{c}_{\mathbf{k}-\mathbf{k}', \downarrow} + \text{h. c.} \right) \quad (2.26)$$

with $\hat{c}_{\mathbf{k}\sigma}^\dagger$ ($\hat{c}_{\mathbf{k}\sigma}$) the fermionic creation (annihilation) operator for a particle at momentum $\hbar\mathbf{k}$ with spin $\sigma \in \{\uparrow, \downarrow\}$. In this model, the interactions between the spinful fermions are determined by the coupling strength g and mediated by molecules. These molecules are described by the bosonic creation (annihilation) operators $\hat{a}_{\mathbf{k}}^\dagger$ ($\hat{a}_{\mathbf{k}}$) at momentum $\hbar\mathbf{k}$. Moreover, the bosonic

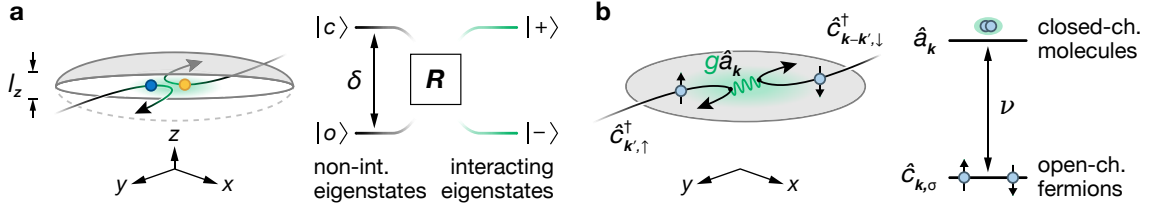


Figure 2.8 | Full and effective model description in quasi-2D. Schematics comparing the full and effective model for an e - g pair in quasi-2D. (a) Full description of the interorbital interactions in a quasi-2D geometry with axial confinement length scale l_z . (Left) Schematic of an in-plane collision for an e - g pair (blue and yellow circle). (Right) Basis transformation of the non-interacting eigenstates $|o\rangle$, $|c\rangle$ (large separation) and interacting eigenstates $|s\rangle$, $|t\rangle$ (small separation) described by the matrix R . Here, δ denotes the detuning of the open and closed channel. (b) Effective two-channel model in a purely 2D geometry with spinful fermions and bosonic molecules. (Left) Schematic of an in-plane collision of a fermionic pair (light-blue circles with arrows) mediated by a bosonic closed-channel molecule (wiggly green line). (Right) Illustration of the open and closed channel with their detuning ν .

molecules occupy a (closed) channel, energetically detuned by ν from the open channel of the collisional pair. The form of $\hat{\mathcal{H}}_{2\text{ch}}$ can be motivated by the nature of narrow Feshbach resonances, for which the energetically closed channel has an increased relevance [133]. Indeed, the model in Eq. (2.26) has been employed to describe the experimental results of an interacting lithium-potassium mixture close to a narrow Feshbach resonance [197]. Therefore, the above model also seems suitable for describing the orbital Feshbach resonance, which also exhibits typical features of a narrow resonance (see Section 1.2.4 in Chapter 1).

The two-channel Hamiltonian in 2D gives rise to the low-energy scattering amplitude [198]

$$f_{2\text{ch}}(k) = \frac{4\pi}{i\pi - \ln(k^2 a_{2\text{D}}^2) + k^2 R_{2\text{D}}^2}, \quad (2.27)$$

which (re-)introduces the s -wave scattering length $a_{2\text{D}}$ and the effective range $R_{2\text{D}}$, both related to the bare model parameters ν and g [198]. Note that in contrast to Eq. (2.11), this scattering amplitude contains higher orders in k , in particular, k^2 as parameterized by the effective range $R_{2\text{D}}$. This parameter is specific to the 2D scattering problem and not trivially related to the effective range in 3D [198]. In the following, we are interested in relating the parameters of the orbital Feshbach resonance to $a_{2\text{D}}$ and $R_{2\text{D}}$. To this end, we directly compare the low-order energy expansion of f_{q2D} to $f_{2\text{ch}}(E)$. This straightforward but tedious process can be found in Appendix B. Here, we only present the results, i. e., the scattering length [109]

$$\frac{a_{2\text{D}}}{l_z} = \sqrt{\frac{\pi}{B}} \exp \left[-\sqrt{2\pi} \frac{\alpha^{-1} \alpha_+^{-1} - \frac{1}{2} \mathcal{F}(\Delta) (\alpha^{-1} + \alpha_+^{-1})}{\alpha^{-1} + \alpha_+^{-1} - 2\mathcal{F}(\Delta)} \right] \quad (2.28)$$

and the effective range [110]

$$\left(\frac{R_{2\text{D}}}{l_z} \right)^2 = \ln 2 - \sqrt{2\pi} \frac{[\alpha^{-1} - \mathcal{F}(\Delta)]^2 \rho_t + [\alpha_+^{-1} - \mathcal{F}(\Delta)]^2 \rho_s + (\alpha^{-1} - \alpha_+^{-1})^2 \mathcal{F}'(\Delta)}{[\alpha^{-1} + \alpha_+^{-1} - 2\mathcal{F}(\Delta)]^2}. \quad (2.29)$$

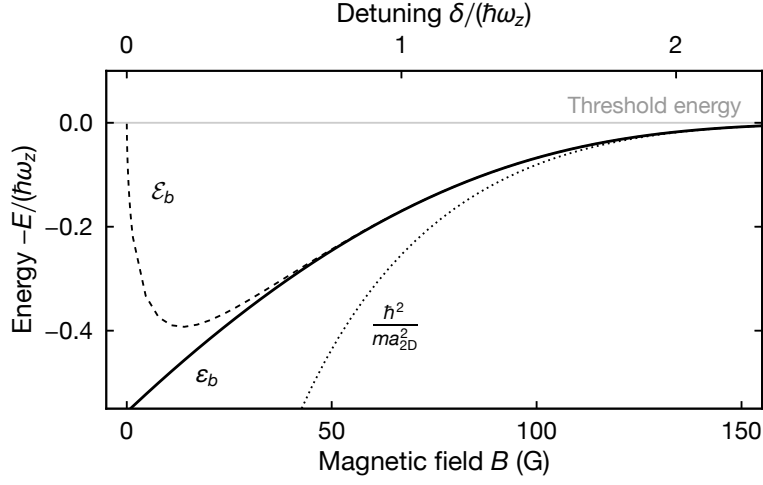


Figure 2.9 | Binding energy of the quasi-2D dimer. Magnetic-field dependence of the binding energy ϵ_b (solid line) for an $e-g$ pair in quasi-2D, numerically calculated from the relation in Eq. (2.30). The dashed line depicts ϵ_b , according to Eq. (2.31), and the dotted line corresponds to the limit $R_{2D} \rightarrow 0$.

Here, $B \approx 0.905$ [182] and $\mathcal{F}'(x)$ denotes the derivative of the transcendental function \mathcal{F} in Eq. (2.21). The atomic properties are considered in natural units of the harmonic oscillator with $\Delta = \delta/(\hbar\omega_z)$, $\rho_{\pm} = r_{\pm}/l_z$, and $\alpha_{\pm}^{-1} = l_z/a_{\pm} - \rho_{\pm}(1 - \Delta)/4$, where the effective-range replacement has been carried out explicitly for the low-energy limit $E \rightarrow 0$.

We now proceed with a verification of our approach describing the orbital Feshbach resonance with an effective model. To this end, we calculate the binding energy of the two-body bound state in the two-channel model and compare it to the solution obtained from the poles of the full T-matrix, which can be found by solving an implicit relation for ϵ_b [109],

$$\left[2\frac{l_z}{a_+} - \tilde{\mathcal{F}}(\epsilon_b) - \tilde{\mathcal{F}}(\epsilon_b + \delta)\right] \left[2\frac{l_z}{a_-} - \tilde{\mathcal{F}}(\epsilon_b) - \tilde{\mathcal{F}}(\epsilon_b + \delta)\right] = [\tilde{\mathcal{F}}(\epsilon_b) - \tilde{\mathcal{F}}(\epsilon_b + \delta)]^2. \quad (2.30)$$

Here, $\tilde{\mathcal{F}}(x) = \mathcal{F}[x/(\hbar\omega_z)]$ and numerical results from the above relation have been verified experimentally with precise spectroscopy [134].

For the two-channel model, the following form parameterizes the binding energy [198]

$$\epsilon_b = \frac{\hbar^2}{mR_{2D}^2} W\left(\frac{R_{2D}^2}{a_{2D}^2}\right), \quad (2.31)$$

where $W(x)$ denotes the Lambert W function. In Fig. 2.9, we compare the numerical results for ϵ_b and ϵ_b , which show good agreement from intermediate to large magnetic fields. In this regime, the closed channel detuning δ corresponds to a significant fraction of the harmonic oscillator level spacing (see dashed line in Fig. 2.9). Let us emphasize that the binding energy disagrees in the limit $R_{2D} \rightarrow 0$, which underlines the importance of R_{2D} to describe the orbital Feshbach resonance correctly (see dotted line in Fig. 2.9).

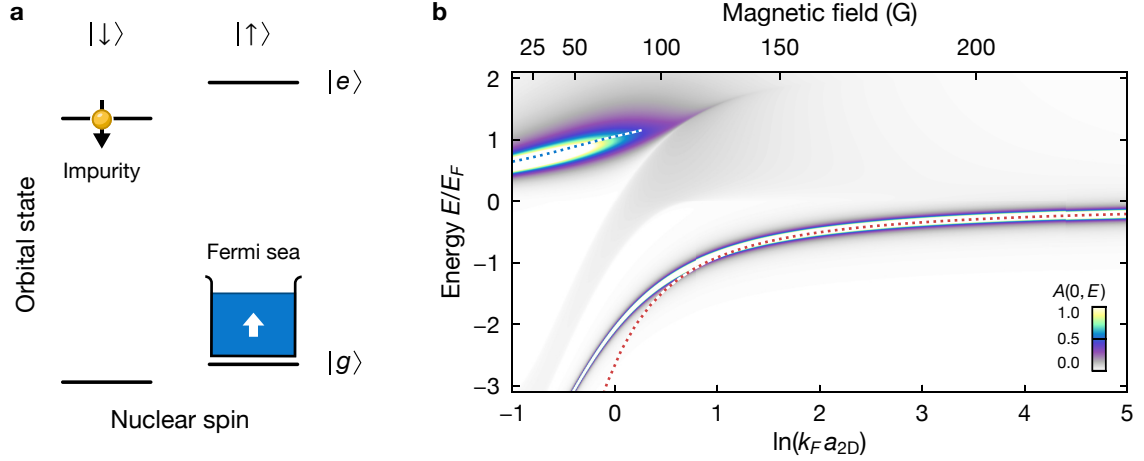


Figure 2.10 | Effective model for the multiorbital Fermi polaron. (a) Illustration of the nuclear spin and orbital degree of freedom in the multiorbital Fermi polaron problem. (b) Numerical calculation of the spectral function $A(0, E)$ within the 1PH approximation for the multiorbital Fermi polaron in quasi-2D. Here, we choose a typical experimental Fermi energy $E_F = 0.1\hbar\omega_z$. This results in $k_F R_{2D} \approx 0.7$ in the strongly interacting regime $\ln(k_F a_{2D}) \sim 0$. Note that a finite broadening has been applied to the spectrum with the replacement $E \rightarrow E + 0.01iE_F$, and the plot range is truncated. Dotted blue (red) lines show the quasiparticle energies of repulsive (attractive) polaron for $R_{2D} = 0$. This limit corresponds to the single-channel model, as realized across a broad Feshbach resonance.

In conclusion, we have derived the effective quantities a_{2D} and R_{2D} for the two-channel model in a purely 2D geometry. These parameters now simplify the description of the two-body problem for the orbital Feshbach resonance in quasi-2D. Next, we employ this result to find the self-energy in the $(N + 1)$ many-body problem, namely, the multiorbital Fermi polaron.

2.3.3 The multiorbital Fermi polaron

In the following, we consider a single $|e \downarrow\rangle$ impurity immersed in a Fermi sea of $|g \uparrow\rangle$ atoms, as illustrated in Fig. 2.10(a). This Fermi polaron occupies the open channel $|o\rangle$ and has been termed *multiorbital* to emphasize the presence of an orbital degree of freedom. This multiorbital nature can significantly alter the quasiparticle properties, as we will explore experimentally in Chapter 3 (see Section 3.6). Here, we discuss the theoretical description of this polaron within the effective model introduced in the previous section. As first shown in Ref. [110], this relatively simple approach leads to almost identical results as the full many-body T-matrix theory [109] with the added benefit of simplified (numerical) calculations.

Again, we calculate the self-energy within Chevy's variational ansatz in Eq. (2.2). For the two-channel Hamiltonian in Eq. (2.26), the minimization of the corresponding energy functional yields the following implicit equation describing the energy of the Fermi polaron at zero momentum [197],

$$E = \sum_{q < k_F} \left[\frac{E - v + \hbar^2 q^2 / (4m)}{g^2} + \sum_{k > k_F}^{\Lambda} \frac{1}{-E + (2m)^{-1} [\hbar^2 k^2 - \hbar^2 q^2 + \hbar^2 (\mathbf{k} - \mathbf{q})^2]} \right]^{-1}. \quad (2.32)$$

For the two-channel model, the relation between the coupling constant g , the channel detuning ν and the bound-state energy \mathcal{E}_b from Eq. (2.31) is given by the relation [198]

$$-\frac{\nu}{g^2} = \frac{\mathcal{E}_b}{g^2} - \sum_{\mathbf{k}}^{\Lambda} \frac{1}{\hbar^2 k^2/m + \mathcal{E}_b}. \quad (2.33)$$

Using $\hbar \equiv 1$ and $R_{2D}^2 = 4\pi/(m^2 g^2)$ [198], we find the following expression for the self-energy in the thermodynamic limit (see Appendix A.4),

$$\frac{\Sigma(0, E)}{E_F} = 2 \int_0^1 dy \left\{ (k_F R_{2D})^2 \left(\frac{E}{2E_F} + \frac{y}{4} + \frac{\mathcal{E}_b}{2E_F} \right) + \ln \left(\frac{\mathcal{E}_b}{E_F} \right) - \ln \left[E' - \frac{y}{2} \pm \sqrt{E'^2 - y} \right] \right\}^{-1}, \quad (2.34)$$

where $E' = 1 - E/(2E_F)$, $\pm = \text{sgn Re } E'$, and \mathcal{E}_b can be obtained from Eq. (2.31). Note that in the limit $R_{2D} \rightarrow 0$, we recover the single-channel result from Eq. (2.14). Figure 2.10(b) depicts the spectral function $A(0, E)$ calculated for the parameters of the orbital Feshbach resonance. Compared to the quasiparticle energies of the single-channel model, we find a significant deviation in the regime of strong interactions with $\ln(k_F a_{2D}) \sim 0$, which underlines the relevance of the effective two-channel model for the multiorbital Fermi polaron.

The above results finalize our discussion of the theoretical framework for the description of Fermi polarons in ultracold quantum gases and, specifically, in orbital mixtures of ^{173}Yb . Having introduced all relevant experimental quantities and the theoretical description in terms of the 1PH approximation both for the single- and two-channel model, we continue with the experimental techniques and measurements in the next chapter.

CHAPTER 3

Multiorbital polarons in two-dimensional Fermi gases

This chapter presents the experimental observation of attractive and repulsive Fermi polarons in a multiorbital two-dimensional quantum gas of ^{173}Yb atoms. In particular, we present measurements of the various quasiparticle properties, i. e., the quasiparticle energy, residue, and repulsive polaron lifetime. First, the key techniques are explained that enable the preparation of population imbalanced mixtures in two nuclear spin states of the ground state. Then, we show how the combination of high-resolution absorption imaging and careful modeling allows us to precisely determine the relevant properties of this initial state. Finally, we present the detailed measurement procedures for the multiorbital Fermi polaron in two dimensions and compare the experimental results to theoretical calculations discussed in the previous chapter. The central findings of this chapter have been published in Ref. [109].

3.1 Population-imbalanced multiorbital Fermi gases

In the following, we first give a brief overview of the complete experimental sequence and then explain the most relevant steps in detail. Our state preparation for the Fermi polaron measurements is based on the procedures described in Chapter 1 (see Section 1.4.1) but includes certain refinements.

The experiment begins with loading a non-degenerate Fermi gas of $\approx 2.5 \times 10^6$ ^{173}Yb atoms into a crossed optical dipole trap (ODT) operated at the wavelength $\lambda = 1064$ nm. Initially, the atoms are equally distributed across the six different nuclear spin states $m_F \in \{-5/2, -3/2, \dots, +5/2\}$. To probe the Fermi polaron, we require a strongly spin-imbalanced Fermi gas, which we prepare by optical pumping, as explained in Section 3.1.1. We first perform forced evaporative cooling in the crossed ODT, and for the final stage, we employ another crossed optical dipole trap operated at the magic-wavelength $\lambda_m \approx 759.4$ nm. At the end of the evaporative cooling sequence, we produce an array of quasi-two-dimensional systems by loading $\approx 50 \times 10^3$ atoms at a temperature $\approx 0.2T_F$ (Fermi temperature T_F) into a deep single-axis optical lattice. Having completed the state preparation, we transfer atoms into the strongly interacting regime with an excitation pulse addressing the clock transition (see Section 3.1.3). By ramping the magnetic field close to the location of the orbital Feshbach

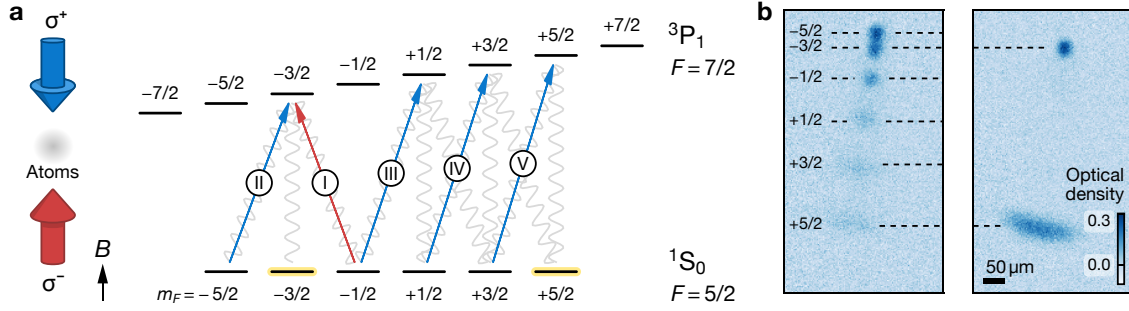


Figure 3.1 | Preparation of spin-imbalanced mixtures. (a) (Left) Illustration of the top and bottom beams driving the σ^\pm transitions for optical pumping. (Right) Relevant nuclear spin states in the $1S_0$ ($F = 5/2$) and $3P_1$ ($F = 7/2$) manifolds are shown as solid black lines. States populated at the end of evaporative cooling are highlighted in yellow. Blue (red) arrows show the optical pumping pulses driving σ^+ (σ^-) transitions. The gray wavy lines indicate the relevant decay channels. (b) Distribution of atoms across different m_F states after evaporative cooling, detected with optical Stern-Gerlach separation [199] for (left) a balanced spin-mixture and (right) the spin-imbalanced sample in $m_F = -3/2, +5/2$ after applying the preparation sequence illustrated in panel (a).

resonance, we set the desired final-state interaction strength before the clock pulse. Finally, resonant absorption imaging yields the state-resolved in-situ atomic density, providing our primary source of information to compare experimental results and theoretical predictions.

3.1.1 Producing spin-imbalanced mixtures

Optical pumping techniques allow us to prepare spin imbalance between the $m_F = -3/2$ (minority, denoted $|g \downarrow\rangle$) and $m_F = +5/2$ (majority, denoted $|g \uparrow\rangle$) atoms in the $1S_0$ ground state. These spin-imbalanced mixtures are characterized by the minority fraction $N_{-3/2}/(N_{-3/2} + N_{+5/2}) \approx 0.2$. We perform the optical pumping on the $1S_0 \rightarrow 3P_1$ intercombination line between the $F = 5/2$ and $F = 7/2$ manifolds at a magnetic bias field of ≈ 50 G. This ensures that the different $m_F \rightarrow m_{F\pm 1}$ transitions are split sufficiently. To drive σ^+ and σ^- transitions, we employ two individual laser beams, as illustrated in Fig. 3.1(a). Five sequential intensity-stabilized pulses prepare the desired spin ratio by transferring a large fraction of atoms initially in $m_F = -5/2, -1/2$ to the target state $m_F = -3/2$. The remaining atoms are distributed non-uniformly across the other nuclear spin states to yield the desired imbalance of approximately 1:4 between $m_F = -3/2$ and $+5/2$ at the end of evaporative cooling [see Fig. 3.1(b)].

We perform the optical pumping sequence at the beginning of the experiment, and the spin mixture is subsequently cooled to quantum degeneracy by forced evaporation. This avoids heating the gas in the degenerate regime, where a significant temperature increase can be caused by dissipative techniques such as optical pumping. On the other hand, preparing a spin imbalance early in the experimental sequence can be challenging as the subsequent evaporative cooling introduces non-linearities, enhancing the initial imbalance. This effect originates from a higher probability of a collision between a low-momentum minority and a high-momentum majority atom compared to the reversed process. While the non-linearities make it particularly challenging to robustly prepare extreme spin imbalances with minority fractions $\ll 0.15$, we can also improve the efficiency of evaporative cooling by initially populating additional spin

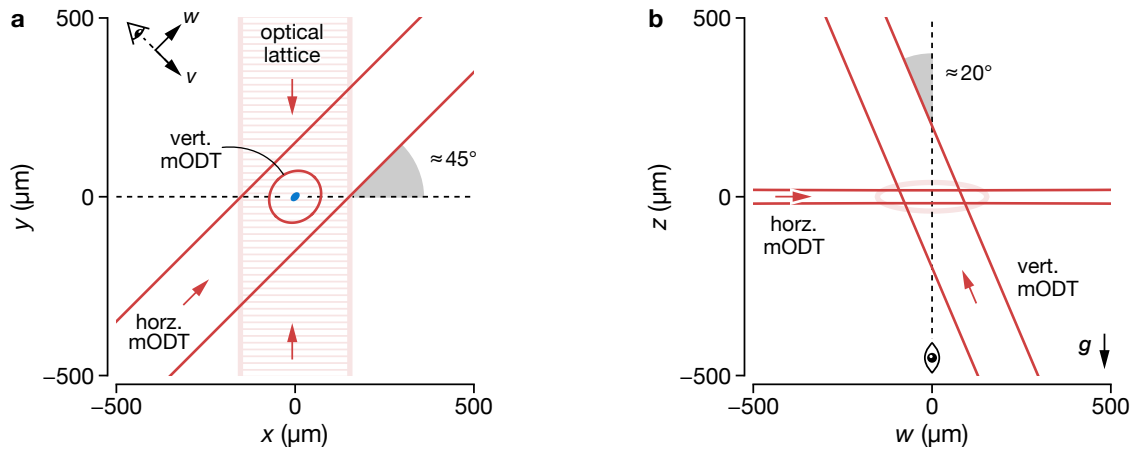


Figure 3.2 | Optical potentials for the quasi-two-dimensional geometry. Illustration of the Gaussian laser beams which generate the trapping potential in the experiment. The red lines and circles indicate the beam diameters (twice the waist). (a) Geometry of the laser beams in the imaging plane (x - y). For the optical lattice, every 50th lattice plane is indicated with a horizontal line. The small blue ellipsis at the center corresponds to a typical size of the atomic cloud. (b) Geometry of the laser beams in the (w - z) plane with the w -axis defined in panel (a). For comparison, the ellipse at the center indicates the beam diameter of the optical lattice shown along its transverse plane [not the (w - z) plane].

states. For an appropriate initial population ratio, the evaporative cooling results in a deeply degenerate two-component mixture with the desired imbalance and no significant population of other nuclear spin states. We optimize this process iteratively while monitoring the overall atom number, the spin imbalance, and the temperature.

3.1.2 Preparing quasi-two-dimensional ensembles

After the optical pumping procedure and the evaporative cooling of the spin mixture in the optical dipole trap, the geometry of the system is still three-dimensional. To achieve the desired quasi-two-dimensional geometry, we load the atoms into a single-axis optical lattice. At the same time, we employ the crossed magic-wavelength optical dipole trap (mODT) to confine the relatively heavy ^{173}Yb atoms against the gravitational potential. The crossed mODT is composed of two independent horizontal and vertical Gaussian laser beams with their orientation approximately parallel and perpendicular to the plane of the optical table (see Fig. 3.2). The horizontal mODT beam is strongly elliptical with waists $\approx 110\ \mu\text{m}$ (horizontal) and $\approx 20\ \mu\text{m}$ (vertical) at the location of the atoms, which produces particular strong confinement against gravity. The vertical mODT beam encloses an angle of $\approx 20^\circ$ with the gradient of the gravitational potential, and the projected in-plane beam waists are nearly equal with $\approx 80\ \mu\text{m}$ and $\approx 70\ \mu\text{m}$. At the end of the evaporative cooling in the crossed mODT, the trap depth is increased with an s-shaped 600 ms long ramp to compress the gas and avoid further undesired evaporation. At this point and before loading the optical lattice, the approximate confinement is given by the harmonic trapping frequencies $\omega_w, \omega_v, \omega_z \approx 2\pi \times (50, 70, 230)$ Hz [see Fig. 3.2(a) for axes]. These trapping frequencies are measured by first exciting the dipole mode with a sudden displacement of the trap center, and then recording the center-of-mass oscillations.

The final step of the state preparation procedure is the loading of the optical lattice generated by retro-reflecting a monochromatic laser beam with waists $\approx 150 \mu\text{m} \times 40 \mu\text{m}$ [132]. This results in an array of lattice planes spaced $d = \lambda_m/2 \approx 380 \text{ nm}$ apart, which are staggered since the lattice and horizontal mODT beams enclose an angle of $\approx 45^\circ$. However, the staggered arrangement does not pose a significant issue for our measurements, which typically only consider a few central layers (see Section 3.2). We employ two consecutive s-shaped ramps with duration 120 ms and 500 ms to load the atoms into the optical lattice. The initial setpoint of $3E_{\text{rec}}$ (recoil energy $E_{\text{rec}} = h \times 2.0 \text{ kHz}$) allows thermalization of the system as atoms still hop between adjacent lattice layers with rate $t/h \sim 200 \text{ Hz}$. Subsequently, we increase the depth to $85E_{\text{rec}}$, where the hopping of atoms between individual lattice planes is effectively frozen out ($t/h \sim 1 \text{ mHz}$). The lattice loading is not fully adiabatic, which we probe by ramping the lattice back down and comparing the temperatures before loading and after unloading. We find a small temperature increase of $\sim 0.05T_F$, and hence we assume that the induced heating is negligible for our initial temperatures $\approx 0.2T_F$.

The optical lattice produces an ensemble of uncoupled quasi-2D systems, which provide the starting point for our Fermi polaron measurements. Each layer of the optical lattice is fully characterized by the transverse and axial trapping frequency both equally important for the theoretical description of the medium in the Fermi polaron problem. Typical trapping frequencies in the experiment are $(\omega_x, \omega_z) \approx 2\pi \times (65, 250) \text{ Hz}$, corresponding to an asymmetric confinement of the atomic cloud. The axial trapping frequency is determined by the depth of the optical lattice, which we determine with lattice modulation spectroscopy. Since our theoretical description generally employs a harmonic potential, we expand the sinusoidal lattice potential up to second-order. This yields the trapping frequency $\omega_y = 2(E_{\text{rec}}/\hbar) \sqrt{V_0/E_{\text{rec}}} \approx 2\pi \times 37 \text{ kHz}$ for the typical lattice depth $V_0 \approx 85E_{\text{rec}}$. For the description of the experiment, the y -axis defines the strongly confined direction contrasting our theoretical description in Chapter 2, which has employed the z -axis for this purpose.

3.1.3 Populating the second orbital

To probe the Fermi polaron at variable interaction strength across the orbital Feshbach resonance, we first have to populate the clock state orbital in addition to the ground state orbital. In general, we transfer the minority atoms from the initial weakly interacting ground state $|g \downarrow\rangle$ ($m_F = -3/2$) to the strongly interacting $|e \uparrow\rangle$ ($m_F = -5/2$) clock state. At zero magnetic field, the transition energies between the six different nuclear spin states in the ground and clock state are degenerate. Figure 3.3(b) shows how the (differential) Zeeman shift lifts this degeneracy at finite magnetic field, as discussed in Chapter 1 (see Section 1.2.3). The number of transitions addressed with the light from the clock laser can be limited by choosing an appropriate polarization of the clock laser beam. For our measurement, the clock laser beam is linearly polarized with the electric field perpendicular to the quantization axes. In this way, the beam addresses both σ^\pm transitions [see Fig. 3.3(a)], and we couple atoms initially in $|g \downarrow\rangle$ to the final state in $|e \uparrow\rangle$ by choosing the detuning of the σ^- transition. However, a minimum magnetic bias field is required to ensure that the other transitions of both $|g \downarrow\rangle$ (minority) and $|g \uparrow\rangle$ (majority) are sufficiently detuned and can be neglected. In Fig. 3.3(c), we show

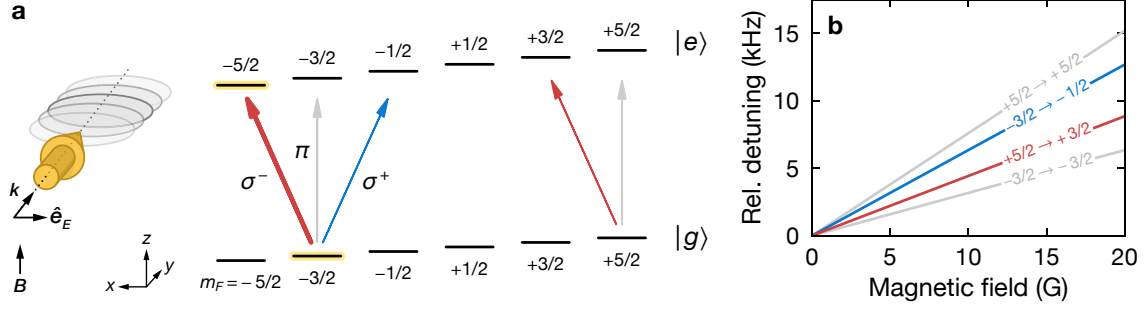


Figure 3.3 | Clock-line excitation scheme. (a) (Left) Schematic of the clock laser beam (yellow arrow) alignment relative to the planes of the optical lattice (gray ellipses). Black arrows indicate the wave vector k , the unit vector of the electric field E , and the quantization axes determined by the magnetic bias field B . (Right) Relevant nuclear spin states in $|g\rangle$ and $|e\rangle$ at finite bias field are shown as solid black lines. Here, the thick red arrow corresponds to the σ^+ transition between the weakly interacting initial state in $|g, 0\rangle$ ($m_F = -3/2$) and the strongly interacting state in $|e, \downarrow\rangle$ ($m_F = -5/2$). The remaining arrows correspond to the (undesired) coupling of other accessible transitions. Note that the π -transitions are generally strongly suppressed by choosing the correct polarization. (b) Detuning of the accessible transition relative to the $m_F = -3/2 \rightarrow -5/2$ transition for variable magnetic field strength.

the detuning of all relevant transitions. On this basis, we estimate that a bias field ~ 10 G already sufficiently splits the transitions for small Rabi frequencies $\Omega \lesssim 2\pi \times 1$ kHz employed in typical spectroscopy experiments.

Our optical traps are operated at the magic-wavelength, where the ac Stark shifts of the $|g\rangle$ and $|e\rangle$ states are identical, which avoids inhomogeneous broadening due to the trapping potential (see Section 1.3 in Chapter 1). In strong contrast to rf spectroscopy with alkali atoms, the coupling between weakly and strongly interacting impurity states is provided by an optical transition. This implies that a photon driving the excitation transfers a non-negligible recoil momentum onto an atom, given by the energy $E_{\text{rec}}^{578\text{nm}} = h \times 3.5$ kHz, and comparable to typical Fermi energies in the system. To avoid this transfer of kinetic energy, we use a clock laser beam co-aligned with the propagation direction of the laser beams generating the optical lattice, as shown in Fig. 3.3(a). In this configuration, the gap of the lowest-lying energy eigenstates far exceeds $E_{\text{rec}}^{578\text{nm}}$, which allows recoil-free spectroscopy in the Lamb-Dicke regime [31]. Any finite (residual) angle between clock laser and lattice beam results in a projection of the photon recoil along the weakly confined transverse axes of the optical lattice. However, we estimate this angle to be below 0.03 rad which results in a negligible transferred recoil energy of only $\approx h \times 2$ Hz $\ll \hbar\omega_x, \hbar\omega_z$.

3.2 Characterization of the initial state

Before turning to the experimental results for the multiorbital Fermi polaron, we explain the characterization of the initial state. This is a crucial step since the medium determines the dominant energy scale and key properties of the many-body problem. The initial spin-imbalanced Fermi gas occupies the electronic ground state and is distributed across the two spin states $m_F = -3/2$ (minority, $|g, 0\rangle$) and $m_F = +5/2$ (majority, $|g, \uparrow\rangle$). We primarily analyze

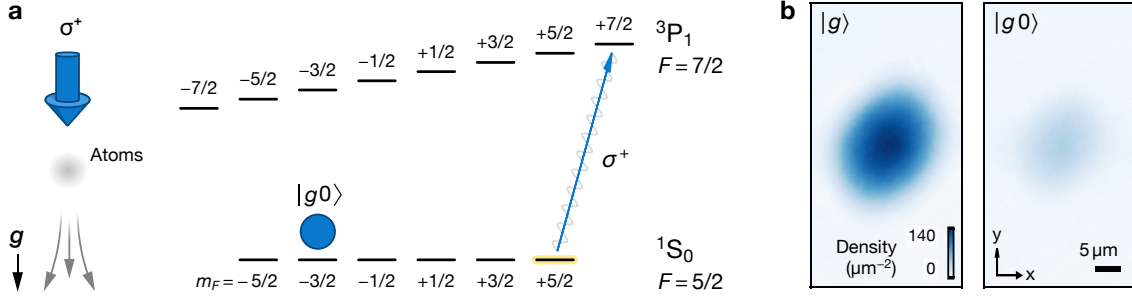


Figure 3.4 | Determination of the minority fraction. (a) (Left) Illustration of the “push” laser beam orientation relative to the atoms. (Right) Relevant nuclear spin states of the 1S_0 and 3P_1 manifold are shown as solid black lines, where the state addressed by the “push” beam are highlighted in yellow. The gray wavy lines indicate the relevant decay channels. The blue circle in the $m_F = -3/2$ state illustrates the remaining minority component after the removal of atoms in $m_F = +5/2$. (b) Exemplary column density of (left) all ground-state atoms in $|g\rangle$ and (right) only the minority atoms in $|g0\rangle$, recorded with absorption imaging before and after applying the “push” pulse. Here, the total atom number is $N_g \approx 58 \times 10^3$ with a minority fraction $N_0/N_g \approx 22\%$.

the properties of this initial state with absorption imaging of the atomic in-situ density. Since our imaging on the broad $^1S_0 \rightarrow ^3P_0$ transition does not resolve individual m_F states, another technique is required to record the density of both spin states independently. To this end, we apply a resonant “push” pulse that addresses the stretched $m_F = +5/2 \rightarrow +7/2$ transition on the intercombination line at a magnetic bias field of 50 G. This stretched transition is essentially closed and allows continuous scattering of photons and transfer of recoil energy onto the atoms during the 0.25 ms long pulse [see Fig. 3.4(a)]. Eventually, the addressed atoms are “pushed” out of the trap and the population in the remaining spin state can be imaged after a short hold time of ≈ 5 ms. This technique allows us to determine the density of majority and minority atoms together (denoted $|g\rangle$) and of minority atoms alone (denoted $|g0\rangle$) with two consecutive experimental shots, as shown in Fig. 3.4(c). From these results, we determine the minority fraction N_0/N_g across the $(x-y)$ -plane, which provides the starting point for the description in terms of effective parameters.

3.2.1 Effective parameters

We now derive effective quantities, namely, the Fermi energy ϵ_F and the Fermi wave vector κ_F , that correspond to equivalent parameters in a homogeneous system. This is a necessary step since our theoretical description in Chapter 2 assumes a homogeneous Fermi gas.

In the experiment, we prepare an ensemble of quasi-2D systems in the optical lattice and the underlying harmonic confinement along the y -axis leads to a significant variation of atom numbers in each of these systems. In Figs. 3.5(a) and 3.5(b), we show the atomic in-situ density together with the inferred distribution of atoms across the different layers of the optical lattice determined with the “push” beam technique discussed above. To increase our measurement fidelity, we only consider ≈ 15 layers of the optical lattice close to the atomic cloud center, which are indicated in Fig. 3.5. In this region, the atomic density and the minority fraction

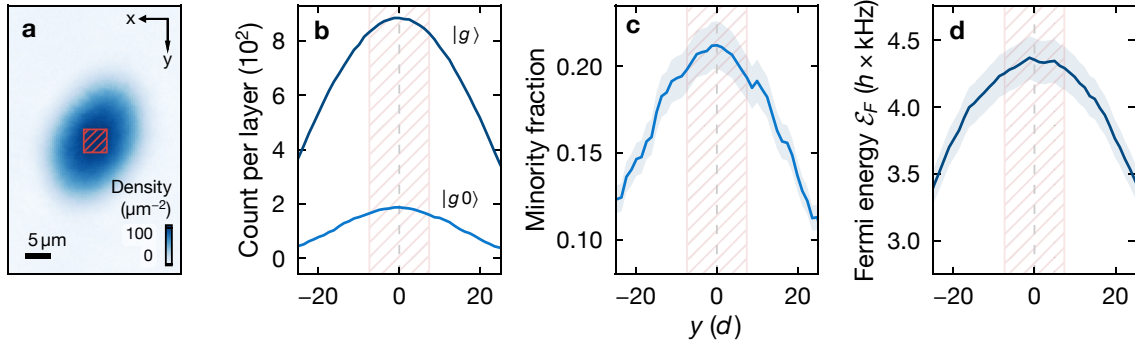


Figure 3.5 | Atomic distribution across layers of the optical lattice. Key properties of the atomic distribution in each lattice layer determined from averaging eight measurements of the in-situ density with the total atom number $N_g \approx 39 \times 10^3$. Note that the “push” beam technique has been employed to determine the atom count of the minority component independently. Here, $d = \lambda_m/2$ denotes the spacing of the optical lattice along y . Shaded areas correspond to estimated uncertainties and the red hatching indicates the region typically sampled in the experiment (size $\approx 5.6 \mu\text{m} \times 15d$). (a) Averaged density distribution obtained from individual absorption images. (b) Atom count in the layers of the optical lattice for all atoms ($|g\rangle$, dark-blue line) and minority atoms ($|g0\rangle$, light-blue line). (c) Minority fraction N_0/N_g and (d) majority Fermi energy \mathcal{E}_F defined in Eq. (3.4).

are nearly constant (standard deviation $< 5\%$), and our experiment essentially probes multiple identical copies of the same system [see Fig. 3.5(a)].

Therefore, only a single quasi-2D system is considered for the description of the minority and majority component. In the following, we assume that only the ground band of the optical lattice is occupied, and the harmonic in-plane potential restricts the momentum of each atom to two dimensions,

$$U(\mathbf{r}) = \frac{1}{2}m(\omega_x^2 r_x^2 + \omega_z^2 r_z^2) \quad (3.1)$$

with coordinate $\mathbf{r} = (r_x, r_z)$, the mass m of a ^{173}Yb atom, and trapping frequencies (ω_x, ω_z) . We describe the system in the local density approximation of a non-interacting ideal Fermi gas with a phase-space distribution of each component according to the Fermi-Dirac distribution [200],

$$f(\mathbf{r}, \mathbf{p}) = \left\{ e^{\beta[\mathbf{p}^2/2m + U(\mathbf{r}) - \mu]} + 1 \right\}^{-1}. \quad (3.2)$$

Here, $\mathbf{p} = (p_x, p_z)$ denotes the momentum, and $\beta = 1/(k_B T)$ with the temperature T . Note that we neglect the gravitational potential, which leads to a small displacement of the atomic cloud along the z -axis. The chemical potential μ is fixed by the total atom number N according to the relation [200]

$$N = \frac{1}{(2\pi\hbar)^2} \int d\mathbf{r} d\mathbf{p} f(\mathbf{r}, \mathbf{p}) = \int_0^\infty dE \frac{\rho(E)}{e^{\beta E}/z + 1} \quad (3.3)$$

with the fugacity $z = e^{\beta\mu}$ and $\rho(E) = E/(\hbar^2\omega_z\omega_y)$ the density of states of the two-dimensional

harmonic oscillator [201]. The Fermi energy \mathcal{E}_F corresponds to the chemical potential at zero temperature and can be obtained from the above relation,

$$\mathcal{E}_F = \hbar\sqrt{2N\omega_x\omega_z}. \quad (3.4)$$

In Fig. 3.5(a), we show \mathcal{E}_F across the different layers of the optical lattice in a typical experimental realization. Finally, integrating Eq. (3.2) over momentum \mathbf{p} yields the in-plane density

$$n(\mathbf{r}) = -\frac{m}{2\pi\hbar^2\beta} \text{Li}_1[-ze^{-\beta U(\mathbf{r})}] \quad (3.5)$$

with polylogarithm $\text{Li}_1(z) = -\ln(1-z)$. The inhomogeneous in-plane density $n(\mathbf{r})$ now allows us to relate properties *locally* to an ideal and homogeneous Fermi gas in 2D. In this case, the Fermi energy E_F ($\neq \mathcal{E}_F$) is related to the density n through $E_F = \hbar^2/(2m) \times (4\pi n)$ [202]. Thus, we define the local Fermi energy and wave vector,

$$E_F(\mathbf{r}) = \frac{\hbar^2}{2m} [4\pi n(\mathbf{r})] \quad \text{and} \quad k_F(\mathbf{r}) = \sqrt{4\pi n(\mathbf{r})} \quad (3.6)$$

with the local density $n(\mathbf{r})$ given by Eq. (3.5).

Our imaging intrinsically integrates over the z -axis of the system, which always yields a finite range of majority density sampled by the minority atoms. However, we do restrict the imaging along x to a $\Delta x = 5.6 \mu\text{m}$ wide central region [see Fig. 3.5(a)] to minimize the sampled inhomogeneity. For this region, we can calculate an effective Fermi energy ϵ_F of the medium (majority component) sampled by the impurities (minority component). Combining Eqs. (3.5) as well as (3.6) and integrating along the x - and z -axis yields

$$\epsilon_F = \frac{1}{N_0(\Delta x)} \int_{-\Delta x/2}^{\Delta x/2} dr_x \int_{-\infty}^{\infty} dr_z n_0(\mathbf{r}) E_F^\uparrow(\mathbf{r}) = \frac{1}{N_0(\Delta x)} \frac{\hbar^2}{2m} 4\pi \int_{-\Delta x/2}^{\Delta x/2} dr_x \int_{-\infty}^{\infty} dr_z n_0(\mathbf{r}) n_\uparrow(\mathbf{r}) \quad (3.7)$$

with $N_0(\Delta x) = \int_{-\Delta x/2}^{\Delta x/2} dr_x \int_{-\infty}^{\infty} dr_z n_0(\mathbf{r})$ and n_0 (n_\uparrow) referring to the density of the minority ($|g \downarrow\rangle$) (majority $|g \uparrow\rangle$) component. For our parameters, $\epsilon_F \approx 0.8 \mathcal{E}_F < \mathcal{E}_F$ due to finite temperature and the non-negligible size of the sampling region, as illustrated in Fig. 3.6. We note that the dependence of ϵ_F on the temperature and minority fraction is relatively weak and approximately linear in our regime of interest with approximate slopes $\partial_{(T/T_F)}\epsilon_F \sim -1$ and $\partial_C\epsilon_F \sim -0.2$, respectively. In analogy to Eq. (3.7), the standard deviation $\Delta\epsilon_F$ can be determined to quantify the width of the underlying distribution, which is typically given as $\Delta\epsilon_F \approx 0.2\epsilon_F$. From the effective Fermi energy ϵ_F , we also calculate the effective Fermi wave vector $\kappa_F = \sqrt{2m\epsilon_F}/\hbar$.

The quantities obtained in the above calculations now allow us to apply the theory to the experiment, as ϵ_F , κ_F , and the magnetic field, fully define the Fermi polaron problem. We refer the interested reader to Appendix C for a derivation of the quantities discussed in this section.

3.2.2 In-situ thermometry

To fully characterize the initial state, we also measure the temperature by fitting the in-situ distribution of the atoms. The orientation of our imaging system averages the atomic den-

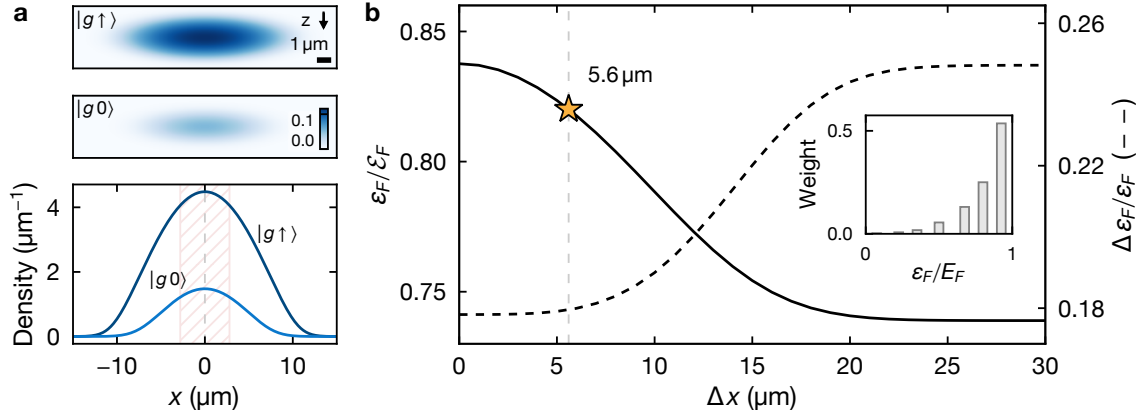


Figure 3.6 | Effective Fermi energy sampled by the minority component. Here, we show data for typical experimental parameters in a single layer of the optical lattice with $N = 600$ atoms, temperature $T/T_F = 0.15$, minority fraction of 20%, and sample region $\Delta x = 5.6 \mu\text{m}$ (red hatching). (a) (Top) In-plane density $n(\mathbf{r}) = n(x, z)$ in atoms/ μm^2 of majority $|g \uparrow\rangle$ and minority $|g 0\rangle$ atoms from a theoretical calculation according to Eq. (3.5). (Bottom) Column density retrieved from integrating the in-plane density in panel (a) along the line of sight (z -axis)—analogous to absorption imaging in the experiment. (b) Effective Fermi energy ε_F (solid black line) and standard deviation $\Delta\varepsilon_F$ (dashed black line, right axes) for variable size of the sample region Δx . The yellow star indicates the typical size of this region, and the inset shows the binned distribution of ε_F along z for that point.

sity along the z -axis resulting in a column density, which can be described theoretically by integrating Eq. (3.5),

$$cd(r_x) = \int_{-\infty}^{\infty} dr_z n(\mathbf{r}) = -\sqrt{\frac{m}{2\pi}} \frac{1}{\hbar^2 \beta^{3/2} \omega_z} \text{Li}_{3/2} \left(-z e^{-\beta m \omega_x^2 x^2 / 2} \right). \quad (3.8)$$

This result yields the fugacity z of an ideal single-component Fermi gas after numerically fitting the in-situ column density. Also, the reduced temperature $T/T_F = k_B T / \varepsilon_F$ can be obtained from the fugacity z (see Appendix C). In contrast to the above considerations, we prepare a spin-imbalanced Fermi gas with weak interactions, and therefore, we expect a systematic error when fitting Eq. (3.8) to the density of the sample. Nevertheless, we first proceed with this simple approach and then later discuss potential shortcomings of our method.

We record the in-situ column density of all ground-state atoms (minority and majority component) and fit Eq. (3.8) along the x -axis for each pixel row obtained from the camera, as shown in Fig. 3.7(a). This technique allows us to obtain fits of the reduced temperature averaged across a few adjacent layers of the optical lattice [see Fig. 3.7(b)].¹ In general, we expect the absolute temperature T across the different layers of the optical lattice to be approximately constant. This assumption is verified by comparing the fitted values to the expected scaling $T/T_F \propto 1/\sqrt{N}$ with the number of atoms N in each layer. Here, the reduced temperature is expected to increase at the edges of the system, $|y| \gg 10d$, where the atom number and Fermi energy ε_F are significantly lower. While the data in Fig. 3.7(b) exhibits fairly large fluctuations, the expected scaling is still qualitatively reproduced. For the outermost regions,

¹Our finite imaging resolution $\approx 3 \mu\text{m}$ causes an effective averaging across approximately ten adjacent layers.

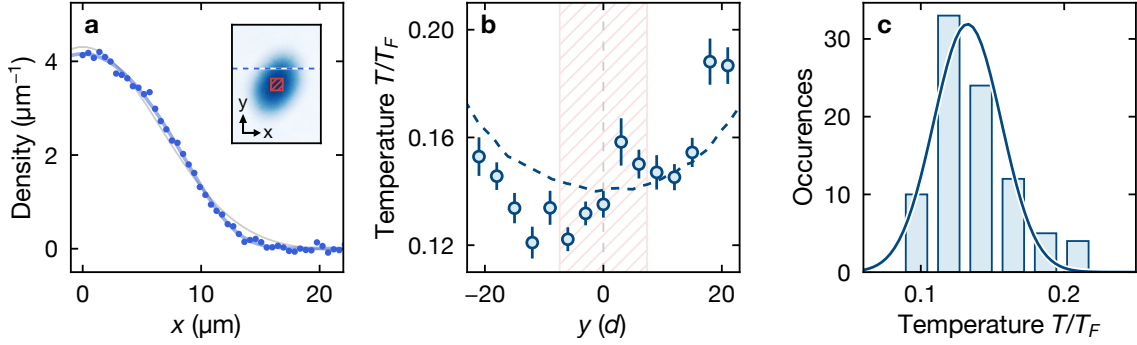


Figure 3.7 | Thermometry in the optical lattice. (a) Typical temperature fit [blue line, $T/T_F = 0.19(3)$] of Eq. (3.8) at a distance of $\approx 20d$ from the center of the cloud (dashed line in the inset). Here, $d = \lambda_m/2 \approx 0.38 \mu\text{m}$ denotes the lattice spacing. Data points are averaged between the left and right halves of the system. For comparison, we also show a Gaussian fit (gray line) corresponding to a Maxwell-Boltzmann distribution (high-temperature limit). (b) Temperatures extracted from eight individual absorption images and averaged for constant distance from the center. Data points spaced less than $3d$ are binned. The dashed line indicates the expected scaling of the reduced temperature (guide to the eye). Red hatching indicates the region typically sampled in the experiment. (c) Histogram of temperatures extracted from individual numerical fits shown in panel (b) restricted to the sampled region. The blue line corresponds to a Gaussian fit with mean (standard deviation) $T/T_F = 0.14(3)$.

we detect an increase of T/T_F up to a factor of two [not shown in Fig. 3.7(b)]. In the central region considered for measurements, we typically extract a reduced temperature $T/T_F \approx 0.15$ [see Fig. 3.7(c)] corresponding to $k_B T/\epsilon_F \approx 0.2$, which considers the typical effective Fermi energy sampled by the minority atoms.

We now turn to the discussion of the systematic errors in the thermometry technique discussed above. Since our sample is strongly spin-imbalanced with a typical ratio of 1 : 4 between the two components, already a non-interacting Fermi gas would feature an overall modified density profile. This regime can be explored by summing the theoretical non-interacting density across both components and numerically fitting the resulting profile with Eq. (3.8), which yields overestimated temperatures. To probe for such an effect in the experiment, we compare the extracted temperatures for different minority fractions, which vary naturally between layers of the optical lattice [see Fig. 3.5(c)]. However, we do not detect a systematic increase of the extracted temperature. We attribute this observation to the presence of weak repulsive interactions that reduce the central density [75]. This leads to an additional deformation of the density profile, potentially canceling the effect of the spin imbalance.

The “push” pulse technique discussed earlier gives access to the density of the minority fraction. When extracting the temperature from the minority density across the central layers of the optical lattice, we find reduced temperatures ≈ 0.4 corresponding to $T/T_F \approx 0.2$ for the majority component. We additionally verify our results by simulating the lattice loading under the assumption of constant entropy of initial and final state (see Section 5.2.1 in Chapter 5). This procedure suggests a reduced temperature $T/T_F \approx 0.2$ in the central layers of the optical lattice for typical initial temperatures in the optical dipole trap.

The presence of the spin imbalance and our analysis indicate that our temperature estimates are most likely biased towards lower temperatures. However, the magnitude of this systematic

Table 3.1 | Typical parameters of a single quasi-2D system in the experiment

Trapping frequency ($2\pi \times$ Hz)			Atom count		Medium (majority component, \uparrow)			
ω_x	ω_y	ω_z	N_\uparrow	N_0/N_g	\mathcal{E}_F	ε_F	$\Delta\varepsilon_F$	$k_B T/\varepsilon_F$
65	37×10^3	250	600	20%	$h \times 4.4$ kHz	$0.8 \mathcal{E}_F$	$0.2 \varepsilon_F$	0.2

Estimated trap and medium properties in a single layer of the optical lattice with the majority (minority) atom count N_\uparrow (N_0), total atom count N_g , Fermi energy \mathcal{E}_F , effective Fermi energy ε_F , standard deviation $\Delta\varepsilon_F$, and temperature T . Note that the interaction parameter $\ln(\kappa_F a_{2D})$ can be tuned relatively freely by utilizing the orbital Feshbach resonance.

error should only have a minor effect on the relevant parameters for the Fermi polaron. The temperature measurements complete our description of the initial state, and we summarize the estimated typical parameters of our experimental system in Table 3.1.

3.3 Inverse clock-line spectroscopy

Two spectroscopic techniques have been established to probe the Fermi polaron experimentally: Direct spectroscopy or *spin ejection* describes the preparation of an equilibrium state at variable interaction strength followed by a subsequent outcoupling of the impurity into a weakly interacting state [71]. Quasiparticle properties can then be inferred from measurements of energies with respect to that state while modifying the interaction strength in the initial state. For a low-temperature medium, this procedure only allows probing states close to the ground state, and excited states like the repulsive Fermi polaron cannot be directly accessed. In contrast, inverse spectroscopy or *spin injection* describes the preparation of a weakly interacting initial state of impurity and medium [73].² Subsequently, the impurity is coupled to a state strongly interacting with the surrounding medium. This method also gives access to excited states since the coupling process can transfer energy and the final state is not necessarily in thermal equilibrium. In our experiment, we employ the inverse spectroscopy technique to probe the energy landscape of the multiorbital Fermi polaron. Here, the clock laser excitation couples the initial weakly interacting impurity state $|g 0\rangle$ and the strongly interacting final state $|e \downarrow\rangle$, as illustrated in Fig. 3.8.

3.3.1 Initial-state interactions

Before describing the experimental results, we briefly discuss the weak but finite interactions in the initial state. The scattering length between the ground-state atoms in the initial state has a significant value with $a_{gg} \approx 199.4a_0$ (see Table 1.1 in Chapter 1). We consider the impurities in the $|g 0\rangle$ initial state to form weakly interacting repulsive Fermi polarons, which can be described by the single-channel theory introduced in Chapter 2 (see Section 2.2). To this end,

²A recent theoretical study has identified a relatively simple relation between the injection and ejection spectra in the limit of a single impurity [193].

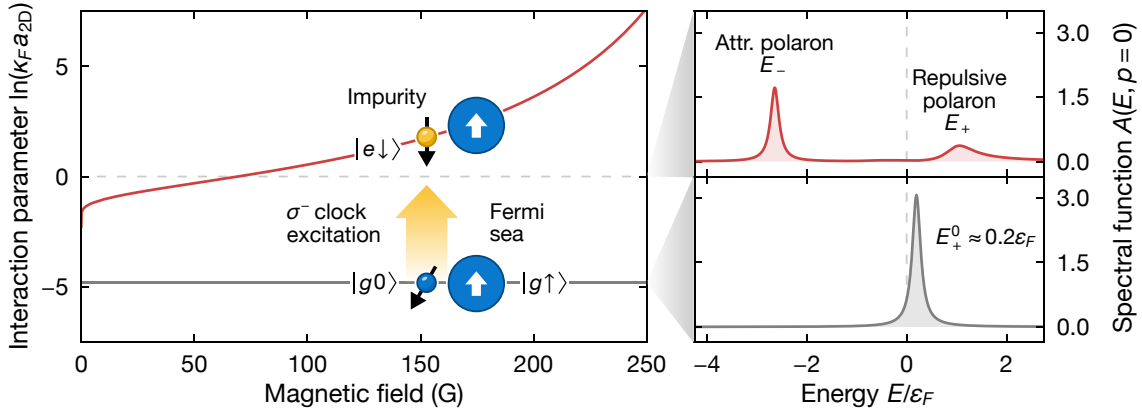


Figure 3.8 | Inverse spectroscopy. Illustration of inverse spectroscopy (spin ejection) on the clock transition as realized in our experiment. (Left) The gray line corresponds to the interaction parameter $\ln(\kappa_F a_{2D}) = -4.9$ in the initial state (impurity in $|g0\rangle$, blue circle with arrow), independent of the magnetic field. In contrast, the red line shows the magnetic field dependence of the interaction parameter in the strongly interacting final state (impurity in $|e\downarrow\rangle$, yellow circle with arrow). (Right) Example spectral functions broadened with $E \rightarrow E + i0.1\epsilon_F$ and calculated for the initial state (gray) as well as the strongly interacting final state (red) at $\ln(\kappa_F a_{2D}) = 0$.

we first determine the scattering length of two ground-state atoms for our typical experimental parameters with the harmonic oscillator length $l_y \approx 750a_0$ [see Eq. (2.20) in Chapter 2],

$$a_{gg,2D} = l_y \sqrt{\frac{\pi}{0.905}} \exp\left(-\sqrt{\frac{\pi}{2}} \frac{l_y}{a_{gg}}\right) \approx 12.5a_0. \quad (3.9)$$

Combining this result with the effective Fermi wave vector $\kappa_F \approx 11 \mu\text{m}^{-1}$ yields the interaction parameter $\ln(\kappa_F a_{gg,2D}) = -4.9(1)$. At zero temperature and zero momentum, we find the approximate energy of the repulsive polaron in $|g0\rangle$, $E_+^0/\epsilon_F = -1/\ln(\kappa_F a_{gg,2D}) \approx 0.2$ (see Section 2.2.2 in Chapter 2). We will employ this energy value in the following measurements to correctly determine the quasiparticle energy in the final state.

3.3.2 Transfer rates

In the experiment, we couple a single particle state to many-body states, i. e., the attractive and repulsive polaron, as well as the molecule-hole continuum. The transfer rate into these final many-body states depends on the laser detuning $\Delta\omega$ and the interacting strength determined by the magnetic field B [66],

$$I(\omega_0 + \Delta\omega; B) \sim \int d\mathbf{p} \int dE F(E) A_0(p, E) A_1(p, E + \hbar\Delta\omega; B). \quad (3.10)$$

Here, ω_0 denotes the clock transition frequency at the given magnetic field, $F(E)$ corresponds to the Fermi-Dirac distribution. Finally, A_0 and A_1 are the spectral functions in the initial $|g0\rangle$ state and final $|e\downarrow\rangle$ state, with the latter strongly depending on the magnetic field due to the

presence of an orbital Feshbach resonance. For a fixed-duration laser pulse,³ the number of atoms transferred into the final state is directly proportional to $I(\omega_0 + \Delta\omega; B)$. Note that the above relation only applies to the regime of linear response with a vanishing small population in the final state $|e \downarrow\rangle$. We assume $A_0(p, E) \approx \delta[E - E_+^0 - p^2/(2m)]$ with the Dirac delta distribution $\delta(x)$, an approximation for the only weakly interacting initial state $|g 0\rangle$ (see Fig. 3.8). With this assumption, we estimate the transfer rate,

$$\begin{aligned} I(\omega_0 + \Delta\omega; B) &\sim \int d\mathbf{p} f[E_+^0 + p^2/(2m)] A_\downarrow[p, E_+^0 + p^2/(2m) + \hbar\Delta\omega; B] \\ &\approx A_\downarrow[p, E_+^0 + p^2/(2m) + \hbar\Delta\omega; B]. \end{aligned} \quad (3.11)$$

In the second approximation, we assume that the spectral function is a constant function of its argument p , which holds strictly only for vanishing momentum or, in practical terms, for a single impurity. In the limit of our approximations, the weak initial-state interaction leads to an energy shift $\sim E_+^0$. The approximation in Eq. (3.11) allows us to relate the measured transfer rate or atom count in an inverse spectroscopy experiment to the theoretically calculated $A_\downarrow(p, E; B)$. Therefore, the inverse spectroscopy experiment can be identified as an approximate measurement of the spectral function.

3.3.3 The many-body spectrum

First, we ramp the magnetic field to a value in the range $15 \text{ G} \leq B \leq 225 \text{ G}$ to set the desired interaction parameter $-1.1 \leq \ln(\kappa_F a_{2D}) \leq 5$. We then drive the σ^- clock transition with a rectangular-shaped laser pulse of duration 2.4 ms, corresponding to a π -pulse of a free particle without the medium and a Fourier-limited energy resolution of $\approx 0.1\epsilon_F$. This pulse transfers a small fraction of the minority component in $|g 0\rangle$ to the clock state in $|e \downarrow\rangle$, which we subsequently detect. To this end, we first remove all remaining atoms in $|g 0\rangle$ and the majority component in $|g \uparrow\rangle$ by off-resonantly addressing the broad $^1S_0 \rightarrow ^1P_1$ transition with a high-power ‘‘push’’ pulse. Then, the magnetic field is rapidly lowered to 1 G by turning off the power supply driving the large-current coils. To ensure that any residual field from Eddy currents has sufficiently decayed, a wait time of ≈ 10 ms is introduced before the excited state detection. The atoms transferred into the clock state $|e \downarrow\rangle$ are detected by first transferring them back to the ground state with a 0.3 ms long repumping pulse on the $^3P_0 \rightarrow ^3D_1$ transition. Subsequently, the atomic in-situ density distribution is recorded via absorption imaging, which yields the approximate in-situ density and number of transferred atoms.

Spectrum and line shapes.—As discussed in Section 3.2.1, the experimental data is only evaluated in a small region close to the cloud center. This allows us to limit the inhomogeneous broadening $\sim 0.2\epsilon_F$ due to varying density across the harmonic trap. Figure 3.9 depicts the recorded raw spectra from this region at selected magnetic fields and variable clock laser detuning relative to the transition of a free particle. At negative detuning, we find a peak at energies that strongly decrease for lower magnetic fields. Moreover, the width increases significantly as well until the peak is merely a single broad feature. At positive detuning,

³Here, we neglect the finite pulse duration which leads to a convolution of the transfer rate with the Fourier transform of the pulse shape.

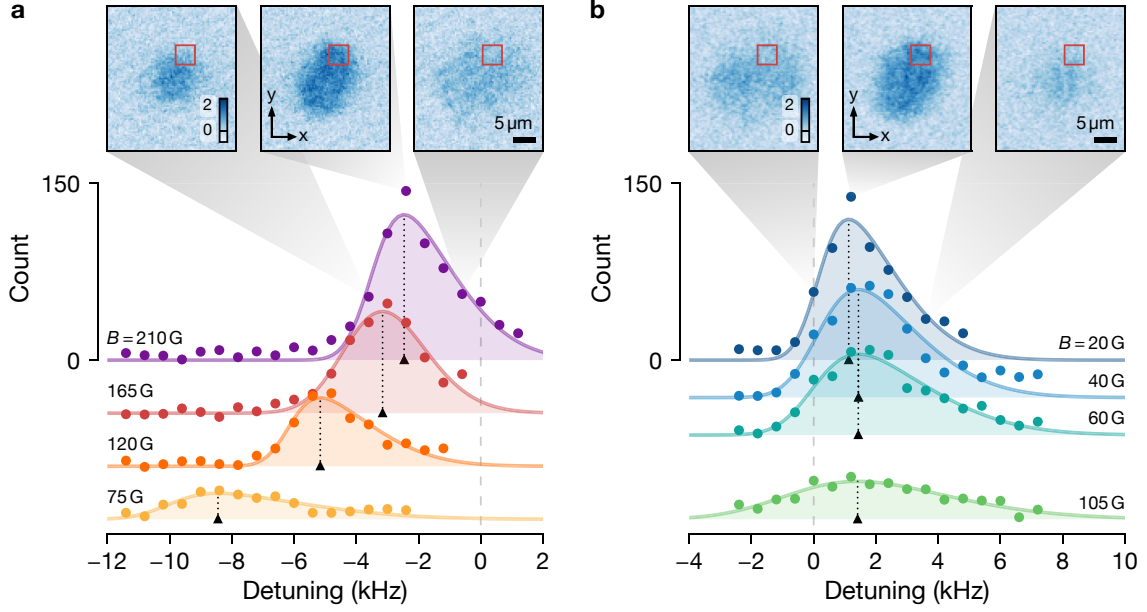


Figure 3.9 | Raw spectra of attractive and repulsive Fermi polaron. Number of atoms detected in $|e\rangle$ (colored circles) for variable detuning of the clock laser and interaction set by the magnetic field B . Here, we show the parts of the spectrum corresponding to the (a) attractive and (b) repulsive Fermi polaron. This measurement is characterized by the effective Fermi energy $\varepsilon_F = h \times 3.7(2)$ kHz, (effective) minority fraction 0.26(2), temperature $k_B T / \varepsilon_F = 0.17(3)$, and clock-laser drive strength $\hbar\Omega \approx 0.1\varepsilon_F$. The solid lines show a numerical fit of the skew normal distribution [203] with the black triangles and dotted lines indicating the maximum. Each point corresponds to the average of three individual measurements with the standard error of the mean comparable to the marker size. The top panels show sample in-situ images (averaged) of the (a) $B = 210$ G and (b) $B = 20$ G datasets. The red rectangle indicates the region considered for the counts shown in the main panels. The displacement of this region is chosen to match the effective Fermi energy of the measurements discussed in following sections.

we find a similar peak but at an energy that only weakly increases with the magnetic field, although the shape of the peak broadens in the same manner. As discussed below, the two peaks can be associated with the attractive and repulsive polaron.

The shape of the features can be reasonably reproduced with an asymmetric Gaussian shape, as demonstrated by the numerical fits in Fig. 3.9. Interestingly, the in-situ density allows us to partly reveal the origin of the strongly asymmetric line shapes. The apparent width of the recorded density changes from narrow to wide when scanning the detuning across the peak [see top panels from left to right in Figs. 3.9(a) and 3.9(b)]. The variable width of the density can be understood when considering that at a given detuning, only certain spatial regions in the (x, z) -plane are resonantly addressed. Thus, the tails towards smaller absolute values of the detuning originate from outer regions of the transverse lattice planes, where the density, Fermi energy, and resulting (absolute) quasiparticle energy are small. In contrast, the tails towards larger absolute values of the detuning originate from the central regions with the largest density and quasiparticle energies.

For all probed magnetic fields, the fraction of impurities driven to $|e \downarrow\rangle$ remains below 15%. This strongly suggests that the system is only weakly driven and the regime of linear response

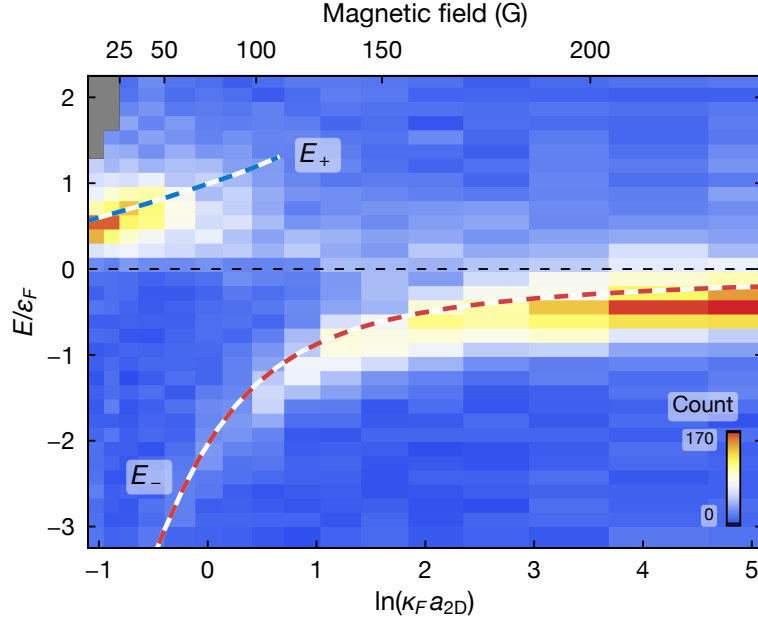


Figure 3.10 | Spectral response of the spin-imbalanced multiorbital Fermi gas. Number of detected clock-state atoms in $|e\rangle$ with a correction for the independently measured losses during the repumping process. The blue-dashed (red-dashed) lines correspond to the energy E_+ (E_-) of the repulsive (attractive) Fermi polaron calculated for a finite-temperature medium and zero-momentum impurity. These theoretical results are adapted from Ref. [109] and contain no free parameter.

still applies. Notably, the observed spectral features are much broader than the Fourier-limited resolution ≈ 0.4 kHz of the excitation pulse, confirming that the spectroscopic resolution is not limited by the finite linewidth of the clock laser (see Section 1.4.2 in Chapter 1).

Comparison of experiment and theory.—For a quantitative comparison of experimental and theoretical results, we normalize the detuning of the clock laser to the energy scale set by the effective Fermi energy ϵ_F . We also subtract the quasiparticle energy $E_+^0 \approx 0.2\epsilon_F$ of the weakly interacting initial state and convert all magnetic fields to the interaction parameter $\ln(\kappa_F a_{2D})$. For example, this enables the comparison of our results to prior experimental work employing a Fermi gas of ^{40}K atoms in quasi-2D [74]. Figure 3.10 displays the resulting spectral response for many interaction strengths and energies determined from the clock laser detuning. In accordance with the raw spectra shown in Fig. 3.9 and for repulsive interactions with $\ln(\kappa_F a_{2D}) < 0$, we find a peak at positive energies which increases up to $\approx 0.8\epsilon_F$ at $\ln(\kappa_F a_{2D}) = 0$. The contrast quickly decreases beyond this point with merely a very broad feature visible. For attractive interactions with $\ln(\kappa_F a_{2D}) > 0$, we find the second peak at negative energies with a relatively strong non-linear but monotonous dependence on the interaction parameter. In the regime of strong interactions at $\ln(\kappa_F a_{2D}) = 0$, this energy decreases to almost $-2.5\epsilon_F$ with a significantly broadened peak and reduced contrast. While we can observe a weak signal between the two peaks for $0 \leq \ln(\kappa_F a_{2D}) \leq 2$, we do not attribute it to the molecule-hole continuum. Instead, we expect the feature to originate from regions with a much smaller local density that exhibit quasiparticle energies closer to $E = 0$. This hypothesis is supported by the fact that the largest contrast of this spurious signal can be found close to zero detuning.

We compare our experimental results to the theoretical predictions from Ref. [109], which employ a many-body T-matrix approach for the calculation of the spectral function and the quasiparticle energies. As explicitly shown in the Supplemental Material of Ref. [110], the results of the T-matrix approach are almost identical to the simplified two-channel model discussed in Chapter 2 (see Section 2.3.2). The theory considers the finite temperature of the medium but not the finite momentum arising from the non-vanishing number of minority atoms forming a small Fermi sea in addition to the medium. For the comparison, we only consider the quasiparticle energies since the intricate details of the experiment make it challenging to compare the experimental results and spectral function quantitatively. Generally, we find excellent agreement between the theoretically calculated quasiparticle energies and both quasiparticle branches appearing in the spectral response recorded in the experiment. Thus, we identify the branch at positive energies with the repulsive Fermi polaron and the one at negative energies with the attractive polaron. Interestingly, the theoretically calculated energy of the attractive polaron slightly disagrees with the experiment for all interaction strengths. This conflict can be resolved by shifting the theoretical curve down in energy by a constant $\approx -0.2\epsilon_F$. The underlying reason for the discrepancy could be an incorrect estimate of the repulsive polaron energy E_+^0 , experimental imperfections, systematic uncertainties of the relevant parameters, or also a combination of multiple error sources. Following our discussion in Chapter 2 (see Section 2.2.3), we do not expect the finite impurity momentum to explain the observed disagreement since it would reduce the observed quasiparticle energy in our measurement. Finally, we note that the attractive-polaron-to-bound-dimer transition is predicted for $-1.1 \leq \ln(\kappa_F a_{2D}) \leq -0.8$ and a broad Feshbach resonance, as typically found in alkali atoms [177, 185–187]. In our measurements, we do not see any direct signatures of this expected change in the ground state of the system.

The observed signatures in the spectral response demonstrate the existence of Fermi polarons in a two-orbital quantum gas with their energies well-described by the many-body T-matrix approach from Ref. [109]. This also implies that the theoretical description within the effective two-channel model is equally accurate [110, 204].

3.4 Coherent Rabi oscillations

We revisit Chevy's variational wave-function ansatz from Chapter 2 [see Eq. (2.2)], which describes the zero-momentum polaron wave function

$$\begin{aligned} |\Psi_P\rangle &= \sqrt{Z} \left(\hat{c}_\downarrow^\dagger |\text{vac}\rangle_\downarrow \right) \otimes |\text{FS}\rangle_\uparrow + \sum_{q < k_F < k} \phi_{kq} \left(\hat{c}_{(q-k)\downarrow}^\dagger |\text{vac}\rangle_\downarrow \right) \otimes \left(\hat{c}_{k\uparrow}^\dagger \hat{c}_{q\uparrow} |\text{FS}\rangle_\uparrow \right) \\ &= \sqrt{Z} \left(\hat{c}_\downarrow^\dagger |\text{vac}\rangle_\downarrow \right) \otimes |\text{FS}\rangle_\uparrow + e^{i\theta_p} \sqrt{1-Z} |\text{inc}\rangle, \end{aligned} \quad (3.12)$$

where $\hat{c}_\downarrow^\dagger$ (\hat{c}_\downarrow) denotes the fermionic creation (annihilation) operator for a zero-momentum impurity in the strongly interacting $|e \downarrow\rangle$ state and $|\text{vac}\rangle$ corresponds to the vacuum state. In the last equation, we have summarized the incoherent part of the wave function into the state $|\text{inc}\rangle$ and the phase θ_p . For simplicity, we assume an impurity at zero-momentum here,

but the following discussion also applies similarly to finite impurity momenta. This zero-momentum impurity in the weakly interacting initial state can be approximately described by the non-interacting wave function

$$|\Psi_i\rangle = (\hat{c}_0^\dagger |\text{vac}\rangle_0) \otimes |\text{FS}\rangle_\uparrow, \quad (3.13)$$

where \hat{c}_0^\dagger (\hat{c}_0) denotes the fermionic creation (annihilation) operator for an impurity in the $|g 0\rangle$ state. Ignoring the internal state $\sigma \in \{0, \downarrow\}$ of the impurity, we observe that the squared overlap of the initial and final (polaron) state is given as $|\langle\Psi_p|\Psi_i\rangle|^2 = Z$ (quasiparticle residue Z). The weight \sqrt{Z} in Eq. (3.12) quantifies the coherent or single-particle-like contribution to the polaron wave function.

The clock laser coupling does not depend on momentum and can be considered to be approximately homogeneous across the typical sample size. Thus, the Hamiltonian describing the on-resonance Rabi coupling of initial and final state within the rotating-wave approximation takes the form [73]

$$\hat{\mathcal{H}}_R = \frac{\Omega_0}{2} \sum_{\mathbf{p}} (\hat{c}_{\mathbf{p}\downarrow}^\dagger \hat{c}_{\mathbf{p}0} + \text{h.c.}) \quad (3.14)$$

with the Rabi frequency Ω_0 , which is experimentally determined by the intensity of the clock laser beam. We can now calculate the matrix element for the transition rate induced by the drive,

$$\langle\Psi_p|\hat{\mathcal{H}}_R|\Psi_i\rangle \sim \Omega_0\sqrt{Z}. \quad (3.15)$$

Note that the incoherent part $|\text{inc}\rangle$ only has contributions from particle-hole excitations of the Fermi sea, which makes it orthogonal to the unperturbed Fermi sea $|\text{FS}\rangle$. The result of Eq. (3.15) is particularly helpful for experiments, as the quasiparticle residue Z can be measured by simply driving Rabi oscillations between the initial and final state [73].

In the experiment, we probe the Rabi coupling with a variable duration of the clock laser pulse tuned to the quasiparticle resonance. This frequency is determined in an independent auxiliary measurement by extracting the quasiparticle energy of the attractive or repulsive polaron from the spectrum with a numerical fit. For the main measurement, we employ a sequence similar to the one for the spectral response discussed in the previous section. However, we drive the clock transition with much larger Rabi frequencies Ω comparable to, or partly even exceeding, the effective Fermi energy $\epsilon_F \approx \hbar \times 3.6$ kHz. A strong drive is required since dephasing processes become relevant on the Fermi time scale $\tau_F = \hbar/\epsilon_F$, which hinders the detection of coherent oscillations and the extraction of Z . In addition to the strong drive, we also employ an altered state detection and determine the number of minority atoms \mathcal{N}_0 remaining in $|g 0\rangle$ after the variable-length clock laser pulse. For the present measurement, this technique proves to be more robust compared to the detection of the atom count in $|e\rangle$. To detect the atom number in $|g 0\rangle$, we first remove all majority atoms of the Fermi sea and then image the remaining atoms in $|g 0\rangle$ via absorption imaging. The state-selective removal is achieved by applying a short 0.25 ms long resonant “push” pulse on the intercombination line that selectively removes all majority atoms in $|g \uparrow\rangle$ (see Section 3.2). In addition to the

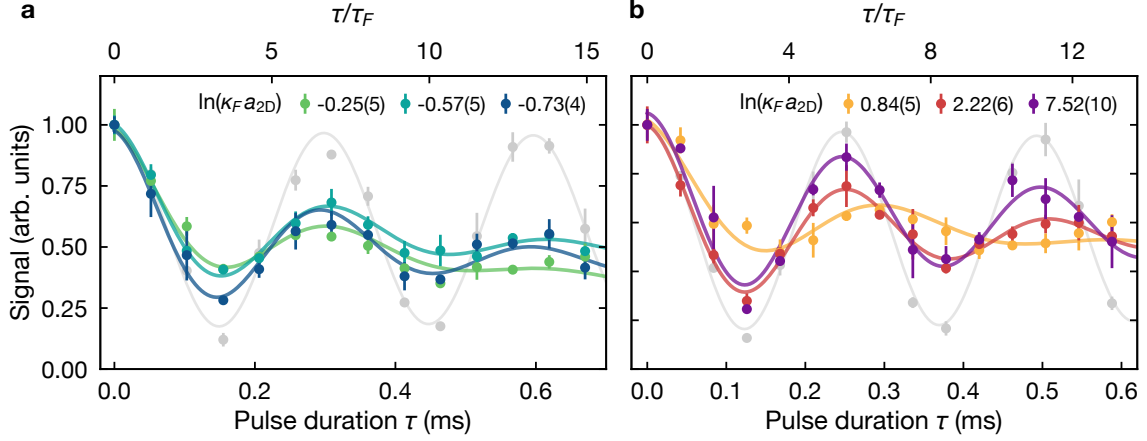


Figure 3.11 | Rabi oscillations of repulsive and attractive Fermi polaron. Oscillations between weakly interacting $|g\rangle$ and strongly interacting $|e\rangle$ impurity states recorded for variable duration τ of the clock laser pulse with Rabi frequency Ω , and for the (a) repulsive [$\hbar\Omega/\varepsilon_F = 0.9(1)$] and (b) attractive Fermi polaron [$\hbar\Omega/\varepsilon_F = 1.1(1)$]. All datasets are characterized by the effective Fermi energy $\varepsilon_F = h \times 3.6(4)$ kHz, Fermi time scale $\tau_F = \hbar/\varepsilon_F = 45(5)$ μ s, (effective) minority fraction 0.28(3), and temperature $k_B T/\varepsilon_F = 0.16(4)$. Colored circles show the signal from the interacting regime (see legend) and gray circles correspond to a reference measurement without interactions. Error bars indicate the standard error of the mean for points with multiple measurements. Solid lines correspond to numerical fits of Eq. (3.16). Each time trace is normalized to its value at $\tau = 0$, which compensates for the slightly varying atom numbers $\lesssim 20\%$. A signal amplitude of one corresponds to $\mathcal{N}_0 \approx 10^3$ atoms inside the central region considered for the data evaluation.

measurements in the interacting regime, we perform a reference measurement without the presence of the Fermi sea in $|g\rangle$, which yields the single-particle Rabi frequency Ω_0 .

Figure 3.11 shows the experimental results for variable interaction strength selected with the magnetic field. For all probed interaction parameters in the range $-0.9 \leq \ln(\kappa_F a_{2D}) \leq 7.5$, we find oscillations with large damping increasing towards the strongly interacting regime at $\ln(\kappa_F a_{2D}) = 0$. Comparing the interacting and non-interacting time traces, we also find a reduced oscillation frequency as the interaction strength increases [see Fig. 3.11(b)].

3.4.1 The quasiparticle residue

For comparing the experimental results to theoretical predictions of the quasiparticle residue, we numerically fit the detected time-dependence of the atom number in $|g\rangle$ to the function

$$\mathcal{N}_0(\tau) = ae^{\Gamma_{bg}\tau} + be^{\Gamma_R\tau} \cos(\Omega t). \quad (3.16)$$

Here, a and b are dimensionless constants, Γ_{bg} is a background decay rate, Γ_R denotes the damping of the Rabi oscillations, and Ω corresponds to the Rabi frequency. According to Eq. (3.15), we can extract Z from the experimental data by calculating $(\Omega/\Omega_0)^2$ with Ω_0 determined from the reference measurements in the absence of a background Fermi sea. In Fig 3.12(a), we show the experimental result and theoretical predictions for Z from the same many-body T-matrix calculation already applied to the spectral response measurement. The quasiparticle residue Z

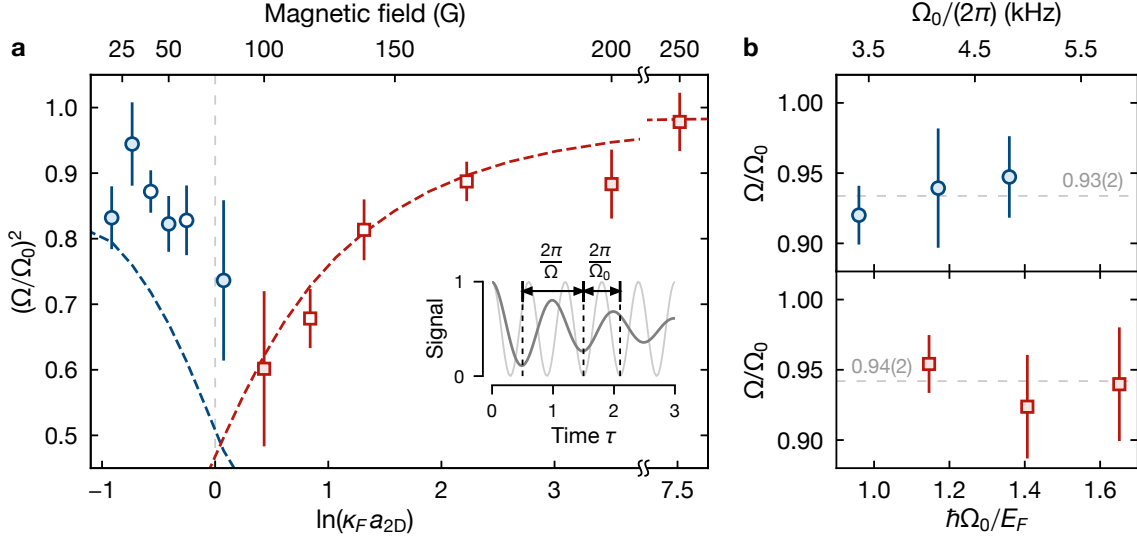


Figure 3.12 | Quasiparticle residue of the multiorbital Fermi polaron. (a) Approximate values of the quasiparticle residue $Z \approx (\Omega/\Omega_0)^2$ for repulsive (blue circles) and attractive (red squares) Fermi polaron, extracted from numerical fits of Rabi oscillations [see inset schematic]. Empty markers indicate weighted averages[†] from two or three separate measurements with variable drive strength at the same magnetic field, and error bars indicate the fit error. The blue (red) dashed lines show the result of a finite-temperature theoretical calculation of the quasiparticle residue Z for the zero-momentum repulsive (attractive) polaron, adapted from Ref. [109]. (b) Linearity of the coupling strength Ω_0 and the measured frequency Ω at $\ln(\kappa_F a_{2D}) = -0.57(5)$ (repulsive polaron, blue circles) and $2.22(6)$ (attractive polaron, red squares). The dashed gray line indicates the weighted average of the individual data points.

[†] The empty markers in Ref. [109] slightly deviate from the results shown above since the weight function differs.

along with the experimental value $(\Omega/\Omega_0)^2$ decrease towards the strongly interacting regime at $\ln(\kappa_F a_{2D}) = 0$ for both polaron branches. For the attractive polaron, we generally find an excellent agreement between experiment and theory, confirming that the Rabi oscillations are indeed suitable for the measurement of the quasiparticle residue. In contrast, the experimental values for the repulsive polaron are systematically shifted by up to ~ 0.2 when compared to the theoretical prediction. For the experimental measurement, a systematic error in determining the polaron energy or the particularly strong damping of the oscillation on the repulsive side could potentially explain the disagreement [see Fig. 3.11(a)]. On the other hand, the theoretical description neglects the finite interaction strength in the initial state, which increases the overlap with the repulsive polaron and could cause a sizable correction of $(\Omega/\Omega_0)^2$. In the following, we provide a simple estimate for the maximum deviation expected from the weakly interacting polaron in the initial $|g\rangle$ state with residue $Z_i = 0.98$. Considering an arbitrary phase of the incoherent background, we can estimate a minimum and maximum overlap of the initial $|\Psi_i\rangle$ and polaron wave function $|\Psi_P\rangle$ [109],

$$|\langle \Psi_i | \Psi_P \rangle| \stackrel{\leq}{\approx} \sqrt{Z_i Z_P} \pm \sqrt{(1 - Z_i)(1 - Z_P)} \approx \sqrt{Z_P} \pm \sqrt{(1 - Z_i)(1 - Z_P)}, \quad (3.17)$$

where the last approximation holds since $\sqrt{Z_i} = 0.99 \approx 1$. The estimated maximum overlap provides an upper bound for the measured value of $(\Omega/\Omega_0)^2$ and takes the value $\approx Z + 0.1$

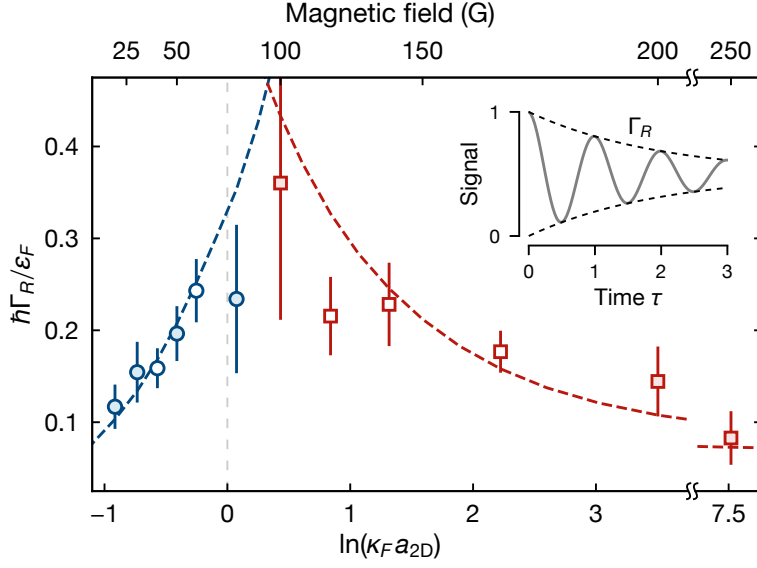


Figure 3.13 | Quasiparticle damping of the multiorbital Fermi polaron. Quasiparticle damping Γ_R extracted from numerical fits of Rabi oscillations (see inset schematic). The blue circles show the extracted values for the repulsive polaron, and the red squares correspond to the attractive polaron. Empty markers indicate weighted averages[†] from two or three separate measurements with variable drive strength at the same magnetic field, and error bars indicate the fit error. The blue dashed line shows the finite-temperature theoretical prediction for the damping of the repulsive polaron, adapted from Ref. [109]. The red dashed line corresponds to $(1 - Z) + c$ with quasiparticle residue Z of the attractive polaron and fit parameter $c = 0.06(2)$. Note that the experimental measurement is generally limited to $\hbar\Gamma_R/\epsilon_F \gtrsim 0.02$ by the typical dephasing of single-particle Rabi oscillations.

[†] The empty markers in Ref. [109] slightly deviate from the results shown above since the weight function differs.

across the relevant range of interaction parameters. Thus, we conclude that the initial state interaction could indeed contribute to the disagreement between experiment and theory on the repulsive side.

The strong drive $\hbar\Omega_0$ comparable to the Fermi energy ϵ_F can pose another potential concern. In principle, the response of the system can be significantly altered, and we explore such an effect by applying variable single-particle Rabi frequencies Ω_0 at the same interaction parameter, as shown in Fig. 3.12(b). In this measurement, we probe the repulsive polaron at $\ln(\kappa_F a_{2D}) = -0.57(5)$ as well as the attractive polaron at $\ln(\kappa_F a_{2D}) = 2.22(6)$ and do not observe a systematic non-linearity within our experimental error bars. This implies that the Rabi oscillation response of the system remains linear for the employed drive strength in the range $0.9\epsilon_F \leq \hbar\Omega_0 \leq 1.7\epsilon_F$.

3.4.2 Damping of the repulsive polaron

The numerical fits of the Rabi oscillations also yield the damping Γ_R , which strongly increases towards the regime of strong interactions at $\ln(\kappa_F a_{2D}) \sim 0$, as can be seen in Fig. 3.13. We first briefly comment on the damping on the attractive side, where a simple description from Ref. [109] appears to capture the physics in the experiment accurately. For this purpose, we as-

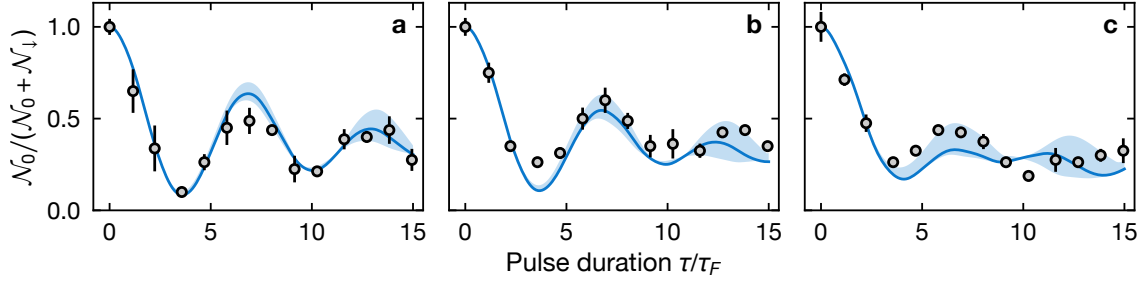


Figure 3.14 | Numerical simulations of Rabi oscillations in the repulsive branch. Comparison of experimental data (black circles) and theoretical calculation of the real-time dynamics (blue lines) within the truncated basis method for interaction parameters (a) $\ln(\kappa_F a_{2D}) = -0.73$, (b) -0.57 , and (c) -0.25 and Fermi time $\tau_F = \hbar/\varepsilon_F = 45(5) \mu\text{s}$. Here, \mathcal{N}_0 and \mathcal{N}_1 correspond to the number of particles in $|g \uparrow\rangle$ and $|g \downarrow\rangle$, where the latter is estimated from $\mathcal{N}_1(\tau) \approx \mathcal{N}_0(0) - \mathcal{N}_0(\tau)$. Error bars indicate the standard error of the mean, and the blue-shaded area corresponds to the estimated experimental uncertainty of the polaron energy. The experimental data has been modified to compensate for an estimated constant offset of ≈ 0.2 from a spurious signal [110]. The theoretical curves and adjusted experimental data points are adapted from Ref. [110] and have been kindly provided by H. S. Adlong.

sume that the Rabi drive couples the initial state not only to the attractive polaron but also to the incoherent continuum of states with weight $\sqrt{1-Z}$. Solving the resulting three-level system with dissipative coupling to the continuum [109] yields the damping rate $\hbar\Gamma_R/\varepsilon_F \sim (1-Z)$. This relation agrees reasonably well with the experimental data on the attractive side, considering a constant offset (see Fig. 3.13).

We now turn to the damping of the repulsive polaron, which increases monotonously from $\hbar\Gamma_R/\varepsilon_F \approx 0.1$ at $\ln(\kappa_F a_{2D}) \approx -1$ to ≈ 0.25 in the strongly interacting regime. In Fig. 3.13, we show the experimentally determined damping together with the quasiparticle width Γ from the theoretical T-matrix calculation, which agrees almost perfectly with the experimental data. Previously, the quasiparticle width Γ has been commonly associated with the lifetime of the repulsive polaron against decay into lower-lying states, i. e., the attractive polaron or molecule [66]. However, this lifetime far exceeds the inverse damping, as we will show in the following section. Notably, earlier observations in a 3D Fermi gas of ${}^6\text{Li}$ atoms [76] have found a similar agreement between the experimental measurement of the Rabi oscillation damping and the theoretically determined quasiparticle width.

Subsequent to both experimental measurements, a novel theoretical approach for modeling the real-time dynamics at finite temperatures has been applied to the problem [110]. This approach, known as truncated basis method (TBM) [205], considers a truncation of the Hilbert space at a fixed number of particle-hole excitations. In this truncated Hilbert space, a variational approach similar to the one for the polaron energy can be extended to the time-dependent case. To this end, the Heisenberg picture introduces the time dependence of operators with $\hat{c}_\sigma^\dagger(\tau) = e^{i\hat{\mathcal{H}}\tau} \hat{c}_\sigma^\dagger e^{-i\hat{\mathcal{H}}\tau}$. Here, the Hamiltonian $\hat{\mathcal{H}}$ describes the time evolution of the system, i. e., after turning on the Rabi coupling. The time propagation of an initial state is then determined by considering the expectation value of the error quantity $\delta_\varepsilon(\tau) = i\partial_t \hat{c}_\sigma^\dagger(\tau) - [\hat{c}_\sigma^\dagger(\tau), \hat{\mathcal{H}}]$ [197]. Variational techniques can minimize the error quantity yielding the approximate evolution of time-dependent observables such as $\mathcal{N}_0(\tau)$.

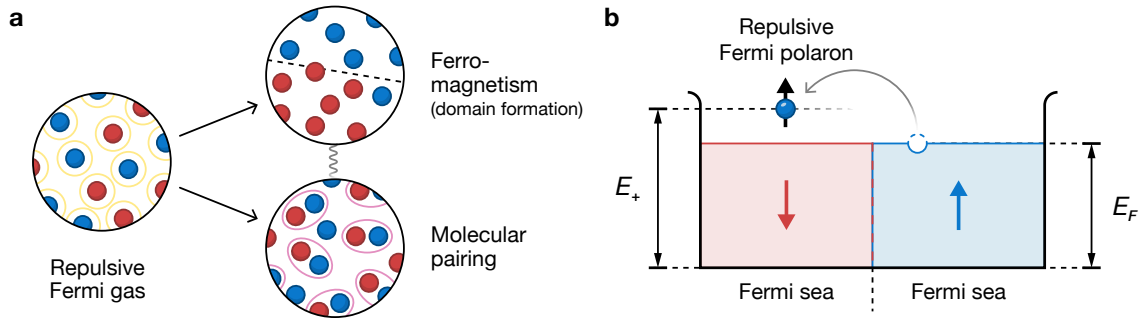


Figure 3.15 | Itinerant ferromagnetism in ultracold Fermi gases. (a) Illustration of competing processes in repulsively interacting Fermi gases with short-range interactions, namely, the formation of spin-polarized domains (ferromagnetism) and molecular pairing. (b) Schematic analysis for the stability of a spin-polarized \uparrow -domain (blue) by considering a particle (blue circle) hopping from the top of the Fermi sea across the domain border into the region of the \downarrow -domain (red).

The numerical simulations of the Rabi oscillations from Ref. [110] are shown in Fig. 3.14. The decay of the repulsive polaron into lower-lying states at negative energies is not captured by this approach since it involves more than a single particle-hole excitation. Therefore, the agreement of theory and experiment strongly suggests that coupling to a quasi-continuum of repulsive polaron states at positive energies dominates the damping of the Rabi oscillations. In particular, this implies that the quasiparticle width Γ does not determine the decay rate to lower-lying states as previously assumed [66]. As an intuitive picture, the finite width of the repulsive branch can be viewed as the result of a series of states at slightly different energies, which consequently dephase when driven. This contrasts with the spectral properties of the attractive polaron described by a Dirac delta distribution at zero temperature. Generally, the lifetime of the repulsive branch against decay into lower-lying states exceeds the time scale over which the repulsive polaron stays a coherent quasiparticle. The two distinct processes, dephasing and decay, can be probed independently in the experiment, either with Rabi oscillations or a double-pulse measurement, which we discuss in the next section.

3.5 Decay of the repulsive branch

The stability of the repulsive Fermi polaron against decay into lower-lying states has direct relevance for the stability of itinerant ferromagnetism in fermionic systems with short-range interactions [80, 81]. Itinerant ferromagnetism, also known as *Stoner magnetism* [206], describes the instability of a repulsively interacting Fermi gas against the formation of spin-polarized domains [see Fig. 3.15(a)]. At a phase boundary of two domains, the hopping of a particle or repulsive polaron is energetically suppressed if its interaction energy E_+ exceeds the Fermi energy ϵ_F [see Fig. 3.15(b)]. To stabilize a ferromagnetic phase, we expect that the energy of the repulsive Fermi polaron has to exceed the Fermi energy of the domain, $E_+ \ll \epsilon_F$. Moreover, the lifetime $1/\Gamma_{\text{rep}}$ of the repulsive Fermi polaron has to be large compared to the Fermi time $\tau_F = \hbar/\epsilon_F$, which sets the dynamical time scale of domain formation.

So far, an experimental realization of itinerant ferromagnetism in cold atomic systems with an unambiguous signature has remained elusive—despite an early observation of potential signatures [207]. However, these have later been attributed to the formation of molecular pairs [208, 209]. For the short-range interactions in ultracold atomic gases, the underlying molecular interaction potential has an attractive nature, and repulsively interacting atomic pairs can decay into the near-threshold molecular bound state. This process naturally competes with the formation of spin-polarized domains and fundamentally hinders the observation of itinerant ferromagnetism once atoms start to decay into molecular pairs. A recent study has chosen a novel approach by first preparing spin-polarized domains with an optical barrier and probing their stability, which has enabled the observation of a metastable phase at intermediate times [210].

Experimental measurement.—To probe the decay of the repulsive polaron into lower-lying states, we employ a double-pulse technique similar to the one from previous experiments with alkali atoms [73, 74, 76]. The experimental sequence for this measurement is almost identical to the Rabi oscillations, but we employ a sequence of two clock pulses with a variable hold time in-between. The frequency of both pulses is chosen to match the energy of the repulsive polaron and the pulse duration corresponds to a π -pulse of a free particle. We choose a particularly strong drive strength $\hbar\Omega_0 \approx 0.8\epsilon_F$ to also address the repulsive polaron branch with its finite width $\sim \epsilon_F$ in the strongly interacting regime. Immediately after the first clock pulse, any remaining atoms in the state $|g 0\rangle$ are removed with resonant “push” pulses⁴ on the intercombination line (two subsequent “push” pulses with a duration of $20 \mu\text{s} + 50 \mu\text{s} = 70 \mu\text{s} \sim \tau_F$). The removal ensures that the second clock pulse can transfer the repulsive polarons in $|e \downarrow\rangle$ back to the $|g 0\rangle$ state without simultaneously addressing potentially remaining atoms in $|g 0\rangle$. After the variable hold time and the second clock pulse, we remove the Fermi sea with an additional resonant “push” pulse (duration $100 \mu\text{s}$). This enables us to detect the number of atoms \mathcal{N}_0 transferred back to the initial $|g 0\rangle$ state.

Figure 3.16(a) depicts the time traces for variable hold time between the two pulses. Across the probed interaction parameters $-1 < \ln(\kappa_F a_{2D}) < 0.25$, we find an exponential decay of the detected number of $|g 0\rangle$ state atoms indicating a continuous loss of the repulsive polarons. From the time traces, we extract a decay rate Γ_{rep} by fitting the experimental data with an exponential decay,

$$\mathcal{N}_0(\tau) = ae^{-\Gamma_{\text{rep}}\tau} + c, \quad (3.18)$$

where a denotes the amplitude and c an offset. In general, we find a fast initial decay and a nearly constant offset $c > 0$ at late times—in agreement with previous measurements employing alkali atoms [74]. In our case, however, this offset strongly depends on the interaction parameter [see Fig. 3.16(a)], which could originate from the finite spin-exchange coupling at low fields.

⁴This technique is slightly modified from the procedure discussed in Section 3.2 as the removal of the $m_F = -3/2$ component requires an additional pulse. This pulse initially transfers atoms to the $m_F = -5/2$ ground state, where the continuous scattering of photons becomes possible on the closed $m_F = -5/2 \rightarrow m_F = -7/2$ intercombination line between the $F = 5/2$ and $F = 7/2$ manifolds. To allow for a fast successive pulse sequence, we use a separate laser beam with rapid frequency switching enabled by a double-passed acousto-optic modulator.

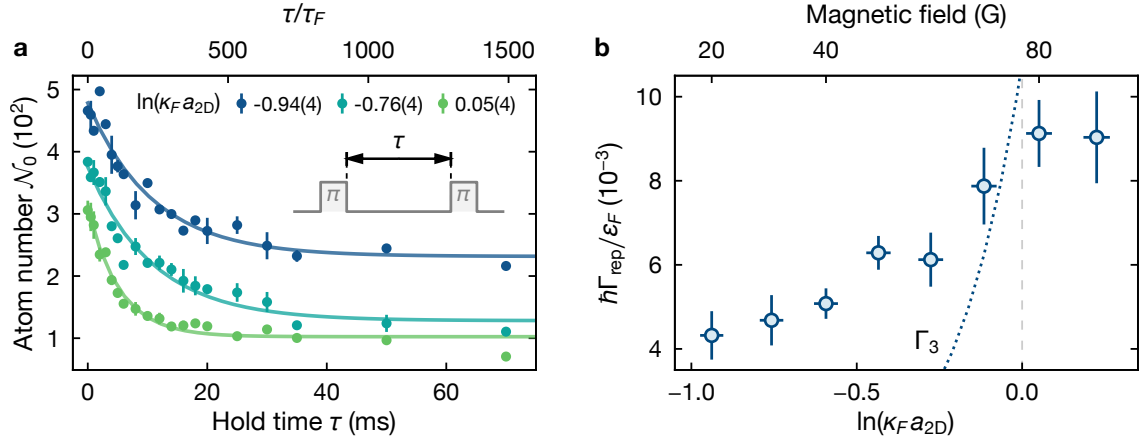


Figure 3.16 | Decay rate of the repulsive Fermi polaron. Measurement of the lifetime in the repulsive branch for experimental parameters $\epsilon_F = 3.4(2)$ kHz, $k_B T/\epsilon_F = 0.14(3)$, and (effective) minority fraction $0.31(1)$. (a) Number of atoms (circles) transferred back to the initial state $|g 0\rangle$ for variable hold time τ and three interaction parameters (see legend). The error bars indicate the standard error of the mean, and solid lines correspond to numerical fits of an exponential function, as given in Eq. (3.19). The inset illustrates how the hold time is defined in the double-pulse sequence, and the top axis indicates the hold time in units of the Fermi time scale $\tau_F = \hbar/\epsilon_F$. (b) Decay rate Γ_{rep} (blue circles) extracted from the fits shown in panel (a). The error bars indicate the fit error of Γ_{rep} and experimental uncertainty of $\ln(\kappa_F a_{2D})$. The dotted line denotes the estimate of the three-body recombination rate Γ_3 (see main text).

This process could populate the otherwise unoccupied $m_F = -5/2$ ground state, which would appear as a constant offset since the absorption imaging does not resolve individual m_F states. The observed monotonous decrease of $\mathcal{N}_0(\tau = 0)$ for increasing interaction strength is most likely caused by a combination of a reduced coupling strength $\Omega/\Omega_0 \sim \sqrt{Z} < 1$ and the constant pulse duration $2\pi/\Omega_0$. The extracted decay rates Γ_{rep} as a function of $\ln(\kappa_F a_{2D})$ are shown in Fig. 3.16(a). The particularly small decay rates of the multiorbital repulsive Fermi polaron, also in comparison to previous work [74], might provide a favorable starting point for the investigation of strongly repulsive Fermi gases and itinerant ferromagnetism [211]. Crucially, Γ_{rep} is more than an order of magnitude below the quasiparticle damping Γ extracted from the self-energy of the Fermi polaron. This confirms the key point discussed in Section 3.4.2, namely, that the quasiparticle width Γ describes the many-body dephasing and not the decay into lower-lying states, which we have probed in this section.

3.5.1 Three-body recombination

A possible decay channel for the repulsive polaron is the three-body recombination into a molecular bound state and a third atom from the Fermi sea absorbing the excess momentum ($\downarrow + \uparrow + \uparrow \rightarrow \downarrow\uparrow + \uparrow$). In three dimensions, the rate of this process was found to match the experimentally obtained repulsive polaron decay rates over a significant range of interaction strengths [76]. The three-body recombination rate $K_3(E)$ has been determined for a purely two-dimensional (2D) geometry in Ref. [212] and is a function of the collisional energy E . Here,

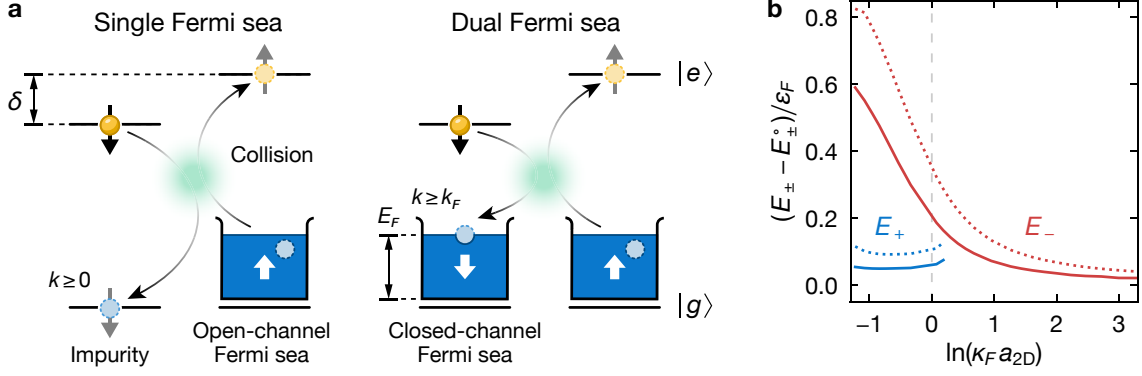


Figure 3.17 | Frustrated interactions at the orbital Feshbach resonance. (a) Schematic illustrating Pauli blocking of the spin-exchange process between an impurity atom in $|e, \downarrow\rangle$ and Fermi sea in $|g, \uparrow\rangle$ (open channel). (b) Expected shifts $(E_{\pm} - E_{\pm}^{\circ})$ of the repulsive (solid blue line) and attractive (solid red line) quasiparticle energies relative to the single Fermi sea configuration for $\epsilon_F^{\downarrow} \approx 0.94\epsilon_F \approx h \times 3$ kHz. Dotted lines show the shift for twice the closed-channel Fermi energy.

we neglect the (small) kinetic energy of the impurity, the finite number of impurities, and model the resulting decay due to three-body recombination as [212]

$$\frac{dn_{\downarrow}}{dt} = n_{\downarrow} [n_{\uparrow}^2 K_3(E)] = n_{\downarrow} \Gamma_3. \quad (3.19)$$

This equation implicitly defines $\Gamma_3 = n_{\uparrow}^2 K_3(E)$ as the decay rate for the impurity density n_{\downarrow} under the assumption of a constant medium density n_{\uparrow} (small minority fraction). The parameter Γ_3 is a function of the interaction parameter as well as the local medium density. We calculate this rate by averaging over the background density of the majority Fermi sea, using the local kinetic energy and local Fermi wave vector (see Section 3.2.1). We show the results for the expected three-body recombination rate in a purely 2D geometry in Fig. 3.16(a). However, the theoretical predictions fail to accurately capture the experimental data apart from a crossing of experiment and theory curves at $\ln(\kappa_F a_{2D}) \sim 0$. The overall significant disagreement can most likely be attributed to the incorrect geometry of the model as the quasi-2D geometry is expected to significantly change the collisional physics (see Section 2.3 in Chapter 2). Future theoretical investigations of the three-body recombination rate in quasi-2D might provide a better understanding of the decay channels for the specific geometry of our experiment.

3.6 Frustrated interactions

The presence of frustration in many-body systems can lead to rich physics, such as in the case of certain heavy fermion compounds. These types of materials feature a quantum critical point located between a magnetically ordered phase and a heavy Fermi liquid phase [143]. Once geometrical frustration is introduced, the interactions causing long-range spin correlations are hindered. Remarkably, this can give rise to an extended critical phase qualitatively different from a single critical point [213].

Interestingly, the orbital Feshbach resonance in ^{173}Yb also provides the opportunity to probe a form of frustration in quantum many-body systems, i. e., the introduction of Pauli blocking or frustration in the interaction channels [109, 214]. In particular, we consider the Fermi polaron in the presence of two Fermi seas, one in the open and another in the closed channel, as illustrated in Fig. 3.17(a). For a two-body collision, the spin-exchange process becomes Pauli blocked up to the Fermi energy ϵ_F^\dagger in the closed channel. For the simultaneous occupation of both the open and closed channel, the effective two-channel model from Chapter 2 (see Section 2.3.2) is not suitable, and we have to adapt the many-body T-matrix formalism. The in-medium or many-body T-matrix for a zero-momentum impurity takes the form [109]

$$\mathbf{T}(\mathbf{k}, E) = \left\{ \left(\mathbf{T}^{(\text{vac})} [E - \hbar^2 k^2 / (4m)] \right)^{-1} + \begin{pmatrix} \Delta\Pi_o(\mathbf{k}, E) & 0 \\ 0 & \Delta\Pi_c(\mathbf{k}, E - \delta) \end{pmatrix} \right\}^{-1} \quad (3.20)$$

with the vacuum T-matrix $\mathbf{T}^{(\text{vac})}$ from Chapter 2 [see Eq. (2.23)]. Here, the diagonal terms account for the occupation in the open and closed channel [109],

$$\Delta\Pi_\sigma(\mathbf{k}, E) = \sum_{\mathbf{q}} \frac{F_\sigma(\mathbf{q})}{E - \hbar^2/(2m) [\mathbf{k}^2 - \mathbf{q}^2 - (\mathbf{k} - \mathbf{q})^2] + i\varepsilon}, \quad (3.21)$$

with the small imaginary part parameterized by $\varepsilon > 0$. The Fermi-Dirac distribution $F_\sigma(\mathbf{q}) = \{1 + e^{\beta[\hbar^2 q^2 / (2m) - \mu_\sigma]}\}^{-1}$ and chemical potential μ_σ describe the occupation of momentum states at medium temperatures $T = 1/(k_B \beta)$ in the open ($\sigma = o$) and closed channel ($\sigma = c$), respectively. With this result, the self-energy of the zero-momentum Fermi polaron in the open channel can be obtained from [109]

$$\Sigma(E) = \sum_{\mathbf{k}} F_o(\mathbf{k}) \langle o | \mathbf{T}(\mathbf{k}, E) | o \rangle. \quad (3.22)$$

Here, the T-matrix has been projected onto the open channel $|o\rangle$. Note that a finite occupation in the closed channel corresponds to a non-vanishing $\Delta\Pi_c(\mathbf{k}, E)$, which leads to a change of the quasiparticle properties. Figure 3.17(b) shows the expected shift of the polaron energy for variable interaction strength and Fermi energy in the closed channel. In particular, a shift of the repulsive polaron branch to energies exceeding ϵ_F could be relevant for stabilizing a ferromagnetic phase in a multiorbital quantum gas.

We realize the dual Fermi sea configuration by initially populating the state $|g \downarrow\rangle \equiv |g, m_F = -5/2\rangle$ with a second majority Fermi sea in addition to minority and majority components in $|g 0\rangle$ and $|g \uparrow\rangle$, respectively. This is achieved by modifying the optical pumping sequence to yield an approximate ratio of 4:1:4 between the populations of the three states.

3.6.1 Fermi-liquid description of the medium

The interaction in the ground state is repulsive and the additional Fermi sea modifies the medium density (Section 3.3.1). We estimate the reduced density by modeling the dual Fermi sea configuration as a weakly interacting repulsive Fermi liquid in two dimensions [215]. To

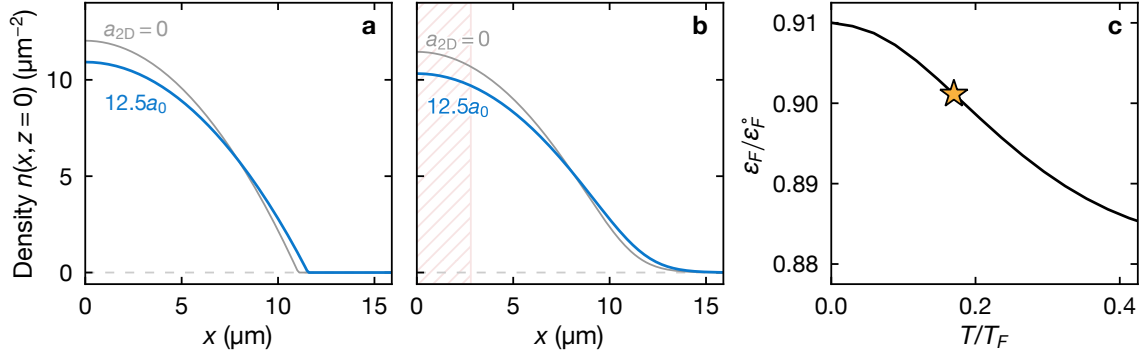


Figure 3.18 | Repulsive Fermi liquid in the ground state. Numerically determined in-plane density and effective Fermi energy of a two-component ground state mixture in the presence of finite interactions and temperature. Parameters are chosen to match typical experimental values in a single-layer with atom number $N = 600$ per nuclear spin state. Comparison of the (a) zero-temperature and (b) finite-temperature ($T/T_F = 0.17$) density along the x -axis for zero (gray) and finite interaction strength (blue). The red hatching indicates the extent of the region typically considered in the experiment ($\Delta x = 5.6 \mu\text{m}$). (c) Effective Fermi energy of the repulsive Fermi liquid with $a_{2D} = 12.5a_0$ for the integration of $x \in [-\Delta x/2, \Delta x/2]$ [central region, see panel (b)] and along the z -axis. Here, ϵ_F^o corresponds to the effective Fermi energy without interactions ($a_{2D} = 0$).

this end, we combine the second-order perturbative expansion of the chemical potential for repulsive interactions [216] and the temperature dependence of the chemical potential in the absence of interactions [202],

$$\mu \approx k_B T \left[1 + 2g + 4g^2(1 - \ln 2) \right] \times \ln \left[e^{E_F/(k_B T)} - 1 \right]. \quad (3.23)$$

Here, T denotes the temperature and the coupling constant $g > 0$ is related to the bound-state energy ϵ_b and Fermi energy E_F by [216]

$$g = \frac{1}{\ln [\epsilon_b / (2E_F)]} = \frac{1}{\ln 2 - 2 \ln (k_F a_{2D})}. \quad (3.24)$$

For the approximate interaction parameter $\ln (k_F a_{2D}) \approx -4.9$ in the ground state, we find $g \approx 0.1$. To account for the inhomogeneous density in the experiment, we apply the local density approximation $\mu(\mathbf{r}) = \mu_0 - U(\mathbf{r})$ for the harmonic trapping potential $U(\mathbf{r})$ given in Eq. (3.1). Here, a dependence of Eq. (3.23) on the local density is introduced by replacing all relevant quantities with their local equivalent forms, e. g., $E_F \rightarrow E_F(\mathbf{r}) = \hbar^2 / (2m) \times [4\pi n(\mathbf{r})]$. The implicit equation for the local density $n(\mathbf{r})$ can be solved numerically at a fixed atom number N by imposing the condition $\int d\mathbf{r} n(\mathbf{r}) = N$.

Figure 3.18 shows the comparison of non-interacting and interacting density at zero and finite temperature. As naively expected, we find a reduction of the density at the center of the trap and an overall increased width of the distribution. For the dual Fermi sea configuration in the experiment, we estimate the effective Fermi energies $\epsilon_F^\downarrow = h \times 2.7(2)$ kHz and $\epsilon_F^\uparrow \equiv \epsilon_F^\dagger = h \times 3.0(2)$ kHz, which are reduced by approximately 10% due to the finite interactions in the ground state [see Fig. 3.18(c)].

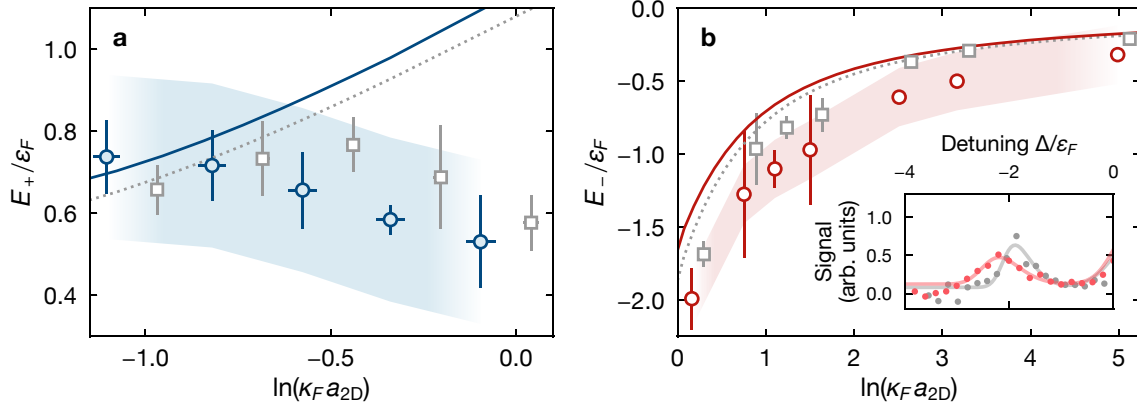


Figure 3.19 | Multiorbital Fermi polaron in the frustrated regime. Energies E_{\pm} of the (a) repulsive (blue circles) and (b) attractive (red circles) Fermi polaron for variable interaction parameter $\ln(\kappa_F a_{2D})$, extracted from spectra recorded in the presence of two Fermi seas [$\varepsilon_F = h \times 3.0(2)$ kHz and $\varepsilon_F^{\perp} = h \times 2.7(2)$ kHz]. The gray squares correspond to the reference measurement without a second Fermi sea [$\varepsilon_F = h \times 3.2(2)$ kHz]. Error bars, partly smaller than the marker size, indicate the fit error of the energy and uncertainty of the interaction parameter. The experimental data is shifted by the estimated initial state interaction energy $0.2\varepsilon_F$ (single Fermi sea). We show the range of $\pm 0.2\varepsilon_F = \pm E_{\pm}^0$ for the dataset with a second Fermi sea as light blue and red bands. Solid blue and red (dotted gray) lines show the theoretical prediction from Ref. [109] for the quasiparticle energies with (without) a second Fermi sea. The inset in panel (b) shows spectra of the attractive polaron for single (gray) and dual (red) Fermi sea configurations at the magnetic field $B = 90$ G, corresponding to $\ln(\kappa_F a_{2D}) = 0.30(2)$ [0.16(4)].

3.6.2 Quasiparticle energies with two Fermi seas

Experimentally, we probe the Fermi polaron in the frustrated regime with the same technique as in the case of a single-component medium (see Section 3.3). We compare the measured spectra with the results from Section 3.3.3 for variable interaction parameters. In the measured spectra, we can still identify two well-defined quasiparticle branches that correspond to the repulsive and attractive Fermi polaron. To compare the experimental results to the theoretical predictions, we extract the quasiparticle energies from the spectra with numerical fits, as shown in Fig. 3.19. For the repulsive branch, however, we do not find any significant deviation between the two configurations. In contrast, for the attractive polaron and interactions $\ln(\kappa_F a_{2D}) < 4$, we find a small shift $\approx 0.2\varepsilon_F$ towards higher energies, which would be inconsistent with the theoretically expected decrease [see Fig. 3.17(b)]. Yet the observed shifts are on a similar scale as our experimental resolution or the Fermi energy corrections, which account for the two-component medium. Moreover, we have not considered any change of the initial state in the presence of a second Fermi sea. For this weakly repulsive polaron, we also expect a modified quasiparticle energy due to simultaneous interactions with both Fermi seas. We explore such an effect by considering the range $[E_{\pm}, E_{\pm} + 2E_{\pm}^0]$ for a potential change of the initial state interaction energy (see Fig. 3.19). This shows that a significant increase of the initial state interaction could indeed explain the apparent disagreement between experiment and theory in the frustrated regime. We finally note that we have also probed the quasiparticle residue and lifetime of the repulsive polaron, which qualitatively agree with the results obtained for a single Fermi sea medium [109].

3.7 Discussion

In this chapter, we have systematically studied the Fermi polaron in two dimensions and presented direct measurements of its signatures in a multiorbital mixture of ^{173}Yb atoms. Importantly, the observed attractive and repulsive polaron branches agree well with the theoretical predictions from a many-body T-matrix calculation and the equivalent two-channel model. We have also probed a novel regime of the multiorbital polaron by introducing a second Fermi sea in the closed channel. While our current experimental capabilities do not allow us to confirm or refute the predicted energetic shifts of the quasiparticle branches, we still find well-defined quasiparticles in this regime.

In future experiments, it would be particularly interesting to study the dual Fermi sea configuration with either larger Fermi energies in the closed channel or a more precise measurement technique. The latter is now within reach as our experiment has recently been upgraded to prepare and image a single quasi-two-dimensional layer [217]. In contrast to the experimental realization discussed in this chapter, the intrinsic integration of the absorption imaging across an inhomogeneous region can be eliminated in this new configuration. Therefore, a much narrower distribution of local Fermi energies $\epsilon_F \pm \Delta\epsilon_F$ can be probed. Moreover, the direct measurement of the in-plane density eliminates the requirement to rely on a theoretical model for the weakly repulsive Fermi liquid in the ground state. This could significantly reduce the error bars and consequently allow an unambiguous statement about the shifts observed in the experiment and how they compare to the theoretical predictions.

CHAPTER 4

Absence of thermalization in quantum many-body systems

In this chapter, we discuss quantum many-body systems that evade the fate of thermalization and ergodic dynamics. First, we give a brief overview of a general theoretical concept to describe thermalization and relaxation in isolated quantum systems. Next, we focus on localization phenomena in disordered models, which exhibit broken ergodicity and an absence of thermalization for arbitrary long observation times. Following this overview, we consider a dynamical form of localization in translationally invariant binary mixtures without static disorder. To set the stage for our experimental realization of a mass-imbalanced mixture presented in Chapter 5, we introduce a specific system of this kind, namely the mass-imbalanced Fermi-Hubbard model. Following previous theoretical work, we numerically study the evolution of long-wavelength density modulations in this system, which allow us to reveal regimes of extremely slow relaxation. The key theoretical findings presented in this chapter are discussed along our experimental work in Ref. [108].

4.1 Thermalization in isolated quantum systems

The absence or presence of thermalization in a many-particle environment determines how and whether a system equilibrates. Once thermal equilibrium is reached, any memory of an initial state is erased, and we can describe it with the laws of statistical mechanics. Key properties then become independent of an initial microscopic state and its intricate details are rather determined by a few macroscopic parameters such as the total energy and particle number [218]. While thermalization for the canonical ensemble can be intuitively understood via energy exchange with a bath, the situation seems more subtle for the microcanonical ensemble. How does an isolated quantum system thermalize, and can we robustly decide when the laws of statistical physics apply? These questions are of elementary importance for understanding the success of statistical mechanics in the description of many-body systems.

Thermalization and its absence in isolated quantum systems have seen renewed interest in the last decades (see, e. g., Ref. [219]). However, analytical methods are only available for few models and numerical methods are typically limited to modest particle numbers or short evolution times. In contrast, multiple emerging experimental platforms now allow

probing isolated quantum systems for relatively long observation times, well outside the regime accessible with numerical simulations. In particular, ultracold atoms in optical lattices offer unprecedented control over the relevant parameters, such as the interaction strength governing the dynamical evolution [1]. Quantum simulation experiments on this versatile platform now provide unique opportunities to study thermalization in the regime of quantum mechanics.

4.1.1 Eigenstate thermalization

At first glance, we expect the mechanisms governing quantum thermalization to be fundamentally different from the classical counterpart since the Schrödinger equation dictates a linear time evolution for quantum states. This behavior strongly deviates for classical systems where dynamical chaos provides a mechanism to transform an arbitrary initial state into a generic thermal state at late times [219]. Nevertheless, experiments demonstrate that thermalization can be observed in isolated quantum systems—even for small system sizes, such as a chain of six interacting bosons [220]. Another illustrative example is evaporative cooling, an integral part of many experiments with ultracold atoms since the first condensation of a degenerate Bose gas [221–223]. Theoretical modeling of this cooling process shows that a few collisions per particle suffice to reach thermal equilibrium after removing part of the initial population from the trap [224].

In the following, we explain how the eigenstate thermalization hypothesis (ETH), first put forward by Deutsch and Srednicki [8, 9], provides a possible generic mechanism for the emergence of thermalization in isolated quantum systems. We emphasize that our discussion of this matter is neither complete nor rigorous but rather serves illustrative purposes and establishes a notion for the phenomenology of ergodic quantum dynamics. Starting with a realistic experimental setting, we consider preparing the pure state $|\Psi_0\rangle$ of an isolated system. This state evolves according to a stationary Hamiltonian $\hat{\mathcal{H}}$ with a finite number of discrete eigenenergies $\{\epsilon_n\}_n$ and orthonormal eigenstates $\{|\psi_n\rangle\}_n$,

$$|\Psi(t)\rangle = e^{-it\hat{\mathcal{H}}/\hbar} |\Psi_0\rangle = \sum_n \alpha_n e^{-i\epsilon_n t/\hbar} |\psi_n\rangle. \quad (4.1)$$

Here, $\alpha_n = \langle \psi_n | \Psi_0 \rangle$, and for simplicity, we assume that the spectrum of $\hat{\mathcal{H}}$ is non-degenerate ($\epsilon_n \neq \epsilon_m$ for $n \neq m$). With the above results, the expectation value of the observable O is simply given as

$$\langle O \rangle_t = \langle \Psi(t) | O | \Psi(t) \rangle = \sum_{m,n} \alpha_m^* \alpha_n e^{i(\epsilon_m - \epsilon_n)t/\hbar} \langle \psi_m | O | \psi_n \rangle. \quad (4.2)$$

The last term in this equation corresponds to the matrix elements $O_{mn} = \langle \psi_m | O | \psi_n \rangle$ of the observable in the stationary basis of the Hamiltonian. For long observation times, we expect the off-diagonal matrix elements to dephase as described by the following infinite-time average

$$\overline{\langle O \rangle} = \lim_{T \rightarrow \infty} \frac{1}{T} \int_0^T dt \langle O \rangle_t = \sum_n |\alpha_n|^2 O_{nn}. \quad (4.3)$$

While the existence of this quantity would indicate that a system equilibrates, we still have to establish whether this limit can coincide with thermal equilibrium. To this end, we consider the prediction of the expectation value within the microcanonical ensemble,

$$\langle O \rangle_{(\text{mc})} = \frac{1}{\mathcal{N}_{\langle E \rangle}} \sum_{n: \epsilon_n \in \Gamma_{\langle E \rangle}} O_{nn}. \quad (4.4)$$

The microcanonical ensemble is defined by a thin energy shell $\Gamma_{\langle E \rangle} = [\langle E \rangle, \langle E \rangle + \Delta E]$ containing $\mathcal{N}_{\langle E \rangle}$ states, and with the initial state $|\Psi_0\rangle$ fixing the total energy $\langle E \rangle = \langle \Psi_0 | \hat{\mathcal{H}} | \Psi_0 \rangle$. Combining the above results yields the relation

$$\sum_n |\alpha_n|^2 O_{nn} = \frac{1}{\mathcal{N}_{\langle E \rangle}} \sum_{n: \epsilon_n \in \Gamma_{\langle E \rangle}} O_{nn}. \quad (4.5)$$

Here, the left-hand side of the equation depends on the details of the initial state via α_n , whereas the right-hand side only depends on the expectation value of the energy $\langle E \rangle$ in the initial state. As discussed below, this equation has significant consequences for the properties of the eigenstates.

The eigenstate thermalization hypothesis formulates the above equality, which is closely connected to the fact that a single eigenstate of the Hamiltonian contains the complete thermal ensemble and can be understood as follows. For the equality to hold in the case of a generic initial state, we have $O_{nn} \rightarrow \langle O \rangle_{(\text{mc})}$ within the thin energy shell defined by $\Gamma_{\langle E \rangle}$. In the extreme case of only a single eigenenergy E_n contained in $\Gamma_{\langle E \rangle}$ (recall the discrete spectrum of the Hamiltonian), the corresponding eigenstate $|\psi_n\rangle$ fully describes the microcanonical ensemble. Hence, Srednicki established the term *eigenstate thermalization* [9]. An intuitive picture for the emergence of thermalization in the dynamics of $\langle O \rangle_t$ is presented in Ref. [10]: While the thermal nature of the stationary eigenstates must already be present initially, the decoherence of the initial state (dephasing off-diagonal matrix elements) eventually reveals it.

Within the ETH, the matrix elements of local observables have been conjectured to take the form [225]

$$O_{mn} = o\left(\frac{\epsilon_m + \epsilon_n}{2}\right) \delta_{mn} + e^{-S[(\epsilon_n + \epsilon_m)/2]/2} f_O\left(\frac{\epsilon_m + \epsilon_n}{2}, \epsilon_m - \epsilon_n\right) R_{mn}, \quad (4.6)$$

where $o(E)$ and $f_O(E)$ are smooth functions of their argument, S denotes the (extensive) thermodynamic entropy, and R_{mn} is a numerical factor. Crucially, the smoothness of $o(E)$ can be directly associated with the eigenstate thermalization, as illustrated in Fig. 4.1(a). Moreover, the strong suppression of off-diagonal matrix elements for sufficiently large systems and entropies also places bounds the fluctuations of the infinite-time average [225]

$$\overline{(\langle O \rangle_t - \overline{\langle O \rangle})^2} = \lim_{T \rightarrow \infty} \frac{1}{T} \int_0^T dt (\langle O \rangle_t - \overline{\langle O \rangle})^2 \sim e^{-S}, \quad (4.7)$$

which has the important implication that the expectation value of the observable takes a value close to $\overline{\langle O \rangle}$ [and $\langle O \rangle_{(\text{mc})}$] most of the time [see Fig. 4.1(b)]. In this form, the ETH also makes

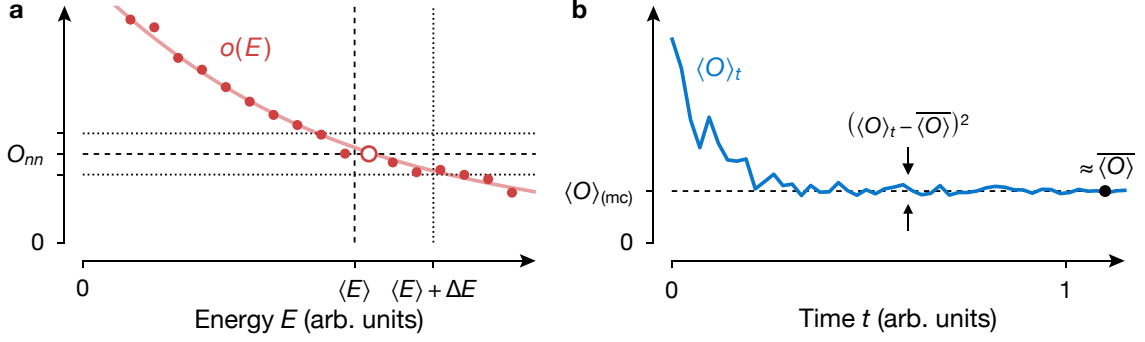


Figure 4.1 | Expectation values of operators within the ETH. Schematic illustrations showing relevant features of observables consistent with the eigenstate thermalization hypothesis (ETH). (a) Function $o(E)$ (red line) describing the nearly smooth behavior of the diagonal ensemble $\{O_{mm}\}_m$ (red circles). Here, the open circle refers to a specific value O_{nn} close to the total energy $\langle E \rangle$, as described by Eq. (4.6). (b) Time-evolution revealing the microcanonical expectation value at late times.

a statement about the dynamical evolution of a system reaching thermal equilibrium from an initial out-of-equilibrium state.

To conclude our brief discussion of the ETH, we state a few important consequences, which we did not explicitly show above but are still relevant for this chapter. First, the ETH implies ergodicity and thermalization, i. e., an isolated quantum system for which the ETH holds, will also exhibit ergodic dynamics [219]. In the upcoming discussions, the terms *ergodic* and *non-ergodic* dynamics are therefore also used to describe thermalization or its absence. Second, it is generally not straightforward to show whether the ETH holds for an arbitrary Hamiltonian and observable—albeit rigorous proofs exist for certain types of systems and local observables [219]. Third, the ETH does not hold for integrable quantum systems as they evade ergodic dynamics through many conserved quantities parameterized by operators $\{P_i\}_i$. In this way, $\langle P_i \rangle \approx \langle P_i \rangle_{(mc)}$ is not necessarily fulfilled. As explored in the next section, certain non-integrable models also feature completely non-ergodic behavior and violate the ETH.

4.2 Evading thermalization

How can isolated quantum many-body systems evade ergodic dynamics and thermalization? Finding answers to this question not only allows us to advance our fundamental understanding of quantum thermalization but could also be highly relevant from a more practical viewpoint. The ever-present decoherence poses a central issue for utilizing many-particle states in quantum sensing or memory applications, and non-ergodicity might offer an elegant way to circumvent such problems. This section introduces possible routes towards non-ergodic dynamics and slow relaxation in quantum many-body systems. In particular, we focus on localization phenomena providing an alternative scenario to thermalization in quantum many-body systems. To this end, we first explore the absence of diffusion for a single particle in a disordered potential—a phenomenon known as Anderson localization. Then, we discuss a similar form of localization persisting in a many-particle environment despite finite interac-

tions, namely many-body localization. Finally, we introduce the emergence of non-ergodic dynamics or extremely slow thermalization in systems without static disorder, i. e., mixtures of heavy and light particles. Motivated by our one-dimensional (1D) experimental system (see Section 5.1.1 in Chapter 5), we exclusively focus on 1D systems. This also aligns with the fact that theoretical descriptions for larger dimensionality are often hindered by the inaccessibility with numerical and analytical methods.

4.2.1 Anderson localization

To start our discussion of localization in many-body systems, we first study how a single particle localizes in a random potential. This problem dates back to Anderson and his seminal work establishing the phenomenon of Anderson localization [226]. The underlying reason for this phenomenon is the destructive interference of the different scattering paths in a random potential landscape, a wave-like phenomenon absent for classical particles. In the following, we consider a single (fermionic) particle hopping on a one-dimensional lattice (tight-binding model) entirely determined by the hopping amplitude t . Besides, each lattice site has a random energy offset ϵ_i uniformly distributed across the interval $[-W, +W]$. The single-particle Hamiltonian for this problem can be written as

$$\hat{\mathcal{H}}_0 = -t \sum_i (\hat{c}_i^\dagger \hat{c}_{i+1} + \text{h.c.}) + \sum_i \epsilon_i \hat{n}_i \quad (4.8)$$

with \hat{c}_i^\dagger and \hat{c}_i the fermionic creation and annihilation operators for a particle on the lattice site labeled with i and $\hat{n}_i \equiv \hat{c}_i^\dagger \hat{c}_i$. Throughout this chapter, we consider systems of finite size such that the sums in Eq. (4.8) and similar following equations are truncated at the system size l . Hopping between neighboring sites becomes off-resonant and significantly suppressed once we introduce strong disorder $W \gg t$. Nevertheless, the higher-order hopping of particles to more distant lattice sites could become relevant once resonances occur for $\epsilon_i \approx \epsilon_j$. It can be rigorously shown that these terms fall off fast enough, and the eigenstates of $\hat{\mathcal{H}}_0$ are localized for any arbitrarily small disorder strength $W/t > 0$ —also in the thermodynamic limit $l \rightarrow \infty$ [227]. Here, the term localization refers to wave functions $\{\psi_n\}_n$ that are finite in some region of space and fall off exponentially at large distance from that region, i. e., $|\langle \psi_n | \hat{n}_i | \psi_n \rangle| \sim e^{-|i-i_n|/\xi}$.

To illustrate the phenomenon of Anderson localization, we perform a “numerical experiment”. In this simulation, we employ exact diagonalization techniques to probe the localized nature of the eigenstates at variable disorder strength W/t with a quantum quench protocol [see Fig. 4.2]. Initially, we prepare the state $|\Psi(\tau = 0)\rangle = \hat{c}_{l/2}^\dagger |0\rangle$, describing a particle localized on the lattice site $i = l/2$ at time $\tau = 0$. Then, the state evolves under the Hamiltonian $\hat{\mathcal{H}}_0$ for multiple hopping times \hbar/t . For vanishing disorder $W = 0$, the wave function expands ballistically in the one-dimensional lattice, as expected for the disorder-free single-particle system. In contrast, for finite disorder strength $W/t = 3$, we can observe a localization over a few central lattice sites—consistent with our earlier discussion of Anderson localization [see Fig. 4.2(b)]. Experimental protocols similar to our simple numerical study have enabled the direct observation of Anderson localization in cold atomic gases [228, 229] following earlier studies in photonic systems [230].

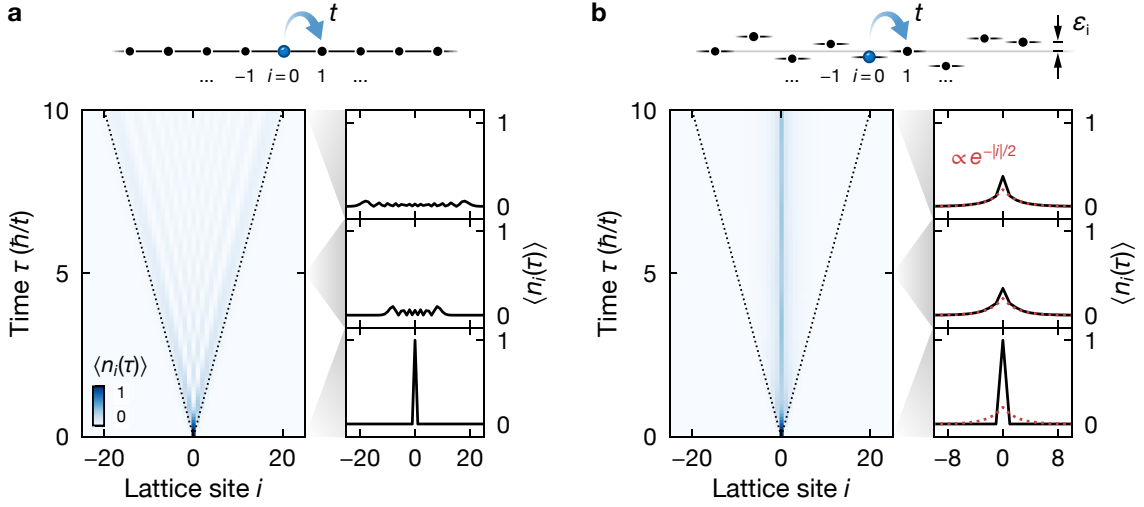


Figure 4.2 | Absence of diffusion in a disordered lattice. Numerically calculated time evolution of the state $|\Psi(\tau = 0)\rangle$ initially localized at the origin in a one-dimensional (a) regular ($W/t = \varepsilon_i = 0$) or (b) disordered lattice ($W/t = 3$) with 51 lattice sites. In both panels, the top schematic illustrates the different terms in the Hamiltonian, the left plot shows the density $\langle n_i(\tau) \rangle = \langle \Psi(\tau) | \hat{n}_i | \Psi(\tau) \rangle$ as a function of time, and the three right plots show times $\tau t/\hbar = 0, 5$, and 10 (from bottom to top). The dotted black lines indicate a ballistic expansion. In panel (b), we average over 10^4 individual realizations of the random disorder potential $\{\varepsilon_i\}_i$. The dotted red lines correspond to the approximate exponential suppression of the density with increasing distance from the origin.

4.2.2 Many-body localization

A natural question concerns how interactions, inherently present in a many-body medium, affect single-particle localization [231]. The phenomenology of Anderson localization can indeed persist in an interacting many-body setting—a phenomenon known as many-body localization (MBL). This intriguing phase of quantum matter corresponds to non-integrable systems that violate the ETH and evade thermalization by retaining the memory of a non-equilibrium initial state for arbitrarily long times [93, 98, 99]. The precise nature of the transition from a thermal to an MBL phase is not fully understood yet, but key properties such as the entanglement structure of eigenstates are drastically changed across this transition [98, 99, 232–234]. This section first explores the phenomenology of MBL by numerically studying the disordered Fermi-Hubbard model. Then, we discuss how the emergence of local integrability in an MBL system leads to logarithmic spreading of entanglement—a hallmark feature of this phase. In Section 4.3.2, these results will allow us to identify typical signatures of MBL in translationally invariant systems without static disorder.

Phenomenology in the disordered Fermi-Hubbard model.—To study the fate of localization in the presence of interactions, we first set up a Hamiltonian similar to Eq. (4.8) but with two internal states $\sigma \in \{\downarrow, \uparrow\}$ and an interaction term U . This resembles the one-dimensional Fermi-Hubbard model with on-site disorder $\{\varepsilon_i\}_i$ [see Fig. 4.3(a)],

$$\hat{\mathcal{H}}_{\text{dFHM}} = -t \sum_{i, \sigma \in \{\downarrow, \uparrow\}} \left[\hat{c}_{i\sigma}^\dagger \hat{c}_{(i+1)\sigma} + \text{h.c.} \right] + U \sum_i \hat{n}_{i\downarrow} \hat{n}_{i\uparrow} + \sum_{i, \sigma \in \{\downarrow, \uparrow\}} \varepsilon_i \hat{n}_{i\sigma}. \quad (4.9)$$

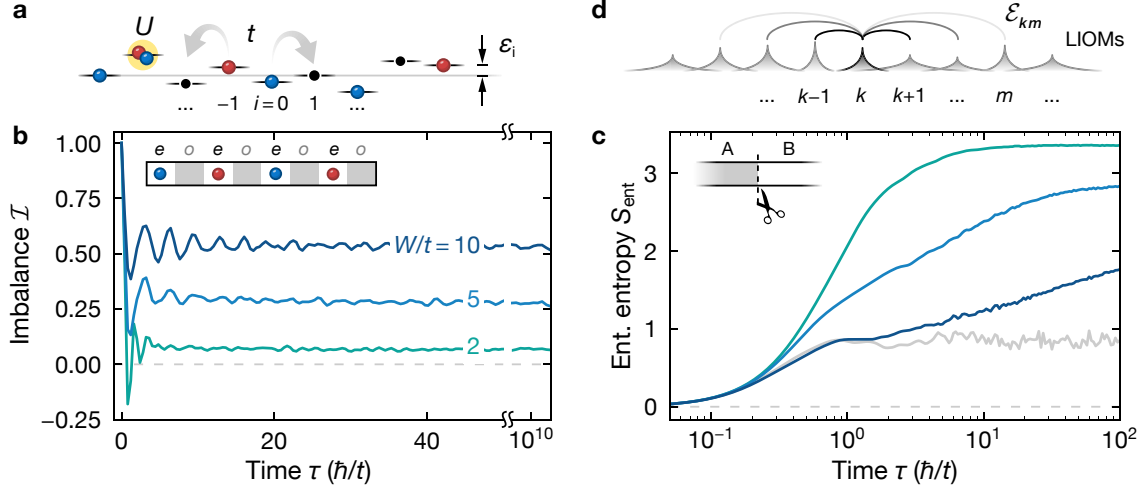


Figure 4.3 | Quench dynamics in the disordered Fermi-Hubbard model. Numerical calculations[†] for four particles on eight lattice sites with periodic boundary conditions. All data points are averaged over 10^2 realizations of the random disorder. (a) Schematic of an example state from the Hilbert space of the Hamiltonian $\hat{\mathcal{H}}_{\text{dFHM}}$ and the relevant Hubbard terms U , t , and $\{\epsilon_i\}$. Here, red and blue circles correspond to \downarrow and \uparrow particles, respectively. (b) Dynamics of the imbalance observable \mathcal{I} for an initial charge density wave state (see schematic), fixed interaction strength $U/t = 2$, and variable disorder strength W/t (colored lines). (c) Dynamics of the entanglement entropy S_{ent} calculated across a central cut of the system (see schematic). The colored lines correspond to the parameters in panel (b), whereas the gray line shows the non-interacting case ($U = 0$, $W/t = 10$). (d) Schematic illustration of the local integrals of motions (LIOMs) and their coupling $\sim \mathcal{E}_{km}$.

[†] Exact diagonalization of the Hamiltonian is performed with the software library QUSPIN [236].

To probe for dynamical signatures of MBL, we again perform a quantum quench experiment within a numerical simulation. In line with the pioneering experimental work in the field of ultracold atoms [91], we consider a charge density wave described by $|\Psi(\tau = 0)\rangle = (\hat{c}_{0\uparrow}^\dagger \hat{c}_{2\uparrow}^\dagger \hat{c}_{4\uparrow}^\dagger \dots) |0\rangle = |\downarrow \cdot \uparrow \cdot \downarrow \cdot \dots\rangle$. In this initial state, the even sites (denoted e) are empty, whereas the odd sites (denoted o) are occupied in an alternating fashion. This pattern corresponds to a modulation of the total density at the largest possible wave vector $k = \pi$. The chosen initial state represents a high-energy state, and therefore dynamics at energies far away from the ground state are probed. This is crucial as the behavior of the ground state can strongly differ from other states in the Hilbert space, in particular for gapped Hamiltonians [235].

In Fig. 4.3(a), we show the dynamics of an experimentally accessible observable [91] as a function of variable hold time and disorder strength at fixed interaction $U/t = 2$. This observable is the time-dependent imbalance $\mathcal{I} = (n_e - n_o)/(n_e + n_o)$ and describes the difference of the density on even (n_e) and odd (n_o) sites. In essence, the imbalance measures the memory of the initial charge density wave state and takes the value $\mathcal{I}(\tau = 0) = 1$ at the start of the time evolution. For finite disorder strength $W/t > 0$, we observe a finite $\mathcal{I} > 0$ that also remains at a stationary value even for extremely long hold times $\tau > 10^{10} \hbar/t$. Although the system relaxes initially, it remains far away from thermal expectation values due to the presence of disorder. This can be understood as a signature of localization [91], which persists in the

presence of interactions.¹ Hence, the term *many-body localization* adequately captures the nature of this quantum phase.

Spreading of entanglement and local integrals of motion.—Many-body localization can be studied from various angles, but a particularly instructive viewpoint originates from quantum information theory, i. e., the analysis of entanglement and its dynamical spreading across the system. The bipartite von-Neumann *entanglement entropy*

$$S_{\text{ent}}(A) = -\text{Tr}(\rho_A \log \rho_A) \quad (4.10)$$

is a measure of the entanglement between two subsystems A and B [235], which for our case are the left and right halves. Here, $\rho_A = \text{Tr}_B(\rho)$ denotes the density matrix of the subsystem A determined from the full density matrix $\rho = |\psi\rangle\langle\psi|$ by tracing out subsystem B . The initial state in our numerical study and other product states can be written as a single tensor product across the two subsystems, $|\psi\rangle = |\psi_A\rangle \otimes |\psi_B\rangle$ and therefore $S_{\text{ent}} \equiv S_{\text{ent}}(A) = S_{\text{ent}}(B) = -\log 1 = 0$. The time evolution of a product state in a many-body environment naturally introduces entanglement of the two subsystems. The induced correlations lead to an increase of $S_{\text{ent}}(A) > 0$ as a function of time, which typically has a linear time dependence for ergodic systems exhibiting thermalization [98]. In Fig. 4.3(b), we show the dynamical evolution of the numerically determined S_{ent} in the disordered Fermi-Hubbard model. For this case, however, we observe a logarithmic growth of S_{ent} in the strongly localized regime ($W/t = 10$)—a characteristic property and signature of the MBL phase.

The logarithmic growth of the entanglement is closely connected to the microscopic description of MBL in terms of local integrals of motion (LIOMs) [237–241]. LIOMs correspond to the extensive number of locally conserved quantities that describe systems deep in the MBL phase [see Fig. 4.3(d)]. Note that this emergent integrability is distinct from integrable systems, which typically exhibit globally conserved quantities. As an illustrative example for the form of LIOMs, one can consider the non-interacting disordered case where these are plain number operators $\hat{n}_k \equiv \hat{c}_k^\dagger \hat{c}_k$. Here, \hat{c}_k^\dagger denotes the creation operator of an eigenstate $|k\rangle$ localized around the k -th lattice site. For an interacting regime deep in the MBL phase, the Hamiltonian of the system in terms of the LIOMs takes the approximate form [238]

$$\hat{\mathcal{H}}_{\text{LIOM}} = \sum_k \mathcal{E}_k \hat{P}_k + \sum_{k \neq m} \mathcal{E}_{km} \hat{P}_k \hat{P}_m + \dots \quad (4.11)$$

with \hat{P}_k projection operators onto the subspace where the k -th integral of motion is invariant. Crucially, the “interaction” energies \mathcal{E}_{km} between individual LIOMs labeled k and m are suppressed exponentially with their distance $r = |k - m|$ [238]. From this relation, we can estimate the time scale $\tau \sim ce^{r/\xi}$ over which two distant regions become correlated. Here, c denotes a constant and ξ a characteristic length scale [100]. The time-dependent propagation

¹Our technique employed for the numerical study of the disordered Fermi-Hubbard model is limited by the fast growth of the Hilbert space with increasing particle number, and our results suffer from finite-size effects. Nevertheless, the analysis serves to illustrate the phenomenology of MBL in a realistic setting for experiments with ultracold atoms. See Ref. [93] and references therein for a discussion of other systems where the MBL phase transition has been studied rigorously.

of entanglement in the system then simply becomes $r(\tau) \sim \ln \tau/c$ —explaining the observed logarithmic spreading of entanglement [see Fig. 4.3(a)]. Finally, we note that the entanglement entropy of individual eigenstates in the MBL phase grows with the boundary of the subsystem [93]. This behavior is known as area-law entanglement and can also be found in ground states of gapped many-body Hamiltonians with short-range interactions [235]. In contrast, the entanglement entropy of an MBL system at infinite time after a quantum quench settles to a finite value, determined by the volume of the system [93]. This also applies to the results in Fig. 4.3(c) and can be understood by considering that our chosen initial state extends across the whole system and thereby has a finite projection onto an extensive number of LIOMs.

To summarize, we have explored the phenomenon of many-body localization, which provides an alternative scenario for thermalization in isolated quantum systems. A system deep in an MBL phase fails to thermalize and retains a memory of the initial state for arbitrarily long times—a unique feature potentially useful for applications in novel quantum devices. Crucially, this phase of quantum matter violates the ETH and is robust against small perturbations of the system [93]. This contrasts with the setting of “fine-tuned” integrable models where a small change breaks integrability and reintroduces ergodicity as, e. g., studied experimentally in Ref. [242]. To date, MBL has been observed in various experiments with probes of a finite initial-state memory but also measures of the entanglement and spectroscopic signatures [91, 92, 96, 97, 240, 243]. All these systems share the presence of static disorder, which breaks translational invariance. In the next section, we explore a complementary regime and discuss the possibility of MBL-like phenomena and non-ergodic dynamics in translationally invariant models without static disorder.

4.2.3 Self-localization of mixtures

In recent years, the question of whether MBL or MBL-like phenomena could also be realized in systems without static disorder has received significant attention across multiple theoretical studies [101–106, 244–249]. One particularly promising route explored in this direction considers systems of interacting heavy and light particles [101–105, 244, 245, 250, 251]. Here, the terms heavy and light refer to distinct dynamical time scales of the non-interacting particles, i. e., the heavy particles move or hop much more slowly compared to the light ones. Numerical studies have considered spin ladders with distinct axial couplings [105], two-component mixtures with inhibited hopping [102], and the mass-imbalanced Fermi-Hubbard model [104].

Notably, the study of such systems dates back to much earlier work of Kagan and Maksimov [107] in the context of helium mixtures. In their study, the diffusion of a small number of mobile ^3He particles within a solid of ^4He is considered. The fermionic ^3He particles interact via a simple power law potential, whereas the ^4He atoms provide a regular crystalline background and otherwise do not enter the model. The authors show that the crystalline host and sufficiently strong interactions of the mobile particles can lead to the formation of local clusters of immobile ^3He particles essentially bound to the crystal [see Fig. 4.4(a)]. The immobility and binding of clusters arise due to the interaction strength far exceeding the kinetic energy in the system. This suppresses any collective motion of the clusters exponentially with the number of its constituent particles. Assuming some form of random seed, e. g., from

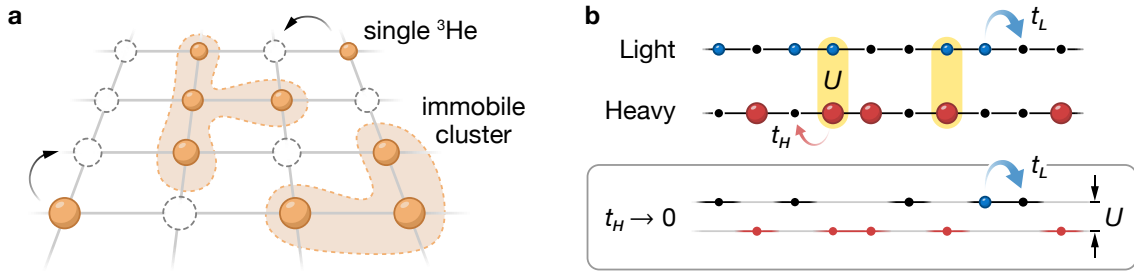


Figure 4.4 | Mixtures of heavy and light particles. Localization phenomena arising in heavy-light mixtures with two vastly different dynamical time scales. (a) Illustration of cluster formation and self-localization in helium mixtures studied by Kagan and Maksimov [107]. Here, we show single ^3He atoms (yellow circles) moving in a background of immobile clusters (shaded areas) on a two-dimensional square lattice. (b) Illustration of a heavy-light mixture with particles (blue and red circles) hopping on a one-dimensional lattice. Here, the relevant energy scales are given by the interaction energy U and the hopping amplitudes $t_L \gg t_H$. (Bottom) Effective single-particle model emerging in the limit of vanishing heavy hopping ($t_H = 0$).

disorder in the crystal or thermal fluctuations, any remaining mobile ^3He particles see the immobile clusters as an effective disorder potential [see Fig. 4.4(a)]. In this way, diffusion ceases entirely, and the system becomes fully localized—analogous to the phenomenon of Anderson localization discussed in the previous section.

While the initial setting of Kagan and Maksimov’s work deviates from binary mixtures carrying the differential mobility by construction, the underlying intuitive picture for the emergence of self-localization remains valid. In the laboratory frame, a heavy-light mixture is translationally invariant, but each instantaneous configuration of the heavy particles realizes a form of random binary disorder for the light species. As explicitly shown in the next section, this leads to single-particle localization once the motion of heavy particles is completely frozen [see Fig. 4.4(b)]. Whether introducing a small mobility of the heavy species destroys this form of self-localization and re-enables transport presents a central question. Existing theoretical studies [103–105, 251] suggest that finite mobility of the heavy species leads to dynamics consistent with ergodicity at late times. However, such mixtures still exhibit extremely slow relaxation compared to the dynamical time scales of both heavy and light species, which could be understood as a form of dynamical localization.

4.3 The mass-imbalanced Fermi-Hubbard chain

In this section, we study the phenomenology of dynamics occurring in a one-dimensional chain described by the mass-imbalanced Fermi-Hubbard model, which we also realize in our experiment (see Chapter 5). This model represents a straightforward realization of the heavy-light mixture shown in Fig. 4.4(b): light and heavy particles hop on a one-dimensional lattice and interact only via an on-site interaction. Notably, this model and similar variants have been



Figure 4.5 | The mass-imbalanced Fermi-Hubbard model. Schematic illustration of the different regimes in the one-dimensional mass-imbalanced Fermi-Hubbard model for finite interaction strengths $|U|/t_L > 0$: the effective single-particle limit described by the Falicov-Kimball model (green, $t_H/t_L = 0$), a transient regime (green-blue gradient, $0 < t_H/t_L < 1$), and the integrable limit of the mass-balanced Fermi-Hubbard model (blue, $t_H/t_L = 1$). Thermalization fails in the Falicov-Kimball model due to single-particle localization and in the mass-balanced Fermi-Hubbard model due to integrability.

explicitly suggested to feature a dynamical form of many-body localization [105], which we will explore in Section 4.3.2. To begin our discussion, we first set up the Hamiltonian of the system,

$$\hat{\mathcal{H}}_{\text{HLM}} = - \sum_{i,\alpha \in \{L,H\}} t_\alpha \left[\hat{c}_{i\alpha}^\dagger \hat{c}_{(i+1)\alpha} + \text{h.c.} \right] + U \sum_i \hat{n}_{iL} \hat{n}_{iH} \quad (4.12)$$

with $\alpha = L$ the light and $\alpha = H$ the heavy species, t_α the species-dependent hopping amplitude, and U the interspecies interaction strength. In Fig. 4.5, we show a schematic diagram of the dynamical regimes in the model. These correspond to the two well-understood single-particle and integrable limits as well as the non-integrable intermediate regime, for which numerical studies predict a rich dynamical behavior [105, 251]. Note that the sign of the interaction parameter U/t_L has no relevance for the observables and initial states discussed in this section due to a dynamical symmetry rooted in the nature of the tight-binding model on a bipartite lattice [252, 253].² We therefore only consider repulsive interactions $U > 0$ and restrict our analysis mostly to the half-filled case with the average on-site density $\langle n_\alpha \rangle = \sum_i \langle n_{i\alpha} \rangle / l = 0.5$.

In the limit $t_L = t_H$, the two species $\alpha = L, H$ can be associated with two spin states, and we recover the mass-balanced Fermi-Hubbard model, which is integrable and can be solved with the Bethe ansatz [254]. However, this presents a “fine-tuned” point in configuration space as a mismatch between t_H and t_L formally breaks integrability. The more relevant limit in the context of localization corresponds to $t_H = 0$, i. e., a completely frozen heavy species. In this limit, the above Hamiltonian corresponds to the spinless Falicov-Kimball model, originally formulated to describe insulator-metal transitions in crystals [255]. In the context of solid-state physics, this model and its extension to more than one dimension has mostly been studied in terms of its ground state and low-temperature physics, e. g., to describe localized f -electrons interacting with itinerant electrons in the conduction band [256]. At low temperature, the model exhibits phases with long-range order [257]. However, we are only interested in the high-temperature (high-energy) limit, where the model instead exhibits interesting dynamical properties.

²This symmetry is generally broken in our experiment due to the harmonic confinement of the optical lattice laser beams (see Section 5.1.1 in Chapter 5).

4.3.1 Single-particle localization

In the following, we explicitly show how the limiting case of immobile heavy particles (Falicov-Kimball model) gives rise to localized eigenstates in analogy to Anderson localization [258]. This study provides an intuitive starting point for understanding the intermediate regime with small but finite mobility of the heavy particles. First, we observe that in the limit $t_H = 0$, the Hamiltonian takes the form

$$\hat{\mathcal{H}}_{\text{HLM}} \xrightarrow{t_H=0} \hat{\mathcal{H}}_{\text{FKM}} = -t \sum_i (\hat{c}_i^\dagger \hat{c}_{i+1} + \text{h.c.}) + U \sum_i h_i \hat{n}_i, \quad (4.13)$$

where we have dropped the orbital indices $\alpha = L$ and replaced the number operators with the classical field $h_i \in \{0, 1\}$ [see bottom panel of Fig. 4.4(b)]. This field is characterized by the filling of the heavy species as determined by $\langle h \rangle = \sum_i h_i / l$ with $h_i \in [0, 1]$. For each static configuration $\{h_i\}_i$, the above expression essentially takes the form of a single-particle Hamiltonian, which we study in the following. For simplicity, we assume a system in the infinite-temperature limit where each configuration has equal probability. In this limit, we can simply consider an ensemble of random binary strings, for example, $\{h_i\}_i = \{0, 1, 0, 0, 1, 1, \dots\}$. With this assumption, the model resembles a special form of the Hamiltonian in Eq. (4.8) with the disorder taking only either of the two values, 0 or U .

To quantify the localization of the eigenstates at variable model parameters $\langle h \rangle$ and U/t , we consider the inverse participation ratio $\text{IPR}(|\Psi\rangle) = \text{IPR}(\sum_i \alpha_i |i\rangle) = \sum_i |\alpha_i|^4$ [259]. For the state $|\psi\rangle = |i_0\rangle = |0 \dots 010 \dots 0\rangle$ localized on the lattice site $i = i_0$, the inverse participation ratio takes the value $\text{IPR}(|\Psi\rangle) = 1$. In contrast, for an extended state $|\psi\rangle = l^{-(1/2)} \sum_i |i\rangle$, the IPR vanishes in the thermodynamic limit $l \rightarrow \infty$. To quantify the parametric localization in the Falicov-Kimball model, we average this quantity over all eigenstates of the Hamiltonian, as shown in Fig. 4.6(a). For increasing $|U|/t > 0$ and $0 < \langle h \rangle \leq 0.5$, the mean IPR $\langle \text{IPR} \rangle$ grows as the eigenstates become increasingly localized due to the effective binary disorder from the heavy species. Another way to determine the level of localization is to consider the finite-size scaling of $\langle \text{IPR} \rangle$. In a localized regime, the IPR averaged over all eigenstates becomes independent of the system size l . Hence, we expect this quantity to settle to a finite value as soon as l exceeds the characteristic localization length. We analyze this regime by adjusting the system size for a fixed set of parameters. For the numerically accessible $l \lesssim 10^3$, we do find a saturation of $\langle \text{IPR} \rangle$ towards a constant value for any finite filling and interaction strength confirming the localized nature of the eigenstates [see 4.6(b)]. In analogy to our analysis of Anderson localization in Section 4.2.1, we also numerically simulate the expansion of an initially localized wave function. The results shown in Fig. 4.6(c) also show a clear absence of diffusion, but the tails of the wave function are extended across a larger region compared to the continuous disorder in Eq. (4.8).

4.3.2 Quasi-many-body localization

Following our discussion of single-particle localization in the Falicov-Kimball model, we are now interested in the transient regime at small but finite hopping of the heavy species to explore the effects on localization and dynamics. Our theoretical approach in this section

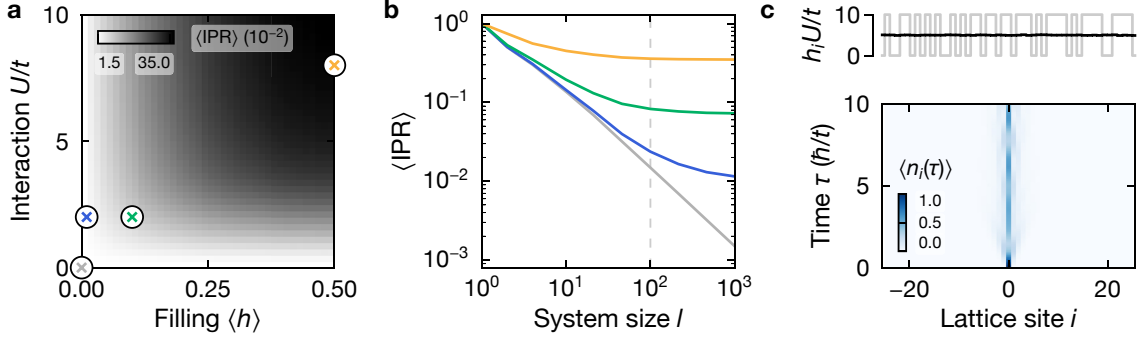


Figure 4.6 | Single-particle localization in the Falicov-Kimball model. Localized nature of the eigenstates in the Falicov-Kimball model. (a) Mean inverse participation ratio (IPR) for variable filling $\langle h \rangle$ and interaction strength U/t . Each data point is calculated for a system size of 100 lattice sites and averaged over 10^2 random binary strings $\{h_i\}_j$. Note that the plot is axially symmetric around $U = 0$ and $\langle h \rangle = 0.5$. (b) Finite-size scaling of the mean IPR for parameters indicated by colored crosses in panel (a). The gray-dashed line indicates the system size employed for the calculation in panel (a). (c) Expansion of a wave function initially ($\tau = 0$) localized at the origin in a background of stationary heavy atoms with $U/t = 10$, $\langle h \rangle = 0.5$. Here, we average the probability distribution over 10^4 realizations of the random binary string $\{h_i\}_j$. (Top) Random binary string corresponding to a single realization of the disorder potential generated by the stationary heavy species (gray) and averaged over all realizations (black).

is based on the results from Yao et al. for a two-leg spin ladder [105]. This spin system can be mapped onto the mass-imbalanced Fermi-Hubbard model by employing a Jordan-Wigner transformation [251, 260].

Numerical techniques.—Since a dynamical form of MBL is believed to occur in the mass-imbalanced Fermi-Hubbard with extremely slow relaxation and equilibration, we have to time-evolve initial states for long times $\tau \gg 10^{10} \hbar/t_L$. This presents a challenge for various approximate numerical techniques such as matrix product state algorithms [90] as well as Lanczos algorithms [261]. In contrast, exact diagonalization of the complete Hamiltonian yields all eigenvalues $\{\epsilon_n\}_n$ and eigenstates $\{|\psi_n\rangle\}_n$. This allows the time-propagation of any initial state for arbitrary long times with computational effort independent of τ , $|\Psi(\tau)\rangle = \sum_n \langle \psi_n | \Psi_0 \rangle e^{i\tau\epsilon_n/\hbar} |\psi_n\rangle$. Therefore, we use exact diagonalization techniques for our numerical calculations, which limits the accessible system size to $l \leq 8$. We do note that more advanced numerical methods have been employed to study larger system sizes, but the achieved increases remain relatively modest [105, 251]. In Appendix D, we show approximate results for intermediate system sizes $l \leq 12$ but limited to small mass imbalances and short evolution times.

Dynamical correlators.—To illustrate the emergence of metastability and extremely slow relaxation in the regime of quasi-MBL, we study the density dynamics in the mass-imbalanced Fermi-Hubbard model [see Eq. (4.12)]. This sets the stage for the experimental results in Chapter 5, where we also probe non-equilibrium density dynamics. In line with the analysis from Refs. [105, 108], we consider a dynamical correlator which measures the decay of a variable wavelength density modulation described by the wave vector $k = 2\pi/\Lambda$. First, we introduce the operator $\hat{N}_{k\alpha} = \sum_j e^{ikj} \hat{n}_{j\alpha}$, which can be understood as Fourier transform of

the real-space number operators $\hat{n}_{j\alpha}$. We quantify how correlations at the wave vector k decay during the time evolution with $\hat{\mathcal{H}}_{\text{HLM}}$ by calculating the dynamical correlator [105, 108]

$$C_{k\alpha}(\tau) = \left\langle \hat{N}_{k\alpha}^\dagger e^{i\tau\hat{\mathcal{H}}_{\text{HLM}}/\hbar} \hat{N}_{k\alpha} e^{-i\tau\hat{\mathcal{H}}_{\text{HLM}}/\hbar} \right\rangle = \frac{1}{d} \sum_{n,m} e^{i\tau(\epsilon_m - \epsilon_n)/\hbar} |\langle m | \hat{N}_{k\alpha} | n \rangle|^2. \quad (4.14)$$

Here, $\{\epsilon_i\}_i$ ($\{|i\rangle\}_i$) are the eigenenergies (eigenstates) of $\hat{\mathcal{H}}_{\text{HLM}}$ and d is the dimension of the corresponding Hilbert space. We consider an infinite temperature ensemble represented by the density matrix $\rho = \mathbb{1}/d$. In essence, this allows us to sample the thermalization and relaxation behavior across all states of the Hilbert space and the full spectrum of the Hamiltonian. For the expectation value, we find $\langle \dots \rangle = \text{Tr}(\rho \dots) = \text{Tr}(\dots)/d$. In the following, we consider a normalized version of the above correlator determined by the replacement $C_{k\alpha}(\tau) \rightarrow C_{k\alpha}(\tau)/C_{k\alpha}(0)$.

The above correlator can be understood to measure transport in the mass-imbalanced mixture at infinite temperature, as previously considered for a different system [232]. For a localized system, an equilibration of $C_{k\alpha}$ is expected but without a full relaxation to zero—in analogy to the imbalance observable discussed in Section 4.2.2 ($k = \pi$). In contrast, for the heavy-light mixture studied here, the value of $C_{k\alpha}$ at infinite time must vanish due to the underlying translational invariance of the Hamiltonian and the non-zero momentum carried by $\hat{N}_{k\alpha}$ [105]. This does not exclude the possibility that the duration over which the correlator vanishes diverges with the system size. Such behavior could be considered a natural definition of MBL in translationally invariant systems. However, this seems not to be the case for the mass-imbalanced Fermi-Hubbard model as suggested by numerical studies for small system sizes or short evolution times [105, 248, 251]. Instead, a rich dynamical behavior with an emergence of metastability can be observed, as shown below.

Our numerical analysis focuses on the largest accessible system size $l = 8$ with the modulation wave vector $k = 2\pi/l$. In this setting, we study the dependence of the density dynamics on the model parameters, namely the interacting strength U/t_L and the hopping ratio t_H/t_L . The choice of a long-wavelength modulation is motivated by our experimental realization, where we also exclusively probe the system at small k . Figure 4.7 shows the time evolution of the dynamical correlator $C_{(\pi/4)\alpha}$ individually for both species $\alpha = L, H$. In the time traces, we do find a separation of different time scales, which appears particularly clear in the signal for the heavy species. The first regime ① corresponds to the natural time scale $\tau \sim \hbar/t_H$ of the heavy species, where the dynamics sets in, and the heavy particles have started to hop between different lattice sites. These dynamics are governed by an expansion of on-site wave functions to neighboring lattice sites and a significant amount of contrast from the initial density modulation remains at that point. This regime appears to mark a metastable plateau for the light species without a noticeable decay of $C_{(\pi/4)L}$. This feature can be intuitively understood as a form of single-particle localization in the background of heavy particles [102, 105]—in analogy to the single-particle localization in the Falicov-Kimball model. The behavior changes significantly in regime ②, where the contrast decays strongly for both species. Interestingly, the system enters another metastable regime ③ at $\tau \sim \hbar U/t_H^2$, where a small but finite amplitude remains for the light species. The approximate scaling of the time scale for this last plateau with U/t_L and t_H/t_L is explicitly shown in Figs. 4.7(b) and 4.7(c) and agrees with the results

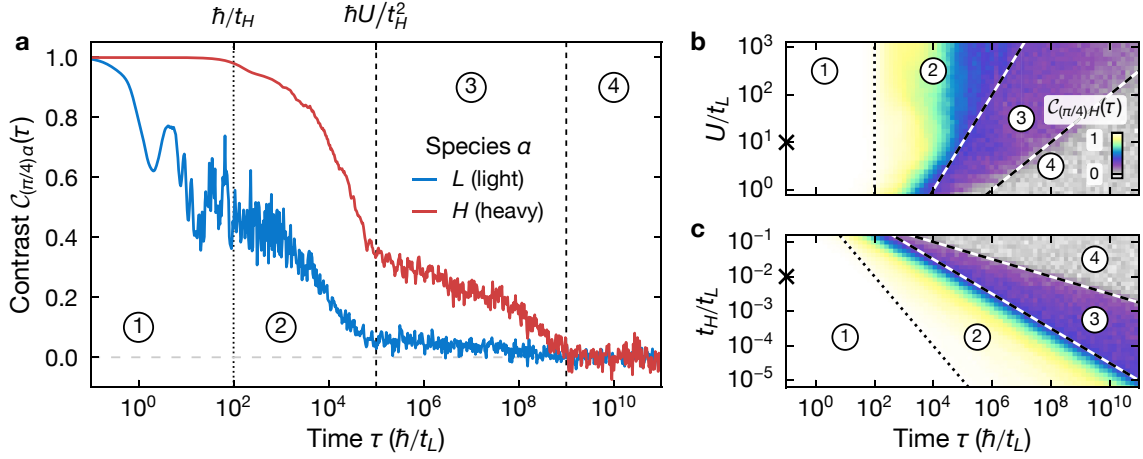


Figure 4.7 | Emergence of metastability in the quasi-MBL regime. Decay of the dynamical density correlator $C_{k\alpha}(\tau)$ for each species $\alpha = L, H$ at the longest wavelength modulation with $k = 2\pi/l$, analogous to results from Refs. [105, 108]. All data points are obtained from a numerical calculation[†] for four particles of each species on eight lattice sites (periodic boundary conditions). The dynamical regimes ①-④ are explained in the main text. In panel (a), we show data for fixed hopping ratio $t_H/t_L = 0.01$ and interaction strength $U/t_L = 10$, whereas panels (b) and (c) display time traces of the heavy species for variable U/t_L (fixed $t_H/t_L = 0.01$) and variable t_H/t_L (fixed $U/t_L = 10$), respectively. Here, the black crosses correspond to the values of the interaction strength and hopping ratio in panel (a). Dotted (dashed) black lines indicate the approximate scaling of the relevant time scales (see main text).

[†] Exact diagonalization of the Hamiltonian is performed with the software library QUSPIN [236].

from Refs. [105, 108]. In Section 4.3.3, we introduce a possible microscopic process, which could explain the relevance of this pronounced time scale. Finally, the contrast completely decays, and the system can be considered fully relaxed in agreement with eventual thermalization at late times (regime ④). However, the duration after which thermal equilibrium is eventually reached appears to be extremely long for this kind of heavy-light mixture. The associated time scale is expected to scale exponentially with the modulation wavelength $\Lambda = 2\pi/k$ for small and intermediate system sizes as studied in Ref. [105].

To connect to our discussion of the ETH in Section 4.1.1, we consider the fluctuations of the dynamical correlator around its vanishing “thermal” expectation value. Following Eq. (4.7), the infinite-time average $\lim_{T \rightarrow \infty} \int_0^T d\tau C_{k\alpha}^2(\tau)/T$ should vanish in the thermodynamic limit. This appears to be consistent with the observed complete relaxation of $C_{(\pi/4)\alpha}(\tau) \rightarrow 0$ for long times $\tau \gg 10^9 \hbar/t_L$ with only small-scale fluctuations around zero remaining [see Fig. 4.7(a)]. Compared to the dynamics of the system $\sim \hbar/t_\alpha$, however, an astronomical time scale has to be considered for the time averaging. In experiments, such long averaging times are typically not accessible, and the observation window is restricted to the metastable regime. In this case, the above relation does not strictly hold, and barely any relaxation of the system can be observed—with observables remaining far away from their thermal expectation values. This distinguishes the dynamical regime of our mass-imbalanced mixture from typical ergodic dynamics but also from the everlasting memory of an initial state, which can be found in a “true” MBL phase.

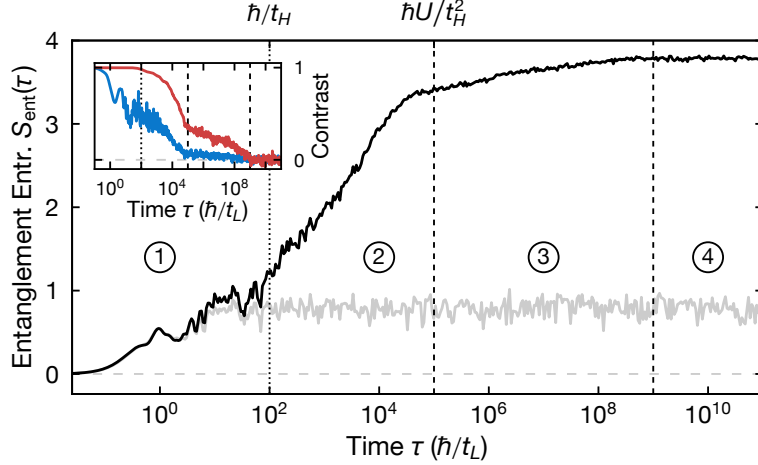


Figure 4.8 | Growth of entanglement in the quasi-MBL regime. Entanglement entropy S_{ent} numerically calculated[†] across a central cut of a system with four particles of each species on eight lattice sites (periodic boundary conditions), analogous to results from Refs. [105, 108]. Here, S_{ent} is obtained by averaging over 10^2 random initial product states. Two datasets are shown for the interaction strength $U/t_L = 10$, either with hopping ratio $t_H/t_L = 0.01$ (black line) or 0 (gray line, Falicov-Kimball model). The dynamical regimes ①-④ are explained in the main text. For comparison, the inset displays data from Fig. 4.7(a).

[†] Exact diagonalization of the Hamiltonian is performed with the software library QUSPIN [236].

Dynamics of the entanglement entropy.—To complement our study of the dynamical density correlator, we also consider the time-evolution of the entanglement entropy S_{ent} for an initial random product state of the form $|\Psi\rangle = |011 \dots\rangle_L |101 \dots\rangle_H$, and a central cut of the system [see Eq. (4.10)]. Figure 4.8 shows the resulting dynamics for finite hopping $t_H > 0$ of the heavy species compared to the regime of the Falicov-Kimball model with vanishing hopping of the heavy species. For both cases, we observe a fast initial growth of the entanglement entropy, which can be attributed to the delocalization of particles to the neighboring lattice sites (see regime ① in Fig. 4.8). While the entanglement entropy remains constant in the case of $t_H = 0$ (expected for single-particle localization, see Section 4.2.2), multi-stage dynamics set in at \hbar/t_H for the case of finite hopping ratio $t_H/t_L = 0.1$. In regime ②, S_{ent} grows quicker and then settles to a finite value, which again grows much slower starting at $\tau \sim \hbar U/t_H^2$ (regime ③). The slow and seemingly logarithmic growth is reminiscent of the entanglement entropy dynamics deep in the MBL phase of the disordered Fermi-Hubbard model [see Fig. 4.3(c)]. Finally, S_{ent} reaches a nearly constant value in regime ④, which coincides with the time scale where the density dynamics cease and thermalization has fully set in. Crucially, the distinct behavior of the entanglement entropy across the different regimes is consistent with the density dynamics and motivates the term quasi-MBL for the emergent metastable regimes [105].

Nature of quasi-MBL.—To conclude this section, we summarize our numerical study and connect the key result to existing theoretical work on the dynamic regime of the mass-imbalanced Fermi-Hubbard model. Non-equilibrium density modulations are expected to relax fully at infinite times as the underlying translationally invariant Hamiltonian suggests. The numerical results from Refs. [105, 251] for intermediate system sizes indicate that the time

scale for this relaxation does not diverge with the system size, and the model consequently does not exhibit a “true” form of MBL or asymptotic localization. However, the evolution in small systems features a clear separation of time scales with emergent metastability. These observations can be considered as signatures of a dynamical form of MBL in line with previous work [105]. While the system eventually thermalizes, consistent with ergodic dynamics at late times, the extremely slow relaxation at intermediate times suggests a peculiar class of quantum dynamics, that appears to be neither truly ergodic nor fully MBL [105, 248]. This behavior can be understood to emerge from dynamical constraints arising at strong interactions. As the natural time scales of both species differ vastly, many constraints are introduced for the hopping of particles to adjacent lattice sites. Such constrained dynamics can cause the emergence of slow time scales once single-particle processes become off-resonant and transport requires collective motion. This general concept connects to other forms of non-ergodic dynamics emerging in strongly constrained models, as found, e. g., in Rydberg arrays with long-range interactions [262–264] or atoms in strongly tilted optical lattices [265, 266].

As explicitly studied in Ref. [104], finite-size effects pose an issue for the analysis of numerical results. Thus, it remains unclear, how the dynamics potentially might change in the thermodynamic limit $l \rightarrow \infty$, which has been probed for short times and large interaction strengths [248]. Nevertheless, existing theoretical work [103, 105, 248, 251] does agree on the fact that the model features an anomalous form of non-equilibrium density and entanglement dynamics—distinct from an ergodic phase [102]. Such an intermediate metastable phase with finite memory of an initial state could also be of practical use for certain quantum devices. The regime of quasi-MBL seems to be favorable for such applications since it does not require static disorder and is solely controlled by the interaction strength, a fully tunable parameter in the setting of ultracold atomic systems.

4.3.3 Few-body bound states

This section introduces a microscopic picture that could explain the time scale $\sim \hbar U/t_H^2$, which signals the beginning of the last metastable density dynamics regime. Second-order perturbation theory suggests the dynamics of doublons (doubly-occupied lattice sites) should scale with $\sim \hbar U/(t_H t_L)$ [267] in the strongly interacting limit $U \gg t_L, t_H$ [see Fig. 4.9(a)]. Thus, the appearance of the time scale $\sim \hbar U/t_H^2$ is somewhat surprising and can likely not be explained with the slower dynamics of doublons in the system. In the following, we show how slowly moving trimers (three-body bound states) could give rise to this slow time scale. The general notion of such few-body bound states is adapted from Schiulaz et al., who also study a heavy-light mixture albeit for a modified Hamiltonian compared to our case [102].

To study the phenomenology of few-body bound states, we consider a toy model with only two heavy particles on neighboring sites and a single light particle delocalized across the two occupied lattice sites [see Fig. 4.9(b)]. Formally, we consider the following state in the Fock basis,

$$|\Psi_3\rangle = \frac{1}{\sqrt{2}} \left(|0 \dots 0 0 1 0 \dots 0\rangle_L + |0 \dots 0 1 0 0 \dots 0\rangle_L \right) \otimes |0 \dots 0 1 1 0 \dots 0\rangle_H, \quad (4.15)$$

and study its dynamics under the Hamiltonian of the mass-imbalanced Fermi-Hubbard model for variable hopping ratio and interaction strength. First, we investigate how the stability of $|\Psi_3\rangle$

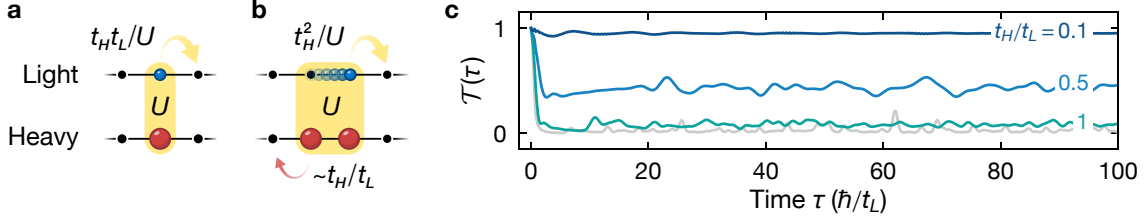


Figure 4.9 | Trimers in the mass-imbalanced Fermi-Hubbard model. Emergence of bound trimer states in the limit of large mass imbalance $t_L \gg t_H$ (small hopping ratio) and large interaction strength $U \gg t_L$. Schematic illustration of (a) bound doublon (doubly occupied lattice site) and (b) bound trimer with blue (red) circles corresponding to light (heavy) particles. Here, we also indicate the dynamical energy scales of the compound objects and how the hopping of a single heavy particle in the bound trimer is suppressed. (c) Numerically calculated[†] number of trimers \mathcal{T} after preparing the trimer state $|\Psi_3\rangle$ from Eq. (4.15) at $\tau = 0$ in a system with 24 lattice sites and periodic boundary conditions. The colored lines correspond to the time evolution for $U/t_L = 10$ and variable hopping ratio t_H/t_L , whereas the gray line shows the non-interacting limit ($U = 0$).

[†] Exact diagonalization of the Hamiltonian is performed with the software library QUSPIN [236].

changes as the hopping ratio is tuned away from the mass-balanced case at $t_H/t_L = 1$. To this end, we introduce the following operator to measure the number of trimers,

$$\mathcal{T} = \sum_{\langle ij \rangle} \hat{n}_{iH} \hat{n}_{jH} (\hat{n}_{iL} + \hat{n}_{jL}) \quad (4.16)$$

with $\langle ij \rangle$ denoting neighboring lattice sites. The expectation value for the initial trimer state in Eq. (4.15) is given as $\langle \Psi_3 | \mathcal{T} | \Psi_3 \rangle = 1$. Figure 4.9(c) shows the dynamical evolution of the correlator $\mathcal{T}(t) \equiv \langle \Psi_3(\tau) | \mathcal{T} | \Psi_3(\tau) \rangle$ for different hopping ratios in the strongly interacting regime with $U/t_L = 10$. While the value of $\mathcal{T}(\tau)$ quickly decays to nearly zero in the mass-balanced case, the correlator remains near unity for $t_H/t_L = 0.1$. This can be understood as the emergence of a bound trimer state, which only exists in the mass-imbalanced regime of the Fermi-Hubbard model. The enhancement of its binding can also be explained with perturbative arguments. The differential hopping amplitude $t_H \neq t_L$ introduces an energetic cost for adjacent heavy particles to move individually and break up once a light particle delocalizes across their sites [see Fig. 4.9(b)]. This energetic cost can be associated with the hybridization energy $\sim t_L$ of the light particle, gained through delocalizing across the neighboring sites occupied by heavy particles. In the limit of small t_H/t_L and large U/t_L , the compound object can then only move through second-order processes. These include the hopping of a single heavy atom $\sim t_H/t_L$ and the movement of the heavy-light doublon $\sim t_H t_L / U$, which yields the overall scale $(t_H/t_L) \times (t_H t_L / U) = t_H^2 / U$, consistent with our observations in Section 4.3.2.

To support our arguments, we explicitly study the density dynamics of the trimer. Again, we consider the initial state $|\Psi_3\rangle$ prepared at the center of a finite system, but this time, we calculate the mean density $\{\langle n_{i\alpha} \rangle\}_i$ of each species ($\alpha = L, H$). This allows us to directly observe the expansion of the wave function for variable Hubbard parameters t_H/t_L and U/t_L . For large mass imbalance $t_H/t_L = 0.1$ and finite interaction strength, we do find a collective expansion of the light and heavy wave functions [see top panels in Figs. 4.10(a) and 4.10(b)]. This strongly

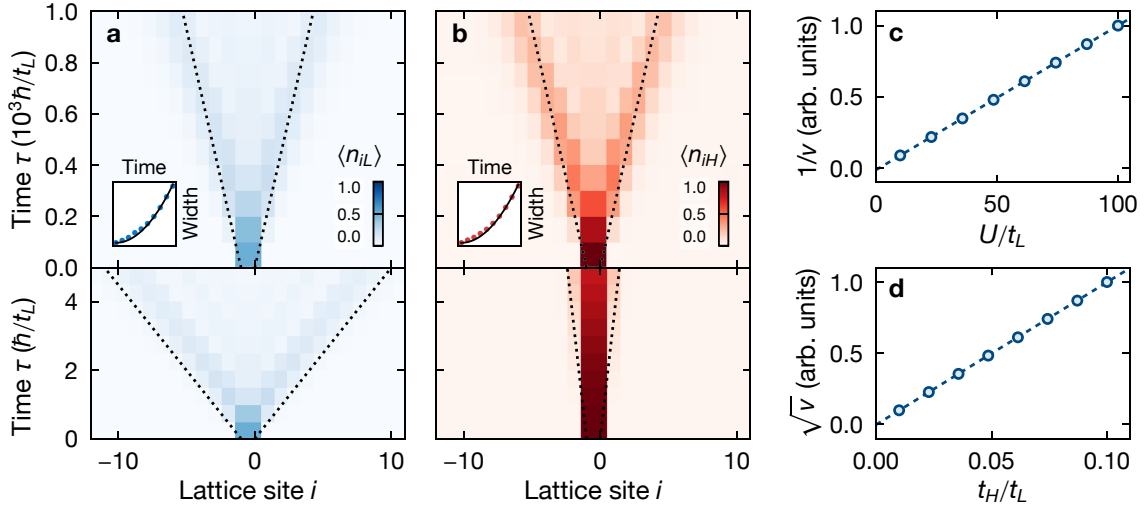


Figure 4.10 | Dynamics of trimers in the strongly mass-imbalanced regime. Numerical simulation[†] of the trimer expansion after preparing the state $|\Psi_3\rangle$ from Eq. (4.15) at $\tau = 0$ in a system with $l = 24$ lattice sites. Here, we show the on-site density $\langle \hat{n}_{i\alpha} \rangle$ of (a) light ($\alpha = L$) and (b) heavy ($\alpha = H$) particles. The top panels correspond to $U/t_L = 10$ and $t_H/t_L = 0.1$, whereas the bottom panels show the contrasting dynamics in the non-interacting ($U/t_L = 0$) limit with the absence of collective motion. The insets show the mean-square widths $w(\tau)$ (circles) of the expanding wave functions with a quadratic fit (solid black lines) yielding the expansion velocity v . (c),(d) Scaling of the expansion velocities (blue circles) for the light particles and variable interaction strength U/t_L or hopping ratio t_H/t_L extracted from the quadratic fit of the mean-square widths. The dashed blue lines are linear fits to the data points and correspond to the scaling $v \sim t_L/U$ and $v \sim (t_H/t_L)^2$ as discussed in the main text.

[†] Exact diagonalization of the Hamiltonian is performed with the software library QUSPIN [236].

contrasts the behavior in the non-interacting regime, where both species show vastly different expansion time scales [see bottom panels in Figs. 4.10(a) and 4.10(b)]. For a ballistic expansion of the wave function, we expect the mean-square width $w(\tau)$ of the density $\langle \hat{n}_{i\alpha} \rangle$ to scale quadratically with time, i. e., $w(\tau) - w(0) = v^2\tau^2/2$ with the expansion velocity v [267]. The evolution of the light and heavy density is approximately consistent with this quadratic scaling. We extract the expansion velocities v for variable Hubbard parameters, as shown in Figs. 4.10(c) and 4.10(d). These results agree nearly perfectly with the linear relation $v \sim t_L/U$ and $v \sim (t_H/t_L)^2$, yielding the relation $vt_L \sim t_H^2/U$ and confirming our perturbative arguments.

Our detailed study of a toy model with a single isolated trimer shows that this state moves collectively with the slow time scale $\sim \hbar U/t_H^2$ at significant mass imbalance. Moreover, the amplitude in Fig. 4.7 shows a strongly asymmetric behavior between light and heavy particles. This appears to be compatible with dynamics dominated by slow compound objects consisting of multiple heavy atoms and fewer light atoms. Nevertheless, a handful of questions arise about a situation with more than three particles. First, it remains unclear whether the trimer continues to exist in the many-body medium or quickly delocalizes. Second, typical states of the mass-imbalanced Fermi-Hubbard model have to be probed in order to check whether the fraction of trimers in such states is appreciable. Third, other few-body states with more than three particles could be similarly bound. A zoo of different compound objects could then

lead to a complex hierarchy of distinct time scales potentially hiding any sharp features in the dynamics. Finally, finite-size effects can also play a role as the system size determines the maximum scale of few-body compound objects spanning multiple lattice sites. Some of these questions require a careful study of the model beyond the scope of this thesis. In the context of the experimental study in Ref. [108], we have confirmed that the trimer states seem stable in a few-body environment and occur in typical initial states. Further details on the relevance of few-body bound states will appear elsewhere [268].

The above results finalize our discussion of non-equilibrium dynamics in the Fermi-Hubbard chain with finite mass imbalance. In this chapter, we have numerically explored extremely slow relaxation and emergent metastability, both exhibiting a strong dependence on the interaction strength and mass imbalance in this system. By studying the dynamics and stability of few-body bound states, namely, trimer states, we have identified a possible mechanism explaining the emergence of distinct time scales in the non-equilibrium density dynamics. These findings will help us to understand the results of our experimental study discussed in the next chapter.

CHAPTER 5

Slow relaxation in mass-imbalanced Fermi-Hubbard chains

This chapter presents the experimental observation of slow relaxation in one-dimensional systems or chains described by the mass-imbalanced Fermi-Hubbard model. We realize this system with an ultracold ytterbium gas in a one-dimensional state-dependent optical lattice. Here, light and heavy particles hop on the lattice with vastly different time scales. First, we introduce our experimental platform in-depth, and we characterize how the relevant parameters can be freely tuned. Then, we probe transport in this system by gradually displacing the minimum of an external trapping potential. This measurement technique is benchmarked in the non-interacting regime and then utilized to demonstrate how interactions significantly suppress the mobility of the light species in the mixture. Finally, we probe the system at late times after the transport and reveal a particularly slow relaxation. These observations agree with the theoretically predicted emergence of metastability and slow thermalization in the mass-imbalanced mixture. The central results of this chapter have been submitted for publication and can be found in Ref. [108].

5.1 Tunable heavy-light mixtures in optical lattices

In the following, we first give a brief overview of the experimental sequence and then explain two important techniques in detail. Our state preparation is based on the procedures described in Chapter 1 (see Section 1.4.1) with essential parameters discussed below.

The starting point for our measurements is a degenerate Fermi gas of ^{171}Yb atoms. We employ sympathetic cooling with ^{174}Yb to reach a low-entropy state with this only weakly interacting isotope. To this end, we initially load $\approx 1.5 \times 10^6$ ^{174}Yb and $\approx 1.0 \times 10^6$ ^{171}Yb atoms into the crossed optical dipole trap (ODT). At the end of the evaporative cooling sequence, typically $6\text{-}10 \times 10^3$ ^{171}Yb atoms remain and are distributed equally across the two nuclear spin states $m_F \in \{-1/2, +1/2\}$ of the ground state. By fitting absorption images of the in-situ atomic distribution in the crossed ODT, we estimate an initial temperature of $T \approx 0.15T_F$ with T_F the Fermi temperature. Although most of the ^{174}Yb atoms are lost from the trap during forced evaporation, we employ a short isotope-selective pulse resonant with the broad $^1\text{S}_0 \rightarrow ^1\text{P}_1$ transition to ensure no residual ^{174}Yb atoms remain.

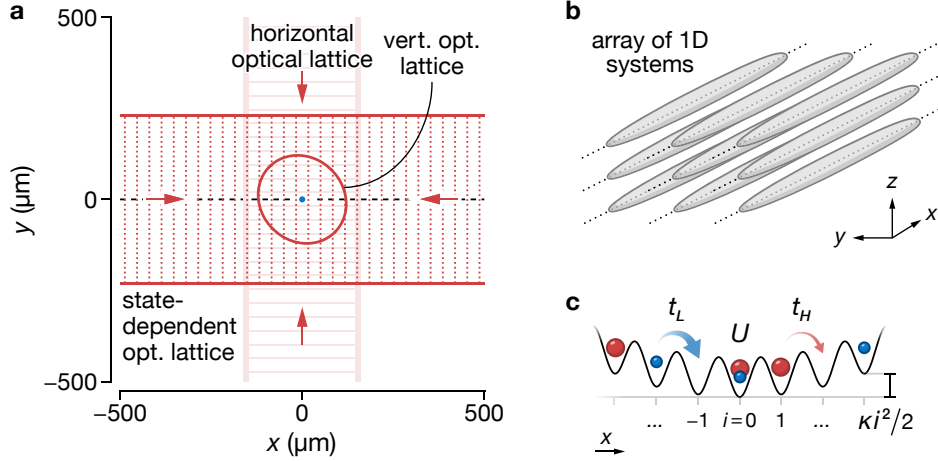


Figure 5.1 | Optical potentials producing the one-dimensional systems. (a) Geometry of the laser beams in the imaging plane (x - y). The red lines and the circle indicate the beam diameters (twice the waist). Horizontal (solid) or vertical (dashed) lines indicate every 100th lattice plane. The small blue circle at the center corresponds to the approximate typical size of the atomic cloud. (b) Illustration of the array of 1D systems generated by the deep perpendicular optical lattices [horizontal and vertical optical lattices in panel (a)]. (c) Schematic of the mass-imbalanced Fermi-Hubbard chain realized in each 1D system of the array shown in panel (b). Here, red (blue) circles correspond to heavy (light) particles, and the Hubbard parameters U , t_L , and t_H are also shown.

5.1.1 One-dimensional systems

The initial step of the state preparation procedure is the subsequent loading of the different lattices, which allows us to prepare an ensemble of nearly isolated one-dimensional (1D) systems with the hopping of individual particles restricted to the axial direction. Our experiment employs multiple optical lattices for this purpose: either state-independent and operated at the magic wavelength ($\lambda_m \approx 759.4$ nm) or state-dependent and operated at the wavelength $\lambda \approx 671.5$ nm. Here, the state independence refers to an optical lattice potential, which does not differ for atoms in the 1S_0 ground state (denoted $|g\rangle$) and excited 3P_0 clock state (denoted $|e\rangle$), as introduced in Chapter 1 (see Section 1.3). In contrast, the state-dependent lattice (SDL) is approximately three times deeper for $|e\rangle$ atoms than for $|g\rangle$ atoms. We employ two perpendicular magic-wavelength optical lattices [horizontal and vertical, see Fig. 5.1(a)], which are produced by retro-reflecting separate Gaussian laser beams with waists $\approx 130 \mu\text{m} \times 130 \mu\text{m}$ and $\approx 150 \mu\text{m} \times 40 \mu\text{m}$ [132]. The SDL potential is also generated with a retro-reflected Gaussian laser beam but with waists $\approx 230 \mu\text{m} \times 115 \mu\text{m}$ [see Fig 5.1(a)].

The atoms are loaded from the dipole trap into the optical lattices using a series of successive s-shaped ramps. First, we ramp up the vertical state-independent lattice within 120 ms to its final depth of $\approx 30E_{\text{rec}}^m$ ($E_{\text{rec}}^m = h \times 2.0$ kHz). Simultaneously, the optical dipole traps are ramped down such that the atoms are held against gravity solely by the vertical lattice. Following this transfer, the second state-independent lattice axis is ramped up to the same depth $\approx 30E_{\text{rec}}^m$ within 300 ms. At this point, the atoms are kinetically constrained to a single axis as the hopping along the perpendicular axes is strongly suppressed with a residual amplitude of $t_{\perp} \approx h \times 1$ Hz. The overall system can now be described by an array of 1D systems (tubes), as depicted in

Fig. 5.1(b). Each of these tubes contains a variable number of atoms due to the combined harmonic confinement from the different lattice beams. Our absorption imaging does not resolve the corresponding distribution due to an intrinsic integration along the z -axis. However, this distribution can be estimated from the initial parameters such as total atom number and temperature (see Section 5.2.1).

Finally, we ramp up the SDL along the axial direction to $7E_{\text{rec}}$ within 300 ms (recoil energy $E_{\text{rec}} = h \times 2.6$ kHz), and each of the tubes can now be described by a one-dimensional tight-binding model, where atoms hop only along the axial direction with the amplitude $t_L \approx h \times 100$ Hz. Subsequently, a clock laser pulse transfers the $m_F = +1/2$ ground-state atoms to the $|e\rangle$ orbital. In essence, this pulse produces an approximately balanced mixture of $|g\rangle$ atoms in $m_F = -1/2$ (denoted $|L\rangle$) and $|e\rangle$ atoms in $m_F = +1/2$ (denoted $|H\rangle$). For the moment, we ignore the details of the state preparation, which will be discussed in Section 5.3.1. Here, we first focus on the theoretical description of the resulting mixture of light ($|L\rangle$) and heavy ($|H\rangle$) atoms in each of the tubes with the Hamiltonian

$$\hat{\mathcal{H}}_{\text{exp}} = - \sum_{i,\alpha \in \{L,H\}} t_\alpha \left[\hat{c}_{i\alpha}^\dagger \hat{c}_{(i+1)\alpha} + \text{h.c.} \right] + U \sum_i \hat{n}_{iL} \hat{n}_{iH} + \frac{1}{2} \kappa \sum_{i,\alpha \in \{L,H\}} (i - i_0)^2 \hat{n}_{i\alpha}, \quad (5.1)$$

which, apart from the last sum, resembles the form of the mass-imbalanced Fermi-Hubbard chain discussed in Chapter 4 [see Eq. (4.12)]. The experimental realization introduces the parameter $\kappa = m\omega^2 d^2 = h \times 3.1(1)$ Hz, which characterizes the harmonic confinement of the system. Here, m denotes the mass of a ^{171}Yb atom, $d = \lambda/2$ the lattice spacing, and $\omega = 2\pi \times 40(1)$ Hz the harmonic trapping frequency.¹ Strictly speaking, the translational invariance of the model is broken for any finite confinement $|\kappa| > 0$. Nevertheless, the confinement term becomes less relevant close to the trap minimum where $\kappa(i - i_0)^2 \lesssim t_\alpha, U$. Since the hopping of both species differs with $t_L \gg t_H$, the confinement generally has an increased relevance for the heavy species ($\kappa/t_H \gg \kappa/t_L$). While the geometry of the lattice beams fixes the parameter κ , the hopping ratio t_H/t_L as well as the interaction strength U/t_L can be tuned experimentally over a wide range. To utilize this independent control of Hubbard parameters, we characterize their tunability in the following.

5.1.2 Tuning the hopping ratio

The state-dependent lattice (SDL) is characterized by a fixed relation set by the ac polarizability α_i in the two relevant states 1S_0 ($i = L$) and 3P_0 ($i = H$) and determines the lattice depth for atoms in either state. The polarizability ratio $p = \alpha_H/\alpha_L$ fully determines this linear relation $V \equiv V_L = V_H/p$. Since the hopping amplitudes are exponentially suppressed with the lattice depth, t_L/t_H depends non-linearly on V and, in this way, gives access to a freely tunable hopping ratio (mass imbalance). However, this tuning range is limited from above to ensure we operate in the tight-binding regime ($V \gtrsim 3E_{\text{rec}}$), where the hopping to distant sites beyond nearest-neighbors becomes negligible [1]. From below, the characteristic dynamical time

¹We measure this parameter in an independent measurement with the SDL turned off. In this way, the trapping frequency can be determined by suddenly displacing the trap center and recording center-of-mass oscillations.

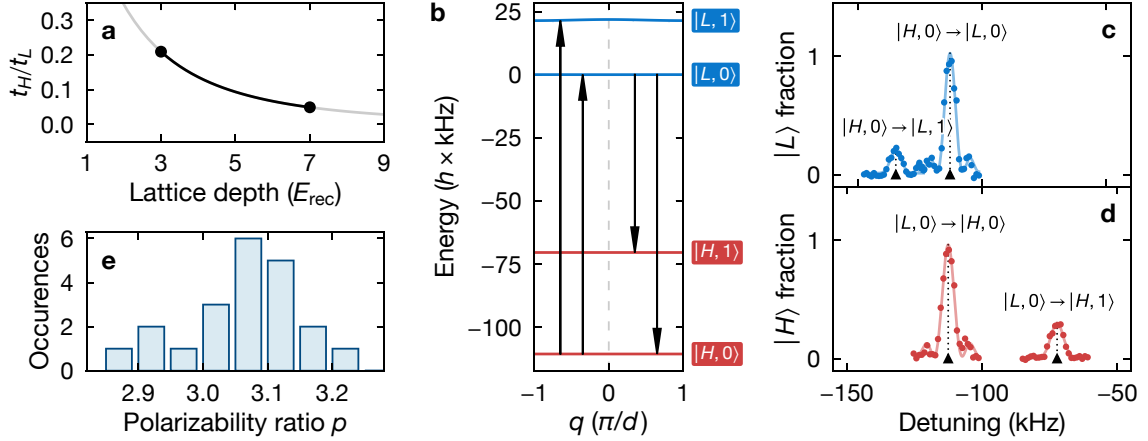


Figure 5.2 | Polarizability ratio in the state-dependent lattice. (a) Numerically calculated hopping ratio t_H/t_L (solid line) at variable lattice depth V for $p = 3.06$. Here, the black circles and solid lines indicate the regime accessible under the considerations discussed in the main text. (b) Typical band structure with the lowest-lying bands for $|L\rangle$ (blue lines) and $|H\rangle$ (red lines) atoms. Energies are shown relative to the mean energy of the $|L, 0\rangle$ band. Black arrows indicate the transition energies relevant for determining the band gaps of each species. (c),(d) Example clock spectra for a $V = 22.6(6)E_{\text{rec}}$ deep SDL featuring the transitions shown in panel (b). Circles correspond to data points, and solid lines show numerical fits employed to extract the transition frequencies. Here, we show the fraction of atoms detected in the state $|L\rangle$ or $|H\rangle$. (e) Binned distribution of the polarizability ratio p extracted from multiple measurements similar to the one shown in panels (b)-(d) but for several different lattice depths. The final result $p = 3.06(4)$ is the weighted average of these measurements.

scale \hbar/t_L introduces another limit of the tuning range, as it becomes increasingly large with growing lattice depth. This makes probing the dynamical evolution of the system challenging within the accessible maximum observation time of the experiment. For our SDL operated at ≈ 671.5 nm, hopping ratios in the range $t_H/t_L \in [0.05, 0.2]$ can be realized within these limits [see Fig. 5.2(a)]. Nevertheless, a larger range of the hopping ratio can still be accessed by changing the wavelength of the SDL, as discussed in Chapter 1 [see Fig. 1.4(b)].

Calibration of the polarizability ratio.—The polarizability ratio p together with the lattice depth V determines the hopping ratio t_H/t_L , a central parameter of the model in Eq. (5.1). For the measurement of the polarizability, we prepare a spin-polarized sample of ground-state atoms to avoid any interaction effects. The clock laser can not only change the orbital state of atoms but can also drive transitions between different motional bands of the SDL. Thus, once an appropriate laser detuning is chosen, we can drive transitions $|L, n\rangle \rightarrow |H, m\rangle$, where the indices n and m describe the initial and final motional band. This provides a technique to spectroscopically measure the band gap, i. e., the relative energy difference of the motional ground band ($n = 0$) and the first excited band ($m = 1$). More precisely, we measure the transition frequencies $\nu_{L,\{0,1\}}$ and $\nu_{H,\{0,1\}}$ by fitting spectra of the clock laser for variable detuning. These transition frequencies correspond to the resonance condition of the transitions $|H, 0\rangle \rightarrow |L, \{0, 1\}\rangle$ and $|L, 0\rangle \rightarrow |H, \{0, 1\}\rangle$ [see Fig. 5.2(b)]. The former transition can be probed by employing two consecutive clock laser pulses with the first one resonantly

driving $|L, 0\rangle \rightarrow |H, 0\rangle$. Combining the results of the transition frequency measurements [see Figs. 5.2(c) and 5.2(d)], we independently obtain the band gaps $E_{\alpha 1}$ for $|L\rangle$ and $|H\rangle$ atoms,

$$E_{L1} = h \times |\nu_{L,1} - \nu_{L,0}| \quad \text{and} \quad E_{H1} = h \times |\nu_{H,1} - \nu_{H,0}|. \quad (5.2)$$

A theoretical band structure calculation [1] then relates the band gaps to the lattice depths $V \equiv V_L$ and V_H . Repeating such spectroscopic measurements multiple times for different lattice depths reduces the statistical uncertainty and yields the polarizability ratio $p = V_H/V_L = 3.06(4)$ at the lattice wavelength $\lambda = 671.509(1)$ nm [see Fig. 5.2(e)]. Note that the same methods employed for determining p allow us to calibrate the lattice depth for measurements with the heavy-light mixture.

Finally, we comment on systematic uncertainties in our measurement of the polarizability ratio. As fermionic atoms are employed for this purpose, many quasimomentum states in the ground band are initially filled. Due to the distinct width of each band, the transition frequency is altered for atoms occupying different quasimomentum states. The presence of harmonic confinement and other experimental uncertainties make it challenging to estimate such an effect precisely. Instead, we approximate each band with its mean energy and assume a systematic error $\sim 1/3$ of the band width.² To minimize this systematic error, an increased lattice depth can be advantageous as the band widths also become successively smaller. This also explains why the above measurement of the polarizability ratio is more precise than our previous measurement for the wavelength 670 nm [43, 132]. For this prior experiment, transitions from the $n = 0$ to the $m = 2$ band have been employed (lattice modulation spectroscopy). However, the $m = 2$ band exhibits a much larger band width, and consequently, the systematic uncertainty also increases. Repeating the lattice modulation spectroscopy of Ref. [132] for the present lattice wavelength ≈ 671.5 nm yields $p = 3.05(19)$, highly consistent with the above result from clock-line spectroscopy but with an increased uncertainty.

5.1.3 Tuning the interaction strength

The interaction term U in Eq. (5.1) is determined from the Wannier functions of the optical lattices and the interspecies s -wave scattering length a_{LH} [1],

$$U = \frac{4\pi\hbar^2}{m} a_{LH} \int d\mathbf{r} |w_L(x)|^2 |w_H(x)|^2 |w_y(y)|^4 |w_z(z)|^4. \quad (5.3)$$

Here, m denotes the mass of a ^{171}Yb atom, and $w_\alpha(x)$ the Wannier function of the light ($\alpha = L$) and heavy ($\alpha = H$) atoms determined by the depth of the state-dependent lattice (SDL). The remaining Wannier functions $w_y \approx w_z$ are fixed by the $\approx 30E_{\text{rec}}$ deep perpendicular magic-wavelength lattices and are therefore identical for both species. To enable tuning the interactions over a wide range $U/t_L \in [-20, 5]$, we apply a large magnetic bias field $B \in [1400 \text{ G}, 1600 \text{ G}]$ in the vicinity of an orbital Feshbach resonance at $\approx 1300 \text{ G}$ [111]. This allows us to adjust

²Here, the most conservative estimate would be to consider the complete band width, which increases the combined uncertainty of p from 0.04 to 0.06. Our choice of $1/3$ is motivated by considering the range of energies in the band as 99.7% confidence interval of a normally distributed random variable such that the corresponding distribution has a full width at half maximum of $\approx 2\sigma$.

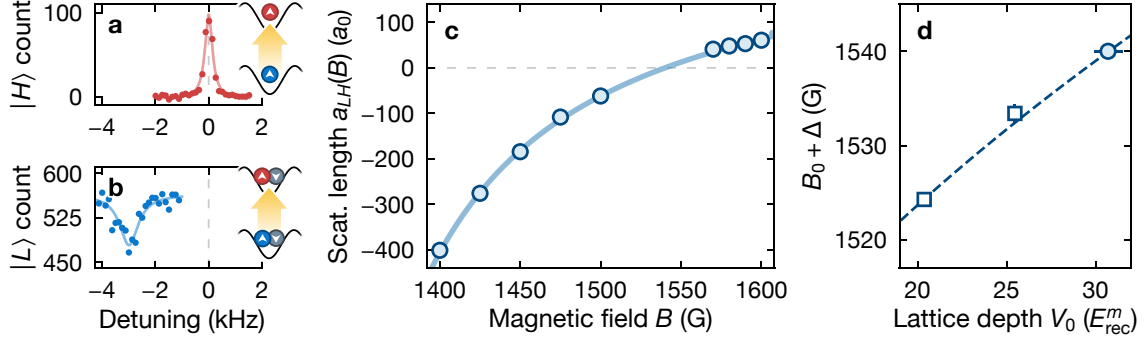


Figure 5.3 | Interspecies scattering length. Characterization of the magnetic-field dependent scattering length in the vicinity of the orbital Feshbach resonance in ^{171}Yb . Unless noted otherwise, the measurements are performed in a nearly isotropic and $30.7(8)E_{\text{rec}}^m$ deep three-dimensional magic-wavelength lattice. (a),(b) Clock spectra obtained at 1450 G: two-particle transition (blue) and single-particle transition (red). The inset schematics show the transitions driven by the clock laser (yellow arrows) and blue (red) circles correspond to $|L\rangle$ ($|H\rangle$) atoms with white arrows indicating the spin state. (c) Scattering length a_{LH} extracted from clock spectra [see panels (a) and (b)] and Eq. (5.3). The solid line shows Eq. (5.4) with the fitted parameters $a_{\text{bg}} = 333(14)a_0$, $\Delta = 255(6)$ G, and $B_0 = 1285(5)$ G.[†] (d) Dependence of the scattering-length zero crossing ($B_0 + \Delta$) on the lattice depth V_0 revealing an effective shift of the Feshbach resonance (see main text). The filled circle corresponds to the dataset shown in panel (c).

[†] The parameters deviate from the results in Ref. [111] since we consider a much smaller magnetic-field range here.

the interaction parameter U/t_L at constant lattice depth and hopping ratio by selecting an appropriate magnetic field.

Calibration of the scattering length.—Since we lack a precise theoretical model for the magnetic-field dependence of the scattering length a_{LH} [111], we determine it in an independent calibration measurement. As we are only interested in a relatively small range of magnetic fields, the following general form [133] proves to capture the functional dependence sufficiently,

$$a_{LH}(B) = a_{\text{bg}} \left(1 - \frac{\Delta}{B - B_0} \right). \quad (5.4)$$

The parameters of this model are the background scattering length a_{bg} , the magnetic-field location of the resonance B_0 , and the width Δ of the resonance. To numerically fit these parameters, we determine $a_{LH}(B)$ at variable magnetic field B with clock-line spectroscopy. For this measurement, a two-component spin mixture of ground-state atoms is loaded into a deep three-dimensional and state-independent optical lattice operated at the magic wavelength. This allows us to overcome the inhomogeneous broadening present in the SDL. Subsequently, we ramp the magnetic field to the value of interest, and a clock laser pulse transfers atoms from the $m_F = +1/2$ ground state to the $m_F = +1/2$ clock state ($|H\rangle$). In this configuration, we can address two distinct transitions: the single-particle transition of an isolated ground-state atom on a single lattice site and the two-particle transition of an $m_F = +1/2, -1/2$ on-site pair [see Fig. 5.3(a)].³ Figure 5.3 shows clock-line spectra, the extracted scattering length, and

³This simple relation only holds here since the interaction energy of the on-site pair in the ground state is negligible due to the particularly small scattering length $a_{\text{gg}} = -2.8(3.6)a_0$ [130].

the numerical fit of the model. Overall, we find excellent agreement between experimental data and the simplified theoretical model.

The approximate relation in Eq. (5.3) breaks down for large scattering lengths or particularly deep lattices [141]. To quantify the associated systematic error in our calibration, we consider the model from Ref. [127], which becomes exact in the limit of an isotropic harmonic oscillator potential. We approximate each lattice site with a harmonic potential $\sim \mathcal{O}(x^2)$, apply first-order perturbation theory with an expansion of the lattice potential up to $\mathcal{O}(x^8)$, extract the scattering lengths $a_{LH}(B)$, and compare the results. At 1400 G, we find a $\approx 20\%$ deviation of the two models, but for most of the experimentally relevant magnetic-field range 1450-1600 G, this deviation reduces to $\lesssim 5\%$. In the following, we ignore this estimated systematic uncertainty of the interaction parameter, as typical calibration uncertainties of other parameters are on a similar scale.

The scattering amplitude giving rise to the finite s -wave scattering length a_{LH} typically has a non-zero energy dependence [214]. Consequently, Eq. (5.4) becomes a function of the parameter E_0 , describing the entrance energy of a collisional pair. To first order, this dependence can be modeled as an effective shift of the magnetic field $B \rightarrow B + B_\delta$ with $B_\delta = E_0/|\delta|$ and the differential Zeeman shift $\delta = -h \times 399.0(1)$ Hz [111]. Neglecting the finite band width in the lattice, the energy E_0 can be obtained from the summed approximate energies of the ground bands of each lattice axis,

$$E_0 = \sum_{i \in \{x,y,z\}} E_{i0} \approx \sum_{i \in \{x,y,z\}} E_{\text{rec}}^m \left(\sqrt{V_i/E_{\text{rec}}^m} - \frac{1}{4} \right). \quad (5.5)$$

We probe this energetic dependence of Eq. (5.4) by repeating our spectroscopic measurement at different lattice depths V_0 . Indeed, we find a significant dependence on V_0 , captured by the phenomenological shift of the magnetic field considered above [see Fig. 5.3(d)]. Applying this correction to the situation in the SDL requires a slight modification of Eq. (5.5). For this case, we consider the summand $E_{x0} = (E_{\text{rec}}/2) [\sqrt{pV/E_{\text{rec}}} + \sqrt{V/E_{\text{rec}}} - (1/2)]$, which is the mean ground band energy of the heavy and light atoms in the SDL. We verify this shift independently with transport measurements (see Section 5.2), which are particularly sensitive to the point where the scattering length vanishes.

We conclude our discussion of the experimental techniques for tuning the relevant parameters of the mass-imbalanced Fermi-Hubbard model with Table 5.1, which shows these parameters for typical lattice depths.

5.2 Probing transport

This section introduces our measurement techniques for probing transport and non-equilibrium dynamics in the mass-imbalanced Fermi-Hubbard model. To benchmark the theoretical description and characterize single-particle phenomena in the harmonic trap, we first exclusively consider the non-interacting limit by preparing the light species alone. The Hamiltonian for a single tube then takes the form

$$\hat{\mathcal{H}}_0 = -t_L \sum_i \left[\hat{c}_{iL}^\dagger \hat{c}_{(i+1)L}^\dagger + \text{h.c.} \right] + \frac{1}{2} \kappa \sum_k \hat{n}_{iL} (i - i_0)^2. \quad (5.6)$$

Table 5.1 | Parameters of the experimentally realized mass-imbalanced Fermi-Hubbard model

Lattice depth		Hopping amplitude			Interaction	Harm. confinement
$V \equiv V_L (E_{\text{rec}})$	$V_H (E_{\text{rec}})$	$t_L (h \times \text{Hz})$	$t_L[2d]$	t_H/t_L	$ U /t_L$	$\kappa/t_L (10^{-2})$
3	9.2	287	0.10	0.21	0 ... 11	1.1
5	15.3	170	0.05	0.09	0 ... 21	1.8
7	21.4	102	0.03	0.05	0 ... 39	3.0

All values are obtained from a theoretical band structure calculation for typical experimental parameters. Here, $t_L[2d]$ denotes the next-nearest neighbor hopping amplitude. Note that the experimentally accessible magnetic field strength limits the interaction strength on the repulsive side ($U > 0$).

In the following, we first model the atomic distribution across the array of tubes, which allows us to perform theoretical simulations and compare their results to the experiment. Next, we introduce the technique to adjust the trap minimum i_0 dynamically over a large distance. Finally, we utilize this technique for a first reference measurement where we characterize single-particle localization occurring at the edge of the harmonic trap. This sets the stage for our measurements in an interacting heavy-light mixture, which will be covered in Section 5.3.

5.2.1 Numerical simulations

Since the Hamiltonian in Eq. (5.6) takes a single-particle form, we can apply exact diagonalization techniques to calculate equilibrium properties and dynamics numerically. The many-particle behavior in the non-interacting limit can then simply be determined from the atom number and temperature in each tube. However, the tube-shaped potentials generated by the perpendicular magic-wavelength lattices are distributed along both the y - and z -axis, and our imaging technique intrinsically averages over many of them [see Fig. 5.1(b)]. To still obtain an estimate for the density distribution, we develop an approximative model that considers the initial entropy in the dipole trap to calculate the final tube distribution. This calculation can be performed under the assumption of an adiabatic lattice loading process which preserves the total entropy [269].

Distribution of atoms across the tubes.—Before loading the two-dimensional optical lattice, the initial state can be described by a degenerate and weakly-interacting Fermi gas in a three-dimensional harmonic trap. The main parameters of this system are the total light atom number $N_{\text{tot}} = 3\text{-}5 \times 10^3$ (in a single m_F state), the temperature $T_i \approx 0.15T_F$ (Fermi temperature T_F), and the trapping frequencies $(\omega_x, \omega_y, \omega_z) = 2\pi \times [38(1), 35(1), 402(1)]$ Hz. These parameters are either determined from numerically fitting absorption images (particle number and temperature) or by exciting the sloshing mode of the trap and observing center-of-mass oscillations (trapping frequencies). The total entropy of a Fermi gas in a harmonic trap of dimension d at temperature T is given as [269]

$$S^{(d)}(\mu, N, T) = \beta(\mathcal{E} - \mu N) + \int_0^\infty dE \rho^{(d)}(E) \log [1 + e^{\beta(\mu - E)}]. \quad (5.7)$$

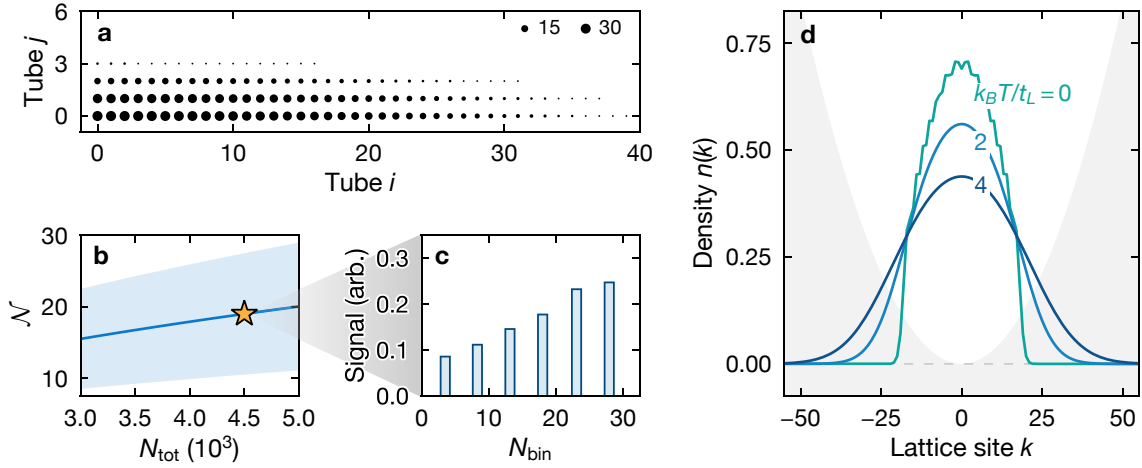


Figure 5.4 | Distribution across the one-dimensional systems. (a) Typical distribution of atoms across the array of one-dimensional systems (1D) generated by the perpendicular state-independent optical lattices, viewed along the (z, y) -plane. Note that the distribution exhibits axial symmetry around $i = 0$ and $j = 0$. (b) Effective atom number \mathcal{N} in a single tube for variable total atom number N_{tot} . The yellow star indicates a typical value in the experiment and the blue-shaded area corresponds to the standard deviation $\Delta\mathcal{N}$. (c) Binned distribution of the atoms across the various tubes, determined by averaging over multiple relative phases of the lattice and dipole trap, i. e., $(i, j) \rightarrow (i + \Delta_i, j + \Delta_j)$ with $\Delta_i, \Delta_j \in [0, 0.5]$. (d) Axial density distribution along the state-dependent lattice within a single tube for a typical atom number $N = 20$ and variable temperature $k_B T / t_L$. Here, the harmonic confinement is indicated by the gray-shaded area and parameterized by $\kappa / t_L = 1.7 \times 10^{-2}$.

Here, $\beta = 1/(k_B T)$, \mathcal{E} denotes the total energy, μ the chemical potential, N the atom number, and $\rho^{(d)}(E)$ the density of states of the d -dimensional harmonic oscillator [201]. For the initial parameters, we find $S_i = S^{(3)}(N_{\text{tot}}, T_i) = N_{\text{tot}} \times 1.4 k_B$.⁴ With this result, we consider the final state in the two-dimensional array of tubes generated by the perpendicular lattices. This state is described by the set of atom numbers $\{N_{ij}\}_{ij}$ and entropies $\{S_{ij}^{(1)}\}_{ij}$ in each of the tubes. The total entropy in this state takes the form

$$S_f = \sum_{i,j} S_{ij}^{(1)}(\mu_0 + \mu_{ij}, N_{ij}, T_f) \quad (5.8)$$

with the chemical potential μ_0 and $\mu_{ij} = m(\lambda_m/2)^2 \times (\omega_y^2 i^2 + \omega_z^2 j^2) / 2$ determined by the harmonic confinement of the traps. With our assumption of a fully adiabatic lattice loading process, we set $S_f \equiv S_i$ and numerically fit the free parameters μ_0 , T_f , and N_{ij} under the condition $\sum_{i,j} N_{ij} = N_{\text{tot}}$. This procedure converges and yields the atomic distribution $\{N_{ij}\}_{ij}$ over the different tubes of the two-dimensional array, as shown in Fig. 5.4(a). From this result, we can calculate the effective atom number and its standard deviation,

$$\mathcal{N} = \frac{1}{N_{\text{tot}}} \sum_{i,j} N_{ij}^2 \quad \text{and} \quad \Delta\mathcal{N}^2 = \frac{1}{N_{\text{tot}}} \sum_{i,j} N_{ij} (\mathcal{N} - N_{ij})^2. \quad (5.9)$$

⁴At low temperatures $T \ll T_F$, the entropy per particle in a three-dimensional harmonic potential scales approximately linearly with the reduced temperature according to $s = S/N \approx \pi^2(T/T_F)k_B \approx 10 \times (T/T_F)k_B$ [269].

These quantities typically take the values $\mathcal{N} = 19$ and $\Delta\mathcal{N} = 9$ [see Fig. 5.4(b)]. To reduce the computational cost for numerical simulations, we distribute the atom numbers of the significantly filled tubes (≈ 300 with $N_{ij} \geq 1$) iteratively across six bins such that the standard deviation calculated across each bin is constant [see Fig. 5.4(c)]. For comparison with experimental data, quantities are calculated for the mean atom number in each of these bins and averaged according to the relative weight of the bins.

Local density in the state-dependent lattice.—Since the tunneling along the perpendicular directions is strongly suppressed by the deep magic-wavelength lattices, we assume that the distribution $\{N_{ij}\}_{ij}$ remains unaltered when eventually loading the state-dependent lattice. The lattice loading process is not fully adiabatic as we can detect an entropy increase of $\approx 30\%$ when loading the atoms back into the crossed optical dipole trap. In the following, we assume that the loading and unloading increases the entropy similarly and account for it with the replacement $S_{ij}^{(1)} \rightarrow 1.15S_{ij}^{(1)}$. To characterize the state in the state-dependent lattice (SDL), we numerically diagonalize the non-interacting Hamiltonian in Eq. (5.6) on a large grid. This yields a set of discrete eigenenergies $\{\epsilon_n\}_n$ and the corresponding eigenstates $\{|\psi_n\rangle\}_n$. Together with the atom number N_{ij} and the bulk entropy $S_{ij}^{(1)}$, we can numerically determine the temperatures in each tube after loading the SDL from the following relation [see Eq. (5.7)]

$$S_{ij}^{(0)}[\mu_{ij}^{(0)}, N_{ij}, T_{ij}^{(0)}] = \beta \left[\mathcal{E}_{ij}^{(0)} - \mu_{ij}^{(0)} N_{ij} \right] + \sum_n \log \left\{ 1 + e^{\beta[\mu_{ij}^{(0)} - \epsilon_n]} \right\} \equiv S_{ij}^{(1)}. \quad (5.10)$$

Here, $\beta = 1/[k_B T_{ij}^{(0)}]$, $\mu_{ij}^{(0)}$ denotes the chemical potential and $\mathcal{E}_{ij}^{(0)}$ the total energy in each tube. All quantities are calculated within the thermodynamics of the one-dimensional lattice. Solving the above equation for a typical lattice depth of $4.7E_{\text{rec}}$ and averaging it over the different tubes, we estimate an effective initial temperature of $k_B T^{(0)}/t_L \equiv k_B T \approx 2$.

In the experiment, we probe the system with absorption imaging, which yields the atomic in-situ density distribution. To compare this key observable with theory, we also obtain the local density in the state-dependent lattice of a single tube. Dropping the explicit indices (i, j), the density on lattice site k can be determined from the Fermi-Dirac distribution and the single-particle eigenstates,

$$n_L(k) = \sum_n \frac{1}{1 + e^{\beta[\epsilon_n - \mu^{(0)}]}} |\langle \psi_n | \hat{c}_{kL}^\dagger | 0 \rangle|^2. \quad (5.11)$$

Figure 5.4(d) shows the temperature dependence of the density. For the typical temperature $k_B T/t_L = 2$ and confinement strength $\kappa/t_L = 1.7 \times 10^{-2}$, we also calculate an effective filling $\langle n_L \rangle = \sum_{i,j,k} N_{ij}^{-1} n_L(k)^2 \approx 0.5$ and the doublon fraction $\mathcal{D} = \sum_{i,j,k} N_{ij}^{-1} n_L(k)^3 \approx 0.3$. To numerically calculate the non-equilibrium density, we replace the eigenstates in Eq. (5.11) with their time-evolution, $|\Psi_n\rangle \rightarrow |\Psi_n(\tau)\rangle = e^{i\epsilon_n \tau/\hbar} |\Psi_n\rangle$. By integrating the Schrödinger equation, this approach also yields the density for a time-dependent Hamiltonian.

Let us emphasize that the above approach is only approximative as we consider a simplified single-step procedure for the loading process. Nevertheless, this modeling approximately reproduces the column density of the atomic cloud recorded with in-situ absorption imaging. In

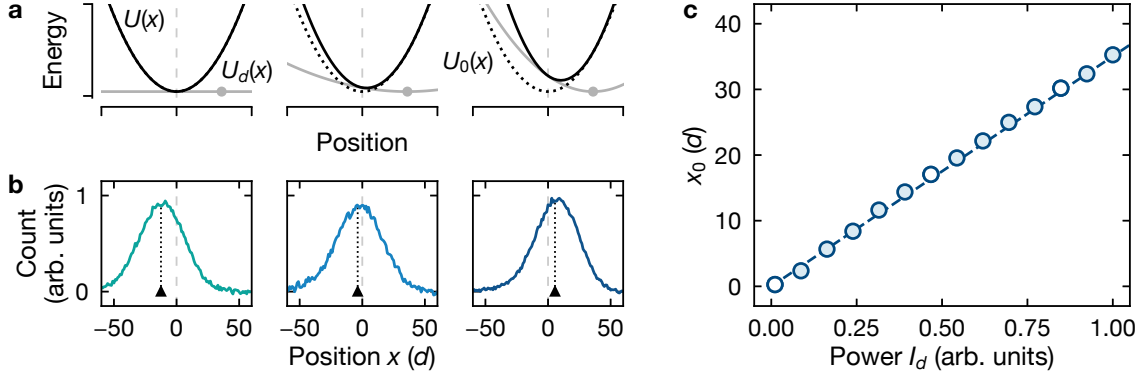


Figure 5.5 | Continuous translation of the trap minimum. (a) Schematic illustration of adjusting the minimum of the combined confinement potential $U(x)$ (solid black line) by varying the strength $U_d(x)$ of an off-centered potential (dark gray line). The dotted black line corresponds to the stationary harmonic potential $U_0(x)$. (b) Sample atomic density integrated perpendicular to the transport direction x for variable power in the additional dipole trap beam. (c) Example calibration of the trap minimum x_0 for variable power P_d in the off-centered dipole trap beam. Empty markers correspond to the power of the dipole trap beam in panel (b).

Sections 5.2.3 and 5.4.1, we will also use the time-evolution of the non-interacting density distribution to make theoretical predictions for our measurements in the non-interacting regime.

5.2.2 Translation of the trap minimum

To probe transport in the system, we systematically translate the trap minimum [see parameter i_0 in Eq. (5.6)] over a finite duration. This translation is achieved by employing an additional potential from a vertical optical dipole trap beam displaced from the vertical lattice beam, as illustrated in Fig. 5.5(a). We operate this beam at the magic wavelength to ensure the same potential for heavy and light atoms. In the following, we briefly discuss an approximation for the combined potential and resulting trap minimum, which we determine directly from an experimental measurement.

The additional dipole trap beam can be described as Gaussian laser beam with the intensity distribution $I_d(x) \sim e^{-(x-x_d)/w_0^2}$ close to the focus, where the $1/e$ beam waist has the value $w_0 \approx 60 \mu\text{m}$. Here, we employ a Taylor expansion to obtain the harmonic approximation of the optical potential

$$U_d(x) = \frac{1}{2}m\omega_d(x - x_d)^2 \left\{ 1 + \mathcal{O}\left[\left(\frac{x - x_d}{w_0}\right)^2\right] \right\} \approx \frac{1}{2}m\omega_d(x - x_d)^2 \quad (5.12)$$

with the trapping frequency $\omega_d \in 2\pi \times [0, 23]$ Hz and the displacement $x_d \approx 50 \mu\text{m}$. The trapping frequency ω_d can be freely tuned by setting the power P_d of the dipole trap laser beam. In the absence of the additional dipole trap, the intrinsic harmonic confinement in each tube is dominated by the Gaussian envelope of the perpendicular lattices, $U_0(x) = (m/2)\omega^2x^2$ with fixed trapping frequency $\omega = 2\pi \times 40(1)$ Hz. Combining the two potentials yields the overall confinement potential $U(x) = U_0(x) + U_d(x)$. To determine the trap minimum at vari-

able ω_d , we find the point x_0 , where the derivative $\partial_x U(x)$ vanishes. This procedure yields an approximately linear relation between x_0 and the power P_d of the additional dipole trap beam,

$$x_0 = x_d \frac{1}{1 + \omega^2/\omega_d^2} \stackrel{\omega_d \ll \omega}{\approx} x_d \frac{\omega_d^2}{\omega^2} \sim x_d P_d. \quad (5.13)$$

The additional potential $U_d(x)$ also slightly changes the trapping frequency according to $\partial_x^2 U(x) \approx m\omega^2[1 + (\omega_d/\omega)^2/2]$, and we neglect this increase typically below 20%.

We probe the linear relation in Eq. (5.13) experimentally by slowly ramping up the additional dipole trap beam before loading atoms into the state-dependent lattice. Then, we record the atomic density with in-situ absorption imaging, which allows us to extract the approximate location of the trap minimum from a numerical fit. Figure 5.5(b) shows data for a wide range of laser powers, and we do find an approximately linear change of the trap minimum, confirming the approximation in Eq. (5.13). Typically, the accuracy and stability of our calibration are mostly limited by drifts of the trap minimum i_0 of order $\approx d$.

5.2.3 Stark localization

The interplay of harmonic confinement κ and hopping t_L leads to single-particle localization at the edge of the trap, closely related to the phenomenon of Wannier-Stark localization [270]. Using a pure sample of light atoms, we probe this form of localization experimentally. In this way, we can precisely characterize this single-particle effect and determine its influence on the measurements for an interacting heavy-light mixture, the primary focus of this chapter. Before discussing the experimental measurement, we first explain how the localization phenomenon arises from the harmonic confinement, as also previously studied in similar cold atomic systems [271–276].

Let us consider the problem of a single particle hopping on a one-dimensional optical lattice subject to harmonic confinement. Figure 5.6(b) shows the probability density of the corresponding eigenstates in the optical lattice, determined from an exact diagonalization of Eq. (5.6). Eigenstates at energies $\epsilon_n \in [-2t_L, +2t_L]$ (within the band) are delocalized across the central region of the trap as determined by the classically allowed region $\epsilon_n > (\kappa/2) \times (i - i_0)^2$ of the confinement potential. This behavior changes dramatically for states with energies above the upper band edge at $+2t_L$, which become increasingly localized to either side of the trap. Here, a second turning point is introduced at the center of the trap, where $\epsilon_n = 2t_L + (\kappa/2) \times (i - i_0)^2$. This point corresponds to $q = \pm\pi/d$ in the band structure of the translationally invariant system, where a Bragg-reflection occurs for the wave function of particles moving in quasi-momentum space. Hence, the increasingly localized eigenstates at large energies can be understood to be a signature of Stark localization controlled by the parameter κ/t_L and the local tilt determined from the derivative of the harmonic potential $\partial_i \hat{\mathcal{H}}_0 = \kappa(i - i_0)\hat{n}_{iL}$. The parameter κ/t_L can be tuned over a wide range by adjusting the lattice depth, which changes t_L significantly but leaves κ unaltered as the perpendicular lattice beams mostly determine the harmonic confinement [see Fig. 5.6(a)]. In the following, we utilize this fact experimentally by probing localization with a transport measurement at variable lattice depth.

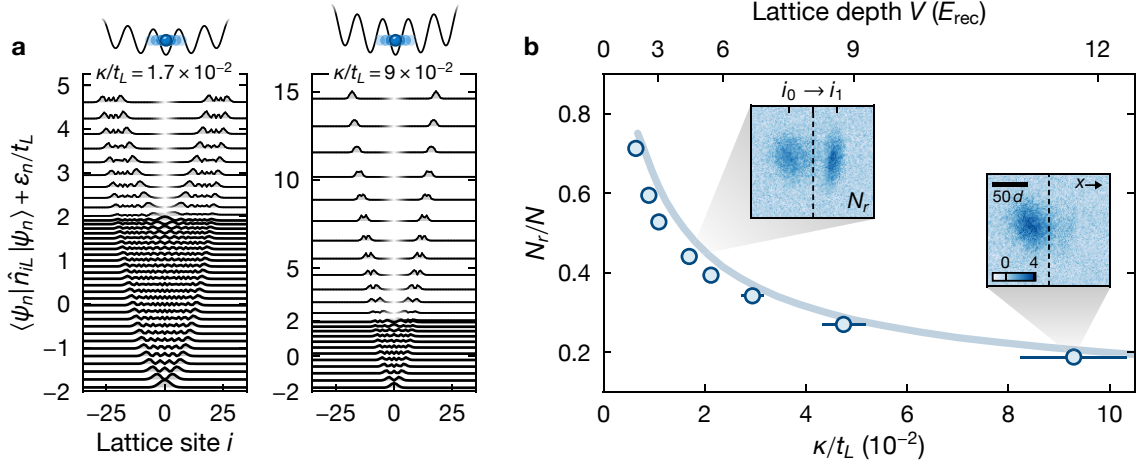


Figure 5.6 | Stark localization in the non-interacting limit. (a) Expectation value of the density for the lowest-lying eigenstates $|\psi_n\rangle$ in a (left) $4.7E_{\text{rec}}$ or (right) $11.8E_{\text{rec}}$ deep state-dependent lattice. Note that we employ a small linear gradient to lift degeneracies, and localized states above the band edge $+2t_L$ are only plotted on either side of the trap. (b) Fraction of light atoms transported to the right of the system (blue circles) by the slowly translated trap minimum, for variable hopping amplitude t_L determined by the lattice depth V . Each point is the average of 2-5 individual measurements and error bars refer to the uncertainty of κ/t_L . The blue line shows the result of a theoretical calculation with no free parameters (see main text). The insets show sample absorption images of the light atoms. For this measurement, the effective atom number per tube is $\mathcal{N} \approx 19$ (standard deviation $\Delta\mathcal{N} \approx 8$) and the hopping amplitude takes values $t_L = h \times 33(4) \dots 488(2)$ Hz. The data contains an estimated constant offset of ≈ 0.1 determined from measurements for zero transport distance $\Delta x = 0$, which most likely originates from the finite extent of the atomic cloud and our finite imaging resolution.

First, the ground state spin mixture is loaded into the perpendicular state-independent lattices and the axial state-dependent lattice. Then, we employ a short resonant and spin-selective “push” pulse on the narrow $^1S_0 \rightarrow ^3P_1$ transition to remove the $m_F = +1/2$ ground-state atoms completely. This procedure prepares a pure and non-interacting sample of $|L\rangle$ atoms in the state-dependent lattice, described by the Hamiltonian in Eq. (5.6) for each tube. Following this initial state preparation, the trap minimum i_0 is linearly translated over a distance $\Delta x \approx 47d$ (lattice spacing $d = \lambda/2$) within the time $\approx 90\hbar/t_L$ using an additional dipole trap as described in Section 5.2.2. Immediately after this translation, the atomic motion is frozen by quickly ramping up the state-dependent lattice, and we record the atomic density with absorption images. In general, we find two clouds well-separated along the direction of translation, one at the initial trap minimum i_0 and one at the final one, $i_1 = i_0 + \Delta x$. We repeat this measurement at variable lattice depth V and quantify the response by counting the atoms in the two regions $i \leq i_0 + \Delta x/2$ (left half, N_l) and $i > i_0 + \Delta x/2$ (right half, N_r). Intuitively, the atoms in the right half of the system can be viewed as the fraction transported to the new trap minimum while the atoms in the left half of the system have remained at the original trap location.

To quantify this behavior robustly, we introduce the fraction of light atoms in the right half of the system $N_r/(N_l + N_r) \equiv N_r/N$ by counting the two regions separately. Figure 5.6(b) displays this characterization of transport in the system for variable confinement strength κ/t_L

as accessed with the variable lattice depth. As we increase κ/t_L at constant atom number per tube, a growing number of the fermionic atoms start to occupy localized states at the edge of the trap. These states cannot efficiently follow the smooth translation of the trap minimum and remain at the initial trap location. Hence, a dramatic reduction of N_r/N can be observed, which signals an increased localization of the system.

Let us also briefly comment on the role of the translation speed, which in the above measurement takes the constant value $v_0 \approx 0.5dt_L/\hbar$. For all lattice depths, N_r/N increases monotonically with a reduction of the translation speed and follows approximately an exponential saturation curve.⁵ Our choice of v_0 corresponds to twice the $1/e$ time constant of this saturation curve, a fairly optimal value in terms of signal amplitude and measurement duration.

We compare our experimental results to predictions from a theoretical calculation of the Hamiltonian in Eq. (5.6) with a linear time-dependence of the trap minimum i_0 . Following the procedure outlined in Section 5.2.1, we numerically calculate the fraction in the right half of the system N_r/N . Overall, we find good agreement between experimental data and numerical calculations with a small systematic shift of the theory to larger values of N_r/N . This disagreement most likely originates from experimental and systematic uncertainties in the modeling of the lattice loading process. For example, a modest increase by 25% of the initial temperature in each tube or the atom number yields a nearly perfect agreement.

Our experimental results are consistent with earlier studies in single-axis optical lattices, which employed a sudden displacement (quench) of the trap minimum to probe transport. A key question in these studies has been what role interactions play and how they could delocalize states at the edge of the trap [271, 275]. In the context of many-body localization, this question has been recently revisited and systematically analyzed with matrix product state simulations for relatively large system sizes [277]. The authors of this study show that the behavior can be understood analogously to Stark localization in the presence of interactions, where a minimum critical strength of the gradient has been identified [247, 249]. In the harmonic trap, localized and extended regions co-exist depending on whether the local gradient $\kappa(i - i_0)\hat{n}_{iL}$ exceeds the critical gradient of $\approx 2t_L$ or not [277]. While these results have been determined within a mass-balanced model, we also expect this behavior to persist for the case of the mass-imbalanced mixture [108]. This has the important consequence that Stark localization should play a less dominant role for measurements with an interacting heavy-light mixture. More precisely, at least a central region of ≈ 30 lattice sites should remain extended and respond to a change of the external confinement [108].

5.3 Mobility in the mixture

Using the methods introduced for the non-interacting limit in the previous section, we now study transport and mobility in a mixture of heavy and light particles described by the Hamiltonian in Eq. (5.1). This allows us to connect to the theoretical discussion of slow dynamics in mass-imbalanced mixtures and the emergence of metastability (see Section 4.3.2 in Chapter 4).

⁵This behavior originates from states with energies close to the upper band edge, which experience a much larger energy change for a fixed displacement due to their spatial extent [see Fig. 5.6(a)]. Thus, the associated time constant for adiabatic transport also takes a significantly larger value, giving rise to a reduced N_r/N at fast translation speeds.

To characterize the dependence on both the interspecies interaction strength and the hopping ratio, we probe the system for multiple combinations of these parameters. Before discussing these experimental results, we describe the details of the initial state preparation.

5.3.1 Initial state preparation

Similar to our experiments in the non-interacting limit, we start with a balanced mixture of ground-state atoms in the two nuclear spin states $m_F = \pm 1/2$ distributed across the array of tube-shaped systems. After loading the atoms into the state-dependent lattice (SDL), a short resonant clock laser pulse drives the $m_F = +1/2$ ground-state atoms to the $m_F = +1/2$ clock state, which produces the desired mass-imbalanced mixture in the states $|L\rangle$ and $|H\rangle$. The excitation pulse is driven by a clock laser beam propagating perpendicular to the one-dimensional tubes (along the y -axis, see Fig. 5.1), which avoids driving any motional excitations along the shallow lattice. To overcome the inhomogeneous broadening of the clock transition in the SDL, we employ a large Rabi frequency $\Omega \approx 2\pi \times 3$ kHz. Before applying the pulse, we ramp the magnetic field to the zero crossing of the orbital Feshbach resonance at ≈ 1530 G, where the scattering length a_{LH} and the corresponding interaction term U vanishes. This allows us to address singly and doubly occupied lattice sites with a single-frequency excitation pulse as the transition energies are degenerate ($U \approx 0$ in the initial and final pair state). Since the duration of the pulse ≈ 0.2 ms is much shorter than the natural dynamical time scale $\hbar/t_L \approx 1.6$ ms, the excitation corresponds to an effective quench of the hopping ratio with $t_H/t_L = 1 \rightarrow t_H/t_L \ll 1$, which produces an out-of-equilibrium state. By measuring the depletion after the clock laser pulse, we estimate that more than 95% of the atoms initially in the $m_F = +1/2$ ground state are driven to $|H\rangle$. Following the quench of the hopping ratio, we ramp down the lattice according to the desired t_H/t_L within 25 ms [see Fig. 5.7(a)]. Since the harmonic confinement depends on the depth of the lattice, this ramp also causes an expansion of the atomic sample along the tubes. To set the interaction parameter, we finally adjust the magnetic field within 75 ms corresponding to 50 - $140\hbar/t_L$ depending on the chosen lattice depth. At this point, we have prepared the tunable heavy-light mixture described by the Hamiltonian in Eq. (5.1). This provides the starting point for our experimental study of dynamics in the mass-imbalanced Fermi-Hubbard model.

For our parametric studies, it is essential to understand the nature of the prepared state at variable interaction strength. The quench of the hopping ratio and the subsequent gradual adjustments of the parameters in the Hamiltonian yield a state distinct from thermal equilibrium. Most importantly, we prepare a state far away from the ground state, which allows us to probe dynamical properties of the system at high energies. A key property of our prepared initial state is the fraction of doubly-occupied lattice sites, which can be estimated from spectroscopy on the clock transition. In such a measurement, immediately after preparing the initial state according to the above protocol, the atomic motion is frozen by quickly ramping up the lattice. Subsequently, we ramp the magnetic field to a value where the peaks of singly- and doubly-occupied lattice sites are well resolved due to a significant interaction shift U . At this point, a second clock pulse with variable detuning can drive atoms in $|H\rangle$ back to the ground state. By comparing the amplitudes of the single- and two-particle peaks in the result-

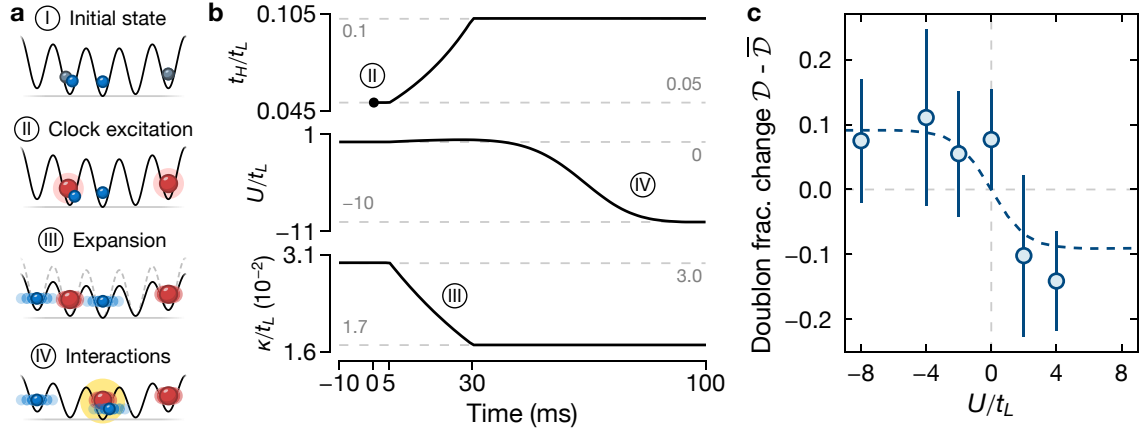


Figure 5.7 | State preparation of the heavy-light mixture. (a) Schematic illustration of the different steps in the state-preparation procedure. (b) Time dependence of the Hubbard parameters during state preparation for sample target values $t_H/t_L = 0.1$ and $U/t_L = -10$. All parameters are estimated from the control voltages in the experiment. Time is given relative to the clock laser excitation pulse, which also suddenly changes the hopping ratio, $t_H/t_L = 1 \rightarrow 0.05$ (black circle). (c) Doublon fraction change $\mathcal{D} - \overline{\mathcal{D}}$ (blue circles) determined from clock-line spectroscopy by comparing the relative amplitudes of the single- and two-particle peaks. Here, $\overline{\mathcal{D}} = 0.22$ (experiment), 0.33 (theory) denotes the mean doublon fraction. Points are partly binned to increase the signal to noise, and error bars denote the uncertainty of \mathcal{D} . The dashed line displays the result of a matrix product state simulation for the experimental sequence and ten particles of each species, kindly provided by P. Zechmann [108, 268].

ing spectrum, an estimate on the ratio of singly and doubly-occupied sites can be made [see Fig. 5.7(b)]. Due to the limitations of our spectroscopic resolution in the SDL, this method has an approximative nature, and we complement it with a theoretical calculation for our system parameters. Qualitatively, the two results agree despite the large error bars of the experimental data. Therefore, we conclude that the doublon fraction of the initial state only weakly depends on the chosen interaction parameter. This allows us to probe the effects of different interaction strengths in dynamical experiments after preparing this state.

Within Ref. [108], we have identified that a full replication of the experimental state preparation procedure is not required to approximately model the initial state. Instead, considering an initially non-interacting thermal heavy-light mixture and performing a quench of the interaction strength yields a qualitative similar state compared to the full preparation procedure. Here, we quantify the similarity of the states by considering the local density of singly and doubly occupied sites in the lattice. The simplified state preparation procedure employed for the theoretical calculations enables prolonged evolution times, which are required for the transport measurements discussed in the following section.

5.3.2 Inhibited transport

After preparing the heavy-light mixture, we probe the effects of interactions on the mobility of the light species by repeating the transport experiment introduced in Section 5.2. We choose a fixed hopping ratio $t_H/t_L = 0.104(7)$ [$V = 4.7(2)E_{\text{rec}}$] and tune the interaction strength U/t_L in the range $-20 \dots 5$ by setting the magnetic field to an appropriate value in the vicinity

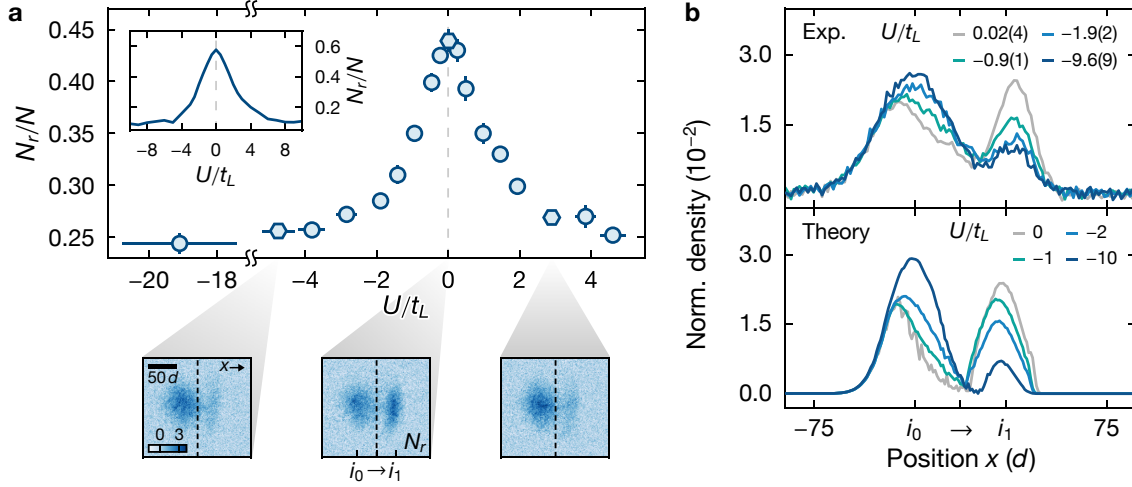


Figure 5.8 | Inhibited mobility in the heavy-light mixture. (a) Fraction of light atoms N_r/N transported to the right half of the system (blue markers) for variable heavy-light interaction strength U/t_L , fixed hopping ratio $t_H/t_L = 0.104(7)$, and confinement strength $\kappa/t_L = 1.7(1) \times 10^{-2}$ [$V = 4.7(2)E_{\text{rec}}$]. Each point is the average of 3-4 individual measurements. Error bars denote the standard error of the mean of N_r/N (partly smaller than the marker size) and the uncertainty in U/t_L . In the bottom panels, we show example absorption images of the light atomic density (hexagonal markers in the main panel). The inset of the main panel shows N_r/N from matrix product state simulations for the experimental parameters but only a single tube with five atoms of each species [108]. (b) Comparison of the experimentally determined light atom density profiles integrated perpendicular to the transport direction (top) and the theoretical prediction (bottom, matrix product state simulation) for various interaction strengths. All curves are averaged across multiple measurements and normalized to their integrated value. The results of the matrix product state simulations have been kindly provided by P. Zechmann [108, 268].

of the orbital Feshbach resonance (see Section 5.1.3). Subsequently, we translate the trap minimum over the distance $\Delta x \approx 47d$ within $\approx 92\hbar/t_L$ corresponding to a translation speed of $\approx 0.5dt_L/\hbar$. Again, the fraction N_r/N of the light atoms transported to the right half of the system is measured with absorption imaging, as shown in Fig. 5.8(a). For increasing interaction strength $|U|/t_L$, we find a significant suppression of the transported atoms compared to the non-interacting limit dominated by Stark localization [see bottom panels of Fig. 5.8(a)]. This suppression reaches almost a factor of two for $|U|/t_L \geq 4$ and saturates as the interaction parameter is further increased beyond the band width ($4t_L$) of the light species. For interactions $|U|/t_L > 1$, the functional dependence of N_r/N is approximately proportional to t_L/U . Remarkably, the signal is nearly symmetric around $U = 0$, which can be potentially attributed to a dynamical symmetry [252, 253] of Eq. (5.1) in the absence of harmonic confinement and for a constant initial state independent of U . Here, we expect the harmonic confinement to only weakly break the dynamical symmetry. In this way, the details of the non-equilibrium density distribution might be affected but not the quasi-global observable N_r/N , which averages across a significant fraction of the system. A similar argument might apply to the weak dependence of the initial state on the chosen interaction parameter U .

The dramatically reduced mobility of the light species at finite interaction strength arises from dynamical constraints due to only slowly hopping heavy atoms. Since we translate

the trap minimum over a large distance $\approx 47d$ exceeding the typical system size $\approx 30d$ (root-mean-square width of the atomic cloud), our measurement can be understood as a long-wavelength probe of transport. This connects to the theoretical study of density dynamics at long wavelengths, as discussed in Chapter 4 (see Section 4.3.2). For early times, we expect the heavy atoms to remain approximately stationary thereby producing a binary disorder potential (see regime ① in Fig. 4.7, Chapter 4). In this picture, the light species experiences localization due to this effective disorder. We assume that our present measurement only probes this early time evolution exclusively due to the sizable local gradient $\kappa(i - i_0 - \Delta x)$ quickly applied to neighboring lattice sites during the transport procedure. Towards the end of the trap minimum translation, this gradient far exceeds the critical value $\approx 2t_L (2t_H)$ [277] in an extended region, and the dynamics at the initial trap minimum should cease because of Stark localization. In general, a more quantitative description and analysis of the system poses a challenge since our experimental probe entails a continuous change of the trapping potential. This measurement technique features the practical advantage of a relatively large signal-to-noise ratio in contrast to the minuscule response after a quench of the trap minimum [276].

Matrix product state simulations.—To benchmark our experimental results, we compare them to a matrix product state simulation [108, 268]. Since our measurement involves a translation of the trap minimum over a significant distance, a sufficiently large system size is required to capture this type of experiment, and exact diagonalization becomes infeasible for the typical particle numbers in each tube. In contrast, matrix product states allow the efficient description of weakly entangled states within large Hilbert spaces. For this description of one-dimensional many-body systems, many numerical techniques have been developed, e. g., for dynamical time evolution and for finite temperature [278]. These methods are commonly restricted to short evolution times or small particle numbers unless the entanglement growth slows down significantly, e. g., deep in a many-body localized phase. For a single tube in our experiment, accuracy limits the simulations to a simplified state-preparation procedure and five particles of each species. We show these results from Ref. [108] in the inset of Fig. 5.8(a). The qualitative behavior of the transported fraction at variable interaction strength is reproduced with this numerical simulation. However, a quantitative agreement is not found, which can be attributed to the much smaller particle number compared to the effective atom number per tube $\mathcal{N} \approx 19$ in the experiment. Besides the N_r/N observable, we also compare the normalized atomic density of the light species in Fig 5.8(b). Here, we also find a qualitative agreement, in particular, at vanishing and maximum interaction strengths.

5.3.3 The mass-balanced regime

Since the hopping ratio in the experiment is tunable, a natural question concerns how the reduced mobility of the light species is affected by this parameter. Specifically, we are interested in the limit of equal masses ($t_H = t_L$), where the slow dynamics and emergent metastability of the quasi-MBL regime should cease to exist. To probe this regime, we replace the state-dependent lattice (SDL) with a state-independent lattice operated at the magic wavelength. For comparison of measurements in the two configurations, we select the lattice depth $2.7E_{\text{rec}}^m$, where the harmonic confinement strength $\kappa/t_L = 1.6(1) \times 10^{-2}$ takes approximately the same

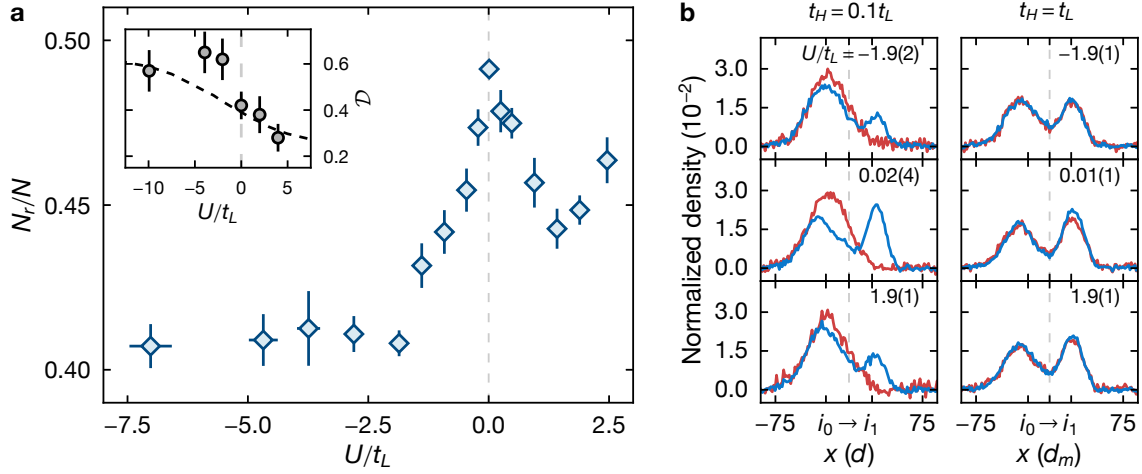


Figure 5.9 | Mobility for equal hopping amplitudes. (a) Fraction of light atoms N_r/N transported to the right half of the system (blue diamonds) for equal masses ($t_H = t_L$), variable interaction strength U/t_L , and confinement strength $\kappa/t_L = 1.6(1) \times 10^{-2}$ [$V = 2.7(3)E_{\text{rec}}^m$]. Each point corresponds to the average of 5-7 individual measurements. The error bars denote the standard error of the mean of N_r/N and the uncertainty in U/t_L . The inset displays the doublon fraction \mathcal{D} (black circles) in a $4.0(1)E_{\text{rec}}^m$ deep state-independent lattice. Data points are obtained from clock-line spectroscopy and the relative amplitudes of the single-/two-particle peak, and error bars denote the uncertainty of \mathcal{D} . The dashed line corresponds to a theoretical prediction from an exact diagonalization calculation for eight lattice sites. (b) Direct comparison of the light (blue lines) and heavy (red lines) atomic density (integrated along y) for variable interaction strength U/t_L (top to bottom) as well as the hopping ratios $t_H/t_L \approx 0.1$ (left, see Fig. 5.8) and $t_H/t_L = 1$ [right, also see main panel in (a)]. All curves are averaged across multiple measurements and normalized with their integrated value. Note that the measurements for the heavy species are subject to systematic uncertainties (see main text).

value as for the $4.7E_{\text{rec}}$ deep SDL considered in the previous section. The lattice depth distinct from the mass-imbalanced configuration leads to potential systematic differences, for example, the hopping beyond neighboring sites becomes increasingly relevant. Moreover, a separate smaller laser beam generates the state-independent lattice. This leads to a larger albeit still small variation of the effective lattice depth and the associated Hubbard parameters when averaging across multiple tubes. Nevertheless, we expect the experimental results for both configurations to be comparable on a qualitative level.

Figure 5.9(a) shows the transported fraction N_r/N of light atoms in the state-independent lattice for variable interaction strength U/t_L after translating the trap center over the distance $\Delta x \approx 44d_m$ within the duration $\approx 94\hbar/t_L$. Here, $d_m = \lambda_m/2$ denotes the spacing of the magic-wavelength lattice. Compared to the configuration with finite mass imbalance, the measurement results at $t_H = t_L$ also exhibit significant suppression of transport for finite interaction strength $|U|/t_L > 0$. However, the parametric dependence on the interaction features two qualitative differences: the amplitude of the suppression is much smaller with a maximum of $\approx 20\%$, and the shape exhibits a strong asymmetry between the attractive ($U < 0$) and repulsive ($U > 0$) side. The suppression also takes systematically smaller values for the latter range of interactions with a maximum of $\approx 10\%$. This does not come as a surprise since the

reduced transport in the mass-imbalanced regime must originate from an effect unrelated to the dynamical constraints at finite mass imbalance.

We attribute the asymmetric signal and reduced transport to doublons arising from an increased sensitivity of the state preparation procedure to the final interaction strength. In contrast to the mass-imbalanced setting, the clock excitation pulse producing the mixture does not quench the hopping ratio. Hence, the state preparation only consists of slowly ramping the interaction parameter [see Fig. 5.7(a)]. Consequently, the doublon fraction in the initial state before translating the trap center depends strongly on the selected interaction parameter U/t_L . We verify this assumption with an experimental measurement shown in the inset of Fig. 5.9(a). In particular, the number of doublons is significantly reduced for repulsive interactions $U > 0$. Since the dynamical time scale of doublon hopping becomes much slower with $\sim \hbar U/t_L^2$ ($U \gg t_L$), the overall fraction of doublons also contributes to suppressing the response after translating the trap minimum. Our measurement in the mass-imbalanced regime can therefore be mainly considered a probe of the doublons and their dynamics, as studied experimentally in Ref. [275].

Direct comparison of the atomic density.—Despite the added complexity due to the initial state, the measurement in the mass-balanced regime provides an important basis for a qualitative comparison of the atomic density. In Fig. 5.9(b), we compare the normalized densities of both species for the mass-imbalanced ($t_H/t_L \approx 0.1$) and the mass-balanced setting ($t_H = t_L$). Note that the density of the heavy atoms likely contains systematic uncertainties, which are not fully characterized at this point.⁶ However, we assume this does not significantly influence the qualitative comparison presented in this paragraph. For equal masses, the densities of both species agrees nearly entirely for the probed interaction parameters. In contrast, a finite mass imbalance leads to a substantial difference between the two species, with the heavy atoms remaining mostly stationary at the initial trap location. But the differences between the two configurations become even more apparent when solely comparing the atoms transported to the right of the system. While almost no differences are discernible between non-interacting and interacting regimes for $t_H = t_L$, a sizable reduction at finite interaction strength can be observed for the mass-imbalanced case [see Fig. 5.9(b)]. This agrees with our understanding of the dynamics in the heavy-light mixture and how interactions with the heavy atoms severely limit the mobility of the light species.

Gradual adjustment of the hopping ratio.—Finally, we briefly comment on results for a continuously adjusted hopping ratio t_H/t_L in the range 0.5 ... 0.2, which can be realized by changing the state-dependent lattice depth. Experimental results for the values $t_H/t_L \approx 0.05, 0.1, 0.2$ suggest that the functional dependence on the interaction parameter appears to be insensitive to t_H/t_L . We only observe a significant dependence of the maximum and minimum values of the transported fraction N_r/N , which can likely be attributed to the confinement strength κ/t_L (changes together with t_H/t_L) and the corresponding number of extended and localized states

⁶Absorption imaging is performed after quickly turning off the magnetic fields. By first repumping on the $^3P_0 \rightarrow ^3D_1$ line, we enable the detection of the heavy atoms on the broad $^1S_0 \rightarrow ^1P_1$ imaging transition. This process can be associated with losses of $\lesssim 30\%$ [111] depending on the local density. Moreover, the fast ramp-down of the magnetic fields projects some heavy-light on-site pairs into the molecular bound state, which appears to be dark to our detection technique. Hence, a precise reconstruction of the in-situ heavy atom density during the main transport experiment poses a challenge.

in the harmonic trap. Overall, the experimental results are consistent with the behavior of the heavy-light mixture in the first regime (see Fig 4.7 in Chapter 4), which features a rather weak dependence on the hopping ratio.

5.4 Late-time dynamics

Having identified strongly inhibited transport of the light species at early times, we now focus on the late-time dynamics in the system. In essence, we investigate whether the density of the light atoms eventually relaxes slowly (regime ② in Fig. 4.7), as predicted by the phenomenology of quasi-MBL and in agreement with thermalization at late times. To answer this question, we enhance our measurement sensitivity by slightly modifying our technique. First, we significantly reduce the transport distance to $\Delta x \approx 20d$ while retaining the translation speed $\approx 0.5dt_L/\hbar$. This distance is below the typical system size $\approx 30d$ and ensures that the atomic cloud stays connected, i. e., a significant fraction of both the heavy and light species remains mobile over the traversed transport range. Second, we reduce the effective number of light (or heavy) atoms per tube to $\mathcal{N} \approx 17$ by loading a smaller total number of atoms into the optical lattices. This reduction helps to lower the occupation of Stark-localized states at the edge of the trap. Following the translation of the trapping potential, we monitor the density of the light atoms for variable hold time $\tau \in [0, 400\hbar/t_L]$ and fixed trap minimum. This allows us to detect a potential relaxation towards the final trap center for atoms that remain at the initial position during the transport sequence due to interactions with the heavy species. In line with our theoretical study of quasi-MBL (see Section 4.3.2), we expect a significant dependence of the relaxation dynamics when adjusting the hopping ratio. Hence, we do not only vary the interaction strength $U/t_L \approx 0, -2, -10$ but also consider two distinct values $t_H/t_L \approx 0.1$ and 0.2 by selecting the appropriate lattice depth.

Figure 5.10 depicts the atomic density integrated perpendicular to the transport direction and obtained for early times $\tau = 0$ as well as late times $\tau \approx 330\hbar/t_L$ using the measurement techniques described above. First, we focus on the $t_H/t_L \approx 0.2$ dataset shown in Fig. 5.10(a) and discuss the time evolution at different interaction strengths. In the non-interacting limit $U/t_L \approx 0$, the density at early and late times is nearly identical, consistent with our expectations that relaxation should not be relevant here. For finite interaction strength $|U| > 0$, the evolution of the density shows a contrasting behavior. Initially, the suppression of transport can be qualitatively identified by observing that the center of mass shifts towards the initial trap minimum. At late times, an evident relaxation of the atomic density towards the final trap center can be observed, which appears to be more significant for the case with weaker interactions $U/t_L = -2$ [see the hatched region in Fig. 5.10(a)]. The $t_H/t_L \approx 0.1$ dataset shown in Fig. 5.10(b) indicates qualitatively similar behavior. However, the overall magnitude of relaxation is significantly reduced, probably caused by an increased relevance of Stark localization and a smaller fraction of atoms remaining mobile [$\kappa/t_L = 1.7(1) \times 10^{-2}$ compared to $1.10(7) \times 10^{-2}$ at $t_H/t_L \approx 0.2$]. In summary, our qualitative comparison of the density at two distinct hold times indicates that this observable indeed relaxes towards a state compatible with thermalization at late times.

We also record the density of the heavy species, which shows a similar form of relaxation,

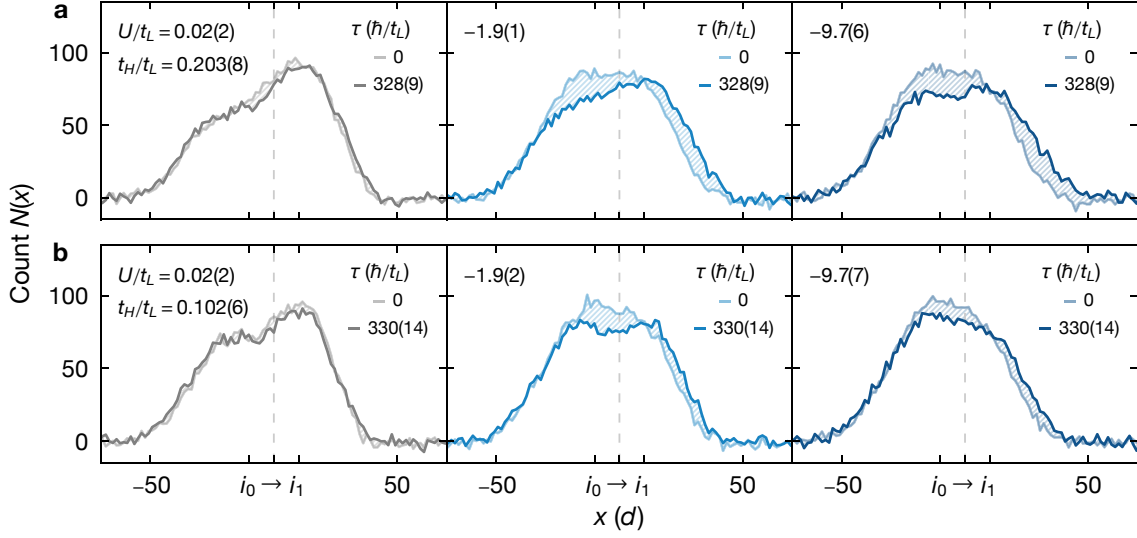


Figure 5.10 | Time evolution of the non-equilibrium density. Atomic density of the light species integrated perpendicular to the transport direction (solid lines) for the hopping ratios (a) $t_H/t_L = 0.203(8)$, (b) $0.102(6)$ and variable interaction strength U/t_L (see top-left label in each panel). Each curve corresponds to the mean of four normalized measurements and variable hold time $\tau \approx 0, 330\hbar/t_L$ after translating the trap minimum from i_0 to i_1 . The hatched region highlights the difference between the curves.

albeit less significant and only appreciable for the maximum hold time $\tau \approx 400\hbar/t_L$ (see Appendix E). This non-stationary density of the heavy species strongly suggests that indeed a finite number of heavy atoms remains mobile after translating the trap minimum. Therefore, we are convinced that our measurement probes the dynamical regime of the heavy-light mixture despite the presence of Stark localization at the edges of the trap. As discussed in Section 5.3.3, however, the density of the heavy species contains systematic uncertainties, which makes a quantitative analysis challenging. For the present measurement, the appreciable loss of heavy atoms (see Section 5.4.2) poses an additional difficulty for comparing the density at early and late times. Hence, we only consider the light species in our following quantitative discussion of relaxation in the system.

5.4.1 Probing relaxation time scales

To probe relaxation more systematically, we introduce a new observable calculated at variable hold time τ from the normalized density $n(x, \tau)$ with $\int dx n(x, \tau) = 1$. This observable is the time-dependent density deviation $\delta n(\tau)$, which rectifies the difference between the density of the light species after translating the trap minimum and at later times,

$$\delta n(\tau) = \left\{ \int dx n(x, \tau) [n(x, \tau) - n(x, 0)]^2 \right\}^{(1/2)}. \quad (5.14)$$

This dimensionless quantity takes positive values and grows monotonously for a continuous relaxation of the density towards the final trap minimum while a constant value of $\delta n(\tau)$ indicates a stationary state. In contrast to the transported fraction of atoms N_r/N or other observables such as the center of mass, the density deviation exhibits less sensitivity to the

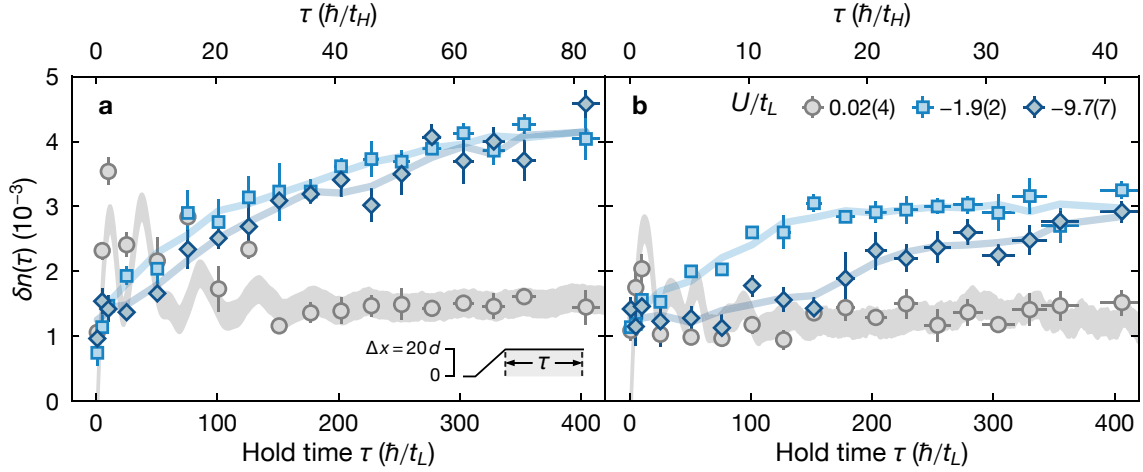


Figure 5.11 | Slow relaxation at late times. Density deviation $\delta n(\tau)$ of the light atoms with respect to the initial distribution after translating the trap minimum from i_0 to i_1 for variable hopping ratio (a) $t_H/t_L = 0.203(8)$, (b) $0.102(6)$ and interaction strength U/t_L [see legend in panel (b)]. Each data point corresponds to the mean of four individual measurements. Error bars (partly smaller than the marker size) denote the uncertainty of $\tau t_L/\hbar$ and standard error of $\delta n(\tau)$ as estimated from jackknife resampling [279]. Colored lines are three-point moving averages of the data points. The gray band shows the result of a numerical simulation in the non-interacting limit, and its height indicates the estimated systematic uncertainty in $\delta n(\tau)$ (see main text). The bottom-right inset in panel (a) illustrates the translation of the trap minimum and the hold time τ .

calibration of the trap minimum. This can be advantageous for the present measurement to significantly reduce the transport distance and ensure the atomic cloud remains connected.

Contribution of technical noise.—Since the density deviation rectifies any difference between $n(x, 0)$ and $n(x, \tau)$ this observable exhibits an increased sensitivity to technical noise. To quantify this dependence, we calculate $\delta n_M(\tau)$ for a variable number of measurements $N_M \in [0, 4]$, which are averaged to obtain $n(x, \tau)$. Assuming uncorrelated noise n_ϵ with vanishing expectation value $\langle n_\epsilon \rangle = 0$, finite variance $\langle n_\epsilon^2 \rangle > 0$, and vanishing third momentum $\langle n_\epsilon^3 \rangle > 0$, we find the contribution of n_ϵ by replacing $n(x, \tau) \rightarrow n(x, \tau) + n_\epsilon$ in Eq. (5.14),

$$\delta n_M^2(\tau) = \frac{\langle n_\epsilon^2 \rangle}{M} + \delta n^2(\tau). \quad (5.15)$$

The noise-free quantity $\delta n^2(\tau)$ can then be calculated from a numerical fit of Eq. (5.15) with the dataset generated by selecting a subset $M \leq 4$ for the averaging of $n(x, \tau)$. Following this procedure, we estimate the noise contribution $\delta n_{M=4}(\tau) - \delta n(\tau) \approx 0.4 \times 10^{-3}$ from a non-interacting dataset. This value remains well below the amplitude of the density deviation, and we consider it as an estimate of the systematic uncertainty in our measurement.

Time-evolution of the density deviation.—In Fig. 5.11, we show the density deviation for the same variable interaction strengths $U/t_L \approx 0, -2, -10$ and hopping ratios $t_H/t_L \approx 0.1, 0.2$ as the bare density discussed previously (see Fig. 5.10). First, we focus on the non-interacting case ($U \approx 0$), which we also simulate numerically with the methods presented in Section 5.2.1. Within this calculation, we average over non-integer offsets ≤ 0.5 of the trap minima. This

procedure accounts for the unstable relative offset between trap minimum and lattice sites in the experiment. At early times $\tau \lesssim 100$, the time evolution of the density deviation shows large-amplitude oscillatory dynamics for both hopping ratios. These transients originate from the absence of collisional damping in the non-interacting case and are qualitatively reproduced with our numerical calculation. A quantitative description would require considering the non-harmonic corrections of the confinement potential, which can affect the precise shape of the early-time dynamics significantly. At late times, the oscillations are damped and the density deviation takes a nearly constant value $\approx 1.5 \times 10^{-3}$. While the constant value would also correspond to a fully relaxed system, the inspection of the raw densities directly shows that the system remains stationary (see Fig. 5.10). At this point, atoms remaining at the initial trap minimum occupy Stark-localized states and, therefore, cannot relax efficiently [276].

For finite interaction strength, the density deviation allows us to analyze dynamics in the system quantitatively. Note that the density deviation does not encode the exact form of relaxation. However, our previous discussion of the bare density has clearly shown that the system does relax towards the final trap position—in agreement with a naive expectation of thermalization for this situation. The behavior of $\delta n(\tau)$ shows a strong dependence on the hopping ratio at finite interaction strength in contrast to the non-interacting setting. For $t_H/t_L \approx 0.2$, the time traces corresponding to $U/t_L \approx -2, -10$ relax similarly starting from initial values comparable to the non-interacting limit and reaching $\approx 4 \times 10^{-3}$ at late times [see Fig. 5.11(a)]. The relaxation can approximately be described by exponential saturation curves and appears slightly slower for the larger interaction parameter $U/t_L \approx -10$. For $t_H/t_L \approx 0.1$, the time traces of the two finite interaction parameters show a strongly deviating behavior. With the amplitude of the relaxation reduced to $\approx 3 \times 10^{-3}$, the $U/t_L \approx -2$ dataset shows a continuous relaxation comparable to the form observed for larger hopping ratio. In contrast, the $U/t_L \approx -10$ time trace shows initially almost no relaxation with a plateau-like feature for $\tau \lesssim 150\hbar/t_L$ at a constant value $\approx 1.5 \times 10^{-3}$. At later times $\tau \gg 150\hbar/t_L$, the density deviation signals the onset of a slow relaxation which appears to extend beyond the maximum observation window [see Fig. 5.11(b)].

Agreement with the phenomenology of quasi-MBL.—The observation of a plateau-like feature at small hopping ratio $t_H/t_L \approx 0.1$ and large interaction strength $U/t_L \approx -10$ is remarkable as it agrees with the expected phenomenology of quasi-MBL (see Section 4.3.2 in Chapter 4). In Ref. [108], the distinct features of the entanglement entropy are employed to extrapolate the time $\tau_3 \approx 270\hbar/t_L \sim \hbar U/t_L^2$ for the onset of the final metastable regime with extremely slow relaxation (see Fig. 4.8 in Chapter 4). This value is roughly compatible with the experimentally observed features for $\tau \gtrsim 250\hbar/t_L$. However, we have to emphasize that it remains unclear how much this extrapolation suffers from finite-size effects. Specifically, numerical simulations for intermediate system sizes and the experimental parameters show an increased smoothness with less distinct separations of time scales (see Appendix E). Nevertheless, the experimental data demonstrates that the hopping ratio and interaction strength dramatically influence the relaxation dynamics after translating the trap center. Even for the larger hopping ratio $t_H/t_L \approx 0.2$, the time scale of the dynamics extracted with an exponential fit is already much slower than the theoretical expectation for the mass-balanced case [108]. This underlines the relevance of the dynamical constraints in the system arising from the two different time

scales and finite interaction strength. Generally, the mass-balanced configuration could also be probed experimentally by replacing the state-dependent lattice with a state-independent lattice. However, this introduces systematic deviations, e. g., due to elevated relevance of dissipation (see Section 5.4.2), and is therefore left for future studies.

Let us emphasize that the density can most likely not completely relax to the shape of the non-interacting configuration. As we translate the trap minimum over a finite duration, some regions of the trap start to exhibit Stark-localization due to the large local gradient. The motion in these locations is subsequently frozen and a memory of the initial dynamics or their absence remains. Consequently, our measurement does not yield a strict statement concerning the ergodicity of the system or whether the eigenstate thermalization hypothesis holds here. We can only report on the observed relaxation as a potential signature of thermalization at late times.

5.4.2 Dissipative dynamics

Besides the closed-system dynamics according to the Hamiltonian in Eq. (5.1), dissipation is also present in the heavy-light mixture. To demonstrate that our observations are not caused by the finite dissipation in the system alone, we precisely characterize the relevant loss channels.

Off-resonant photon scattering.—The heavy atoms reside in the electronic 3P_0 state, and our implementation of the state-dependent lattice is operated only ≈ 20 nm detuned from the $^3P_0 \rightarrow ^3S_1$ transition wavelength (649.1 nm [115]), causing significant off-resonant photon scattering. To characterize this single-particle process, we first consider the relevant atomic states and transitions, which are also schematically shown in Fig. 5.12(a). Once a lattice photon excites a heavy atom to the 3S_1 state, it quickly decays back to either of the $^3P_{J=0,1,2}$ states with the ratio 15:40:45 according to the Clebsch-Gordan coefficients and the transition frequencies. Since atoms decaying to the metastable 3P_2 are likely lost, and the 3P_1 is short-lived, roughly 47% of the population is transferred to the 1S_0 ground state after scattering only two photons [see Fig. 5.12(b)].⁷ Hence, the off-resonant scattering of lattice photons has two consequences: single-particle loss (decay to 3P_2) and a heavy-to-light conversion (decay to 3P_1 and subsequently to 1S_0). We probe this experimentally by preparing a pure sample of heavy atoms and subsequently monitoring the atom number in the 3P_0 and 1S_0 state as a function of hold time. For this measurement, we employ a small magnetic bias field far away from the orbital Feshbach resonance in order to primarily probe single-particle decay. Figure 5.12(c) shows the resulting time traces in a $4.5(3)E_{\text{rec}}$ deep state-dependent lattice (SDL) together with an exponential fit, which confirms the approximative modeling introduced above.

Repeating our measurement for much smaller state-dependent lattice depths $V \ll 5E_{\text{rec}}$, we find time traces which significantly deviate from a simple exponential decay. To capture this deviation, we consider additional two-body loss, such that the combined process can be described by the differential equation

$$\frac{dN_H(t)}{dt} = -\Gamma N_H(t) - \beta N_H(t)^2. \quad (5.16)$$

⁷The off-resonant scattering also scrambles the population across different nuclear spin states. However, independent spin-sensitive measurements show that this effect becomes rather negligible on the time scales considered here.

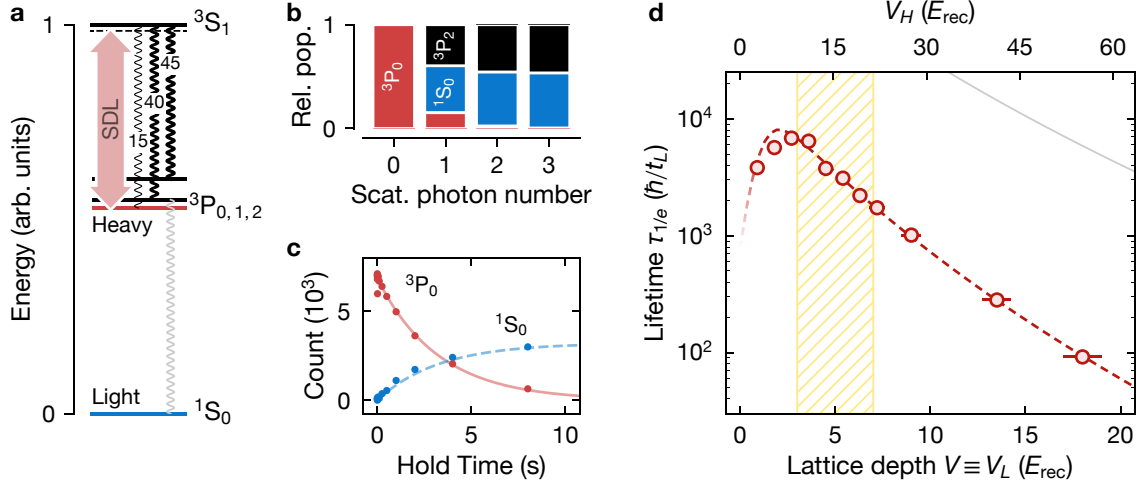


Figure 5.12 | Lifetime of heavy atoms in the state-dependent lattice. (a) Atomic energy levels (horizontal lines) and decay paths (wiggly lines) with estimated branching ratios. The red arrow corresponds to the off-resonant coupling of the state-dependent lattice (SDL). (b) Relative state population after scattering photons on the ${}^3P_0 \rightarrow {}^3S_1$ transition. (c) Measurement of the heavy atom decay in a $4.5(3)E_{\text{rec}}$ deep SDL. The red (blue) circles correspond to the number of detected heavy (light) atoms, and the red line shows a fit of an exponential decay curve. The blue dashed line is inferred from the fitted decay of the heavy atoms and the asymptotic population in 1S_0 [see panel (b)]. (d) Lifetime of the heavy species for variable lattice depth V determined from numerical fits similar to the one shown in panel (c). Error bars indicate the fit error of $\tau_{1/e}$ (smaller than marker size) and the uncertainty in V . The red dashed line corresponds to the model in Eq. (5.16), the solid gray line shows the vacuum lifetime ≈ 100 s [132], and the hatched region indicates typical lattice depths in the experiment.

Here, the decay rate takes the form $\Gamma = \Gamma_{\text{sc}}(V/E_{\text{rec}}) + \gamma$, where Γ_{sc} accounts for loss due to off-resonant scattering of SDL photons and γ describes independent background decay, e. g., induced by the perpendicular magic-wavelength lattices. The parameter β in Eq. (5.16) accounts for two-body losses of heavy atoms in the electronic 3P_0 state [19], which are suppressed by Pauli-blocking for on-site pairs. However, the experimental data suggests a finite contribution most likely originating from neighboring pairs in the lattice,

$$\beta = 2 \langle n_H \rangle \beta_{ee} \sum_{n=1} \int d\mathbf{r} |w_H(x)|^2 |w_H(x + nd)|^2 |w_y(y)|^4 |w_z(z)|^4. \quad (5.17)$$

Here, $w_H(x)$ denotes the Wannier function in the SDL with lattice spacing $d = \lambda/2$, $w_y(y) \approx w_z(z)$ the Wannier functions along the perpendicular magic-wavelength lattices with depth $\approx 30E_{\text{rec}}^m$, $\beta_{ee} = 4.8(2.1) \times 10^{-12}$ cm³/s the bare two-body loss coefficient [111], and $\langle n_H \rangle \approx 0.5$ the filling. Note that the filling could potentially display a complex dynamic due to the build-up of correlations [280]. For each SDL depth probed in the experiment, we fit the parameter Γ in Eq. (5.16) with β calculated according to Eq. (5.17) for $n \leq 3$. With this procedure and for $V \geq 2.7E_{\text{rec}}$, we find the numerical values $\Gamma_{\text{sc}} = 25(1)$ mHz and $\gamma = 179(13)$ mHz—in quantitative agreement with a previous measurement for ${}^{173}\text{Yb}$ [43]. Also, we extract an effective lifetime $\tau_{1/e}$ defined by $N_H(\tau_{1/e}) = N_H(0)/e$ for each lattice depth, as shown in Fig. 5.12(d).

These findings underline that a significant lattice depth $V \gtrsim 3E_{\text{rec}}$ is required to suppress the otherwise substantial two-body losses of neighboring pairs. On the other hand, the off-resonant photon scattering increases with V and hence, an optimal region at intermediate lattice depths $\sim 3E_{\text{rec}}$ exists. In this region, the $1/e$ lifetime related to the dynamical time scale \hbar/t_L takes its maximal value and far exceeds $10^3\hbar/t_L$, allowing for long enough observation times in our measurements of the density dynamics.

Few-body losses close to the orbital Feshbach resonance.—Since we lack a precise model for the loss mechanisms at the orbital Feshbach resonance,⁸ we focus on determining the overall particle loss at a variable magnetic field. To this end, we perform an independent measurement where the heavy-light mixture is held in the vicinity of the orbital Feshbach resonance and a constant SDL depth of $\approx 3.6E_{\text{rec}}$. We monitor the total number of atoms (both light and heavy) and numerically fit the short-term time dependence with the linear relation

$$N(t) \equiv N_L(t) + N_H(t) = N_0 - Rt. \quad (5.18)$$

Here, the initial atom count N_0 and the linear decay rate R are the two fit parameters. The experimental data suggests negligible atom loss with $R \approx 0.12(5) \times 10^{-3} t_L/\hbar$ for the relevant range of magnetic fields 1450-1600 G. The relative short observation times $\lesssim 400$ ms are limited by the maximum duration our magnetic field coils can sustain the large currents of ≈ 300 A. For smaller magnetic fields towards the location of the orbital Feshbach resonance [111], losses increase approximately linearly with the magnetic field and reach the value $R = 0.55(7) \times 10^{-3} t_L/\hbar$ at 1300 G. Additionally, we verify that the observed decay rate R only weakly depends on the SDL depth by adjusting it over the range $3-7E_{\text{rec}}$ at fixed magnetic field 1350 G. Overall, we do not expect any significant dependence of loss on the chosen interaction parameter considering the invariant behavior for the relevant range of magnetic fields.

Atom loss during the dynamical measurements.—Finally, we consider the evolution of the atom number of both the light and heavy species during the measurements of the density deviation discussed in the previous section. Figure 5.13 shows the number of atoms for the hopping ratio $t_H/t_L \approx 0.1, 0.2$ and the interaction parameters $U/t_L \approx 0, -2, -10$. We do find a significant reduction of $\approx 20-30\%$ of the heavy atoms over the maximum hold time $\tau \approx 400\hbar/t_L$, which is more pronounced for the smaller hopping ratio. This is expected from our measurements in the single-particle limit, where the lifetime for the lattice depth $V \approx 4.7E_{\text{rec}}$ (corresponding to $t_H/t_L \approx 0.1$) is significantly reduced [see Fig. 5.12(b)]. For $t_H/t_L \approx 0.2$ and $U/t_L = -10$, these losses become much more significant, which can probably be attributed to the magnetic field ≈ 1410 G in close vicinity of the orbital Feshbach resonance. The number of light atoms remains relatively stable, and no significant loss can be detected, which can be partly attributed to heavy atoms converted to light atoms by off-resonant photon scattering. We conclude that the rather weak dependence on the hopping ratio and interaction strength suggests that the observations reported in the previous section are unlikely to be caused by dissipation. Instead, they are signatures of the strongly constrained dynamics in the heavy-light mixture.

⁸A likely loss channel could be three-body recombination [133], where a heavy and light atom form a molecular state and a third atom carries away the excess binding energy ($L + H + \alpha \rightarrow LH + \alpha$ with $\alpha = L, H$).

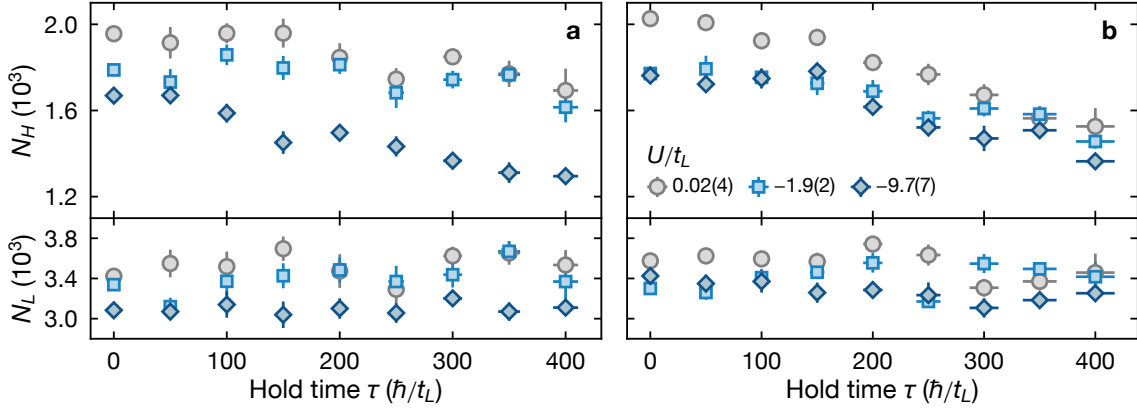


Figure 5.13 | Atom loss during the density dynamics measurement. Detected number of light (N_L) and heavy (N_H) atoms during the density dynamics shown in Fig. 5.11 for the hopping ratios (a) $t_H/t_L = 0.203(8)$, (b) $0.102(6)$ and variable interaction strength U/t_L [see legend in panel (b)]. Note that N_H does not faithfully represent the absolute number of heavy atoms due to our detection technique (see main text). To reduce visual clutter, data points spaced less than $50\hbar/t_L$ are binned.

5.5 Discussion

This chapter has described the experimental realization of the mass-imbalanced Fermi-Hubbard model with fully tunable hopping ratio and interaction strength [108]. We have identified a significant suppression of transport for strong interactions and large mass imbalance. Moreover, the density deviation observable has allowed us to reveal the slow relaxation of the system at late times. For the largest mass imbalance and interaction strength realized in the experiment, we find the emergence of metastability at early times and the onset of extremely slow relaxation at intermediate times. These results are in qualitative agreement with theoretical predictions and therefore suggest that the mass-imbalanced Fermi-Hubbard model exhibits ergodic dynamics but features an extremely slow time scale for thermalization.

For follow-up studies, the experimental findings could be extended by significantly reducing the strength of the harmonic confinement so that the heavy species remains mobile across a larger region of the trap. In this way, features of the dynamical behavior arising due to heavy-light interactions and Stark localization at the edge of the trap could likely be identified individually. A simple approach to reduce the confinement could be to increase the laser beam diameters of the perpendicular state-independent lattice axes. Of course, the maximum available laser power presents a fundamental limit but this approach should still allow for a significant increase of typical system sizes. However, the effective confinement $\kappa/t_H \gg \kappa/t_L$ would remain much larger for the heavy species. To introduce an equal confinement strength for both species, part of the harmonic potential could be canceled selectively for the heavy species with an additional blue-detuned dipole trap beam such that $\kappa/t_L \approx \kappa/t_H$.

Conclusions and outlook

The work presented in this thesis firmly establishes ytterbium quantum gases as a powerful platform for probing multiorbital many-particle phenomena. By utilizing the electronic ground and metastable clock state, we have realized an orbital degree of freedom in interacting ytterbium mixtures confined by optical potentials of different dimensionality. Specifically, the techniques developed within this thesis have provided experimental access to the quasiparticle properties of multiorbital Fermi polarons and non-equilibrium dynamics in the mass-imbalanced Fermi-Hubbard model.

The first experiment presented in this thesis has utilized the orbital Feshbach resonance in ^{173}Yb to systematically study the polaron problem in a two-dimensional Fermi gas [109]. To this end, the preparation of strongly spin-imbalanced Fermi gases has been the experimental starting point for this quasiparticle that forms when a mobile impurity is immersed into a Fermi sea. To analyze the quasiparticle properties, we have driven the minority component to the strongly interacting regime by employing clock-line spectroscopy. In this way, we have precisely determined the quasiparticle energy of attractive and repulsive polaron for various interaction strengths. These results agree well with theoretical predictions within the ladder approximation, underlining the accuracy of this theory, also for two dimensions and the complex interactions across the orbital Feshbach resonance. For the metastable repulsive polaron, we have identified particularly long lifetimes exceeding hundreds of Fermi times, which could be favorable for realizing strongly repulsive Fermi gases.

For the first time, we have observed coherent Rabi oscillations into the attractive and repulsive polaron branches in two dimensions, complementing previous experiments with alkali atoms [74, 75]. A theoretical study has later utilized a novel variational approach to model the real-time dynamics of Rabi oscillations in our experiment [110]. In this way, results from a three-dimensional implementation [76] and our measurements have enabled a significantly improved understanding of the repulsive polaron. In particular, its quasiparticle width can be associated with many-body dephasing, which also dominates the observed damping of Rabi oscillations in the experiment [110].

The developed control and measurement techniques provide an excellent starting point for future experiments. In particular, this applies to investigating the many-body physics of a spin-balanced Fermi gas across the orbital Feshbach resonance. Here, the nature of the resonance is expected to give rise to especially rich physics, such as two-band superfluidity and the elusive breached pair phase with unusual pairing in momentum space [281–286]. A potential challenge for experiments exploring this direction would be to overcome the intrinsic dissipation in the orbital mixture or to identify probes in the transient regime [287].

Other interesting directions to explore build on impurity physics, where the presence of strong spin-exchange interaction in ytterbium allows studying impurity spins coupled to a bath [45–47, 59, 288]. Moreover, state-dependent lattices could directly tune the mobility of the impurities such that examining the crossover from mobile to localized magnetic moments becomes feasible [43]. In this limit, the Kondo problem could be investigated with ultracold atoms [19, 154, 155]. Even in the absence of spin-exchange interactions, a system with localized impurities offers access to Anderson’s orthogonality catastrophe [62, 82, 289, 290]. Here, a quench of the impurity-bath interactions leads to a characteristic response of the medium as the system is driven into a final state (nearly) orthogonal to its initial non-interacting state [289, 290]. In this context, we also highlight recent developments with alkaline-earth(-like) atoms in tweezer arrays, which have been demonstrated in multiple experiments [291–293]. Future endeavors might enable this novel platform to complement optical lattice techniques in settings similar to quantum gas experiments but with faster cycle times and local state-dependent potentials [294]. Such a system could be an ideal platform for careful studies of impurity-bath coupling with full control over the impurity and bath degrees of freedoms.

The second experiment within this thesis has probed the non-equilibrium dynamics of heavy and light particles in the one-dimensional mass-imbalanced Fermi-Hubbard model. Our novel and robust implementation with an orbital mixture of ^{171}Yb atoms in a state-dependent optical lattice has enabled the observation of dynamics for hundreds of tunneling times. Moreover, we have realized mass-imbalance and interaction-strength tunability to probe for parametric dependence of thermalization time scales, which have been extensively studied with numerical simulations [104, 105]. Such studies have suggested the emergence of metastability in the relaxation dynamics, which we have examined experimentally by recording the density dynamics after gradually translating the external trapping potential. At short times, compared to the tunneling time scale of the heavy species, we have found a strong suppression of transport for the light species, which depends directly on the heavy-light interaction strength. This observation can be understood as a single-particle localization effect since the heavy species initially takes on the role as a disorder potential for the light one. In contrast, we have identified finite relaxation at late times, strongly suggesting that the system exhibits ergodic behavior and eventually thermalizes. Our results for variable interaction strengths and mass imbalances demonstrate that the relaxation time scales strongly depend on these parameters—qualitatively consistent with numerical simulations of much smaller systems. Reducing the harmonic confinement strength in the experiment should allow future observations of signatures in the heavy species density, which have not been accessible in our current implementation.

Our experiments have established a promising platform to study extremely slow thermalization. While the behavior of this system is consistent with ergodicity at late times, the emergence of metastability makes it distinct from other types of ergodic systems, which exhibit much faster thermalization [105, 219, 248]. At the same time, the observed dynamics are distinct from a “true” many-body localized phase, which features finite memory of initial states for arbitrarily long times [93]. Our regime, dubbed quasi-many-body localization [105], presents a notable extension to the classification of thermalization in isolated quantum many-body systems and shares similarities with other forms of constrained quantum matter [264–266, 295, 296]. An interesting question concerns whether future theoretical studies could apply new approaches to

the problem and capture dynamical properties beyond the limits of current numerical calculations. Few-body bound states could provide the starting point for such an analysis in the context of the mass-imbalanced Fermi-Hubbard model [268]. Notably, their role could also be probed in the experiment by introducing a variable population imbalance between light and heavy atoms. Such an experimental study would also naturally benefit from our state preparation techniques developed for population imbalance within the context of the Fermi polaron.

The mass-imbalanced Fermi-Hubbard model is also believed to feature interesting dynamical behavior close to mass balance, where it becomes integrable [297]. A tunable mass imbalance close to one presents a unique opportunity to address the intriguing question of how emergent integrability affects thermalization and transport [219]. Conceptually related studies of strongly interacting dipolar atoms have identified a separation of time scales for thermalization close to an integrable point [242]. Similar experimental measurements for the Fermi-Hubbard model could be realized with an orbital ytterbium mixture in a state-independent optical lattice by slightly detuning the lattice laser and introducing a minuscule mass imbalance.

In conclusion, our experiments have illustrated how rich quantum many-body physics can arise in the presence of an orbital degree of freedom. Due to the relevance of orbital physics in solid-state materials, various exciting opportunities emerge for orbital mixtures of ytterbium atoms. In particular, recent advancements should allow engineering an impurity-bath coupling, which features the essential physics of the Kondo effect with dominant spin-exchange interaction between localized and itinerant particles [43, 45, 61, 154, 155]. This will open up exciting new research directions for multiorbital quantum gases and pave the way towards probing even richer phenomena in the Kondo lattice [5].

Appendices

Appendix A Derivation of the Fermi polaron self-energy

Throughout this section, we set $\hbar \equiv 1$, which generally does not affect our final results given in units of the Fermi energy $E_F = k_F^2/(2m)$ with the atomic mass m . Note that we exclusively consider a two-dimensional medium for the following calculations, as discussed in Chapter 2.

A.1 Zero temperature and zero momentum

We first present the calculation for the Fermi polaron at zero momentum and in a zero-temperature medium. As discussed in Chapter 2 (see Section 2.2.1), the coupling constant g characterizes the two-body problem and is given by [182]

$$-\frac{1}{g} = \sum_k^\Lambda \frac{1}{\epsilon_b + k^2/m}. \quad (\text{A.1})$$

Here, ϵ_b is the binding energy of the two-body bound state and Λ is a cutoff, which will be sent to infinity in the many-body expressions. For the self-energy $\Sigma(\mathbf{p} = 0, E)$ of the zero-momentum Fermi polaron, we find according to Eq. (2.14) from Chapter 2,

$$\begin{aligned} \Sigma(0, E) &= \sum_{q < k_F} \left\{ \frac{1}{g} + \sum_{k > k_F}^\Lambda \frac{1}{-E + (2m)^{-1} [k^2 - q^2 + (\mathbf{k} - \mathbf{q})^2]} \right\}^{-1} \\ &= \sum_{q < k_F} \left\{ - \sum_{k < k_F} \frac{1}{\epsilon_b + k^2/m} + \sum_{k > k_F}^\Lambda \frac{1}{-E + (2m)^{-1} [k^2 - q^2 + (\mathbf{k} - \mathbf{q})^2]} - \frac{1}{\epsilon_b + k^2/m} \right\}^{-1}. \end{aligned} \quad (\text{A.2})$$

In the thermodynamic limit, we convert the sums to integrals, $\sum_{k=k_0}^\Lambda \rightarrow (2\pi)^{-2} \int_{k_0}^\Lambda d\mathbf{k}$, and send the cutoff to infinity, $\Lambda \rightarrow \infty$. With this procedure, we arrive at the integral equation

$$\begin{aligned} \Sigma(0, E) &= \int_{q < k_F} d\mathbf{q} \left\{ - \int_{k < k_F} d\mathbf{k} \frac{1}{\epsilon_b + k^2/m} \right. \\ &\quad \left. + \int_{k > k_F} d\mathbf{k} \frac{1}{-E + (2m)^{-1} [k^2 - q^2 + (\mathbf{k} - \mathbf{q})^2]} - \frac{1}{\epsilon_b + k^2/m} \right\}^{-1}. \end{aligned} \quad (\text{A.3})$$

Here, we note that the factor $(2\pi)^2$ from replacing the sums cancels for the present combination of outer and inner integrals.

We solve the integrals inside the curly brackets, and for the first one, we find

$$\int_0^{2\pi} d\varphi \int_0^{k_F} dk k \frac{1}{\epsilon_b + k^2/m} = \pi m \ln \left(1 + 2 \frac{E_F}{\epsilon_b} \right). \quad (\text{A.4})$$

Defining the angle $\varphi = \angle(\mathbf{k}, \mathbf{q})$ between the two vectors yields $\mathbf{k} \cdot \mathbf{q} = kq \cos \varphi$, and we solve the second integral using this result

$$\begin{aligned} & \int_0^{2\pi} d\varphi \int_{k_F}^{\infty} dk k \left(-E + \frac{k^2}{m} - \frac{kq}{m} \cos \varphi \right)^{-1} - k \left(\epsilon_b + \frac{k^2}{m} \right)^{-1} \\ &= 2m \int_0^{2\pi} d\varphi \int_1^{\infty} dk' k' \left(-\frac{E}{E_F} + 2k'^2 - 2k'q' \cos \varphi \right)^{-1} - k' \left(\frac{\epsilon_b}{E_F} + 2k'^2 \right)^{-1} \\ &= 4\pi m \int_1^{\infty} dk' k' \left\{ \pm \left[\left(\frac{E}{E_F} - 2k'^2 \right)^2 - 4k'^2 q'^2 \right]^{-1/2} \right\} - k' \left(\frac{\epsilon_b}{E_F} + 2k'^2 \right)^{-1} \\ &= 2\pi m \int_1^{\infty} dx \left\{ \pm \left[\left(\frac{E}{E_F} - 2x \right)^2 - 4xq'^2 \right]^{-1/2} \right\} - \left(\frac{\epsilon_b}{E_F} + 2x \right)^{-1} \\ &= \pi m \left\{ \ln \left(\frac{\epsilon_b}{E_F} + 2 \right) - \ln \left[1 - \frac{E}{2E_F} - \frac{q'^2}{2} \pm \sqrt{\left(1 - \frac{E}{2E_F} \right)^2 - q'^2} \right] \right\}. \end{aligned} \quad (\text{A.5})$$

Here, we have defined the variables $q' = q/k_F$, $k' = k/k_F$, and $x = k'^2$. Finally, we determine the self-energy by combining the solutions of the two inner integrals,

$$\frac{\Sigma(0, E)}{E_F} = 2 \int_0^1 dy \left\{ \ln \left(\frac{\epsilon_b}{E_F} \right) - \ln \left[1 - \frac{E}{2E_F} - \frac{y}{2} \pm \sqrt{\left(1 - \frac{E}{2E_F} \right)^2 - y} \right] \right\}^{-1}, \quad (\text{A.6})$$

where $y = (q/k_F)^2 q'^2$ and $\pm = \text{sgn Re} [1 - E/(2E_F)]$. Note that the outer integral transforms as $E_F^{-1} \int_{q < k_F} d\mathbf{q} \rightarrow (2m/k_F^2) \times 2\pi m \int_0^{k_F} dq q \rightarrow \pi m \int_0^1 dy$, and that we perform the integration over y numerically.

A.2 Zero temperature and finite momentum

Here, we proceed with a description of the finite-momentum Fermi polaron. We consider the self-energy for an impurity at momentum \mathbf{p} ,

$$\Sigma(\mathbf{p}, E) = \int_{q < k_F} d\mathbf{q} \left\{ \int_{k > k_F} d\mathbf{k} \frac{1}{-E + (2m)^{-1} [k^2 - q^2 + (\mathbf{k} - \mathbf{p} - \mathbf{q})^2]} - \frac{1}{\epsilon_b + k^2/m} \right\}^{-1}. \quad (\text{A.7})$$

The inner integral can be solved using a change of variables,

$$\begin{aligned}
& \int_{k>k_F} d\mathbf{k} \frac{1}{-E + (2m)^{-1} [k^2 - q^2 + (\mathbf{k} - \mathbf{p} - \mathbf{q})^2]} - \frac{1}{\epsilon_b + k^2/m} \\
&= \int_0^{2\pi} d\varphi \int_{k_F}^{\infty} dk k \left\{ -E + \frac{1}{2m} [k^2 - q^2 + (\mathbf{k} - \tilde{\mathbf{q}})^2] \right\}^{-1} - k \left(\frac{\epsilon_b}{E_F} + 2k^2 \right)^{-1} \quad (\text{A.8}) \\
&= \int_0^{2\pi} d\varphi \int_{k_F}^{\infty} dk k \left(-\tilde{E} + \frac{k^2}{m} - \frac{k\tilde{q}}{m} \cos \varphi \right)^{-1} - k \left(\frac{\epsilon_b}{E_F} + 2k^2 \right)^{-1}
\end{aligned}$$

with $\tilde{\mathbf{q}} = \mathbf{q} + \mathbf{p}$ and $\tilde{E} = E + q^2/(2m) - \tilde{q}^2/(2m)$. The remaining integration can be performed analogously to the zero-momentum calculation such that we obtain for the self-energy at momentum $\mathbf{p}' = \mathbf{p}/(\hbar k_F)$,

$$\begin{aligned}
\frac{\Sigma(\mathbf{p}', E)}{E_F} &= \frac{2}{\pi} \int_0^{2\pi} d\theta \int_0^1 dq' q' \left\{ \ln \left(\frac{\epsilon_b}{E_F} \right) - \ln \left[1 - \frac{\tilde{E}}{2E_F} - \frac{r^2}{2} \pm \sqrt{\left(1 - \frac{\tilde{E}}{2E_F} \right)^2 - r^2} \right] \right\}^{-1} \\
&= \frac{2}{\pi} \int_0^{2\pi} d\theta \int_0^1 dq' q' \left\{ \ln \left(\frac{\epsilon_b}{E_F} \right) - \ln \left[E(q') \pm \sqrt{\left(E(q') + \frac{r^2}{2} \right)^2 - r^2} \right] \right\}^{-1}, \quad (\text{A.9})
\end{aligned}$$

with the angle $\theta = \angle(\mathbf{q}, \mathbf{p})$, $r = (q' + p' \cos \theta)$, $E(q') = 1 - [E/E_F + q'^2]/2$, and the symbol $\pm = \text{sgn Re}[E(q') + r^2/2]$. In contrast to the zero-momentum result, we perform the integral over θ with numerical techniques as well.

A.3 Finite temperature and zero momentum

Finally, we consider the case of a zero-momentum impurity in a finite-temperature medium. At finite temperature, the integration goes over all momenta (\mathbf{q} and \mathbf{k}) weighted with the Fermi-Dirac distribution $F(x, T) = [e^{(x-\mu)/(k_B T)} + 1]^{-1}$. For the two-dimensional case considered here, the chemical potential takes the form $\mu = k_B T \ln [e^{E_F/(k_B T)} - 1]$ at temperature T . With these considerations, we find the self-energy

$$\Sigma(0, E; T) = \int d\mathbf{q} \frac{F[q^2/(2m), T]}{\mathcal{I}(q, T)}, \quad (\text{A.10})$$

and the expression

$$\mathcal{I}(q, T) = \int d\mathbf{k} \frac{1 - F[k^2/(2m), T]}{-E + (2m)^{-1} [k^2 - q^2 + (\mathbf{k} - \mathbf{q})^2]} - \frac{1}{\epsilon_b + k^2/m}. \quad (\text{A.11})$$

In Eqs. (A.5) and (A.6), we have derived an analytical solution for the case of zero temperature and, therefore, also for $\mathcal{I}(q, T = 0)$. Thus, we can consider the finite-temperature contribution

$\Delta_T(q) = \mathcal{I}(q, T) - \mathcal{I}(q, T = 0)$ to obtain $\mathcal{I}(q, T)$ at arbitrary temperature. By using the results from Eq. (A.5), we find the finite-temperature contribution,

$$\Delta_T(q) = \mathcal{I}(q, T) - \mathcal{I}(q, T = 0) = \int d\mathbf{k} \frac{F[k^2/(2m), T = 0] - F(k^2/(2m), T)}{-E + (2m)^{-1} [k^2 - q^2 + (\mathbf{k} - \mathbf{q})^2]} \quad (\text{A.12})$$

$$\Leftrightarrow \Delta_T(y) = \pi m \int_0^\infty dx \frac{F(xE_F, 0) - F(xE_F, T)}{\pm \sqrt{[x - E/(2E_F)]^2 - xy}}, \quad (\text{A.13})$$

with $\pm = \text{sgn Re}[x - E/(2E_F)]$ in the last equation. Combining the finite-temperature contribution and Eq. (A.6),

$$\mathcal{I}(y, T) = \pi m \left\{ \ln\left(\frac{\epsilon_b}{E_F}\right) - \ln\left[1 - \frac{E}{2E_F} - \frac{y}{2} \pm \sqrt{\left(1 - \frac{E}{2E_F}\right)^2 - y}\right] \right\} + \Delta_T(y), \quad (\text{A.14})$$

yields the expression for the self-energy given in the main text,

$$\frac{\Sigma(0, E; T)}{E_F} = 2 \int_0^1 dy F(yE_F, T) \left\{ \ln\left(\frac{\epsilon_b}{E_F}\right) - \ln\left[E' - \frac{y}{2} \pm \sqrt{E'^2 - y}\right] + \frac{\Delta_T(y)}{\pi m} \right\}^{-1}. \quad (\text{A.15})$$

Here, $E' = 1 - E/(2E_F)$, and the symbol \pm is redefined with $\pm = \text{sgn Re } E'$.

A.4 Two-channel model

As discussed in Chapter 2 (see Section 2.3.2), the two-channel model provides an accurate description of the multiorbital Fermi polaron. The additional complexity of the orbital interactions is captured by the effective range in two dimensions, R_{2D} .

The relation between the coupling constant g , the detuning of the closed channel ν , and the binding energy \mathcal{E}_b of the two-body bound state is given as [198]

$$\frac{\nu + \mathcal{E}_b}{g^2} = \sum_k^\Lambda \frac{1}{\mathcal{E}_b + k^2/m}. \quad (\text{A.16})$$

The self-energy of the zero-momentum polaron in the two-channel model takes the form [197]

$$\Sigma(0, E) = \sum_{q < k_F} \left\{ \frac{E - \nu + q^2/(4m)}{g^2} + \sum_{k > k_F}^\Lambda \frac{1}{-E + (2m)^{-1} [k^2 - q^2 + (\mathbf{k} - \mathbf{q})^2]} \right\}^{-1}. \quad (\text{A.17})$$

With the above renormalization procedure and $g^2 = 4\pi/(m^2 R_{2D}^2)$ [198], we find for the first term of the above expression,

$$\frac{E - \nu + q^2/(4m)}{g^2} = \frac{E + q^2/(4m) + \mathcal{E}_b}{g^2} - \sum_k^\Lambda \frac{1}{\mathcal{E}_b + k^2/m} \quad (\text{A.18})$$

$$\begin{aligned}
\frac{E - \nu + q^2/(4m)}{g^2} &= \frac{m^2}{4\pi} R_{2D}^2 \left(E + \frac{q^2}{4m} + \mathcal{E}_b \right) - \sum_k^\Lambda \frac{1}{\mathcal{E}_b + k^2/m} \\
&= m \frac{(R_{2D}k_F)^2}{8\pi} \left(\frac{E}{E_F} + \frac{1}{2} \frac{q^2}{k_F^2} + \frac{\mathcal{E}_b}{E_F} \right) - \sum_k^\Lambda \frac{1}{\mathcal{E}_b + k^2/m}. \quad (\text{A.19})
\end{aligned}$$

In the thermodynamic limit (sum replacement and $\Lambda \rightarrow \infty$), we therefore obtain

$$\begin{aligned}
\frac{\Sigma(0, E)}{E_F} &= \frac{2m}{k_F^2} 2\pi \int_0^{k_F} dq q \left\{ (2\pi)^2 m \frac{(R_{2D}k_F)^2}{8\pi^2} \left(\frac{E}{E_F} + \frac{1}{2} \frac{q^2}{k_F^2} + \frac{\mathcal{E}_b}{E_F} \right) - \int d\mathbf{k} \frac{1}{\mathcal{E}_b + k^2/m} \right. \\
&\quad \left. + \int_{k>k_F} d\mathbf{k} \frac{1}{-E + m^{-1}(k^2 + \mathbf{k} \cdot \mathbf{q})/m} \right\}^{-1} \\
&= 2 \int_0^1 dy \left\{ (R_{2D}k_F)^2 \left(\frac{E}{2E_F} + \frac{y}{4} + \frac{\mathcal{E}_b}{2E_F} \right) + \ln \left(\frac{\epsilon_b}{E_F} \right) \right. \\
&\quad \left. - \ln \left[1 - \frac{E}{2E_F} - \frac{y}{2} \pm \sqrt{\left(1 - \frac{E}{2E_F} \right)^2 - y} \right] \right\}^{-1}. \quad (\text{A.20})
\end{aligned}$$

Here, we have used the results from Eq. (A.5) and $y = (q/k_F)^2$. Note that the factor of $(2\pi)^2$ in the first line of Eq. (A.20) arises due to the replacement of the sums, i. e., $\sum_{k=k_0}^\Lambda \rightarrow (2\pi)^{-2} \int_{k_0}^\Lambda d\mathbf{k}$. For the two-channel model, the interaction parameter $\ln(k_F a_{2D})$ is related to the bound-state energy with $\mathcal{E}_b/E_F = 2W\left[(R_{2D}k_F)^2 e^{-2\ln(k_F a_{2D})}\right]/(R_{2D}k_F)^2$, where $W(x)$ denotes the Lambert W function [see Eq. (2.31) in Chapter 2]. To illustrate how the spectral function changes for finite effective range, we show a direct comparison in Fig. A.1.

Appendix B Derivation of the low-energy scattering amplitude

Throughout this section, we set $\hbar \equiv 1$ and consider lengths in units of the characteristic harmonic oscillator length $l_z = 1/\sqrt{m\omega_z}$ as well as energies in units of the (angular) harmonic oscillator trapping frequency ω_z . The central result of this section is the low-energy expansion of the scattering amplitude in quasi-two dimensions [see Eq. (2.25) from Chapter 2]. This yields the magnetic-field-dependent scattering length a_{2D} and effective range R_{2D} in two dimensions for the orbital Feshbach resonance. The derivation in this section follows the results discussed by Adlong et al. [110].

For the low-energy limit, $|x| \ll 1$, we approximate the transcendental function $\mathcal{F}(x)$ [182],

$$\mathcal{F}(x) = \frac{1}{\sqrt{2\pi}} \ln \left(\frac{\pi x}{B} \right) + \frac{\ln 2}{\sqrt{2\pi}} x + \mathcal{O}(x^2). \quad (\text{B.1})$$

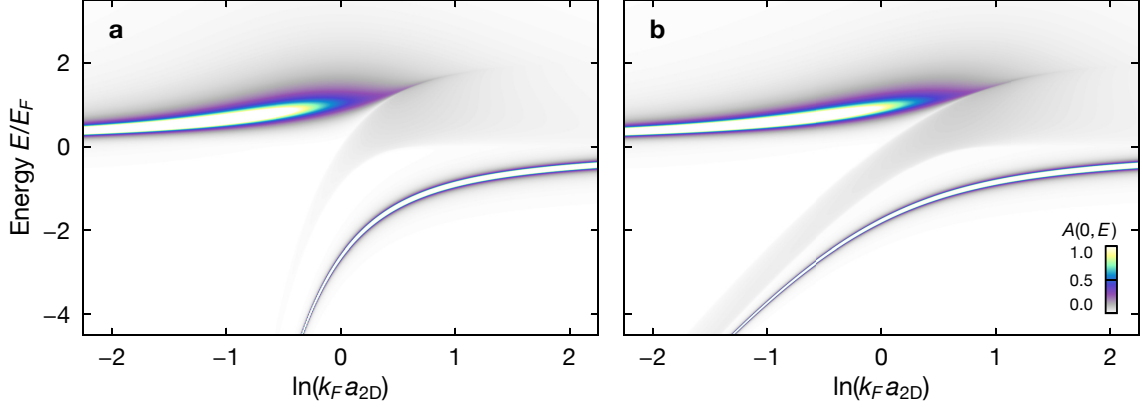


Figure A.1 | Single- and two-channel description of the Fermi polaron. Comparison of the spectral function $A(\rho = 0, E)$ for the (a) single-channel ($k_F R_{2D} = 0$) and (b) two-channel model ($k_F R_{2D} = 1$). Note that a finite broadening has been applied to the spectrum with the replacement $E \rightarrow E + 0.01iE_F$, and the plot range is truncated.

Here, we define the numerical factor $B \approx 0.905$ [182]. Expanding $\mathcal{F}(-E + \delta)$ and $\mathcal{F}(-E)$ up to order $\mathcal{O}(E)$ yields the following approximations,

$$\mathcal{F}(-E) \stackrel{E \rightarrow 0}{\approx} \frac{1}{\sqrt{2\pi}} \ln(-\pi E/B) - \frac{\ln 2}{\sqrt{2\pi}} E = \frac{1}{\sqrt{2\pi}} [-i\pi - \ln(\pi E/B) - E \ln 2] \quad (\text{B.2})$$

$$\mathcal{F}(-E + \delta) \stackrel{E \rightarrow 0}{\approx} \mathcal{F}(\delta) - \left. \frac{d\mathcal{F}(x)}{dx} \right|_{x=\delta} E = \mathcal{F}(\delta) - \mathcal{F}'(\delta)E. \quad (\text{B.3})$$

Here, $\mathcal{F}'(x)$ denotes the derivative of $\mathcal{F}(x)$ and can be calculated from

$$\mathcal{F}'(x) = \frac{d}{dx} \int_0^\infty du \frac{1}{\sqrt{4\pi u^3}} \left[1 - \frac{e^{-xu}}{\sqrt{(1 - e^{-2u})/(2u)}} \right] = - \int_0^\infty du \frac{1}{\sqrt{4\pi u}} \frac{e^{-xu}}{\sqrt{(1 - e^{-2u})/(2u)}}. \quad (\text{B.4})$$

We now use the effective range replacement

$$a_\pm^{-1} \rightarrow a_\pm^{-1} - \frac{r_\pm}{2} \left(E - \frac{\delta}{2} + \frac{1}{2} \right) \stackrel{E \rightarrow 0}{\approx} a_\pm^{-1} - \frac{1}{4} r_\pm (1 - \delta) \equiv \alpha_\pm^{-1} \quad (\text{B.5})$$

and with $\rho_\pm \equiv r_\pm$ as well as $\Delta \equiv \delta$, we find for the first term in the above expression,

$$\frac{(a_- a_+)^{-1} - \frac{1}{2} \mathcal{F}(-E + \delta) (a_-^{-1} + a_+^{-1})}{a_-^{-1} + a_+^{-1} - 2\mathcal{F}(-E + \delta)} \stackrel{E \rightarrow 0}{\approx} \left\{ \frac{(\alpha_- \alpha_+)^{-1} - \frac{1}{2} \mathcal{F}(\Delta) (\alpha_-^{-1} + \alpha_+^{-1})}{\alpha_-^{-1} + \alpha_+^{-1} - 2\mathcal{F}(\Delta)} - \frac{E [\alpha_-^{-1} - \mathcal{F}(\Delta)]^2 \rho_+ + [\alpha_+^{-1} - \mathcal{F}(\Delta)]^2 \rho_- + (\alpha_-^{-1} - \alpha_+^{-1})^2 \mathcal{F}'(\Delta)}{2 [\alpha_-^{-1} + \alpha_+^{-1} - 2\mathcal{F}(\Delta)]^2} \right\} \equiv \mathcal{A}_0 - \frac{1}{2} \mathcal{A}_1 E. \quad (\text{B.6})$$

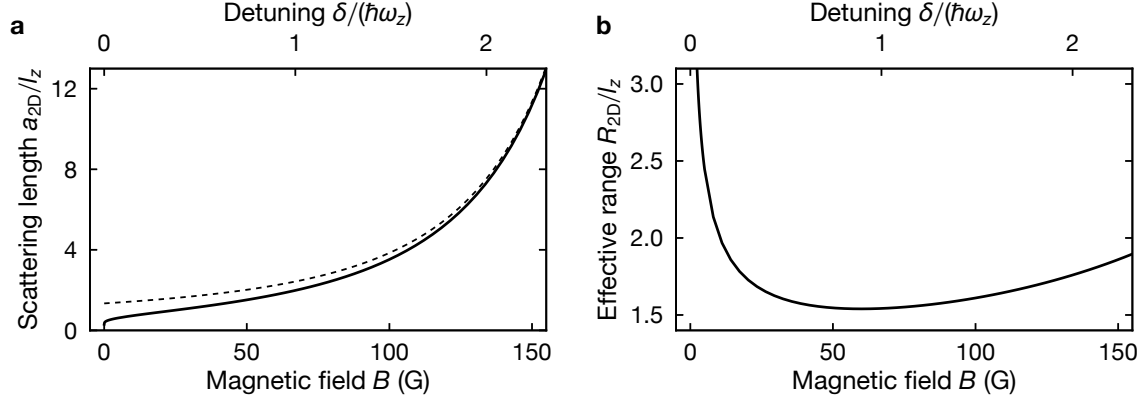


Figure B.1 | Scattering length and effective range for the orbital Feshbach resonance. Magnetic field dependence of the parameters for typical experimental parameters $\omega_z \approx 2\pi \times 37$ kHz and $l_z \approx 750a_0$, where a_0 denotes the Bohr radius. (a) Scattering length a_{2D} (solid line) calculated from Eq. (B.9). Here, the dashed line corresponds to a naive approximation calculated from the bound state energy ε_b alone, $a_{2D} = \hbar/\sqrt{m\varepsilon_b}$ [see Eq. (2.12) in Chapter 2]. (b) Effective range R_{2D} (solid line) calculated from Eq. (B.10).

For the low-energy scattering amplitude, this yields the form

$$f_{q2D}(E) \stackrel{E \rightarrow 0}{\approx} \sqrt{2\pi} \left[\mathcal{A}_0 - \frac{1}{2} \mathcal{A}_1 E - \frac{1}{2\sqrt{2\pi}} \ln(-\pi E/B) - \frac{\ln 2}{2\sqrt{2\pi}} E \right]^{-1} \quad (\text{B.7})$$

$$= \frac{4\pi}{-i\pi - \ln \left[\left(e^{-2\sqrt{2\pi}\mathcal{A}_0} \pi/B \right) E \right] + (\ln 2 - \sqrt{2\pi}\mathcal{A}_1) E}.$$

We note that the complex conjugate of f_{q2D} can be considered equivalently, as the physical observable (scattering cross section) depends on the squared complex modulus $\sim |f_{q2D}|^2$.

By direct comparison of the above expression with the low-energy scattering amplitude of the two-channel model [see Eq. (2.27) from Chapter 2],

$$f_{2ch}(E) = \frac{4\pi}{i\pi - \ln(a_{2D}^2 E) + R_{2D}^2 E}, \quad (\text{B.8})$$

we identify the scattering length and effective range given in Eqs. (2.28) and (2.29),

$$\frac{a_{2D}}{l_z} = \sqrt{\frac{\pi}{B}} \exp \left[-\sqrt{2\pi} \frac{\alpha_-^{-1} \alpha_+^{-1} - \frac{1}{2} \mathcal{F}(\Delta) (\alpha_-^{-1} + \alpha_+^{-1})}{\alpha_-^{-1} + \alpha_+^{-1} - 2\mathcal{F}(\Delta)} \right] \quad \text{and} \quad (\text{B.9})$$

$$\left(\frac{R_{2D}}{l_z} \right)^2 = \ln 2 - \sqrt{2\pi} \frac{[\alpha_-^{-1} - \mathcal{F}(\Delta)]^2 \rho_t + [\alpha_+^{-1} - \mathcal{F}(\Delta)]^2 \rho_s + (\alpha_-^{-1} - \alpha_+^{-1})^2 \mathcal{F}'(\Delta)}{[\alpha_-^{-1} + \alpha_+^{-1} - 2\mathcal{F}(\Delta)]^2}. \quad (\text{B.10})$$

Figure B.1 shows these quantities for typical experimental parameters at variable magnetic field. While the effective range diverges at small fields, the value takes a nearly constant value once the singlet and triplet channels fully mix at intermediate fields.

Appendix C Fermi gases in two dimensions

Throughout this section, we use $\beta = 1/(k_B T)$ with temperature T , the fugacity $z = e^{\beta\mu}$ with chemical potential μ , and m generally denotes the atomic mass. In the following, we derive key properties of the homogeneous and harmonically trapped Fermi gas in two dimensions. These results allow us to derive the effective quantities discussed in Chapter 3 (see Section 3.2.1). Following the convention of this chapter, we choose x and z to describe the coordinates in the two-dimensional plane.

C.1 The homogeneous Fermi gas

To describe the homogeneous Fermi gas, we consider periodic boundary conditions in a two-dimensional box with volume $V = L^2$. Considering the number of states within the Fermi sphere of radius k_F , we obtain the total number of particles [202]

$$N = \pi k_F^2 \frac{V}{(2\pi)^2}. \quad (\text{C.1})$$

We use this result to relate the Fermi wave vector and energy to the density $n = N/V$,

$$k_F = \sqrt{4\pi n} \quad \text{and} \quad E_F = \frac{\hbar^2}{2m} k_F^2 = \frac{\hbar^2}{2m} 4\pi n. \quad (\text{C.2})$$

These results will find application in determining the local density approximation of inhomogeneous systems, in particular, the harmonically trapped Fermi gas.

C.2 The harmonically trapped Fermi gas

Our derivation of the relevant quantities starts with Eq. (3.3) from Chapter 3. Integration of the phase space distribution [see Eq. (3.2) in Chapter 3] over momentum in polar coordinates yields the real-space density of the Fermi gas,

$$\begin{aligned} n(\mathbf{r}) &= \frac{1}{(2\pi\hbar)^2} 2\pi \int_0^\infty dp p \frac{1}{e^{\beta U(\mathbf{r})} e^{\beta p^2/(2m)} / z + 1} = \frac{1}{2\pi\hbar^2} \frac{m}{\beta} \int_0^\infty d\xi \frac{1}{e^{\beta U(\mathbf{r})} e^\xi / z + 1} \\ &= -\frac{m}{2\pi\hbar^2\beta} \text{Li}_1[-ze^{-\beta U(\mathbf{r})}] \end{aligned} \quad (\text{C.3})$$

with $\xi = \beta p^2$ and the harmonic oscillator potential $U(\mathbf{r}) = (m/2) \times (\omega_x^2 r_x^2 + \omega_z^2 r_z^2)$. Here, the polylogarithm can be expressed as natural logarithm with $\text{Li}_1(x) = -\ln(1-x)$.

Integration of Eq. (C.3) along the line of sight (z -axis) yields the column density, which we measure in the experiment using absorption imaging,

$$\begin{aligned} n(r_x) &= -\frac{m}{2\pi\hbar^2\beta} \int_{-\infty}^\infty dr_z \text{Li}_1[-ze^{-\beta m(\omega_x^2 r_x^2 + \omega_z^2 r_z^2)/2}] \\ &= -\frac{m}{2\pi\hbar^2\beta} \sqrt{\frac{2\pi}{\beta m \omega_z^2}} \text{Li}_{3/2}[-ze^{-r_x^2/(2\sigma_x^2)}] = -\frac{m\sigma_y}{\sqrt{2\pi}\hbar^2\beta} \text{Li}_{3/2}[-ze^{-r_x^2/(2\sigma_x^2)}]. \end{aligned} \quad (\text{C.4})$$

Here, $\sigma_{x,z}^2 = 1/(\beta m \omega_{x,z}^2)$ and $\text{Li}_s(x)$ denotes the polylogarithmic function of order s . To extract the fugacity $z = e^{\beta\mu}$ from experimental data, we employ the practical fit function

$$n_{\text{fit}}(r_x) = A \frac{\text{Li}_{3/2} \left[-z e^{-r_x^2/(2\sigma_x^2)} \right]}{\text{Li}_{3/2}(-z)} + c \quad (\text{C.5})$$

with the amplitude A and constant offset c . We relate the fugacity to the reduced temperature T/T_F (Fermi temperature $T_F = \mathcal{E}_F/k_B$) by determining the total number of particles

$$N = \int_0^\infty dE \frac{\rho(E)}{e^{\beta E}/z + 1} = \frac{1}{\hbar^2 \omega_x \omega_z} \int_0^\infty dE \frac{E}{e^{\beta E}/z + 1} = -\frac{1}{\hbar^2 \omega_x \omega_z \beta^2} \text{Li}_2(-z), \quad (\text{C.6})$$

which yields $T/T_F = 1/\sqrt{-2 \text{Li}_2(-z)}$ with Dilogarithm $\text{Li}_2(x)$. Note that the density of states takes the form $\rho(E) = E/(\hbar^2 \omega_x \omega_z)$ for the two-dimensional harmonic oscillator [201].

C.3 Effective Fermi energy in the harmonic trap

Our derivation of the effective Fermi energy for the harmonically trapped Fermi gas starts with Eq. (3.7) from Chapter 3. This equation defines the effective Fermi energy ϵ_F sampled by the minority component of a spin-imbalanced mixture,

$$\epsilon_F(\Delta x) = \frac{1}{N_0(\Delta x)} \frac{\hbar^2}{2m} 4\pi \int_{-\Delta x/2}^{+\Delta x/2} dr_x \int_{-\infty}^{\infty} dr_z n_0(\mathbf{r}) n_\uparrow(\mathbf{r}) \quad (\text{C.7})$$

with $N_0(\Delta x)$ the atom number of the minority fraction in the region of interest defined by $r_x \in [-\Delta x/2, +\Delta x/2]$, and n_0 (n_\uparrow) the density of the minority (majority) component. The above result follows from the Fermi energy of a homogeneous two-dimensional Fermi gas, as discussed in Appendix C.1. First, we calculate the total atom number in the region of interest by integrating Eq. (C.4),

$$N(\Delta x) = -\frac{m\sigma_z}{\sqrt{2\pi\hbar^2\beta}} \int_{-\Delta x/2}^{+\Delta x/2} dr_x \text{Li}_{3/2} \left[-z e^{-x^2/(2\sigma_x^2)} \right] = -\frac{2m\sigma_y\sigma_x}{\sqrt{\pi\hbar^2\beta}} \int_0^{\Delta\eta/2} d\eta \text{Li}_{3/2} \left(-z e^{-\eta^2} \right). \quad (\text{C.8})$$

Here, we have used that the integral features a symmetry, $\eta = x/(\sqrt{2}\sigma_x)$, and $\Delta\eta = \Delta x/(\sqrt{2}\sigma_x)$. Relating the effective Fermi energy ϵ_F to $\mathcal{E}_F = \hbar\sqrt{2N\omega_x\omega_z}$ yields a dimensionless equation with the fugacity z_0 (z_\uparrow) of the minority (majority) component,

$$\frac{\epsilon_F(\Delta\eta)}{\mathcal{E}_F} = -\frac{1}{\sqrt{-2\pi \text{Li}_2(-z_\uparrow)}} \frac{\int_0^{\Delta\eta/2} d\eta \int_{-\infty}^{\infty} d\zeta \text{Li}_1 \left(-z_0 e^{-\eta^2-\zeta^2} \right) \text{Li}_1 \left(-z_\uparrow e^{-\eta^2-\zeta^2} \right)}{\int_0^{\Delta\eta/2} d\eta \text{Li}_{3/2} \left(-z_0 e^{-\eta^2} \right)}. \quad (\text{C.9})$$

The value of this expression can be obtained from numerical integration for the region of interest determined by $\Delta\eta$, which implicitly depends on the temperature and the trapping frequency ω_x .

C.4 Integrals of polylogarithmic functions

Finally, we show the technique to solve a generic form of integral relevant in multiple equations of Appendices C.2 and C.3, e. g., Eq. (C.4). The polylogarithm Li_s of order s can be defined as power series on the complex unit disk $|z| < 1$ [298, Eq. 25.12.10],

$$\text{Li}_s(z) = \sum_{k=1}^{\infty} \frac{z^k}{k^s}, \quad (\text{C.10})$$

and by analytic continuation also for $|z| \geq 1$. For constant $\mathcal{A} > 0$, we solve the following integral by employing the power series defined above,

$$\begin{aligned} \int_{-\infty}^{\infty} dx \text{Li}_n(-ze^{-\mathcal{A}x^2}) &= \int_{-\infty}^{\infty} dx \sum_{k=1}^{\infty} \frac{(-ze^{-\mathcal{A}x^2})^k}{k^n} = \sum_{k=1}^{\infty} \frac{(-z)^k}{k^n} \int_{-\infty}^{\infty} dx e^{-k\mathcal{A}x^2} \\ &= \sum_{k=1}^{\infty} \frac{(-z)^k}{k^n} \sqrt{\frac{\pi}{k\mathcal{A}}} = \sqrt{\frac{\pi}{\mathcal{A}}} \sum_{k=1}^{\infty} \frac{(-z)^k}{k^{n+1/2}} = \sqrt{\frac{\pi}{\mathcal{A}}} \text{Li}_{n+1/2}(-z). \end{aligned} \quad (\text{C.11})$$

Appendix D Approximate calculations of the dynamical correlator

In Chapter 4 (see Section 4.3.2), we numerically calculate the dynamical correlator $\mathcal{C}_{k\alpha}(\tau)$ with exact diagonalization techniques for the small system sizes $l = 8$. Here, we employ an approximative method, known as quantum typicality, to study the evolution of this correlator for larger system sizes up to $l = 12$ but restricted to times $\tau \lesssim 10^4 \hbar/t_L$. This range of accessible times is sufficient to explore the dynamics of the system for the moderate mass-imbalance $t_H/t_L \leq 0.1$ and interaction strength $|U|/t_L \leq 10$, as also realized in the experiment.

D.1 Quantum typicality

For system sizes exceeding $l = 8$, the large size of the Hilbert space makes an exact diagonalization of the complete Hamiltonian unfeasible on a desktop computer. Fortunately, the matrix elements are only sparsely filled and can be stored efficiently in the computer's memory. In this way, the action of the Hamiltonian or other operators onto a state can still be calculated relatively quickly. To further reduce the computational cost, we employ (dynamical) quantum typicality, i. e., a feature of a many-body Hamiltonian $\hat{\mathcal{H}}$ and the associated large Hilbert spaces. Remarkably, the expectation value $\langle O \rangle_{\psi_T}$ of an operator O calculated for a weighted random state $|\psi_T\rangle$ can sufficiently approximate the expectation value of the thermal ensemble $\langle O \rangle_T \sim \text{Tr} \left[O e^{-\hat{\mathcal{H}}/(k_B T)} \right]$ at temperature T [299]. More precisely, this feature can be expressed with the relation

$$\langle O \rangle_T = \langle O \rangle_{\psi_T} + \varepsilon(\hat{\mathcal{H}}) = \frac{\langle \psi_T | O | \psi_T \rangle}{\langle \psi_T | \psi_T \rangle} + \varepsilon(\hat{\mathcal{H}}). \quad (\text{D.1})$$

Here, $|\psi_T\rangle = e^{-\hat{\mathcal{H}}/(2k_B T)} \sum_j (a_j + ib_j) |j\rangle$ denotes a state with the normally distributed (independent) random parameters (a_j, b_j) and $\{|j\rangle\}_j$ an orthonormal basis of the Hilbert space.

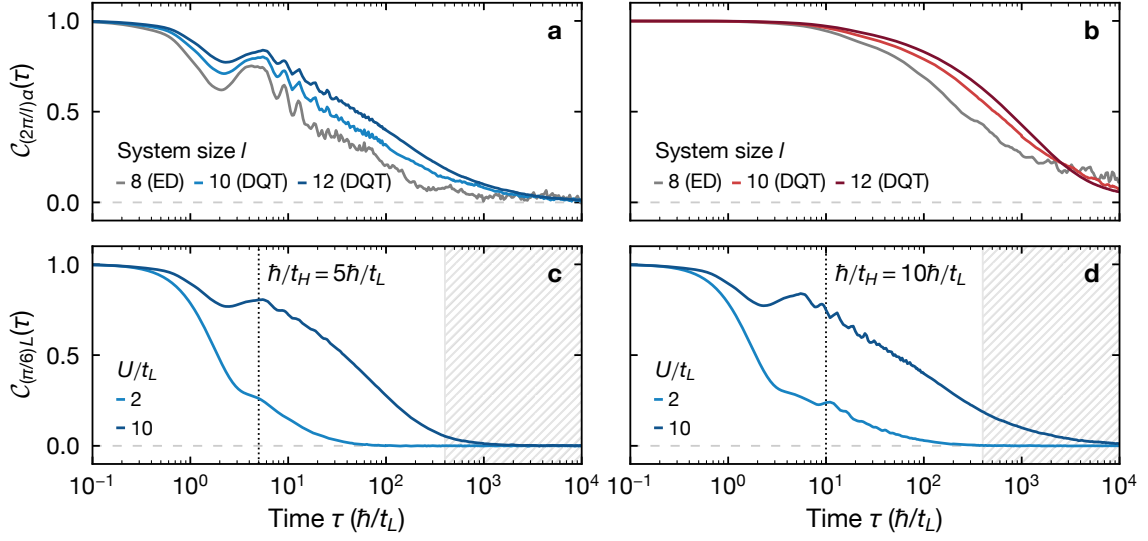


Figure D.1 | Time evolution of the dynamical correlator. Time traces are obtained from evolving a single random state (DQT, $l > 8$) or from exact diagonalization (ED, $l = 8$). The upper panels show the finite-size scaling of the dynamical correlator $C_{(2\pi/l)\alpha}$ (system size l) for the (a) light ($\alpha = L$) and (b) heavy ($\alpha = H$) species with parameters $t_H/t_L = 0.1$ and $U/t_L = 10$. The lower panels display time traces for the experimentally relevant hopping ratios (c) $t_H/t_L = 0.2$ and (d) 0.1 calculated for the light species and the largest accessible system size $l = 12$. The hatched region marks the observation times, which are typically not accessible in the experiment.

For the calculation of $C_{k\alpha}(\tau)$, we are exclusively interested in the infinite-temperature (high-energy) limit, where $e^{\hat{\mathcal{H}}/(2k_B T)} \rightarrow 1$ and all states have equal occupation probability. In this limit, the standard deviation of the error quantity $\varepsilon(\hat{\mathcal{H}})$ scales with $1/\sqrt{d}$ where d denotes the dimension of the Hilbert space [299]. Since d generally grows exponentially with the particle number, the standard deviation is extremely small—even for modest system sizes. Therefore, we can calculate the approximate time evolution of expectation values by time-propagating only a single random state $|\psi_{T=\infty}\rangle \equiv |\psi_r\rangle$.

The concept of quantum typicality is not equivalent to the eigenstate thermalization hypothesis (ETH), which makes a much stronger statement about the matrix elements of observables in the basis of the eigenstates [299]. The random state considered above remains random also in the eigenbasis of the Hamiltonian. Thus, quantum typicality can rather be seen as utilizing the largeness of the Hilbert space and not the structure of the eigenstates, which constitutes the central statement of the ETH.

D.2 Numerical simulations and results

Following the concept of dynamical quantum typicality, we approximate the time evolution of the dynamical correlator,

$$C_{k\alpha}(\tau) \approx \frac{1}{\langle \psi_r | \psi_r \rangle} \text{Re} \left(\left\langle \psi_r \left| \hat{N}_{k\alpha}^\dagger e^{i\tau \hat{\mathcal{H}}_{\text{HLM}}/\hbar} \hat{N}_{k\alpha} e^{-i\tau \hat{\mathcal{H}}_{\text{HLM}}/\hbar} \right| \psi_r \right\rangle \right). \quad (\text{D.2})$$

Here, the action of the time propagator $e^{-i\tau \hat{\mathcal{H}}_{\text{HLM}}/\hbar}$ onto the states $|\psi_r\rangle$ and $\hat{N}_{k\alpha} |\psi_r\rangle$ is numerically approximated by the highly optimized `expm_multiply_parallel` function from the

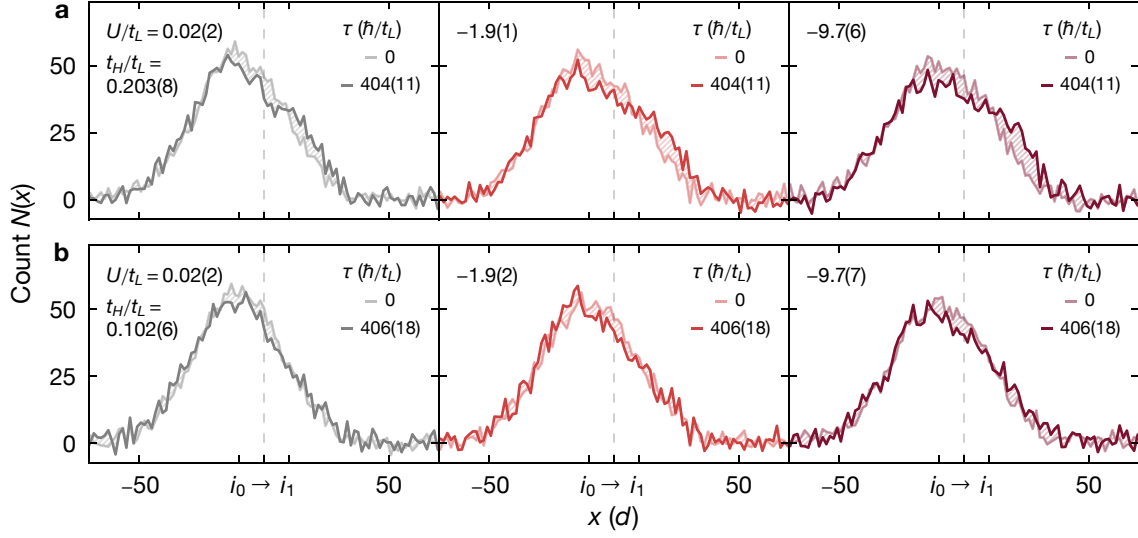


Figure E.1 | Evolution of the non-equilibrium density distribution. Atomic density of the heavy species integrated perpendicular to the transport direction (colored lines) for the hopping ratios (a) $t_H/t_L = 0.203(8)$, (b) $0.102(6)$ and variable interaction strength U/t_L (see top left label in each panel). Each curve is the mean of four individual normalized measurements and corresponds to a variable hold time $\tau \approx 0, 405\hbar/t_L$ after translating the trap minimum from i_0 to i_1 . Note that the density is normalized to their integral value, thereby compensating for a significant loss of heavy atoms at late times. The hatched region highlights the difference between the two curves at different hold times.

software library QUSPIN [236], which implements an algorithm from Ref. [300]. The approximative nature of this procedure has the consequence that the computational cost at constant truncation error increases dramatically with large time steps. With the commodity hardware available to us, the accessible system sizes are limited to $l \leq 12$. Figure D.1 shows the result of this calculation for the experimentally relevant parameters $|U|/t_L = 2, 10$ and $t_H/t_L = 0.1, 0.2$. For increasing system size, we find time traces which exhibit less distinct separation of different time scales [see Figs. D.1(a) and D.1(b)].

Appendix E Density dynamics of the heavy species

Here, we present the raw density of the heavy species after translating the trap minimum, as mentioned in Chapter 5 (see Section 5.4). Figure E.1 shows the corresponding plots for variable interaction strength $U/t_L \approx 0, -2, -10$ and hopping ratios $t_H/t_L \approx 0.1, 0.2$. In particular, for the larger hopping ratio $t_H/t_L \approx 0.2$, a relaxation towards the final trap minimum at i_1 can be observed.

References

- [1] I. Bloch, J. Dalibard, and W. Zwerger, *Many-body physics with ultracold gases*, *Rev. Mod. Phys.* **80**, 885 (2008).
- [2] C. Gross and I. Bloch, *Quantum simulations with ultracold atoms in optical lattices*, *Science* **357**, 995 (2017).
- [3] E. Altman et al., *Quantum Simulators: Architectures and Opportunities*, arXiv:1912.06938.
- [4] R. P. Feynman, *Simulating physics with computers*, *Int. J. Theor. Phys.* **21**, 467 (1982).
- [5] A. C. Hewson, *The Kondo Problem to Heavy Fermions* (Cambridge University Press, Cambridge, 1993).
- [6] P. A. Lee, N. Nagaosa, and X.-G. Wen, *Doping a Mott insulator: Physics of high-temperature superconductivity*, *Rev. Mod. Phys.* **78**, 17 (2006).
- [7] D. I. Khomskii, *Transition Metal Compounds* (Cambridge University Press, Cambridge, 2014).
- [8] J. M. Deutsch, *Quantum statistical mechanics in a closed system*, *Phys. Rev. A* **43**, 2046 (1991).
- [9] M. Srednicki, *Chaos and quantum thermalization*, *Phys. Rev. E* **50**, 888 (1994).
- [10] M. Rigol, V. Dunjko, and M. Olshanii, *Thermalization and its mechanism for generic isolated quantum systems*, *Nature (London)* **452**, 854 (2008).
- [11] L. Tarruell and L. Sanchez-Palencia, *Quantum simulation of the Hubbard model with ultracold fermions in optical lattices*, *C. R. Phys.* **19**, 365 (2018).
- [12] R. Jördens, N. Strohmaier, K. Günter, H. Moritz, and T. Esslinger, *A Mott insulator of fermionic atoms in an optical lattice*, *Nature (London)* **455**, 204 (2008).
- [13] U. Schneider, L. Hackermüller, S. Will, T. Best, I. Bloch, T. A. Costi, R. W. Helmes, D. Rasch, and A. Rosch, *Metallic and Insulating Phases of Repulsively Interacting Fermions in a 3D Optical Lattice*, *Science* **322**, 1520 (2008).
- [14] R. A. Hart, P. M. Duarte, T.-L. Yang, X. Liu, T. Paiva, E. Khatami, R. T. Scalettar, N. Trivedi, D. A. Huse, and R. G. Hulet, *Observation of antiferromagnetic correlations in the Hubbard model with ultracold atoms*, *Nature (London)* **519**, 211 (2015).
- [15] M. Boll, T. A. Hilker, G. Salomon, A. Omran, J. Nespolo, L. Pollet, I. Bloch, and C. Gross, *Spin- and density-resolved microscopy of antiferromagnetic correlations in Fermi-Hubbard chains*, *Science* **353**, 1257 (2016).
- [16] L. W. Cheuk, M. A. Nichols, K. R. Lawrence, M. Okan, H. Zhang, E. Khatami, N. Trivedi, T. Paiva, M. Rigol, and M. W. Zwierlein, *Observation of spatial charge and spin correlations in the 2D Fermi-Hubbard model*, *Science* **353**, 1260 (2016).

-
- [17] J. H. Drewes, L. A. Miller, E. Cocchi, C. F. Chan, N. Wurz, M. Gall, D. Pertot, F. Brennecke, and M. Köhl, *Antiferromagnetic Correlations in Two-Dimensional Fermionic Mott-Insulating and Metallic Phases*, *Phys. Rev. Lett.* **118**, 170401 (2017).
- [18] A. Mazurenko, C. S. Chiu, G. Ji, M. F. Parsons, M. Kanász-Nagy, R. Schmidt, F. Grusdt, E. Demler, D. Greif, and M. Greiner, *A cold-atom Fermi–Hubbard antiferromagnet*, *Nature (London)* **545**, 462 (2017).
- [19] A. V. Gorshkov, M. Hermele, V. Gurarie, C. Xu, P. S. Julienne, J. Ye, P. Zoller, E. Demler, M. D. Lukin, and A. M. Rey, *Two-orbital $SU(N)$ magnetism with ultracold alkaline-earth atoms*, *Nat. Phys.* **6**, 289 (2010).
- [20] M. Foss-Feig, M. Hermele, and A. M. Rey, *Probing the Kondo lattice model with alkaline-earth-metal atoms*, *Phys. Rev. A* **81**, 051603(R) (2010).
- [21] M. Foss-Feig, M. Hermele, V. Gurarie, and A. M. Rey, *Heavy fermions in an optical lattice*, *Phys. Rev. A* **82**, 053624 (2010).
- [22] H. Nonne, E. Boulat, S. Capponi, and P. Lecheminant, *Phase diagram of one-dimensional alkaline-earth cold fermionic atoms*, *Mod. Phys. Lett. B* **25**, 955 (2011).
- [23] J. Silva-Valencia and A. M. C. Souza, *Ground state of alkaline-earth fermionic atoms in one-dimensional optical lattices*, *Eur. Phys. J. B* **85**, 5 (2012).
- [24] I. Kuzmenko, T. Kuzmenko, Y. Avishai, and G.-B. Jo, *Coqblin-Schrieffer model for an ultracold gas of ytterbium atoms with metastable state*, *Phys. Rev. B* **93**, 115143 (2016).
- [25] A. Sotnikov, N. Darkwah Oppong, Y. Zambrano, and A. Cichy, *Orbital ordering of ultracold alkaline-earth atoms in optical lattices*, *Phys. Rev. Research* **2**, 023188 (2020).
- [26] O. Mandel, M. Greiner, A. Widera, T. Rom, T. W. Hänsch, and I. Bloch, *Coherent Transport of Neutral Atoms in Spin-Dependent Optical Lattice Potentials*, *Phys. Rev. Lett.* **91**, 010407 (2003).
- [27] T. Müller, S. Fölling, A. Widera, and I. Bloch, *State Preparation and Dynamics of Ultracold Atoms in Higher Lattice Orbitals*, *Phys. Rev. Lett.* **99**, 200405 (2007).
- [28] B. Gadway, D. Pertot, R. Reimann, and D. Schneble, *Superfluidity of Interacting Bosonic Mixtures in Optical Lattices*, *Phys. Rev. Lett.* **105**, 045303 (2010).
- [29] G. Jotzu, M. Messer, F. Görg, D. Greif, R. Desbuquois, and T. Esslinger, *Creating State-Dependent Lattices for Ultracold Fermions by Magnetic Gradient Modulation*, *Phys. Rev. Lett.* **115**, 073002 (2015).
- [30] C. He, E. Hajiyev, Z. Ren, B. Song, and G.-B. Jo, *Recent progresses of ultracold two-electron atoms*, *J. Phys. B* **52**, 102001 (2019).
- [31] A. D. Ludlow, M. M. Boyd, J. Ye, E. Peik, and P. O. Schmidt, *Optical atomic clocks*, *Rev. Mod. Phys.* **87**, 637 (2015).
- [32] N. Hinkley, J. A. Sherman, N. B. Phillips, M. Schioppo, N. D. Lemke, K. Beloy, M. Pizzocaro, C. W. Oates, and A. D. Ludlow, *An Atomic Clock with 10^{-18} Instability*, *Science* **341**, 1215 (2013).
- [33] T. L. Nicholson, S. L. Campbell, R. B. Hutson, G. E. Marti, B. J. Bloom, R. L. McNally, W. Zhang, M. D. Barrett, M. S. Safronova, G. F. Strouse, W. L. Tew, and J. Ye, *Systematic evaluation of an atomic clock at 2×10^{-18} total uncertainty*, *Nat. Comm.* **6**, 6896 (2015).
- [34] I. Ushijima, M. Takamoto, M. Das, T. Ohkubo, and H. Katori, *Cryogenic optical lattice clocks with a relative frequency difference of 1×10^{-18}* , [arXiv:1405.4071](https://arxiv.org/abs/1405.4071).
- [35] P. Wcisło et al., *New bounds on dark matter coupling from a global network of optical atomic clocks*, *Sci. Adv.* **4**, eaau4869 (2018).

- [36] C. J. Kennedy, E. Oelker, J. M. Robinson, T. Bothwell, D. Kedar, W. R. Milner, G. E. Marti, A. Derevianko, and J. Ye, *Precision Metrology Meets Cosmology: Improved Constraints on Ultralight Dark Matter from Atom-Cavity Frequency Comparisons*, *Phys. Rev. Lett.* **125**, 201302 (2020).
- [37] M. A. Cazalilla, A. F. Ho, and M. Ueda, *Ultracold gases of ytterbium: ferromagnetism and Mott states in an $SU(6)$ Fermi system*, *New J. Phys.* **11**, 103033 (2009).
- [38] M. A. Cazalilla and A. M. Rey, *Ultracold Fermi gases with emergent $SU(N)$ symmetry*, *Rep. Prog. Phys.* **77**, 124401 (2014).
- [39] F. Gerbier and J. Dalibard, *Gauge fields for ultracold atoms in optical superlattices*, *New J. Phys.* **12**, 033007 (2010).
- [40] D. Banerjee, M. Bögli, M. Dalmonte, E. Rico, P. Stebler, U.-J. Wiese, and P. Zoller, *Atomic Quantum Simulation of $U(N)$ and $SU(N)$ Non-Abelian Lattice Gauge Theories*, *Phys. Rev. Lett.* **110**, 125303 (2013).
- [41] C. Laflamme, W. Evans, M. Dalmonte, U. Gerber, H. Mejía-Díaz, W. Bietenholz, U.-J. Wiese, and P. Zoller, *$CP(N-1)$ quantum field theories with alkaline-earth atoms in optical lattices*, *Ann. Phys.* **370**, 117 (2016).
- [42] A. J. Daley, M. M. Boyd, J. Ye, and P. Zoller, *Quantum Computing with Alkaline-Earth-Metal Atoms*, *Phys. Rev. Lett.* **101**, 170504 (2008).
- [43] L. Riegger, N. Darkwah Oppong, M. Höfer, D. R. Fernandes, I. Bloch, and S. Fölling, *Localized Magnetic Moments with Tunable Spin Exchange in a Gas of Ultracold Fermions*, *Phys. Rev. Lett.* **120**, 143601 (2018).
- [44] A. Heinz, A. J. Park, N. Šantić, J. Trautmann, S. G. Porsev, M. S. Safronova, I. Bloch, and S. Blatt, *State-dependent optical lattices for the strontium optical qubit*, *Phys. Rev. Lett.* **124**, 203201 (2020).
- [45] K. Ono, Y. Amano, T. Higomoto, Y. Saito, and Y. Takahashi, *Observation of spin-exchange dynamics between itinerant and localized ^{171}Yb atoms*, [arXiv:2012.08708](https://arxiv.org/abs/2012.08708).
- [46] F. Scazza, C. Hofrichter, M. Höfer, P. C. De Groot, I. Bloch, and S. Fölling, *Observation of two-orbital spin-exchange interactions with ultracold $SU(N)$ -symmetric fermions*, *Nat. Phys.* **10**, 779 (2014).
- [47] G. Cappellini, M. Mancini, G. Pagano, P. Lombardi, L. Livi, M. Siciliani de Cumis, P. Cancio, M. Pizzocaro, D. Calonico, F. Levi, C. Sias, J. Catani, M. Inguscio, and L. Fallani, *Direct Observation of Coherent Interorbital Spin-Exchange Dynamics*, *Phys. Rev. Lett.* **113**, 120402 (2014).
- [48] Y. Takasu, K. Komori, K. Honda, M. Kumakura, T. Yabuzaki, and Y. Takahashi, *Photoassociation Spectroscopy of Laser-Cooled Ytterbium Atoms*, *Phys. Rev. Lett.* **93**, 123202 (2004).
- [49] X. Zhang, M. Bishof, S. L. Bromley, C. V. Kraus, M. S. Safronova, P. Zoller, A. M. Rey, and J. Ye, *Spectroscopic observation of $SU(N)$ -symmetric interactions in Sr orbital magnetism*, *Science* **345**, 1467 (2014).
- [50] L. Franchi, L. F. Livi, G. Cappellini, G. Binella, M. Inguscio, J. Catani, and L. Fallani, *State-dependent interactions in ultracold ^{174}Yb probed by optical clock spectroscopy*, *New J. Phys.* **19**, 103037 (2017).
- [51] R. Bouganne, M. B. Aguilera, A. Dureau, E. Soave, J. Beugnon, and F. Gerbier, *Clock spectroscopy of interacting bosons in deep optical lattices*, *New J. Phys.* **19**, 113006 (2017).
- [52] A. Goban, R. B. Hutson, G. E. Marti, S. L. Campbell, M. A. Perlin, P. S. Julienne, J. P. D’Incao, A. M. Rey, and J. Ye, *Emergence of multi-body interactions in a fermionic lattice clock*, *Nature (London)* **563**, 369 (2018).

-
- [53] K. Ono, J. Kobayashi, Y. Amano, K. Sato, and Y. Takahashi, *Antiferromagnetic interorbital spin-exchange interaction of ^{171}Yb* , *Phys. Rev. A* **99**, 032707 (2019).
- [54] R. Zhang, Y. Cheng, H. Zhai, and P. Zhang, *Orbital Feshbach Resonance in Alkali-Earth Atoms*, *Phys. Rev. Lett.* **115**, 135301 (2015).
- [55] M. Höfer, L. Riegger, F. Scazza, C. Hofrichter, D. R. Fernandes, M. M. Parish, J. Levinsen, I. Bloch, and S. Fölling, *Observation of an Orbital Interaction-Induced Feshbach Resonance in ^{173}Yb* , *Phys. Rev. Lett.* **115**, 265302 (2015).
- [56] G. Pagano, M. Mancini, G. Cappellini, L. Livi, C. Sias, J. Catani, M. Inguscio, and L. Fallani, *Strongly Interacting Gas of Two-Electron Fermions at an Orbital Feshbach Resonance*, *Phys. Rev. Lett.* **115**, 265301 (2015).
- [57] R. Zhang, Y. Cheng, P. Zhang, and H. Zhai, *Controlling the interaction of ultracold alkaline-earth atoms*, *Nat. Rev. Phys.* **2**, 213 (2020).
- [58] A. J. Leggett, S. Chakravarty, A. T. Dorsey, M. P. A. Fisher, A. Garg, and W. Zwerger, *Dynamics of the dissipative two-state system*, *Rev. Mod. Phys.* **59**, 1 (1987).
- [59] M. Knap, D. A. Abanin, and E. Demler, *Dissipative Dynamics of a Driven Quantum Spin Coupled to a Bath of Ultracold Fermions*, *Phys. Rev. Lett.* **111**, 265302 (2013).
- [60] H. Fröhlich, *Electrons in lattice fields*, *Adv. Phys.* **3**, 325 (1954).
- [61] J. Kondo, *Resistance Minimum in Dilute Magnetic Alloys*, *Prog. Theor. Phys.* **32**, 37 (1964).
- [62] P. W. Anderson, *Infrared Catastrophe in Fermi Gases with Local Scattering Potentials*, *Phys. Rev. Lett.* **18**, 1049 (1967).
- [63] L. D. Landau, *The Theory of a Fermi Liquid*, *J. Exptl. Theoret. Phys.* **3**, 920 (1956).
- [64] F. Chevy, *Universal phase diagram of a strongly interacting Fermi gas with unbalanced spin populations*, *Phys. Rev. A* **74**, 063628 (2006).
- [65] R. Combescot, A. Recati, C. Lobo, and F. Chevy, *Normal State of Highly Polarized Fermi Gases: Simple Many-Body Approaches*, *Phys. Rev. Lett.* **98**, 180402 (2007).
- [66] P. Massignan, M. Zaccanti, and G. M. Bruun, *Polarons, dressed molecules and itinerant ferromagnetism in ultracold Fermi gases*, *Rep. Prog. Phys.* **77**, 034401 (2014).
- [67] J.-G. Chen, T.-S. Deng, W. Yi, and W. Zhang, *Polarons and molecules in a Fermi gas with orbital Feshbach resonance*, *Phys. Rev. A* **94**, 053627 (2016).
- [68] T.-S. Deng, Z.-C. Lu, Y.-R. Shi, J.-G. Chen, W. Zhang, and W. Yi, *Repulsive polarons in alkaline-earth-metal-like atoms across an orbital Feshbach resonance*, *Phys. Rev. A* **97**, 013635 (2018).
- [69] J. Xu and R. Qi, *Polaronic and dressed molecular states in orbital Feshbach resonances*, *Eur. Phys. J. D* **72**, 65 (2018).
- [70] J.-G. Chen, Y.-R. Shi, X. Zhang, and W. Zhang, *Polarons in alkaline-earth-like atoms with multiple background Fermi surfaces*, *Front. Phys.* **13**, 136702 (2018).
- [71] A. Schirotzek, C.-H. Wu, A. Sommer, and M. W. Zwierlein, *Observation of Fermi Polarons in a Tunable Fermi Liquid of Ultracold Atoms*, *Phys. Rev. Lett.* **102**, 230402 (2009).
- [72] S. Nascimbène, N. Navon, K. J. Jiang, L. Tarruell, M. Teichmann, J. McKeever, F. Chevy, and C. Salomon, *Collective Oscillations of an Imbalanced Fermi Gas: Axial Compression Modes and Polaron Effective Mass*, *Phys. Rev. Lett.* **103**, 170402 (2009).
- [73] C. Kohstall, M. Zaccanti, M. Jag, A. Trenkwalder, P. Massignan, G. M. Bruun, F. Schreck, and R. Grimm, *Metastability and coherence of repulsive polarons in a strongly interacting Fermi mixture*, *Nature (London)* **485**, 615 (2012).

- [74] M. Koschorreck, D. Pertot, E. Vogt, B. Fröhlich, M. Feld, and M. Köhl, *Attractive and repulsive Fermi polarons in two dimensions*, *Nature (London)* **485**, 619 (2012).
- [75] W. Ong, C. Cheng, I. Arakelyan, and J. E. Thomas, *Spin-Imbalanced Quasi-Two-Dimensional Fermi Gases*, *Phys. Rev. Lett.* **114**, 110403 (2015).
- [76] F. Scazza, G. Valtolina, P. Massignan, A. Recati, A. Amico, A. Burchianti, C. Fort, M. Inguscio, M. Zaccanti, and G. Roati, *Repulsive Fermi Polarons in a Resonant Mixture of Ultracold ^6Li Atoms*, *Phys. Rev. Lett.* **118**, 083602 (2017).
- [77] L. Pollet, *Recent developments in quantum Monte Carlo simulations with applications for cold gases*, *Rep. Prog. Phys.* **75**, 094501 (2012).
- [78] R. Schmidt, M. Knap, D. A. Ivanov, J.-S. You, M. Cetina, and E. Demler, *Universal many-body response of heavy impurities coupled to a Fermi sea: a review of recent progress*, *Rep. Prog. Phys.* **81**, 024401 (2018).
- [79] S. Pilati, G. Bertaina, S. Giorgini, and M. Troyer, *Itinerant Ferromagnetism of a Repulsive Atomic Fermi Gas: A Quantum Monte Carlo Study*, *Phys. Rev. Lett.* **105**, 030405 (2010).
- [80] R. Schmidt and T. Enss, *Excitation spectra and rf response near the polaron-to-molecule transition from the functional renormalization group*, *Phys. Rev. A* **83**, 063620 (2011).
- [81] P. Massignan and G. M. Bruun, *Repulsive polarons and itinerant ferromagnetism in strongly polarized Fermi gases*, *Eur. Phys. J. D* **65**, 83 (2011).
- [82] M. Cetina, M. Jag, R. S. Lous, I. Fritsche, J. T. M. Walraven, R. Grimm, J. Levinsen, M. M. Parish, R. Schmidt, M. Knap, and E. Demler, *Ultrafast many-body interferometry of impurities coupled to a Fermi sea*, *Science* **354**, 96 (2016).
- [83] Z. Yan, P. B. Patel, B. Mukherjee, R. J. Fletcher, J. Struck, and M. W. Zwierlein, *Boiling a Unitary Fermi Liquid*, *Phys. Rev. Lett.* **122**, 093401 (2019).
- [84] G. Ness, C. Shkedrov, Y. Florshaim, O. K. Diessel, J. von Milczewski, R. Schmidt, and Y. Sagi, *Observation of a Smooth Polaron-Molecule Transition in a Degenerate Fermi Gas*, *Phys. Rev. X* **10**, 041019 (2020).
- [85] M. Sidler, P. Back, O. Cotlet, A. Srivastava, T. Fink, M. Kroner, E. Demler, and A. Imamoglu, *Fermi polaron-polaritons in charge-tunable atomically thin semiconductors*, *Nat. Phys.* **13**, 255 (2016).
- [86] T. Kinoshita, T. Wenger, and D. S. Weiss, *A quantum Newton's cradle*, *Nature (London)* **440**, 900 (2006).
- [87] M. Gring, M. Kuhnert, T. Langen, T. Kitagawa, B. Rauer, M. Schreitl, I. Mazets, D. A. Smith, E. Demler, and J. Schmiedmayer, *Relaxation and Prethermalization in an Isolated Quantum System*, *Science* **337**, 1318 (2012).
- [88] S. Trotzky, Y.-A. Chen, A. Flesch, I. P. McCulloch, U. Schollwöck, J. Eisert, and I. Bloch, *Probing the relaxation towards equilibrium in an isolated strongly correlated one-dimensional Bose gas*, *Nat. Phys.* **8**, 325 (2012).
- [89] T. Langen, R. Geiger, M. Kuhnert, B. Rauer, and J. Schmiedmayer, *Local emergence of thermal correlations in an isolated quantum many-body system*, *Nat. Phys.* **9**, 640 (2013).
- [90] U. Schollwöck, *The density-matrix renormalization group in the age of matrix product states*, *Ann. Phys.* **326**, 96 (2011).
- [91] M. Schreiber, S. S. Hodgman, P. Bordia, H. P. Lüschen, M. H. Fischer, R. Vosk, E. Altman, U. Schneider, and I. Bloch, *Observation of many-body localization of interacting fermions in a quasi-random optical lattice*, *Science* **349**, 842 (2015).

-
- [92] J.-y. Choi, S. Hild, J. Zeiher, P. Schauß, A. Rubio-Abadal, T. Yefsah, V. Khemani, D. A. Huse, I. Bloch, and C. Gross, *Exploring the many-body localization transition in two dimensions*, *Science* **352**, 1547 (2016).
- [93] D. A. Abanin, E. Altman, I. Bloch, and M. Serbyn, *Colloquium: Many-body localization, thermalization, and entanglement*, *Rev. Mod. Phys.* **91**, 021001 (2019).
- [94] N. Y. Yao, C. R. Laumann, and A. Vishwanath, *Many-body localization protected quantum state transfer*, [arXiv:1508.06995](https://arxiv.org/abs/1508.06995).
- [95] S. Choi, N. Y. Yao, S. Gopalakrishnan, and M. D. Lukin, *Quantum Control of Many-body Localized States*, [arXiv:1508.06992](https://arxiv.org/abs/1508.06992).
- [96] J. Smith, A. Lee, P. Richerme, B. Neyenhuis, P. W. Hess, P. Hauke, M. Heyl, D. A. Huse, and C. Monroe, *Many-body localization in a quantum simulator with programmable random disorder*, *Nat. Phys.* **12**, 907 (2016).
- [97] P. Roushan et al., *Spectroscopic signatures of localization with interacting photons in superconducting qubits*, *Science* **358**, 1175 (2017).
- [98] E. Altman and R. Vosk, *Universal Dynamics and Renormalization in Many-Body-Localized Systems*, *Annu. Rev. Condens. Matter Phys.* **6**, 383 (2015).
- [99] R. Nandkishore and D. A. Huse, *Many-Body Localization and Thermalization in Quantum Statistical Mechanics*, *Annu. Rev. Condens. Matter Phys.* **6**, 15 (2015).
- [100] D. A. Abanin and Z. Papić, *Recent progress in many-body localization*, *Ann. Phys.* **529**, 1700169 (2017).
- [101] W. De Roeck and F. Huveneers, *Asymptotic Quantum Many-Body Localization from Thermal Disorder*, *Comm. Math. Phys.* **332**, 1017 (2014).
- [102] M. Schiulaz and M. Müller, *Ideal quantum glass transitions: Many-body localization without quenched disorder*, *AIP Conf. Proc.* **1610**, 11 (2014).
- [103] M. Schiulaz, A. Silva, and M. Müller, *Dynamics in many-body localized quantum systems without disorder*, *Phys. Rev. B* **91**, 184202 (2015).
- [104] Z. Papić, E. M. Stoudenmire, and D. A. Abanin, *Many-body localization in disorder-free systems: The importance of finite-size constraints*, *Ann. Phys.* **362**, 714 (2015).
- [105] N. Y. Yao, C. R. Laumann, J. I. Cirac, M. D. Lukin, and J. E. Moore, *Quasi-Many-Body Localization in Translation-Invariant Systems*, *Phys. Rev. Lett.* **117**, 240601 (2016).
- [106] M. Brenes, M. Dalmonte, M. Heyl, and A. Scardicchio, *Many-Body Localization Dynamics from Gauge Invariance*, *Phys. Rev. Lett.* **120**, 030601 (2018).
- [107] Y. Kagan and L. A. Maksimov, *Localization in a subsystem of interacting particles diffusing in a regular crystal*, *JETP* **60**, 201 (1984).
- [108] N. Darkwah Oppong, G. Pasqualetti, O. Bettermann, P. Zechmann, M. Knap, I. Bloch, and S. Fölling, *Probing transport and slow relaxation in the mass-imbalanced Fermi-Hubbard model*, [arXiv:2011.12411](https://arxiv.org/abs/2011.12411).
- [109] N. Darkwah Oppong, L. Riegger, O. Bettermann, M. Höfer, J. Levinsen, M. M. Parish, I. Bloch, and S. Fölling, *Observation of Coherent Multiorbital Polarons in a Two-Dimensional Fermi Gas*, *Phys. Rev. Lett.* **122**, 193604 (2019).
- [110] H. S. Adlong, W. E. Liu, F. Scazza, M. Zaccanti, N. Darkwah Oppong, S. Fölling, M. M. Parish, and J. Levinsen, *Quasiparticle Lifetime of the Repulsive Fermi Polaron*, *Phys. Rev. Lett.* **125**, 133401 (2020).

- [111] O. Bettermann, N. Darkwah Oppong, G. Pasqualetti, L. Riegger, I. Bloch, and S. Fölling, *Clock-line photoassociation of strongly bound dimers in a magic-wavelength lattice*, [arXiv:2003.10599](https://arxiv.org/abs/2003.10599).
- [112] S. L. Campbell, R. B. Hutson, G. E. Marti, A. Goban, N. Darkwah Oppong, R. L. McNally, L. Sonderhouse, J. M. Robinson, W. Zhang, B. J. Bloom, and J. Ye, *A Fermi-degenerate three-dimensional optical lattice clock*, *Science* **358**, 90 (2017).
- [113] J. Emsley, *The elements* (Oxford University Press, New York, 1998).
- [114] M. S. Safronova, D. Budker, D. DeMille, D. F. J. Kimball, A. Derevianko, and C. W. Clark, *Search for new physics with atoms and molecules*, *Rev. Mod. Phys.* **90**, 025008 (2018).
- [115] A. Kramida, Y. Ralchenko, J. Reader, and NIST ASD Team, *NIST Atomic Spectra Database*, available online at <https://physics.nist.gov/asd> (version 5.8).
- [116] B. H. Bransden and C. J. Joachain, *Physics of atoms and molecules* (Pearson Education, Essex, 2003).
- [117] M. M. Boyd, T. Zelevinsky, A. D. Ludlow, S. Blatt, T. Zanon-Willette, S. M. Foreman, and J. Ye, *Nuclear spin effects in optical lattice clocks*, *Phys. Rev. A* **76**, 022510 (2007).
- [118] K. Beloy, J. A. Sherman, N. D. Lemke, N. Hinkley, C. W. Oates, and A. D. Ludlow, *Determination of the $5d6s\ ^3D_1$ state lifetime and blackbody-radiation clock shift in Yb*, *Phys. Rev. A* **86**, 051404(R) (2012).
- [119] S. G. Porsev and A. Derevianko, *Hyperfine quenching of the metastable $^3P_{0,2}$ states in divalent atoms*, *Phys. Rev. A* **69**, 042506 (2004).
- [120] J. W. Cho, H.-g. Lee, S. Lee, J. Ahn, W.-K. Lee, D.-H. Yu, S. K. Lee, and C. Y. Park, *Optical repumping of triplet-P states enhances magneto-optical trapping of ytterbium atoms*, *Phys. Rev. A* **85**, 035401 (2012).
- [121] F. Scazza, *Probing $SU(N)$ -symmetric orbital interactions with ytterbium Fermi gases in optical lattices*, *Ph.D. thesis*, Ludwigs-Maximilians-Universität München (2015).
- [122] A. V. Taichenachev, V. I. Yudin, C. W. Oates, C. W. Hoyt, Z. W. Barber, and L. Hollberg, *Magnetic Field-Induced Spectroscopy of Forbidden Optical Transitions with Application to Lattice-Based Optical Atomic Clocks*, *Phys. Rev. Lett.* **96**, 083001 (2006).
- [123] BIPM, *Le Système international d'unités / The International System of Units ('The SI Brochure')* (Bureau international des poids et mesures, 2019).
- [124] C. W. Chou, D. B. Hume, T. Rosenband, and D. J. Wineland, *Optical Clocks and Relativity*, *Science* **329**, 1630 (2010).
- [125] M. Takamoto, I. Ushijima, N. Ohmae, T. Yahagi, K. Kokado, H. Shinkai, and H. Katori, *Test of general relativity by a pair of transportable optical lattice clocks*, *Nat. Photonics* **14**, 411 (2020).
- [126] A. Messiah, *Quantum Mechanics*, Vol. 2 (North Holland Publishing Company, Amsterdam, 1965).
- [127] T. Busch, B.-G. Englert, K. Rzazewski, and M. Wilkens, *Two Cold Atoms in a Harmonic Trap*, *Found. Phys.* **28**, 549 (1998).
- [128] W. V. Liu, F. Wilczek, and P. Zoller, *Spin-dependent Hubbard model and a quantum phase transition in cold atoms*, *Phys. Rev. A* **70**, 033603 (2004).
- [129] C. Hofrichter, *Probing the $SU(N)$ Fermi-Hubbard model with ytterbium atoms in an optical lattice*, *Ph.D. thesis*, Ludwig-Maximilians-Universität München (2016).

-
- [130] M. Kitagawa, K. Enomoto, K. Kasa, Y. Takahashi, R. Ciuryło, P. Naidon, and P. S. Julienne, *Two-color photoassociation spectroscopy of ytterbium atoms and the precise determinations of s-wave scattering lengths*, *Phys. Rev. A* **77**, 012719 (2008).
- [131] B. Abeln, K. Sponselee, M. Diem, N. Pintul, K. Sengstock, and C. Becker, *Interorbital Interactions in an $SU(2)\times SU(6)$ -Symmetric Fermi-Fermi Mixture*, [arXiv:2012.11544](https://arxiv.org/abs/2012.11544).
- [132] L. Riegger, *Interorbital spin exchange in a state-dependent optical lattice*, *Ph.D. thesis*, Ludwig-Maximilians-Universität München (2019).
- [133] C. Chin, R. Grimm, P. Julienne, and E. Tiesinga, *Feshbach resonances in ultracold gases*, *Rev. Mod. Phys.* **82**, 1225 (2010).
- [134] M. Höfer, *A two-orbital quantum gas with tunable interactions*, *Ph.D. thesis*, Ludwig-Maximilians-Universität München (2017).
- [135] O. Bettermann, *Ph.D. thesis*, Ludwigs-Maximilians-Universität München, in preparation.
- [136] R. Grimm, M. Weidemüller, Y. B. Ovchinnikov, B. Bederson, and H. Walther, *Optical Dipole Traps for Neutral Atoms*, in *Advances in atomic, molecular, and optical physics*, Vol. 42 (Academic Press, 2000), 95.
- [137] N. D. Lemke, A. D. Ludlow, Z. W. Barber, T. M. Fortier, S. A. Diddams, Y. Jiang, S. R. Jefferts, T. P. Heavner, T. E. Parker, and C. W. Oates, *Spin-1/2 Optical Lattice Clock*, *Phys. Rev. Lett.* **103**, 063001 (2009).
- [138] D. A. Steck, *Quantum and Atom Optics*, available online at <http://steck.us/teaching> (revision 0.10.3, 13 April 2016).
- [139] S. G. Porsev, Y. G. Rakhлина, and M. G. Kozlov, *Electric-dipole amplitudes, lifetimes, and polarizabilities of the low-lying levels of atomic ytterbium*, *Phys. Rev. A* **60**, 2781 (1999).
- [140] V. A. Dzuba and A. Derevianko, *Dynamic polarizabilities and related properties of clock states of the ytterbium atom*, *J. Phys. B* **43**, 074011 (2010).
- [141] H. P. Büchler, *Microscopic Derivation of Hubbard Parameters for Cold Atomic Gases*, *Phys. Rev. Lett.* **104**, 090402 (2010).
- [142] G. J. van den Berg, *Anomalies in Dilute Metallic Solutions of Transition Metals*, in *Low temperature physics LT9* (1965), 955.
- [143] P. Coleman, *Heavy Fermions: Electrons at the Edge of Magnetism*, in *Handbook of magnetism and advanced magnetic materials* (2007).
- [144] K. G. Wilson, *The renormalization group: Critical phenomena and the Kondo problem*, *Rev. Mod. Phys.* **47**, 773 (1975).
- [145] D. C. Ralph and R. A. Buhrman, *Kondo-assisted and resonant tunneling via a single charge trap: A realization of the Anderson model out of equilibrium*, *Phys. Rev. Lett.* **72**, 3401 (1994).
- [146] S. M. Cronenwett, T. H. Oosterkamp, and L. P. Kouwenhoven, *A Tunable Kondo Effect in Quantum Dots*, *Science* **281**, 540 (1998).
- [147] D. Goldhaber-Gordon, H. Shtrikman, D. Mahalu, D. Abusch-Magder, U. Meirav, and M. A. Kastner, *Kondo effect in a single-electron transistor*, *Nature (London)* **391**, 156 (1998).
- [148] W. G. van der Wiel, S. D. Franceschi, T. Fujisawa, J. M. Elzerman, S. Tarucha, and L. P. Kouwenhoven, *The Kondo Effect in the Unitary Limit*, *Science* **289**, 2105 (2000).
- [149] C. Latta, F. Haupt, M. Hanl, A. Weichselbaum, M. Claassen, W. Wuester, P. Fallahi, S. Faelt, L. Glazman, J. von Delft, H. E. Türeci, and A. Imamoglu, *Quantum quench of Kondo correlations in optical absorption*, *Nature (London)* **474**, 627 (2011).

- [150] J. Park, S.-S. B. Lee, Y. Oreg, and H.-S. Sim, *How to Directly Measure a Kondo Cloud's Length*, *Phys. Rev. Lett.* **110**, 246603 (2013).
- [151] I. V. Borzenets, J. Shim, J. C. H. Chen, A. Ludwig, A. D. Wieck, S. Tarucha, H. -S. Sim, and M. Yamamoto, *Observation of the Kondo screening cloud*, *Nature (London)* **579**, 210 (2020).
- [152] H. Prüser, P. E. Dargel, M. Bouhassoune, R. G. Ulbrich, T. Pruschke, S. Lounis, and M. Wenderoth, *Interplay between the Kondo effect and the Ruderman–Kittel–Kasuya–Yosida interaction*, *Nat. Comm.* **5**, 5417 (2014).
- [153] R. Zhang, D. Zhang, Y. Cheng, W. Chen, P. Zhang, and H. Zhai, *Kondo effect in alkaline-earth-metal atomic gases with confinement-induced resonances*, *Phys. Rev. A* **93**, 043601 (2016).
- [154] M. Kanász-Nagy, Y. Ashida, T. Shi, C. P. Moca, T. N. Ikeda, S. Fölling, J. I. Cirac, G. Zaránd, and E. A. Demler, *Exploring the anisotropic Kondo model in and out of equilibrium with alkaline-earth atoms*, *Phys. Rev. B* **97**, 155156 (2018).
- [155] S. Goto and I. Danshita, *Quasiexact Kondo Dynamics of Fermionic Alkaline-Earth-Like Atoms at Finite Temperatures*, *Phys. Rev. Lett.* **123**, 143002 (2019).
- [156] A. A. Abrikosov, *Electron scattering on magnetic impurities in metals and anomalous resistivity effects*, *Phys. Phys. Fiz.* **2**, 5 (1965).
- [157] A. Gleis, S.-S. B. Lee, and J. von Delft, private communications, Dec. 2019.
- [158] R. Yamamoto, J. Kobayashi, T. Kuno, K. Kato, and Y. Takahashi, *An ytterbium quantum gas microscope with narrow-line laser cooling*, *New J. Phys.* **18**, 023016 (2016).
- [159] R. Yamamoto, J. Kobayashi, K. Kato, T. Kuno, Y. Sakura, and Y. Takahashi, *Site-resolved imaging of single atoms with a Faraday quantum gas microscope*, *Phys. Rev. A* **96**, 033610 (2017).
- [160] M. Miranda, R. Inoue, N. Tambo, and M. Kozuma, *Site-resolved imaging of a bosonic Mott insulator using ytterbium atoms*, *Phys. Rev. A* **96**, 043626 (2017).
- [161] C. Hooley and J. Quintanilla, *Single-Atom Density of States of an Optical Lattice*, *Phys. Rev. Lett.* **93**, 080404 (2004).
- [162] J. Korringa, *Nuclear magnetic relaxation and resonance line shift in metals*, *Physica* **16**, 601 (1950).
- [163] J. Kondo, *The Physics of Dilute Magnetic Alloys* (Cambridge University Press, New York, 2012).
- [164] G. Pasqualetti, *Isotopic mixtures of ytterbium for quantum simulation of Kondo physics*, Master thesis, Ludwig–Maximilians–Universität München (2018).
- [165] R. V. Pound, *Electronic Frequency Stabilization of Microwave Oscillators*, *Rev. Sci. Instrum.* **17**, 490 (1946).
- [166] R. W. P. Drever, J. L. Hall, F. V. Kowalski, J. Hough, G. M. Ford, A. J. Munley, and H. Ward, *Laser phase and frequency stabilization using an optical resonator*, *Appl. Phys. B* **31**, 97 (1983).
- [167] A. Impertro, *Improvement of a laser system to drive the ultranarrow clock transition in ^{173}Yb* , Praktikumsbericht, Sept. 2019.
- [168] G. Pasqualetti, *Design and characterization of a repump laser for clock state detection using the $^3P_0 \rightarrow ^3D_1$ transition in ^{173}Yb* , Praktikumsbericht, Aug. 2017.
- [169] C. Tornow, *Stabilisierung eines Lasers für den 3P_0 - 3D_1 -Übergang von Ytterbium*, Bachelor thesis, Ludwig-Maximilians-Universität München (2019).
- [170] C.-L. Hung, X. Zhang, L.-C. Ha, S.-K. Tung, N. Gemelke, and C. Chin, *Extracting density–density correlations from in situ images of atomic quantum gases*, *New J. Phys.* **13**, 075019 (2011).

-
- [171] G. Reinaudi, T. Lahaye, Z. Wang, and D. Guéry-Odelin, *Strong saturation absorption imaging of dense clouds of ultracold atoms*, *Opt. Lett.* **32**, 3143 (2007).
- [172] S.-i. Tomonaga, *Remarks on Bloch's Method of Sound Waves applied to Many-Fermion Problems*, *Prog. Theor. Phys.* **5**, 544 (1950).
- [173] J. M. Luttinger, *An Exactly Soluble Model of a Many-Fermion System*, *J. Math. Phys.* **4**, 1154 (1963).
- [174] M. Kutschera and W. Wójcik, *Proton impurity in the neutron matter: A nuclear polaron problem*, *Phys. Rev. C* **47**, 1077 (1993).
- [175] M. M. Forbes, A. Gezerlis, K. Hebeler, T. Lesinski, and A. Schwenk, *Neutron polaron as a constraint on nuclear density functionals*, *Phys. Rev. C* **89**, 041301 (2014).
- [176] R. Schmidt, T. Enss, V. Pietilä, and E. Demler, *Fermi polarons in two dimensions*, *Phys. Rev. A* **85**, 021602(R) (2012).
- [177] M. M. Parish and J. Levinsen, *Highly polarized Fermi gases in two dimensions*, *Phys. Rev. A* **87**, 033616 (2013).
- [178] A. L. Fetter and J. D. Walecka, *Quantum Theory of Many-Particle Systems* (Dover, New York, 2003).
- [179] T. Lancaster and S. J. Blundell, *Quantum Field Theory for the Gifted Amateur* (Oxford University Press, New York, 2014).
- [180] R. Haussmann, M. Punk, and W. Zwerger, *Spectral functions and rf response of ultracold fermionic atoms*, *Phys. Rev. A* **80**, 063612 (2009).
- [181] D. S. Petrov and G. V. Shlyapnikov, *Interatomic collisions in a tightly confined Bose gas*, *Phys. Rev. A* **64**, 012706 (2001).
- [182] J. Levinsen and M. M. Parish, *Strongly interacting two-dimensional Fermi gases*, in *Annual review of cold atoms and molecules*, Vol. 3 (2015).
- [183] P. Bloom, *Two-dimensional Fermi gas*, *Phys. Rev. B* **12**, 125 (1975).
- [184] M. Klawunn and A. Recati, *Fermi polaron in two dimensions: Importance of the two-body bound state*, *Phys. Rev. A* **84**, 033607 (2011).
- [185] M. M. Parish, *Polaron-molecule transitions in a two-dimensional Fermi gas*, *Phys. Rev. A* **83**, 051603(R) (2011).
- [186] J. Vlietinck, J. Ryckebusch, and K. Van Houcke, *Diagrammatic Monte Carlo study of the Fermi polaron in two dimensions*, *Phys. Rev. B* **89**, 085119 (2014).
- [187] P. Kroiss and L. Pollet, *Diagrammatic Monte Carlo study of quasi-two-dimensional Fermi polarons*, *Phys. Rev. B* **90**, 104510 (2014).
- [188] S. Zöllner, G. M. Bruun, and C. J. Pethick, *Polarons and molecules in a two-dimensional Fermi gas*, *Phys. Rev. A* **83**, 021603(R) (2011).
- [189] R. Liu, Y.-R. Shi, and W. Zhang, *Non-Gaussian variational approach to Fermi polarons in one- and two-dimensional lattices*, *Phys. Rev. A* **102**, 033305 (2020).
- [190] V. Ngampruetikorn, J. Levinsen, and M. M. Parish, *Repulsive polarons in two-dimensional Fermi gases*, *Europhys. Lett.* **98**, 30005 (2012).
- [191] H. Tajima and S. Uchino, *Thermal crossover, transition, and coexistence in Fermi polaronic spectroscopies*, *Phys. Rev. A* **99**, 063606 (2019).

- [192] B. C. Mulkerin, X.-J. Liu, and H. Hu, *Breakdown of the Fermi polaron description near Fermi degeneracy at unitarity*, *Ann. Phys.* **407**, 29 (2019).
- [193] W. E. Liu, Z.-Y. Shi, J. Levinsen, and M. M. Parish, *Radio-Frequency Response and Contact of Impurities in a Quantum Gas*, *Phys. Rev. Lett.* **125**, 065301 (2020).
- [194] H. Hu, B. C. Mulkerin, J. Wang, and X.-J. Liu, *Attractive Fermi polarons at nonzero temperatures with a finite impurity concentration*, *Phys. Rev. A* **98**, 013626 (2018).
- [195] H. Tajima and S. Uchino, *Many Fermi polarons at nonzero temperature*, *New J. Phys.* **20**, 073048 (2018).
- [196] H. Takahasi and M. Mori, *Double exponential formulas for numerical integration*, *Publ. Res. Inst. Math. Sci.* **9**, 721 (1974).
- [197] W. E. Liu, J. Levinsen, and M. M. Parish, *Variational Approach for Impurity Dynamics at Finite Temperature*, *Phys. Rev. Lett.* **122**, 205301 (2019).
- [198] T. Kirk and M. M. Parish, *Three-body correlations in a two-dimensional $SU(3)$ Fermi gas*, *Phys. Rev. A* **96**, 053614 (2017).
- [199] S. Taie, Y. Takasu, S. Sugawa, R. Yamazaki, T. Tsujimoto, R. Murakami, and Y. Takahashi, *Realization of a $SU(2) \times SU(6)$ System of Fermions in a Cold Atomic Gas*, *Phys. Rev. Lett.* **105**, 190401 (2010).
- [200] S. Giorgini, L. P. Pitaevskii, and S. Stringari, *Theory of ultracold atomic Fermi gases*, *Rev. Mod. Phys.* **80**, 1215 (2008).
- [201] K. Kirsten and D. J. Toms, *Density of states for Bose-Einstein condensation in harmonic oscillator potentials*, *Phys. Lett. A* **222**, 148 (1996).
- [202] C. Kittel, *Introduction to Solid State Physics* (Wiley, New York, 2004).
- [203] Wolfram Research, *SkewNormalDistribution*, available online at <https://reference.wolfram.com/language/ref/SkewNormalDistribution.html> (updated 2016).
- [204] R. Bombín, V. Cikojević, J. Sánchez-Baena, and J. Boronat, *Finite-range effects in the two-dimensional repulsive Fermi polaron*, *arXiv:2008.10510*.
- [205] M. M. Parish and J. Levinsen, *Quantum dynamics of impurities coupled to a Fermi sea*, *Phys. Rev. B* **94**, 184303 (2016).
- [206] E. C. Stoner, *LXXX. Atomic moments in ferromagnetic metals and alloys with non-ferromagnetic elements*, *Philos. Mag.* **15**, 1018 (1933).
- [207] G.-B. Jo, Y.-R. Lee, J.-H. Choi, C. A. Christensen, T. H. Kim, J. H. Thywissen, D. E. Pritchard, and W. Ketterle, *Itinerant Ferromagnetism in a Fermi Gas of Ultracold Atoms*, *Science* **325**, 1521 (2009).
- [208] H. Zhai, *Correlated versus ferromagnetic state in repulsively interacting two-component Fermi gases*, *Phys. Rev. A* **80**, 051605(R) (2009).
- [209] C. Sanner, E. J. Su, W. Huang, A. Keshet, J. Gillen, and W. Ketterle, *Correlations and Pair Formation in a Repulsively Interacting Fermi Gas*, *Phys. Rev. Lett.* **108**, 240404 (2012).
- [210] G. Valtolina, F. Scazza, A. Amico, A. Burchianti, A. Recati, T. Enss, M. Inguscio, M. Zaccanti, and G. Roati, *Exploring the ferromagnetic behaviour of a repulsive Fermi gas through spin dynamics*, *Nat. Phys.* **13**, 704 (2017).
- [211] F. Scazza, G. Valtolina, A. Amico, P. E. S. Tavares, M. Inguscio, W. Ketterle, G. Roati, and M. Zaccanti, *Exploring emergent heterogeneous phases in strongly repulsive Fermi gases*, *Phys. Rev. A* **101**, 013603 (2020).

-
- [212] V. Ngampruetikorn, M. M. Parish, and J. Levinsen, *Three-body problem in a two-dimensional Fermi gas*, *Europhys. Lett.* **102**, 13001 (2013).
- [213] H. Zhao, J. Zhang, M. Lyu, S. Bachus, Y. Tokiwa, P. Gegenwart, S. Zhang, J. Cheng, Y.-f. Yang, G. Chen, Y. Isikawa, Q. Si, F. Steglich, and P. Sun, *Quantum-critical phase from frustrated magnetism in a strongly correlated metal*, *Nat. Phys.* **15**, 1261 (2019).
- [214] E. K. Laird, Z.-Y. Shi, M. M. Parish, and J. Levinsen, *Frustrated orbital Feshbach resonances in a Fermi gas*, *Phys. Rev. A* **101**, 022707 (2020).
- [215] J. R. Engelbrecht and M. Randeria, *Low-density repulsive Fermi gas in two dimensions: Bound-pair excitations and Fermi-liquid behavior*, *Phys. Rev. B* **45**, 12419 (1992).
- [216] J. R. Engelbrecht, M. Randeria, and L. Zhang, *Landau f function for the dilute Fermi gas in two dimensions*, *Phys. Rev. B* **45**, 10135 (1992).
- [217] A. F. Impetro, *Preparation and Study of 1D and 2D Many-Body Systems with Fermionic Ytterbium*, Master thesis, Ludwig-Maximilians-Universität München (2020).
- [218] W. Greiner, L. Niese, and H. Stöcker, *Thermodynamics and Statistical Mechanics* (Springer-Verlag, New York, 1997).
- [219] L. D'Alessio, Y. Kafri, A. Polkovnikov, and M. Rigol, *From quantum chaos and eigenstate thermalization to statistical mechanics and thermodynamics*, *Adv. Phys.* **65**, 239 (2016).
- [220] A. M. Kaufman, M. E. Tai, A. Lukin, M. Rispoli, R. Schittko, P. M. Preiss, and M. Greiner, *Quantum thermalization through entanglement in an isolated many-body system*, *Science* **353**, 794 (2016).
- [221] M. H. Anderson, J. R. Ensher, M. R. Matthews, C. E. Wieman, and E. A. Cornell, *Observation of Bose-Einstein Condensation in a Dilute Atomic Vapor*, *Science* **269**, 198 (1995).
- [222] C. C. Bradley, C. A. Sackett, J. J. Tollett, and R. G. Hulet, *Evidence of Bose-Einstein Condensation in an Atomic Gas with Attractive Interactions*, *Phys. Rev. Lett.* **75**, 1687 (1995).
- [223] K. B. Davis, M. -O. Mewes, M. R. Andrews, N. J. van Druten, D. S. Durfee, D. M. Kurn, and W. Ketterle, *Bose-Einstein Condensation in a Gas of Sodium Atoms*, *Phys. Rev. Lett.* **75**, 3969 (1995).
- [224] H. Wu and C. J. Foot, *Direct simulation of evaporative cooling*, *J. Phys. B* **29**, L321 (1996).
- [225] M. Srednicki, *The approach to thermal equilibrium in quantized chaotic systems*, *J. Phys. A* **32**, 1163 (1999).
- [226] P. W. Anderson, *Absence of Diffusion in Certain Random Lattices*, *Phys. Rev.* **109**, 1492 (1958).
- [227] P. A. Lee and T. V. Ramakrishnan, *Disordered electronic systems*, *Rev. Mod. Phys.* **57**, 287 (1985).
- [228] J. Billy, V. Josse, Z. Zuo, A. Bernard, B. Hambrecht, P. Lugan, D. Clément, L. Sanchez-Palencia, P. Bouyer, and A. Aspect, *Direct observation of Anderson localization of matter waves in a controlled disorder*, *Nature (London)* **453**, 891 (2008).
- [229] G. Roati, C. D'Errico, L. Fallani, M. Fattori, C. Fort, M. Zaccanti, G. Modugno, M. Modugno, and M. Inguscio, *Anderson localization of a non-interacting Bose-Einstein condensate*, *Nature (London)* **453**, 895 (2008).
- [230] D. S. Wiersma, P. Bartolini, A. Lagendijk, and R. Righini, *Localization of light in a disordered medium*, *Nature (London)* **390**, 671 (1997).
- [231] L. Fleishman and P. W. Anderson, *Interactions and the Anderson transition*, *Phys. Rev. B* **21**, 2366 (1980).
- [232] A. Pal and D. A. Huse, *Many-body localization phase transition*, *Phys. Rev. B* **82**, 174411 (2010).

-
- [233] H. P. Lüschen, P. Bordia, S. Scherg, F. Alet, E. Altman, U. Schneider, and I. Bloch, *Observation of Slow Dynamics near the Many-Body Localization Transition in One-Dimensional Quasiperiodic Systems*, *Phys. Rev. Lett.* **119**, 260401 (2017).
- [234] M. Rispoli, A. Lukin, R. Schittko, S. Kim, M. E. Tai, J. Léonard, and M. Greiner, *Quantum critical behaviour at the many-body localization transition*, *Nature (London)* **573**, 385 (2019).
- [235] J. Eisert, M. Cramer, and M. B. Plenio, *Colloquium: Area laws for the entanglement entropy*, *Rev. Mod. Phys.* **82**, 277 (2010).
- [236] P. Weinberg and M. Bukov, *QuSpin: a Python Package for Dynamics and Exact Diagonalisation of Quantum Many Body Systems. Part II: bosons, fermions and higher spins*, *SciPost Phys.* **7**, 20 (2019).
- [237] R. Vosk and E. Altman, *Many-Body Localization in One Dimension as a Dynamical Renormalization Group Fixed Point*, *Phys. Rev. Lett.* **110**, 067204 (2013).
- [238] M. Serbyn, Z. Papić, and D. A. Abanin, *Local Conservation Laws and the Structure of the Many-Body Localized States*, *Phys. Rev. Lett.* **111**, 127201 (2013).
- [239] D. A. Huse, R. Nandkishore, and V. Oganesyan, *Phenomenology of fully many-body-localized systems*, *Phys. Rev. B* **90**, 174202 (2014).
- [240] A. Lukin, M. Rispoli, R. Schittko, M. E. Tai, A. M. Kaufman, S. Choi, V. Khemani, J. Léonard, and M. Greiner, *Probing entanglement in a many-body-localized system*, *Science* **364**, 256 (2019).
- [241] B. Chiaro et al., *Direct measurement of non-local interactions in the many-body localized phase*, [arXiv:1910.06024](https://arxiv.org/abs/1910.06024).
- [242] Y. Tang, W. Kao, K.-Y. Li, S. Seo, K. Mallayya, M. Rigol, S. Gopalakrishnan, and B. L. Lev, *Thermalization near Integrability in a Dipolar Quantum Newton's Cradle*, *Phys. Rev. X* **8**, 021030 (2018).
- [243] S. S. Kondov, W. R. McGehee, W. Xu, and B. DeMarco, *Disorder-Induced Localization in a Strongly Correlated Atomic Hubbard Gas*, *Phys. Rev. Lett.* **114**, 083002 (2015).
- [244] T. Grover and M. P. A. Fisher, *Quantum disentangled liquids*, *J. Stat. Mech.: Theory Exp.* **2014**, P10010 (2014).
- [245] W. De Roeck and F. Huveneers, *Scenario for delocalization in translation-invariant systems*, *Phys. Rev. B* **90**, 165137 (2014).
- [246] A. Smith, J. Knolle, D. L. Kovrizhin, and R. Moessner, *Disorder-Free Localization*, *Phys. Rev. Lett.* **118**, 266601 (2017).
- [247] M. Schulz, C. A. Hooley, R. Moessner, and F. Pollmann, *Stark Many-Body Localization*, *Phys. Rev. Lett.* **122**, 040606 (2019).
- [248] J. Sirker, *Exploration of the existence of a distinct quasi many-body localized phase: Numerical study of a translationally invariant system in the thermodynamic limit*, *Phys. Rev. B* **99**, 075162 (2019).
- [249] E. van Nieuwenburg, Y. Baum, and G. Refael, *From Bloch oscillations to many-body localization in clean interacting systems*, *Proc. Natl. Acad. Sci. U.S.A.* **116**, 9269 (2019).
- [250] F. Jin, R. Steinigeweg, F. Heidrich-Meisner, K. Michielsen, and H. De Raedt, *Finite-temperature charge transport in the one-dimensional Hubbard model*, *Phys. Rev. B* **92**, 205103 (2015).
- [251] T. Heitmann, J. Richter, T. Dahm, and R. Steinigeweg, *Density dynamics in the mass-imbalanced Hubbard chain*, *Phys. Rev. B* **102**, 045137 (2020).

-
- [252] U. Schneider, L. Hackermüller, J. P. Ronzheimer, S. Will, S. Braun, T. Best, I. Bloch, E. Demler, S. Mandt, D. Rasch, and A. Rosch, *Fermionic transport and out-of-equilibrium dynamics in a homogeneous Hubbard model with ultracold atoms*, *Nat. Phys.* **8**, 213 (2012).
- [253] J. Yu, N. Sun, and H. Zhai, *Symmetry Protected Dynamical Symmetry in the Generalized Hubbard Models*, *Phys. Rev. Lett.* **119**, 225302 (2017).
- [254] B. Sutherland, *Beautiful Models* (World Scientific, Singapore, 2004).
- [255] L. M. Falicov and J. C. Kimball, *Simple Model for Semiconductor-Metal Transitions: SrB_6 and Transition-Metal Oxides*, *Phys. Rev. Lett.* **22**, 997 (1969).
- [256] C. Gruber and N. Macris, *The Falicov-Kimball model: a review of exact results and extensions*, *Helv. Phys. Acta* **69**, 850 (1996).
- [257] T. Kennedy and E. H. Lieb, *An itinerant electron model with crystalline or magnetic long range order*, *Physica A* **138**, 320 (1986).
- [258] I. V. Plyushchay, R. A. Römer, and M. Schreiber, *Three-dimensional Anderson model of localization with binary random potential*, *Phys. Rev. B* **68**, 064201 (2003).
- [259] D. Thouless, *Electrons in disordered systems and the theory of localization*, *Phys. Rep.* **13**, 93 (1974).
- [260] P. Jordan and E. Wigner, *Über das Paulische Äquivalenzverbot*, *Z. Phys.* **47**, 631 (1928).
- [261] E. Koch, *The Lanczos Method*, in *The LDA+DMFT approach to strongly correlated materials*, Vol. 1, edited by E. Pavarini, E. Koch, D. Vollhardt, and A. Lichtenstein (Forschungszentrum Jülich, Jülich, 2011).
- [262] H. Bernien, S. Schwartz, A. Keesling, H. Levine, A. Omran, H. Pichler, S. Choi, A. Zibrov, M. Endres, M. Greiner, V. Vuletic, and M. D. Lukin, *Probing many-body dynamics on a 51-atom quantum simulator*, *Nature (London)* **551**, 579 (2017).
- [263] E. Guardado-Sanchez, B. M. Spar, P. Schauss, R. Belyansky, J. T. Young, P. Bienias, A. V. Gorshkov, T. Iadecola, and W. S. Bakr, *Quench Dynamics of a Fermi Gas with Strong Long-Range Interactions*, [arXiv:2010.05871](https://arxiv.org/abs/2010.05871).
- [264] D. Bluvstein, A. Omran, H. Levine, A. Keesling, G. Semeghini, S. Ebadi, T. T. Wang, A. A. Michailidis, N. Maskara, W. W. Ho, S. Choi, M. Serbyn, M. Greiner, V. Vuletic, and M. D. Lukin, *Controlling many-body dynamics with driven quantum scars in Rydberg atom arrays*, [arXiv:2012.12276](https://arxiv.org/abs/2012.12276).
- [265] E. Guardado-Sanchez, A. Morningstar, B. M. Spar, P. T. Brown, D. A. Huse, and W. S. Bakr, *Subdiffusion and Heat Transport in a Tilted Two-Dimensional Fermi-Hubbard System*, *Phys. Rev. X* **10**, 011042 (2020).
- [266] S. Scherg, T. Kohlert, P. Sala, F. Pollmann, B. H. M., I. Bloch, and M. Aidelsburger, *Observing non-ergodicity due to kinetic constraints in tilted Fermi-Hubbard chains*, [arXiv:2010.12965](https://arxiv.org/abs/2010.12965).
- [267] R. Rausch and M. Potthoff, *Filling-dependent doublon dynamics in the one-dimensional Hubbard model*, *Phys. Rev. B* **95**, 045152 (2017).
- [268] P. Zechmann, Master thesis, Technische Universität München, in preparation.
- [269] M. Köhl, *Thermometry of fermionic atoms in an optical lattice*, *Phys. Rev. A* **73**, 031601 (2006).
- [270] G. H. Wannier, *Dynamics of Band Electrons in Electric and Magnetic Fields*, *Rev. Mod. Phys.* **34**, 645 (1962).

- [271] H. Ott, E. de Mirandes, F. Ferlaino, G. Roati, G. Modugno, and M. Inguscio, *Collisionally Induced Transport in Periodic Potentials*, *Phys. Rev. Lett.* **92**, 160601 (2004).
- [272] G. Orso, L. P. Pitaevskii, and S. Stringari, *Umklapp Collisions and Center-of-Mass Oscillations of a Trapped Fermi Gas*, *Phys. Rev. Lett.* **93**, 020404 (2004).
- [273] L. Pezzè, L. Pitaevskii, A. Smerzi, S. Stringari, G. Modugno, E. de Mirandes, F. Ferlaino, H. Ott, G. Roati, and M. Inguscio, *Insulating Behavior of a Trapped Ideal Fermi Gas*, *Phys. Rev. Lett.* **93**, 120401 (2004).
- [274] M. Rigol and A. Muramatsu, *Confinement control by optical lattices*, *Phys. Rev. A* **70**, 043627 (2004).
- [275] N. Strohmaier, Y. Takasu, K. Günter, R. Jördens, M. Köhl, H. Moritz, and T. Esslinger, *Interaction-Controlled Transport of an Ultracold Fermi Gas*, *Phys. Rev. Lett.* **99**, 220601 (2007).
- [276] M. Schulz, C. A. Hooley, and R. Moessner, *Slow relaxation and sensitivity to disorder in trapped lattice fermions after a quench*, *Phys. Rev. A* **94**, 063643 (2016).
- [277] T. Chanda, R. Yao, and J. Zakrzewski, *Coexistence of localized and extended phases: Many-body localization in a harmonic trap*, *Phys. Rev. Research* **2**, 032039(R) (2020).
- [278] S. Paeckel, T. Köhler, A. Swoboda, S. R. Manmana, U. Schollwöck, and C. Hubig, *Time-Evolution Methods for Matrix-Product States*, *Ann. Phys. (N. Y.)* **411**, 167998 (2019).
- [279] B. Efron and C. Stein, *The Jackknife Estimate of Variance*, *Ann. Stat.* **9**, 586 (1981).
- [280] K. Sponselee, L. Freystatzky, B. Abeln, M. Diem, B. Hundt, A. Kochanke, T. Ponath, B. Santra, L. Mathey, K. Sengstock, and C. Becker, *Dynamics of ultracold quantum gases in the dissipative Fermi–Hubbard model*, *Quantum Sci. Technol.* **4**, 014002 (2018).
- [281] M. McNeil Forbes, E. Gubankova, W. V. Liu, and F. Wilczek, *Stability Criteria for Breached-Pair Superfluidity*, *Phys. Rev. Lett.* **94**, 017001 (2005).
- [282] M. Iskin, *Two-band superfluidity and intrinsic Josephson effect in alkaline-earth-metal Fermi gases across an orbital Feshbach resonance*, *Phys. Rev. A* **94**, 011604 (2016).
- [283] J. Xu, R. Zhang, Y. Cheng, P. Zhang, R. Qi, and H. Zhai, *Reaching a Fermi-superfluid state near an orbital Feshbach resonance*, *Phys. Rev. A* **94**, 033609 (2016).
- [284] M. Iskin, *Trapped ^{173}Yb Fermi gas across an orbital Feshbach resonance*, *Phys. Rev. A* **95**, 013618 (2017).
- [285] P. Zou, L. He, X.-J. Liu, and H. Hu, *Strongly interacting Sarma superfluid near orbital Feshbach resonances*, *Phys. Rev. A* **97**, 043616 (2018).
- [286] D. Yu, W. Zhang, and W.-M. Liu, *Enhanced Fulde-Ferrell-Larkin-Ovchinnikov and Sarma superfluid states near an orbital Feshbach resonance*, *Phys. Rev. A* **100**, 053612 (2019).
- [287] K. Yamamoto, M. Nakagawa, K. Adachi, K. Takasan, M. Ueda, and N. Kawakami, *Theory of Non-Hermitian Fermionic Superfluidity with a Complex-Valued Interaction*, *Phys. Rev. Lett.* **123**, 123601 (2019).
- [288] A. Recati, P. O. Fedichev, W. Zwerger, J. von Delft, and P. Zoller, *Atomic Quantum Dots Coupled to a Reservoir of a Superfluid Bose-Einstein Condensate*, *Phys. Rev. Lett.* **94**, 040404 (2005).
- [289] J. Goold, T. Fogarty, N. Lo Gullo, M. Paternostro, and T. Busch, *Orthogonality catastrophe as a consequence of qubit embedding in an ultracold Fermi gas*, *Phys. Rev. A* **84**, 063632 (2011).
- [290] M. Knap, A. Shashi, Y. Nishida, A. Imambekov, D. A. Abanin, and E. Demler, *Time-Dependent Impurity in Ultracold Fermions: Orthogonality Catastrophe and Beyond*, *Phys. Rev. X* **2**, 041020 (2012).

-
- [291] A. Cooper, J. P. Covey, I. S. Madjarov, S. G. Porsev, M. S. Safronova, and M. Endres, *Alkaline-Earth Atoms in Optical Tweezers*, *Phys. Rev. X* **8**, 041055 (2018).
- [292] M. A. Norcia, A. W. Young, and A. M. Kaufman, *Microscopic Control and Detection of Ultracold Strontium in Optical-Tweezer Arrays*, *Phys. Rev. X* **8**, 041054 (2018).
- [293] S. Saskin, J. T. Wilson, B. Grinkemeyer, and J. D. Thompson, *Narrow-Line Cooling and Imaging of Ytterbium Atoms in an Optical Tweezer Array*, *Phys. Rev. Lett.* **122**, 143002 (2019).
- [294] M. R. Sturm, M. Schlosser, G. Birkl, and R. Walser, *Rapid generation of Mott insulators from arrays of noncondensed atoms*, *Phys. Rev. A* **97**, 063608 (2018).
- [295] B. Yang, H. Sun, R. Ott, H.-Y. Wang, T. V. Zache, J. C. Halimeh, Z.-S. Yuan, P. Hauke, and J.-W. Pan, *Observation of gauge invariance in a 71-site Bose–Hubbard quantum simulator*, *Nature (London)* **587**, 392 (2020).
- [296] W. Morong, F. Liu, P. Becker, K. S. Collins, L. Feng, A. Kyprianidis, G. Pagano, T. You, A. V. Gorshkov, and C. Monroe, *Observation of Stark many-body localization without disorder*, [arXiv:2102.07250](https://arxiv.org/abs/2102.07250).
- [297] B. Bertini, F. Heidrich-Meisner, C. Karrasch, T. Prosen, R. Steinigeweg, and M. Znidaric, *Finite-temperature transport in one-dimensional quantum lattice models*, [arXiv:2003.03334](https://arxiv.org/abs/2003.03334).
- [298] F. W. J. Olver, D. W. Lozier, R. F. Boisvert, and C. W. Clark, eds., *NIST Handbook of Mathematical Functions* (Cambridge University Press, New York, 2010).
- [299] T. Heitmann, J. Richter, D. Schubert, and R. Steinigeweg, *Selected applications of typicality to real-time dynamics of quantum many-body systems*, *Z. Naturforsch. A* **75**, 421 (2020).
- [300] A. H. Al-Mohy and N. J. Higham, *Computing the action of the matrix exponential, with an application to exponential integrators*, *SIAM J. Sci. Comput.* **33**, 488 (2011).

Acknowledgements

I thank Immanuel Bloch for supervising my thesis work and giving me the opportunity to join his research group, which has been an extraordinarily privileged and exciting experience. Throughout my time in Munich, I have continuously admired his positive spirit, excellent ideas, and exceptional understanding of many-body physics. Also, I would like to thank Simon Fölling for managing and overseeing our work on the ytterbium experiment. I greatly appreciate that he has always been available to discuss physics while, at the same time, has given us the freedom to explore things on our own. Even today, I am still impressed by the depth of his knowledge and intuitive access to physical mechanisms.

I acknowledge funding from the International Max Planck Research School for Quantum Science and Technology (IMPRS-QST) and thank Sonya Gzyl for coordinating this great program. In addition, I wish to thank Jun Ye for encouraging me to pursue a Ph. D. in the first place, and being part of my thesis advisory board within the IMPRS-QST program.

Our experimental work is a team effort, and I am especially indebted to my colleagues who have worked on the ytterbium experiment during the last four and a half years: Diogo Rio Fernandes, Moritz Höfer, Luis Riegger, Oscar Bettermann, and Giulio Pasqualetti. I have really enjoyed working with this group of highly talented people. While my time on the experiment did not overlap with the first generation of students and postdocs, I still wish to express my thanks to them, particularly Francesco Scazza and Christian Hofrichter, for building a fantastic apparatus. Moreover, I also thank the group leaders, postdocs, and my fellow graduate students in the Bloch group for many friendly and interesting discussions, especially during our group retreats.

Various technical advancements have enabled our experimental studies, and I would like to give thanks to the many students and interns working on such projects and contributing to our experiments: Torsten Bähr, Giulio Pasqualetti, Maximilian Rinnagel, Javid Javadzade, Benjamin Schiffer, Florian Fertig, Alexander Impertro, and Caroline Tornow.

We have been extremely fortunate to have support from theory collaborators for both experiments discussed in this thesis. In particular, I would like to thank Haydn Adlong, Meera Parish, and Jesper Levinsen, as well as Philip Zechmann and Michael Knap, for the fruitful collaboration and numerous insightful discussions about various aspects of physics. I am indebted to Haydn Adlong and Philip Zechmann for openly sharing their numerical results, which partly found their way into this thesis.

Also, I acknowledge many fruitful discussions with Agnieszka Cichy, Andrii Sotnikov, Eugene Demler, Richard Schmidt, as well as Jan von Delft and his research group.

For their help with various aspects of our research work, I would like to thank the staff at LMU and MPQ, especially: Ildiko Kecskesi, Bodo Hecker, Kristina Schuldt, Doreen Seidl, Karsten Förster, Olivia Mödl, Anton Mayer, the team from the purchasing department at MPQ, as well as Jürgen Aust and the team from the LMU workshop.

Last but not least, I thank my family for their continuous support and Sarah for her understanding and great patience during the ups and downs of my graduate education.